The Etiologies of White Matter Damage in Aging and Alzheimer's Disease

By

Elizabeth Ellen Moore

Dissertation
Submitted to the Faculty of the
Graduate School of Vanderbilt University
in partial fulfillment of the requirements
for the degree of

DOCTOR OF PHILOSOPHY

in

Neuroscience

June 30, 2021

Nashville, Tennessee

Approved:

Timothy J. Hohman, Ph.D.

Angela L. Jefferson, Ph.D.

Bennett A. Landman, Ph.D.

Matthew S. Schrag, M.D., Ph.D.

Danny G. Winder, Ph.D.

Henrik Zetterberg, M.D., Ph.D.

DEDICATION

To my grandmother, who taught me there is nothing I can’t handle. From, your baby doll.

ACKNOWLEDGEMENTS

I would like to thank the Vanderbilt Memory and Aging Project participants and their loved ones who made this work possible. I would also like to thank the Vanderbilt MSTP, the Vanderbilt Memory and Alzheimer's Center, and my funding (F30-AG064847). I would like to thank my committee for providing excellent mentorship and sponsorship over the last three years, especially Drs. Timothy Hohman and Angela Jefferson. I would like to thank Dr. Chris Williams and the entire MSTP leadership team and my MSTPeeps for their support, guidance, and friendship. Finally, I would like to thank my family, who have supported me from the very beginning in everything I do.

TABLE OF CONTENTS

LIST OF TABLES

LIST OF FIGURES

Figure Page

CHAPTER 1

INTRODUCTION

Alzheimer's Disease

Alzheimer's disease (AD) is the most common form of dementia and currently afflicts 6.2 million adults over age 65 in the United States.[1] As the population ages, the prevalence is expected to rise,[1] so there is an urgent need to develop more effective treatment and prevention strategies. Currently, there are no disease modifying therapies approved for AD, and the drugs currently used for AD only manage symptoms.[1] Thus, a better understanding of the neurobiology and pathogenesis of AD is necessary to identify new prevention or therapeutic targets.

AD is pathologically defined by 2 primary protein abnormalities, including amyloid-β (Aβ) plaques and neurofibrillary tangles. Aβ is a normal protein that undergoes abnormal processing and aggregation to form extracellular plaques.[2] Aβ begins as amyloid precursor protein, a transmembrane protein primarily expressed in neuronal synapses. Normally, amyloid precursor protein is cleaved by α-secretase, followed by γ-secretase, releasing the amyloid precursor protein intracellular domain into the cell and releasing p3, a peptide fragment, into the extracellular space.[2] In AD, amyloid precursor protein is first cleaved at a different location by β-secretase, followed by γ-secretase. This process releases the Aβ peptide into the extracellular space as well as the amyloid precursor protein intracellular domain into the cell.[2] Aβ is released as a monomer peptide, but its hydrophobic properties lend it to aggregate together to form

oligomers, protofibrils, fibrils, and eventually extracellular plaques.[2] Plaque deposition begins in the inferior frontal and temporal lobes, but as the disease progresses, Aβ deposition can be detected in the frontal, temporal, and occipital lobes, sparing only the primary motor and sensory cortices.[3] Aβ deposition can be measured *in vivo* by either cerebrospinal fluid (CSF) or positron emission tomography (PET) imaging. Aβ is usually cleared into the CSF, but as monomers aggregate and plaques form, less Aβ is detectable within the CSF.[4] Alternatively, PET imaging detects the formation of Aβ plaques and shows increased uptake as Aβ burden increases.[5]

The second primary protein abnormality in AD is hyperphosphorylated tau, resulting in neurofibrillary tangles. Tau is a normal axonal protein that stabilizes microtubules and supports axonal transport and structural integrity.[6] While it normally oscillates between a dephosphorylated and phosphorylated state, in AD, tau becomes hyperphosphorylated by dysregulated kinase proteins, including glycogen synthase kinase 3 beta.[6] The process prevents tau from stabilizing the microtubules and damages the neuron. Hyperphosphorylated tau aggregates together to form neurofibrillary tangles within the neuron, eventually leading to cell death. Tangle formation begins in the deep temporal lobe, specifically the transentorhinal cortex and hippocampus, and then spreads through functionally connected neurons.[7] As the disease worsens, tangles continue to accumulate in the hippocampus as they spread outward into the amygdala, thalamus, and neocortical regions.[3] Similar to Aβ, tau can also be measured *in vivo* by PET or CSF. Importantly, tau PET tracers are not specific to the hyperphosphorylated species, so tau PET imaging shows increased uptake in normal aging as well as other neurodegenerative conditions.[8] CSF allows for the

measure of total tau (t-tau), reflecting general neurodegeneration, or phosphorylated tau (p-tau), which is more specific to AD.[4]

Pathogenesis

The most pervasive model of AD pathogenesis[9] suggests that Aβ forms first, up to 15 years prior to symptom onset. Aβ is followed by an increase in p-tau, which leads to subsequent neurodegeneration and cognitive decline. Much of the data supporting this model comes from the familial form of AD. These individuals have inherited a mutation in the amyloid precursor protein processing cascade, leading to early onset AD with a mean age at symptomatic onset of 46.[10] Because AD develops early in these individuals, there is a relative lack of additional age-related changes and pathologies that are often present in older adults. Therefore, the familial form of AD provides an excellent *in vivo* model of pure AD. However, investigators have recently discovered that sporadic AD rarely exists in isolation and up to 95% of cases of pathologic AD at autopsy have additional pathologies present.[11] These concomitant pathologies likely alter the pathologic cascade, highlighting a need to increase understanding of how these pathologies interact with AD to contribute to disease onset or progression.

Vascular disease is the most common pathology to co-occur with AD and contributes to over half of pathologically confirmed dementia cases

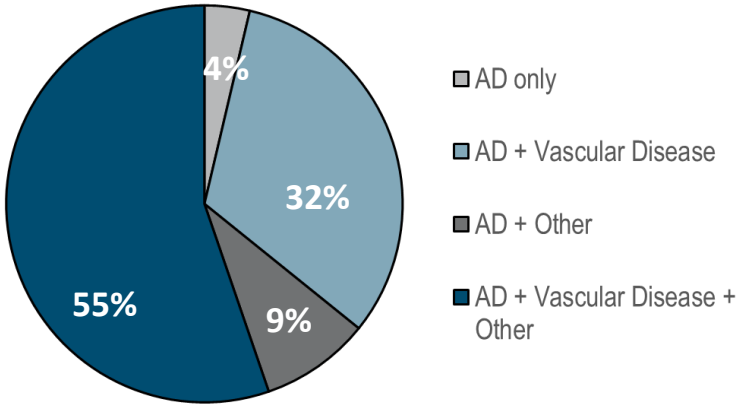

Figure 1.1. Overlapping pathologies with AD. In a series of individuals clinically diagnosed with AD, 87% had both AD and cerebrovascular pathology at autopsy. Adapted from Kapasi et. al., 2017.

(**Figure 1.1**).[11] Cardiovascular and cerebrovascular abnormalities are increasingly linked to cognitive impairment, and cerebral small vessel disease (SVD) confers earlier symptom onset[12] and faster decline.[13,14] Cerebrovascular disease and Aβ deposition on PET contribute additively to cognitive decline among older adults with normal cognition.[15] Additionally, systemic vascular risk interacts with Aβ deposition such that cognition declines at a greater rate in the presence of increased cerebral Aβ and increased vascular risk.[16] Cerebrovascular disease also interacts with tau on cognition, as increased tau deposition assessed on PET is associated with worse cognitive performance among individuals with subcortical vascular cognitive impairment compared to individuals without.[17] Finally, alterations in both cerebral blood flow[18] and cerebrovascular resistance,[19] a measure of cerebral vasoreactivity, are associated with cognitive decline among non-demented amyloid positive but not amyloid negative individuals. Thus, it is imperative to study how both systemic and cerebral vascular disease interact with AD pathology to drive clinical progression to better inform models of typical aging and disease.

Neurobiology and Biochemical Function of White Matter

Cerebral white matter is composed of myelinated axons and functions to increase signal propagation speed across neurons. White matter changes occur in up to 90% of older adults[20,21] and are associated with cognitive decline,[22,23] though the etiology of those changes varies. While white matter damage is most commonly associated with vascular disease,[24] it has been increasingly implicated in AD and may play a critical part in the spread of AD pathology,[25] suggesting that white matter damage

may be one pathway through which vascular disease and AD intersect to hasten clinical decline.

White Matter Development

Cerebral white matter is composed of axon bundles, containing neurofilaments, microtubules, and stabilizing proteins, surrounded by myelin. Myelin, synthesized by oligodendrocytes in the central nervous system, is primarily composed of water, proteins, and lipids. Formation of fiber bundles begins around the 16th week of gestation as oligodendrocyte precursor cells (OPCs) migrate from subventricular zones and ventral regions of the neural tube. Once OPCs reach their destination, they extend cellular processes out toward axons and attach via contactin[26] and contactin-associated protein.[27] Growth factors on the neuron signal the OPC to begin differentiation and myelin formation, beginning at the nodes of Ranvier and progressing outward. To form a node, gliomedin is expressed on oligodendrocyte processes, which recruit ankyrin G within axons.[28,29] Ankyrin G recruits and binds sodium channels to this region, accounting for their abundance in the nodes. Next, paranodes develop, as neurofascin-155 expressed on oligodendrocytes binds with contactin on axons to ensure proper attachment of myelin.[30] Finally, juxtaparanodes are formed, primarily regulated by contactin associated protein 2 and potassium channels.[31] The abundance of potassium channels in this region functions to maintain the resting membrane potential and may provide a way of communication between the oligodendrocyte and axon.[32] After myelin has surrounded the axon, myelin basic protein and proteolipid protein,[33] among other phospholipids, bind together and compact the myelin. This final step is critical for the

insulating function, so alteration of the cholesterol content within oligodendrocytes may lead to less effective myelination. See **Figure 1.2** for an illustration of normal fiber bundle anatomy. In normal development, myelination begins with the cranial nerves, and progresses in caudal to cranial and posterior to anterior gradients.[34] Thus, anterior white matter is often the first to undergo age-related damage.[35]

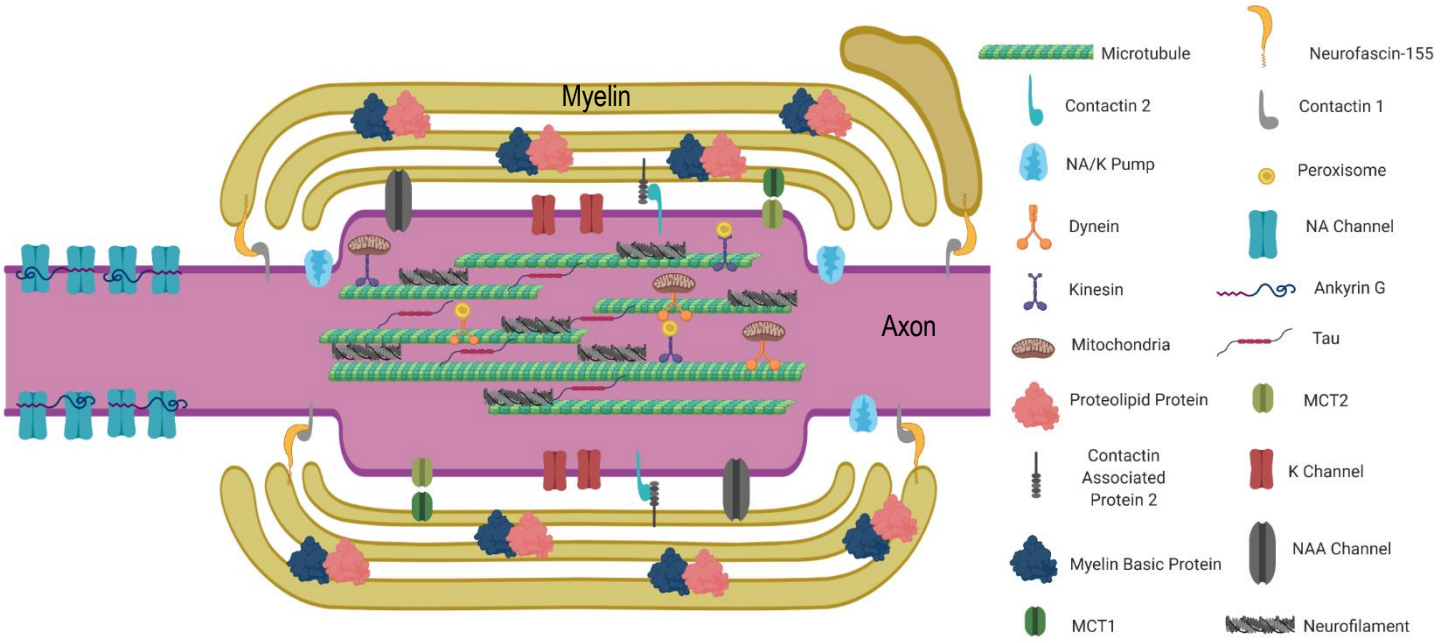

Figure 1.2. Anatomy of a myelinated axon. Sodium channels are concentrated in the nodes of Ranvier to facilitate saltatory conduction. Throughout different axon segments, a variety of proteins and channels function to maintain the homeostasis and connection between the axon and myelin. Myelin basic protein and proteolipid protein bind to compact the myelin sheath. Within the axon, microtubules and neurofilaments support axonal structure while dynein and kinesin molecules transport organelles throughout the neuron. Created with BioRender.com. K=potassium; MCT=monocarboxylate transporter; NA=sodium; NAA=N-acetyl aspartate.

White Matter Function

White matter, and more specifically myelination, is essential for saltatory conduction, increasing the speed action potentials are propagated. In an unmyelinated neuron, once the threshold potential for excitation is met, a segment of the axon is depolarized. Sodium channels open, leading to rapid sodium influx, followed by potassium channel opening and slower potassium efflux. Action potentials are self-

propagating, as diffusion of ions across one part of the axon leads to depolarization of adjacent segments. However, in a myelinated axon, sodium channels are only present and active in the nodes of Ranvier.[36] As an action potential begins and sodium enters, it diffuses rapidly down its concentration gradient throughout the myelinated segment. Since myelin causes the axonal membrane to be impermeable, diffusion is rapid and sodium quickly reaches the next node, depolarizing this segment. Myelin also increases signal propagation speed by increasing the diameter of the axon,[37] which reduces ability of the myelinated segment to store electrical charge.[38] Additionally, axons are essential for maintaining neuronal structural integrity, as filaments within the axon are critical for maintaining axon diameter,[39] and regulating conduction velocity.[40] Finally, the axon serves as the major transport system throughout the neuron, as cellular contents are transported between the cell body and the presynaptic terminal anterograde via kinesin and retrograde via dynein motor proteins.

However, the oligodendrocyte and axon do not operate in isolation. Given most of the axon is surrounded by myelin, it is inefficient for the axon to receive its entire nutrient supply from the nodes of Ranvier. Therefore, oligodendrocytes play a critical role in delivering energy, specifically mitochondria,[41] to the axon. Oligodendrocytes also express monocarboxylate transporter 1 (MCT 1) and 2 (MCT 2) to transport lactate to axons in energy deprived states.[42] Further, oligodendrocytes are partially dependent on the axon for proper function. N-acetyl aspartate (NAA), a molecular biproduct of metabolism in axons, is transported back into oligodendrocytes, where it is thought to contribute to myelin synthesis.[43] Therefore, given the functional link between oligodendrocytes and axons, pathology affecting one will lead to damage in the other,

likely resulting in white matter damage detectable on magnetic resonance imaging (MRI).

White Matter and Cognition

Individual fiber bundles are organized into larger white matter tracts that transmit information between grey matter regions. Each tract is characterized as a projection, commissural, or association tract. Projection tracts connect the cerebral cortex to non-cortical structures (e.g., cerebellum, brainstem, spinal cord) and primarily function for movement (e.g., corticospinal tract) and sensation (e.g., medial lemniscus, optic radiation). Commissural tracts connect identical cortical regions in the right and left cerebral hemispheres, most notably the corpus callosum. Other commissural tracts include the anterior commissure, connecting the temporal lobes and responsible for olfactory function; the posterior commissure, connecting structures critical for eye movements; and the hippocampal commissure, which connects the hippocampi and is important for memory. Finally, association tracts connect two regions within the same hemisphere. These tracts are categorized as either short or long, with short tracts connecting adjacent gyri and long tracts connecting more distant regions across lobes. The connections and

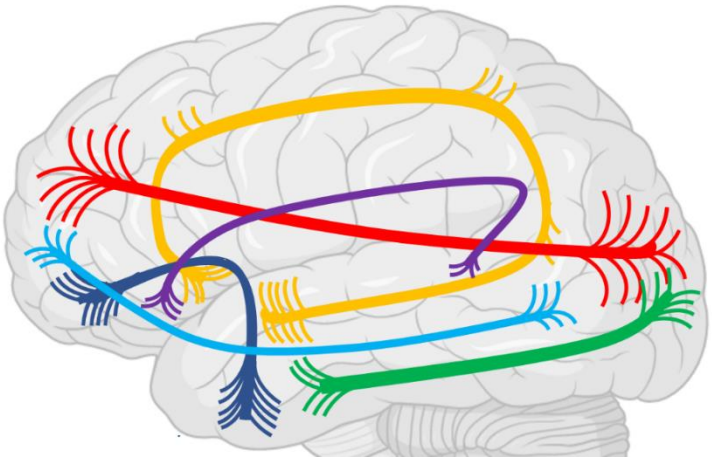

Figure 1.3. Major association tracts. The **uncinate fasciculus** is critical for emotional regulation, behavior, long-term memory, and executive function. The **cingulum bundle** functions for learning and working memory. The **superior longitudinal fasciculus** contributes to information processing speed and executive function. The **inferior longitudinal fasciculus** is primarily responsible for lexical processing, object recognition. and visual memory. The **occipitofrontal fasciculus** is critical for visual processing. Finally, the **arcuate fasciculus** is important for language processing and production. Created with BioRender.com.

functions of primary long association tracts are summarized in **Figure 1.3**. The functions of tracts primarily depend on the grey matter regions they connect. For example, tracts in the frontal lobe are implicated in processing speed and executive function.[44] Temporal lobe and hippocampal tracts are necessary for learning[45] and episodic memory consolidation.[46] Finally, the deep white matter is responsible for connecting subcortical and cortical structures throughout the brain, Thus, deep tracts are implicated in multiple cognitive functions, including information processing speed, executive function,[44] and memory retrieval.[47]

Pathways to White Matter Injury

Based on the complex processes of myelination, axonal transport, and homeostasis maintained between the oligodendrocyte and the axon, damage to either the oligodendrocyte or axon will compromise the white matter. In aging and in AD, multiple pathologies may lead to white matter damage through different mechanisms, including but not limited to systemic vascular changes, cerebrovascular changes, and AD pathology.

Systemic and Cerebrovascular Changes

Vascular disease is the most common etiology of white matter changes in aging adults.[24] White matter macrostructural disease, assessed as white matter hyperintensities (WMHs), and microstructural disease, assessed with diffusion tensor imaging (DTI), are associated with cardiovascular risk factors (e.g. hypertension, diabetes, smoking)[48] and observed after stroke[49] and transient ischemic attacks.[49,50]

However, even in the absence of acute ischemia or overt cerebrovascular disease, subtle age-related changes in systemic and cerebrovascular health also affect white matter. Elastic arteries, most notably the aorta, are responsible for buffering normal changes in blood pressure throughout the cardiac cycle.[51] However, the vessel wall undergoes multiple structural changes during aging that lead to increased transmission of pulsatile energy to the periphery and damage to the microcirculation. Elastin, an abundant protein in the vessel wall in younger individuals, is increasingly degraded in older age.[52] Further, calcium concentrations within the vessel wall increase,[53] leading to calcification of elastin and subsequent loss of elastic wall properties. Collagen, the other primary determinant of vessel wall physiology, becomes increasingly cross-linked,[54] adding to the stiffness of the vessel. Due to these changes in vessel wall properties, the systemic vasculature, particularly the aorta, is less able to absorb energy from pulsatile blood flow exiting the heart[55] and properly adapt to maintain appropriate blood flow throughout the cardiac cycle.[51] Subsequent blood flow to the capillary beds is reduced,[56] leading to reduced perfusion of high-flow organs, including the brain.

Hypoxia in watershed regions is thought to be the most prominent pathway through which systemic vascular changes damage white matter. In the setting of relatively reduced flow, brain regions most distal to the heart are at highest risk for hypoxia. Global reductions in cerebral blood flow primarily affect watershed regions of the brain, as these regions have minimal sources of collateral blood flow. Thus, brain tissue underlying these border-zones, including much of the white matter,[57] is susceptible to decreased perfusion. As illustrated in **Figure 1.4**, watershed regions between main cerebral arteries are located in the frontal lobe (between the anterior

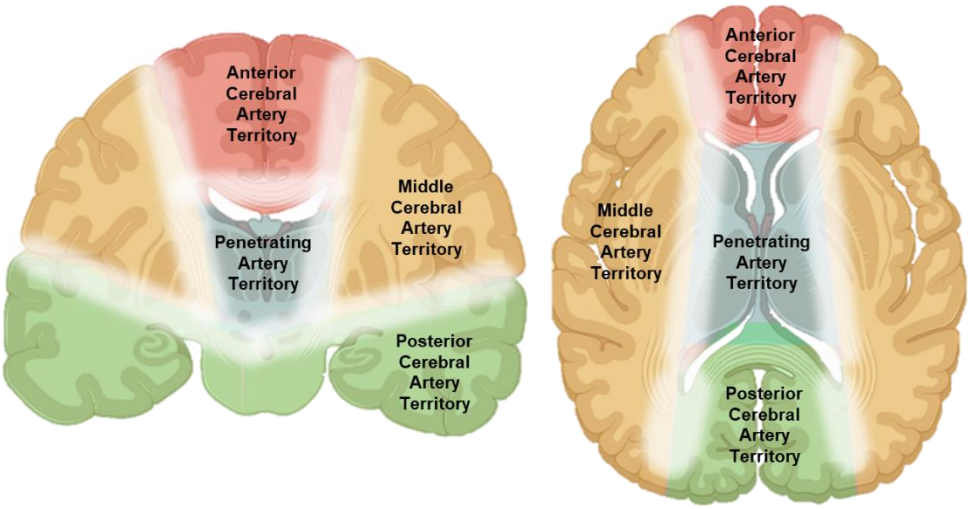

Figure 1.4. Cerebral artery territories. Watershed regions are shown in white. Cortical regions and underlying white matter between the anterior and middle cerebral artery territories and the middle and posterior cerebral artery territories are susceptible to hypoperfusion. Deep white matter tracts between the large artery and the small, penetrating artery territories are also vulnerable to hypoperfusion. Created with BioRender.com.

cerebral artery and middle cerebral artery territories) and at the parieto-occipital junction (between the posterior cerebral artery and middle cerebral artery territories). Watershed regions also exist in deep, subcortical regions of the brain, between the large arterial supply and smaller penetrating arteries. Penetrating arteries are typically unbranched vessels extending from larger arteries at acute angles[58] and are less responsive to neurotransmitters and vasoactive substances.[59] Thus, in the setting of increased arterial stiffness and consequential reduced perfusion,[56] these vessels cannot adequately respond to maintain homeostatic blood supply to underlying subcortical white matter, leading to white matter damage.

A second pathway by which age-related systemic arterial stiffening may lead to white matter damage is through greater transmission of harmful pulsatile energy to the periphery, as vessels lose the ability to absorb the pulsatile energy of blood exiting the heart.[55] This process is particularly relevant for high flow organs, such as the brain. Increased pulsatility damages endothelial and smooth muscle cells in the cerebral microcirculation,[60] further leading to reductions in blood flow and hypoxia.[56] The

penetrating arteries, and thus the subcortical white matter perfused by them, are highly susceptible to this pulsatile energy due to their proximity to the Circle of Willis, consistent with data showing cerebral small vessel disease is most severe in these locations.[61] All blood enters the brain through the Circle of Willis, and the smaller penetrating arteries extend from the segments within the Circle. Therefore, they are highly susceptible to the harmful pulsatile energy of blood as it enters the brain, possibly leading to white matter damage in deep white matter tracts.

In addition to the regional vulnerability of perfusing vessels, biochemical evidence suggests oligodendrocytes are uniquely susceptible to hypoxic damage due to age-related arterial stiffness. In animal models of ischemia, oligodendrocytes swell and undergo necrosis hours prior to changes in cortical neurons,[62] possibly via caspase activation[63] or alterations in calcium and sodium channel signaling.[64] Since the resting membrane potential of neurons is maintained by a sodium potassium pump that requires adenosine triphosphate, hypoxia and subsequent decline in aerobic metabolism results in disruption of the resting membrane potential and excess sodium inside the cell. Intracellular sodium excess leads to depolarization, neuronal glutamate release, and glutamate excitotoxicity. Neurons from aged mice show increased glutamate efflux post-ischemia compared to young mice, exacerbating the known detrimental effect of glutamate on oligodendrocytes.[65] Finally, oligodendrocytes contain low levels of glutathione and high levels of iron compared to other glial cells,[66] diminishing their ability to respond to oxidative stress. Thus, oligodendrocytes are vulnerable to damage from nitrous oxide released as surrounding cells are injured during hypoxia,[67] further damaging oligodendrocytes beyond the initial insult.

Collectively, these data suggest oligodendrocytes are highly vulnerable to hypoxia resulting from age-related vascular changes, specifically in the watershed regions of the brain.

Beyond systemic arterial changes, small vessels within the cerebrovasculature also undergo age-related changes.[24,68] As we age, the blood-brain barrier (BBB), which regulates transport into and out of the central nervous system and is necessary for proper neurovascular coupling,[69] increases in permeability and undergoes structural remodeling.[70] This remodeling is partially regulated by matrix metalloproteinases (MMPs),[71] which are a set of enzymes that degrade extracellular matrix proteins. In aging, MMPs contribute to elastin degradation[72] in the vessel wall and subsequent increased thickness of the basement membrane.[73] MMPs have been associated with BBB opening,[74] and both increased BBB permeability and MMPs have been associated with white matter damage in individuals with subcortical ischemic vascular disease.[75,76] Thus, it is likely that these age-related changes in BBB permeability and extracellular matrix remodeling also lead to changes in white matter damage even in the absence of disease.

AD Pathology

Though AD is traditionally considered a disease of grey matter damage, recent studies propose white matter damage may commonly accompany AD pathology. Observed white matter changes were initially thought to be secondary to grey matter degeneration, but more recent evidence suggests white matter changes precede and are spatially independent of grey matter changes during the prodromal phases of

disease.[77] In familial AD, white matter damage assessed with WMHs[78] and DTI occurs at least 10 years prior to symptom onset and precedes detectable changes in hippocampal volume.[25] While there may be many pathways to white matter injury in AD, notable *in vivo* and *in vitro* work suggests primary AD pathology (including Aβ and p-tau) has a direct effect on oligodendrocytes and axon structure, contributing to white matter damage.

Cerebral Aβ burden is associated with WMHs and DTI changes among non-demented older adults.[79,80] Further, these white matter changes localize to frontal[81] and temporal regions,[82] corresponding to early regions of Aβ deposition. While Aβ plaques are not traditionally thought to deposit within white matter, soluble Aβ is detectable in white matter in AD brains post-mortem, particularly in anterior tracts.[83] Thus, it is possible this neurotoxic species contributes to white matter damage prior to deposition of plaques in surrounding grey matter. Though the regional specificity of these findings suggests Aβ is responsible for white matter damage in AD, a limitation of these studies in older adults is the high rate of co-occurring cerebrovascular disease and age-associated white matter damage. It is possible age-related vascular disease or Wallerian degeneration is responsible for white matter changes, rather than amyloidosis. However, more precise disease models isolating AD pathology suggest otherwise. Decreased levels of CSF Aβ are associated with DTI changes in familial AD, once again localizing to areas of Aβ deposition.[25] Familial AD is characterized by the early development of AD pathology in the absence of age-related vascular risk factors or additional pathologies,[84] supporting the hypothesis that white matter damage may be a direct consequence of Aβ. Finally, multiple transgenic mouse models of familial AD,

including PDAPP,[85] 3xTg-AD,[86] and 5xFAD mice,[87] show white matter changes compared to age-matched controls assessed by *in vivo* DTI and post-mortem imaging. These mutations primarily result in overproduction of Aβ, in the absence of tau or other concomitant pathologies, suggesting Aβ is associated with white matter damage. Importantly, many white matter changes detected in mouse models of amyloidosis localize to regions where Aβ is known to accumulate, including inferior regions in the frontal[87] and temporal lobes.[86,87]

Beyond *in vivo* and post-mortem imaging evidence for Aβ contributing to white matter damage, *in vitro* models suggest Aβ leads to oligodendrocyte dysfunction and myelin dysregulation. It is hypothesized Aβ disturbs glutathione metabolism,[88] activating neutral sphingomyelinase within oligodendrocytes[89] and upregulating ceramide production. Ceramide is a critical second messenger in apoptotic signaling cascades[90] resulting in cell death. Beyond outright cell death, Aβ also interferes with the ability of the oligodendrocyte to properly myelinate axons. Aβ inhibits neuronal cholesterol transport,[91] the main component of myelin, and AD cases have less total cholesterol, myelin basic protein, and proteolipid protein in white matter compared to age-matched controls,[92] suggesting Aβ has a direct effect on myelin production or maintenance. Aβ also affects the structure of white matter, as the protein induces cytoskeletal disorganization of oligodendrocytes, affecting their ability to extend cellular processes, differentiate, and form a myelin sheath.[93] Any disruption of oligodendrocytes or myelin will affect saltatory conduction, perhaps resulting in some of the early cognitive deficits in AD. Finally, Aβ induces an inflammatory cascade that may indirectly lead to white

matter damage, as immune activation is a known etiology of white matter damage both in aging and other neurologic disorders.

It is possible that associations between Aβ and white matter damage are confounded by vascular deposition of Aβ. While Aβ42 primarily accumulates in the parenchyma in AD, Aβ40 accumulates in cerebral blood vessel walls (known as cerebral amyloid angiopathy (CAA)) in up to 80% of AD patients.[94,95] CAA leads to fractured blood vessels and microbleeds,[94] likely leading to hypoxic damage in downstream white matter. Thus, it is unclear which form of Aβ is driving white matter damage seen in AD.

Recent evidence also suggests that p-tau may be a primary contributor to white matter damage, though the protein is traditionally considered to be a correlate of grey matter damage.[96] Among older adults, increased tau accumulation measured with PET relates to white matter damage in the temporal lobe,[97] and individuals with a high tau pathology burden have greater decline in white matter integrity over time, specifically in hippocampal tracts.[98] In post-mortem studies, DTI changes are observed among brains with a high NFT burden in the entorhinal cortex and limbic system[99] and cortical p-tau burden is associated with WMHs,[100] statistically independent of associations with other SVD markers.[101] In familial AD, increased CSF p-tau is associated with reduced white matter microstructural integrity assessed on DTI.[25] Finally, animal models of tauopathy (rTg4510)[102,103] show white matter changes assessed with DTI and with post-mortem microscopy compared to age-matched controls.[103] These effects appear in the hippocampus,[102,104] corresponding to the region NFTs first develop. Collectively, this evidence suggests p-tau has a regionally specific effect on white matter. It is plausible

that some of the white matter damage observed in these studies may be due to Wallerian degeneration.[96] However, data from the Dominantly Inherited Alzheimer's Network suggest white matter damage precedes hippocampal atrophy in individuals with familial AD, supporting the hypothesis that p-tau directly contributes to white matter damage.[25]

In vitro models suggest p-tau likely affects the white matter through axonal injury. Phosphorylation promotes mislocalization of tau so it accumulates in dendrites rather than axons,[105] compromising its ability to promote axonal growth and regulate cellular transport. While axonopathy as a consequence of p-tau is well-established, recent evidence describing the metabolic dependence of axons and oligodendrocytes[42] suggests hyperphosphorylation of tau may have direct effects on the white matter. First, p-tau may induce white matter damage through changes in glutamate homeostasis. Animal models of axonal injury cause the release of glutamate into the extracellular space,[106] and oligodendrocytes are highly vulnerable to glutamate-mediated excitotoxicity.[107] Second, p-tau alters energy homeostasis within the axons, affecting NAA transport. NAA is normally transferred to oligodendrocytes where it plays a critical role in steroid synthesis for myelin production.[108] Thus, in the presence of p-tau, NAA is not adequately produced and transported in the axon, impairing myelin synthesis.

Non-Specific Neurodegeneration

Additional pathologies that often co-occur with vascular disease or AD in aging must also be considered as etiologies of white matter damage. While vascular disease is presumed to be the most prevalent etiology of white matter damage,[24] Wallerian

degeneration due to concurrent neurodegeneration is also common in the aging brain.[109] Wallerian degeneration is the process by which damage to cell bodies in the grey matter leads to progressive damage of associated axons.[109] This etiology is supported extensive evidence showing that general markers of neurodegeneration, including total tau,[110] neurofilament light,[81,111] and grey matter volume on structural MRI,[112] are cross-sectionally associated with white matter damage. Thus, white matter damage due to general neurodegeneration must be considered when examining other etiologies, such as AD pathology.

Assessment of White Matter Damage

White matter damage is primarily assessed *in vivo* through two MRI sequences. T_2 fluid attenuated inversion recovery is a T_2-weighted sequence that nulls the CSF signal, optimized to visualize WMHs. WMHs represent the accumulation of fluid, most often interpreted as ischemic white matter damage.[24] However, other etiologies, including gliosis[113] or inflammation,[114] also contribute to WMH formation. Due to the heterogeneity of WMHs,[111] more sensitive methods of imaging white matter have been developed.

DTI is an MRI sequence that estimates the microstructural integrity of white matter tracts. It is more sensitive that T_2-weighted imaging, as DTI changes can be detected in normal appearing white matter prior to WMH development.[23] DTI measures the diffusion of water throughout the brain to estimate the structural integrity of white matter fiber bundles. Within neuronal cells bodies comprising cerebral grey matter, there is little regular structure that will restrict the diffusion of water. This model is

referred to as isotropic diffusion, as water theoretically will diffuse the same amount in any direction (**Figure 1.5**).

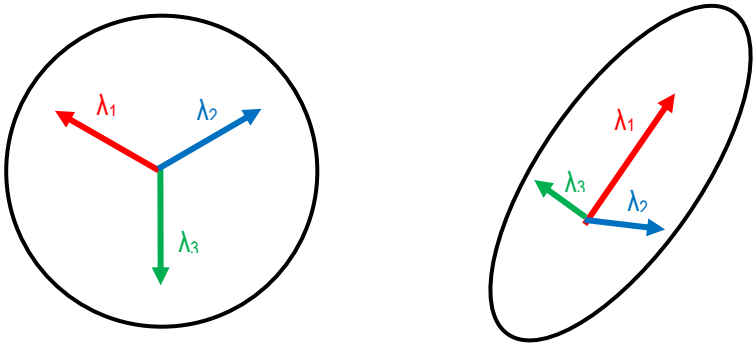

Figure 1.5. Isotropic (left) and anisotropic diffusion (right).

However, within the white matter, water should diffuse primarily along the direction of the axon (anisotropic diffusion, **Figure 1.5**). DTI leverages the difference in water diffusion properties between white and grey matter to quantify white matter microstructural integrity. To assess the direction and strength of diffusion, a magnetic field is applied, exciting water molecules. Then, a magnetic field of equal strength is applied in the precise opposite direction. If there is no diffusion of the water molecules, the excitation of the second magnetic field will excite water molecules equally in the opposite direction, canceling out the excitation from the first magnetic field and leading to no signal loss. However, if diffusion was occurring and the water molecules move between the first pulse and the second pulse, signal loss will occur. The loss in signal is then used to calculate the direction and magnitude of diffusion throughout the brain.

Diffusion tensors are calculated using the Stejskal-Tanner equation[115] (**Equation 1**) and weighted-least squares estimation.[116]

$$S_k = S_0 e^{-b\hat{g}_k^T D \hat{g}_k} \quad [1]$$

This equation uses the difference between the signal when no diffusion gradient is applied (S_0) and the signal after each gradient is applied (S_k), the b-value (b), and gradient pulse (g) to calculate the diffusion tensor (D). D represents a diffusion matrix with 6 independent components, representing diffusion in 6 primary directions (D_{xx}, D_{xy}, D_{xz}, D_{yy}, D_{yz}, D_{zz}). This matrix is diagonalized to determine the 3 primary diffusion directions within each voxel (λ_1, λ_2, λ_3). The 4 primary DTI metrics are calculated from the three eigenvectors, according to the following equations: [2]

$$Axial\ Diffusivity = \lambda_1 \quad [3]$$

$$Radial\ Diffusivity = \frac{\lambda_2 + \lambda_3}{2} \quad [4]$$

$$Mean\ Diffusivity = \frac{\lambda_1 + \lambda_2 + \lambda_3}{3} \quad [5]$$

$$Fractional\ Anisotropy = \sqrt{\frac{1}{2}}\ \frac{\sqrt{(\lambda_1 - \lambda_2)^2 + (\lambda_1 - \lambda_3)^2 + (\lambda_2 - \lambda_3)^2}}{\sqrt{({\lambda_1}^2 + {\lambda_2}^2 + {\lambda_3}^2)}}$$

Axial diffusivity represents the primary direction of diffusion, radial diffusivity represents the secondary direction of diffusion, mean diffusivity represents a mean of all three eigenvectors, and fractional anisotropy represents how intact diffusion is through an axon accounting for how much diffusion is expected in all three primary directions. As axons are damaged or demyelination occurs, the eigenvalues increase, leading to increased values in mean, radial, and axial diffusivity, and decreased values in FA. Thus, lower FA and higher mean, radial, and axial diffusivity indicate white matter damage. However, some data suggest that in early stages of damage, diffusion in the primary direction (λ_1) decreases, leading to decreased axial diffusivity.[117] Increases in

axial diffusivity are thought to be specific to axonal injury,[118] whereas increases in radial diffusivity are thought to be specific to demyelination.[119] However, more post-mortem human studies are needed to confirm this interpretation. DTI is commonly used to assess white matter injury in AD, though the neuropathological correlates of this damage remain unknown.

Rationale and Aims

It is well established that vascular disease interacts with AD pathology to worsen clinical outcomes,[120] though the exact pathways remain unknown. While AD is the most common cause of dementia, cerebrovascular pathology contributes to at least one half of all pathologically-confirmed cases of dementia and is the most common pathology that co-occurs with AD.[11] Cardiovascular and cerebrovascular abnormalities are increasingly linked to cognitive impairment, and cerebral small vessel disease confers earlier symptom onset[12,121] and faster decline.[13,14] Thus, it is critical to develop a better understanding of how vascular disease and AD pathology intersect to affect clinical decline.

Based on evidence implicating Aβ and p-tau as etiologies of oligodendrocyte and axonal injury, white matter damage may be one pathway by which vascular disease and AD pathology intersect. Certain tracts may be susceptible to multiple pathologies, resulting in greater cognitive decline primarily in the domains that are supported by those tracts (**Figure 1.6**). For example, frontal lobe tracts may be susceptive to both Aβ and vascular disease, leading to faster decline in processing speed and executive

function. Similarly, temporal lobe white matter tracts may be susceptible to vascular disease, Aβ, and p-tau, leading to faster decline in memory.

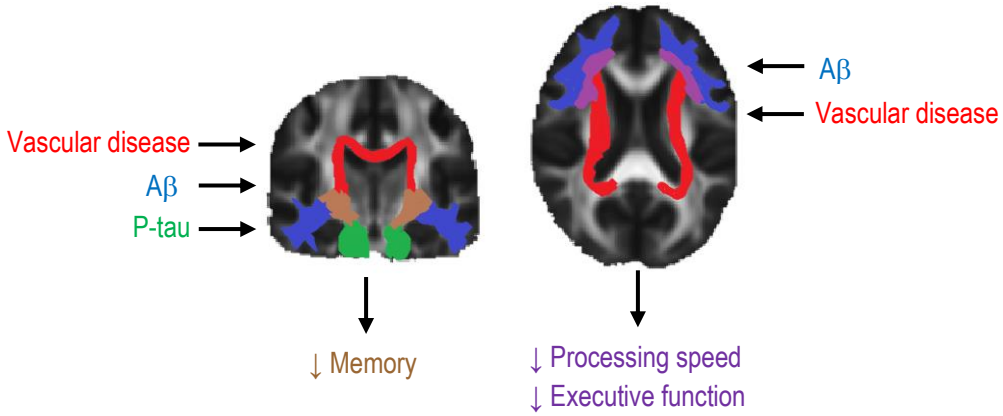

Figure 1.6. Theoretical model of where AD pathology and vascular disease effect white matter health. Border-zone and deep white matter tracts vulnerable to age-related vascular changes are indicated in red. Frontal and temporal lobe tracts vulnerable to Aβ are indicated in blue. Hippocampal tracts vulnerable to p-tau are indicated in green. These pathologies may regionally intersect on certain white matter tracts, hastening clinical manifestation and decline in specific domains, including processing speed, executive function, and memory.

Understanding the etiologies of white matter damage in normal aging and AD is necessary for advancing our understanding of AD pathogenesis. A comprehensive characterization of the vulnerability of white matter tracts to age and AD related pathologies (including vascular disease, Aβ, tau, and neurodegeneration) will enhance understanding of the neurobiology underlying cognitive decline and improve the precision by which structural imaging of white matter changes is leveraged in clinical settings as a complementary biomarker of abnormal cognitive aging. To answer these questions, we leveraged data from the Vanderbilt Memory and Aging Project, a longitudinal cohort of older adults free of stroke and dementia. We utilized sensitive CSF and cardiac magnetic resonance biomarkers systemic vascular health, cerebrovascular heath, AD pathology, and neurodegeneration in combination with longitudinal DTI data to investigate the following aims:

Aim 1: Identify white matter tracts regionally vulnerable to age-related vascular changes, including arterial stiffness, extracellular matrix remodeling, and BBB permeability. Hypothesis: Increased vascular changes (higher pulse wave velocity, higher CSF MMP concentrations, greater BBB permeability) will relate to white matter microstructure decline over 7 years, especially in watershed white matter tracts lacking extensive collateral blood supply.

Aim 2: Identify white matter tracts regionally vulnerable to amyloidosis. Hypothesis: Greater amyloidosis (lower CSF Aβ42 reflecting increased cerebral amyloid) will relate to white matter microstructure decline over 7 years, especially in frontal and temporal lobe tracts (where Aβ42 first accumulates). Greater levels of Aβ40 will relate to white matter tracts adjacent to cortical areas where Aβ40 accumulates.

Aim 3: Identify white matter tracts regionally vulnerable to p-tau and neurodegeneration. Hypothesis: Greater p-tau (higher CSF p-tau) will relate to white matter microstructure decline over 7 years, especially in tracts connected to the hippocampus (where p-tau first deposits). Greater levels of neurodegeneration (higher CSF t-tau and NFL) will globally relate to white matter microstructure decline over 7 years.

Aim 4: Identify white matter tracts vulnerable to more than one pathology and relate damage in vulnerable tracts to cognitive decline. Hypothesis: CSF Aβ, CSF p-tau, and vascular changes will have overlapping effects in frontal and temporal lobe white matter. Tracts susceptible to arterial stiffness or Aβ will relate to decline in processing speed, executive function, and episodic memory. Tracts susceptible to p-tau will relate to decline in episodic memory. Tracts susceptible to arterial stiffness and AD

pathology (either Aβ or p-tau) will be the strongest predictors of cognitive decline over 7 years.

These studies characterized which white matter tracts are susceptible to certain pathologies and the cognitive consequences of damage in those tracts. Understanding the etiology of age-related white matter changes and corresponding clinical changes will provide critical information regarding the neurobiology underlying cognitive decline and better inform models of typical aging and disease.

CHAPTER 2

THE EFFECTS OF SYSTEMIC AND CEREBRAL ARTERIAL HEALTH ON WHITE MATTER INTEGRITY

Introduction

White matter changes occur in up to 90% of older adults[20,21] and the most common etiology is thought to be age-related vascular changes.[24] In aging adults, systemic and cerebral arteries undergo stiffening and remodeling, both of which may have effects on white matter health. Given the heterogeneity underlying white matter damage in older adults and individuals at risk for Alzheimer's disease (AD), it is critical to identify which tracts are most vulnerable to age-related changes in systemic and cerebral vascular health to better differentiate etiologies of white matter damage and inform treatment approaches.

Specifically, age-related arterial stiffening, most commonly assessed by pulse wave velocity (PWV), may result in white matter injury. Elastic arteries, most notably the aorta, are responsible for buffering normal changes in blood pressure throughout the cardiac cycle,[51] but age-related stiffening of the vessel walls leads to increased transmission of pulsatile energy to downstream organs[122] and damage to the microcirculation.[60] Subsequent blood flow to the capillary beds is reduced,[56] leading to reduced perfusion of high-flow organs, including the brain. Given the vulnerability of white matter to vascular disease,[57] it is likely that age-related arterial stiffness is a

robust contributor to future white matter damage. However, it is unknown which white matter tracts are most susceptible to age-related arterial stiffening among older adults.

Beyond systemic arterial changes, cerebrovascular remodeling and changes to blood-brain barrier (BBB) integrity may also impact white matter integrity. The BBB is critical to maintaining the neurovascular unit, which ensures adequate oxygen delivery to the brain. However, BBB permeability increases with age,[70] leading to microvascular injury[123] and hypoxia,[124] implicating BBB permeability as an etiology of white matter injury.[123] BBB permeability is also associated with extracellular matrix (ECM) remodeling,[125] which is regulated by matrix-metalloproteinases (MMPs). MMPs, specifically MMP-2,[126] MMP-3,[127] and MMP-9,[128] are upregulated in response to microvascular injury and have been associated with BBB opening and white matter damage in subcortical ischemic vascular disease.[74,75] Thus, it is possible that even in the absence of overt cerebrovascular disease, age-related changes in BBB permeability and MMP regulation affect white matter health. However, it is unknown which tracts are susceptible to BBB permeability and ECM remodeling.

The aim of the present chapter was to examine how age-related changes in systemic vascular health (arterial stiffness) and cerebrovascular health (BBB permeability and MMP regulation) relate to white matter integrity, assessed by diffusion tensor imaging (DTI), among older adults free of clinical stroke and dementia. We hypothesized that higher arterial stiffness, higher cerebrospinal fluid (CSF) MMP concentrations, and great BBB permeability would relate to compromised white matter microstructure at baseline and faster decline in white matter microstructural integrity over time, specifically in watershed tracts lacking extensive collateral blood supply.

Since vascular pathology is present in up to 80% of AD cases,[11] we also investigated whether associations of arterial stiffness, BBB permeability, and MMP regulation with white matter integrity were modified by cognitive diagnosis (normal cognition (NC) versus mild cognitive impairment (MCI)) or *APOE*-ε4 status, that largest genetic risk factor for sporadic AD.[129] We hypothesized that associations would be stronger among participants with MCI and *APOE*-ε4 positive participants.

Methods

Study Cohort

The Vanderbilt Memory and Aging Project[130] is a longitudinal observational study investigating vascular health and brain aging. Inclusion criteria required participants be at least 60 years of age, speak English, have adequate auditory and visual acuity for testing, and have a reliable study partner. At eligibility, participants underwent a comprehensive medical history and record review, clinical interview, and neuropsychological testing for cognitive diagnosis by consensus, including NC, early MCI (eMCI),[131] or MCI.[132] NC was defined as (a) Clinical Dementia Rating (CDR)=0 (no dementia), (b) no deficits in activities of daily living directly attributable to cognitive impairment, and (c) no evidence of neuropsychological impairment defined as standard scores falling within 1.5 standard deviations of the age-adjusted normative mean. eMCI was defined as (a) CDR=0.5 (reflecting mild severity of impairment), (b) no deficits in activities of daily living attributable to cognitive issues, and (c) no neuropsychological impairment defined as standard scores falling within 1.5 standard deviations of the age-adjusted normative mean.[131] Finally, MCI was defined as (a) CDR=0 or 0.5 (reflecting mild severity of impairment), (b) relatively spared activities of daily living, (c)

neuropsychological impairment within at least one cognitive domain (i.e., performances falling greater than 1.5 standard deviations outside the age-adjusted normative mean or pre-morbid level of functioning), (d) concern of a cognitive change by the participant, informant, or clinician, and (e) absence of a dementing syndrome.[132] Participants were excluded for a cognitive diagnosis other than NC, eMCI, or MCI, magnetic resonance imaging (MRI) contraindication, history of neurological disease (e.g., stroke), heart failure, major psychiatric illness, head injury with loss of consciousness>5 minutes, or a systemic or terminal illness affecting follow-up participation. At enrollment, participants completed a comprehensive examination including (but not limited to) fasting blood draw, physical examination, neuropsychological testing, clinical interview, echocardiogram, cardiac magnetic resonance (CMR), multi-modal brain MRI, and optional lumbar puncture. Serial brain MRI and neuropsychological testing were performed at 18-month, 3-year, 5-year, and 7-year follow up. The protocol was approved by the Vanderbilt University Medical Center Institutional Review Board. Written informed consent was obtained prior to data collection.

CMR Imaging

Baseline CMR imaging was acquired at Vanderbilt University Medical Center using a 1.5T Siemens Avanto system (Siemens Medical Solutions USA, Inc., Malvern, PA) with a phased-array torso receiver coil. Velocity-encoded flow data were acquired from the ascending and descending thoracic aorta. Under the supervision of a board-certified radiologist, trained raters blinded to clinical information used the 2-dimensional flow sequence to draw contours on the ascending and descending aorta using QFLOW

5.6 Enterprise Solution (Medis, Leiden, Netherlands). The thoracic aorta centerline length (cm) from the ascending aorta to descending aorta was measured using OsiriX (PIXMEO SARL, Bernex, Switzerland). Transit time was calculated using a custom MATLAB script to calculate the difference in time (milliseconds) at half-max between the leading edges of the ascending and descending aortic flow curves. PWV (m/sec) was calculated as distance traveled across the aorta (m) divided by time delay in onset of velocity waves (seconds). Inter-reader reliability (coefficient of variation=6.6%) was determined by independent review of 34 scans by two readers. This method has been described in detail elsewhere.[133] Pulsatile wave transmission increases with decreasing arterial wall elasticity, so higher PWV indicates higher arterial stiffness. The direct measurement of PWV at the aortic arch, the vessel primarily responsible for buffering pulsatile flow, with CMR allows for local assessment of proximal aortic stiffness without the confound of the distal arterial tree with varied vascular wall properties and tortuosity.

Biofluid Acquisition & Biochemical Analysis

A subset of participants completed an optional fasting lumbar puncture at enrollment (n=155). CSF was collected with polypropylene syringes using a Sprotte 25-gauge spinal needle in an intervertebral lumbar space. Samples were immediately mixed and centrifuged. Supernatants were aliquoted in 0.5 mL polypropylene tubes and stored at -80°C. Samples were analyzed in a single batch using commercially available immunoassays to measure CSF concentrations of MMP-2 (R&D systems, Minneapolis, MN, USA), MMP-3 (Human MMP 3-plex Ultra-Sensitive, MSD® Multi-Spot, MesoScale Discovery, Rockville, MD, USA), MMP-9 (Human MMP 3-plex Ultra-Sensitive, MSD®

Multi-Spot, MesoScale Discovery, Rockville, MD, USA),[134] and albumin (Roche Diagnostics, Penzberg, Germany). Assay details have been provided elsewhere.[135] Board-certified laboratory technicians processed data blinded to clinical information. Intra-assay coefficients of variation were <12%.

Plasma albumin levels were obtained from a fasting venous blood draw. Plasma was separated from participant blood samples via centrifugation at 2000g and 4ºC for 15 minutes and subsequently stored at Vanderbilt. To quantify BBB permeability, a CSF/plasma albumin ratio was calculated by dividing the CSF albumin concentration by plasma albumin concentration.

Brain MRI Acquisition & Post-Processing

DTI was used to quantity white matter microstructural integrity. Participants were scanned at the Vanderbilt University Institute of Imaging Science on a 3T Philips Achieva system (Best, the Netherlands) using an 8-channel SENSE reception coil array at baseline, 18-month, and 3-year follow-up. A 32-channel coil was used for part of 3-year and all of 5 and 7-year data collection. DTI data were acquired along 32 diffusion gradient vectors (TR/TE=10000/60ms, spatial resolution=2x2x2mm^3, b-value=1000s/mm^2) with one non-diffusion weighted image (B_0). Each gradient image was normalized to the B_0 image to account for Brownian motion. Then distortion correction was completed using Synbo-Disco.[136] Since only one B_0 image was collected, this tool uses a T_1-weighted image collected at the same time to create a synthetic B_0 image that is theoretically undistorted. The synthetic B_0 was used to correct the original image for spatial distortions using FSL's TOPUP.[137,138] The eddy tool[139]

was then used to correct for eddy currents. After eddy correction, if the average motion (calculated by the root mean squared) across all gradients was >2, the data were not used. Finally, the diffusion tensor model was fit using Diffusion Imaging in Python,[140] and fractional anisotropy (FA), mean diffusivity, radial diffusivity, and axial diffusivity values were calculated. After calculation of the DTI metrics, a chi-squared value was calculated to determine the goodness-of-fit of the tensor. If the chi-square value exceeded 0.2 in at least 10% of the gradients, the data were not used.

For cross-sectional analyses, DTI data were post-processed through an established tract-based spatial statistics (TBSS) pipeline using the FSL version 4.1.4 (http://fsl.fmrib.ox.ac.uk/fsl/fslwiki/FSL).[141] Briefly, all baseline FA images for each participant were non-linearly registered to the FMRIB58_FA template in MNI-152 space, merged into a 4D image, and a mean image was created. The mean image was used to generate a mean skeleton representing the center voxel of major white matter tracts. A threshold was applied to exclude voxels that did not overlap among 80% or more of participants. The maximum FA values from the center of each participant's white matter tracts were projected onto the mean skeleton, and these skeleton projections were combined into one 4D file containing all skeletonized FA data from all participants. Identical non-linear registration was used to move the mean diffusivity, radial diffusivity, and axial diffusivity images to MNI-152 space for all participants. For each metric, all participant data were merged into one 4D file and projected onto the mean skeleton, as previously described.

For longitudinal analyses, the TBSS pipeline was adapted to better account for longitudinal variability across each participant and variability in the number of images

collected per participant. For each participant, FA images across all timepoints were non-linearly registered to the FMRIB58_FA template in MNI-152 space and an average FA image for each participant was created. Each mean FA image was used to generate a mean skeleton representing the center voxel of major white matter tracts. A threshold was applied to exclude voxels that did not overlap among 80% or more of participants. In this approach, each participant is equally represented within the skeleton, regardless of the number of follow-up images acquired. Due to attrition of the sickest participants over time, this method ensures that the skeleton is not biased towards healthier participants. Then, FA images across all participants and timepoints were projected onto the mean skeleton and these skeleton projections were combined into one 4D file containing all skeletonized FA data from all participants at all timepoints. Identical non-linear registration was used to move the mean diffusivity, radial diffusivity, and axial diffusivity images to MNI-152 space for all participants across all timepoints. For each metric, all participant data were merged into one 4D file and projected onto the mean skeleton, as previously described.

APOE Genotyping

As previously published,[130] a TaqMan® single-nucleotide polymorphism (SNP) genotyping assay from Applied Biosystems (Foster City, California, USA) was used to determine the two SNPs that define the ε2, ε3, and ε4 alleles. Polymerase chain reaction (PCR) in 5 µl reactions was performed on a Life Technologies 7900HT real-time PCR machine, and results were analyzed using Life Technologies SDS 2.4.1

software. *APOE*-ε4 status was defined as positive (ε2/ε4, ε3/ε4, ε4/ε4) or negative (ε2/ε2, ε2/ε3, ε3/ε3).

Covariates

Covariates were collected at the enrollment visit and selected *a priori* for their potential to confound analytical models. Systolic blood pressure was the mean of two measurements. Hypertension was defined as current antihypertensive medication use, systolic blood pressure ≥140 mmHg, or diastolic blood pressure ≥90 mmHg. Diabetes mellitus was defined as fasting blood glucose ≥126 mg/dL, hemoglobin A1C ≥6.5%, or oral hypoglycemic or insulin medication usage. Medication review determined anti-hypertensive medication use. Left ventricular (LV) hypertrophy was defined on echocardiogram as LV mass index >115 g/m^2 in men or >95 g/m^2 in women. Self-report or history of atrial fibrillation was corroborated by any one of the following sources: echocardiogram, CMR, documented prior procedure/ablation for atrial fibrillation, or medication usage for atrial fibrillation. Current cigarette smoking (yes/no within the year prior to baseline) was ascertained by self-report. Self-report prevalent cardiovascular disease (CVD) with medical record documentation included coronary heart disease, angina, or myocardial infarction (heart failure was a parent study exclusion). Framingham Stroke Risk Profile (FSRP) score was calculated based on sex, age, systolic blood pressure (accounting for anti-hypertensive medication usage), diabetes, current cigarette smoking, LV hypertrophy, CVD, and atrial fibrillation.[142]

Analytical Plan

For cross-sectional analyses, voxel-wise linear regressions were conducted using the FSL randomise[143] procedure with 5000 permutations. General linear models using permutation testing related PWV, CSF MMP-2, CSF MMP-3, CSF MMP-9, and the CSF/plasma albumin ratio to FA, mean diffusivity, radial diffusivity, and axial diffusivity, adjusting for baseline age, sex, education, race/ethnicity, FSRP (excluding points assigned to age), cognitive diagnosis, *APOE-ε4* status (one predictor per model). Multiple comparison correction was performed using the established cluster enhancement permutation procedure in FSL.[144]

For longitudinal analyses, voxel-wise linear mixed effects models with random intercepts and slopes and a follow-up time interaction related baseline PWV, CSF MMP-2, CSF MMP-3, CSF MMP-9, and the CSF/plasma albumin ratio to DTI metric trajectory. Models adjusted for identical covariates as cross-sectional analyses, plus follow-up time. Cluster-wise inference[145] was used to identify clusters of results and spatially correct the output images. Clusters were further corrected for multiple comparisons using a family-wise error rate of α=0.05.

All cross-sectional and longitudinal models were repeated with *predictor x cognitive diagnosis* (excluding individuals with eMCI due to the small sample size) and *predictor x APOE-ε4 status* interactions. Models were subsequently stratified by cognitive diagnosis (NC, MCI) and *APOE-ε4* status (positive or negative). Parametric estimates of statistically significant associations were calculated in R version 3.6.0 (www.r-project.org) using least squares regression for illustration and interpretation purposes. Sensitivity analyses were also performed in R, excluding participants with predictor or outcome variables ±4 standard deviations from the group mean.

Significance was set *a priori* at p<0.05.

Results

Arterial Stiffness Analyses

Participant Characteristics

For the 298 participants included in these analyses (73±7 years, 59% male, 87% non-Hispanic White), mean follow-up time was 3.6 years. Baseline PWV ranged 3.5 m/s to 25.5 m/s. See **Table 2.1** for participant characteristics for the entire sample and stratified by diagnosis.

Table 2.1. Participants Characteristics for Pulse Wave Velocity Sample

	Total n=298	NC n=158	Early MCI n=23	MCI n=117	p-value
Age, years	73±7	72±7	73±6	73±7	0.75
Sex, % male	59	58	74	58	0.34
Race, % Non-Hispanic White	87	87	87	87	0.99
Education, years	16±3	16±3	16±3	15±3	**<0.001**‡
APOE-ε4, % positive	33	29	17	43	**0.01***‡
FSRP, total score§	12±4	12±4	13±3	13±4	0.06
Systolic blood pressure, mmHg	143±18	139±17	153±16	145±18	**<0.001***†‡
Antihypertensive medication usage, %	52	53	52	51	0.98
Diabetes, %	18	17	26	19	0.52
Current smoking, %	2	1	0	3	0.35
Atrial fibrillation, %	6	6	4	7	0.87
Prevalent CVD, %	5	6	4	3	0.68
Left ventricular hypertrophy, %	4	3	4	6	0.52
Pulse wave velocity, m/sec	8±3	8±3	9±3	8±3	0.62
Follow-up time, years	3.6±1.8	4.0±1.7	3.4±1.8	3.2±1.9	**0.003**‡

Note. Values denoted as mean±standard deviation or frequency. Participant characteristics were compared across cognitive diagnosis using Kruskal-Wallis test for continuous variables and chi-square test for categorical variables. *Early MCI different than MCI, †Early MCI different than NC, ‡NC different from MCI. §a modified FSRP score was included in statistical models excluding points assigned to age (Total=7±3, NC=6±3, Early MCI=8±2, MCI=7±3); *APOE*=apolipoprotein E; CVD=cardiovascular disease; FSRP=Framingham Stroke Risk Profile; MCI=mild cognitive impairment; NC=normal cognition.

PWV & DTI Metrics

In the whole sample, PWV was not cross-sectionally associated with DTI metrics (corrected p-values>0.18). However, baseline PWV was associated with faster decline in white matter integrity over time (**Table 2.2, Figure 2.1**). Specifically, higher baseline PWV was associated with a greater decline in FA over time primarily in the posterior thalamic radiation (corrected p-values<0.04). Higher baseline PWV was associated with a greater increase in mean, radial, and axial diffusivity over time, particularly in the superior temporal gyrus, middle temporal gyrus, and insular gyrus (corrected p-values<0.05). When removing outliers, a majority of clusters remained significant (**Table 2.2**).

PWV x Diagnosis Interactions & DTI Metrics

In cross-sectional analyses, PWV interacted with diagnosis on DTI metrics (corrected p-values<0.05, **Table 2.3, Figure 2.2**). Specifically, PWV interacted with diagnosis on mean diffusivity in the inferior frontal gyrus (corrected p-value=0.019) and axial diffusivity primarily in the splenium of the corpus callosum (corrected p-values<0.05). In stratified analyses in all clusters, higher baseline PWV was associated with worse white matter microstructure among NC participants only (corrected p-values<0.05), but associations were null among MCI participants. Specifically, higher

baseline PWV was associated with higher mean, radial, and axial diffusivity primarily in the striatum, insular gyrus, and external capsule (corrected p-values<0.05) among NC participants. These associations persisted when removing outliers (**Table 2.3**).

In longitudinal analyses, baseline PVW interacted with diagnosis on DTI metric trajectory (**Table 2.4, Figure 2.1).** Specifically, baseline PWV interacted with diagnosis on trajectory of mean, radial, and axial diffusivity, primarily in the middle and superior temporal gyrus (corrected p-values<0.05). Stratification revealed that among 16 clusters, associations between higher baseline PWV and faster decline in white matter microstructure were present in participants with NC, but associations were null among participants with MCI. However, when removing outliers, a majority of clusters driven by NC participants were attenuated (**Table 2.4**). In 29 clusters, associations between higher baseline PWV and faster decline in white matter microstructure were present in participants with MCI, but associations were null among participants with NC. When removing outliers, a majority of clusters driven by MCI participants remained significant (**Table 2.4**).

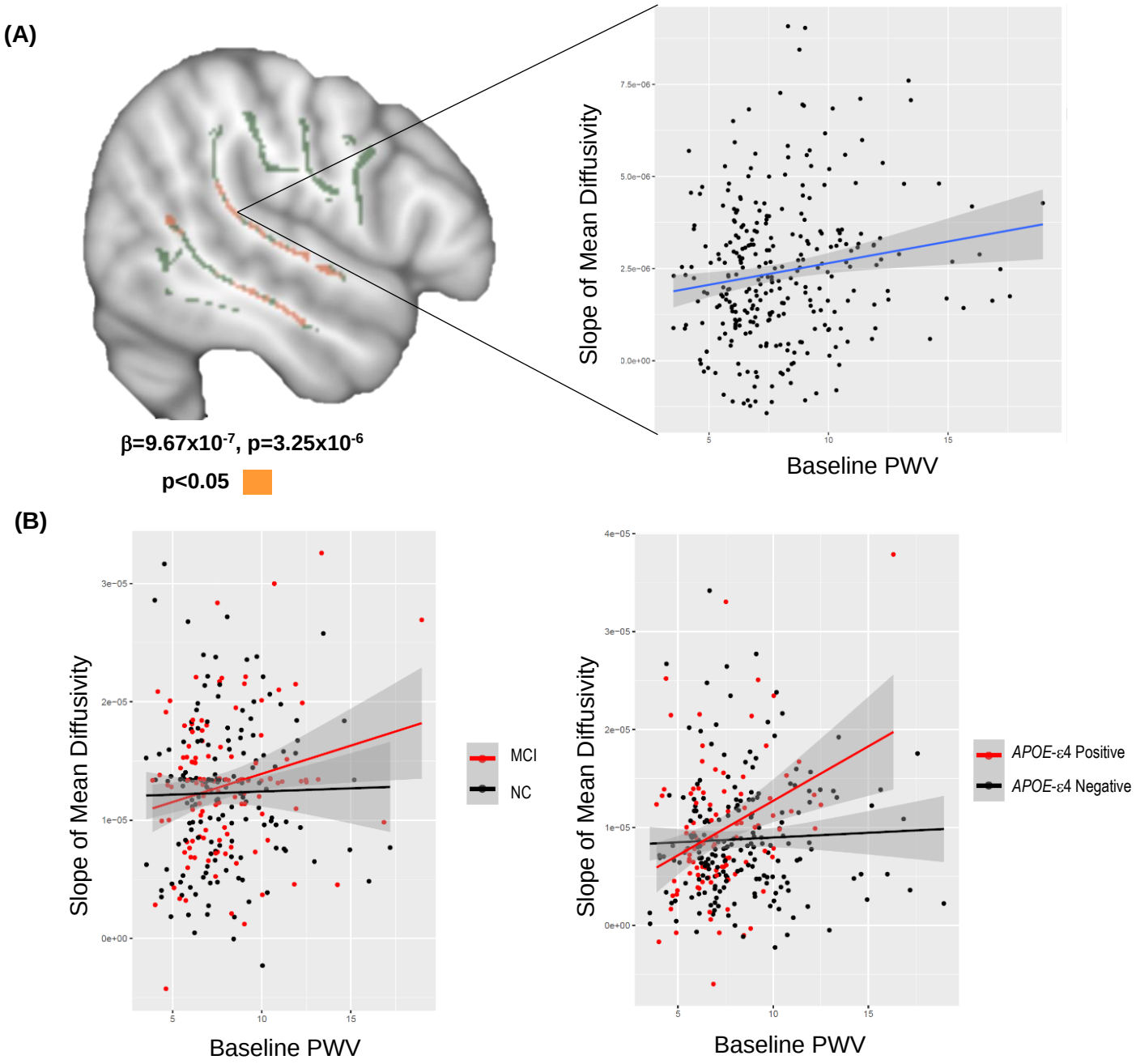

Figure 2.1. Baseline PWV and Longitudinal DTI Trajectory Associations. **(A)** Mean skeleton shows regions where baseline PWV is associated with a faster increase in mean diffusivity over time. Scatterplot shows a linear mixed effects model relating baseline PWV values for every participant to the slope of mean diffusivity values in one specific cluster. Parametric p-value and β listed only represent the cluster displayed here. Image taken at z=73. **(B)** *PWV x diagnosis* interaction on mean diffusivity trajectory (β=-3.68x10^{-6}, p=1.06x10^{-5}) and *PWV x APOE-ε4 status* interaction on mean diffusivity trajectory (β=2.56x10^{-6}, p=1.12x10^{-5}). Scatterplots show interactions at one specific cluster. Parametric p-value and β listed only represent the cluster displayed here. APOE=apolipoprotein E; DTI=diffusion tensor imaging; MCI=mild cognitive impairment; PWV=pulse wave velocity.

PWV x APOE-ε4 Interactions & DTI Metrics

In cross-sectional analyses, PWV did not interact with *APOE*-ε4 status on DTI metrics (corrected p-values>0.08). In longitudinal analyses, baseline PVW interacted with *APOE*-ε4 status on DTI metric trajectory (**Table 2.5, Figure 2.1**). Specifically, baseline PWV interacted with *APOE*-ε4 status on trajectory of FA, mean, radial, and axial diffusivity, primarily in the caudate nucleus, middle occipital gyrus, and posterior thalamic radiation (corrected p-values<0.05). Stratification revealed that among 50 clusters, associations between higher baseline PWV and faster decline in white matter microstructure were present in *APOE*-ε4 positive participants, but associations were null among *APOE*-ε4 negative participants. When removing outliers, a majority of clusters remained significant (**Table 2.5**). However, in 5 clusters, associations between higher baseline PWV and faster decline in white matter microstructure were present in *APOE*-ε4 negative participants, but associations were reversed among *APOE*-ε4 positive participants. When removing outliers, a majority of these clusters were attenuated (**Table 2.5**).

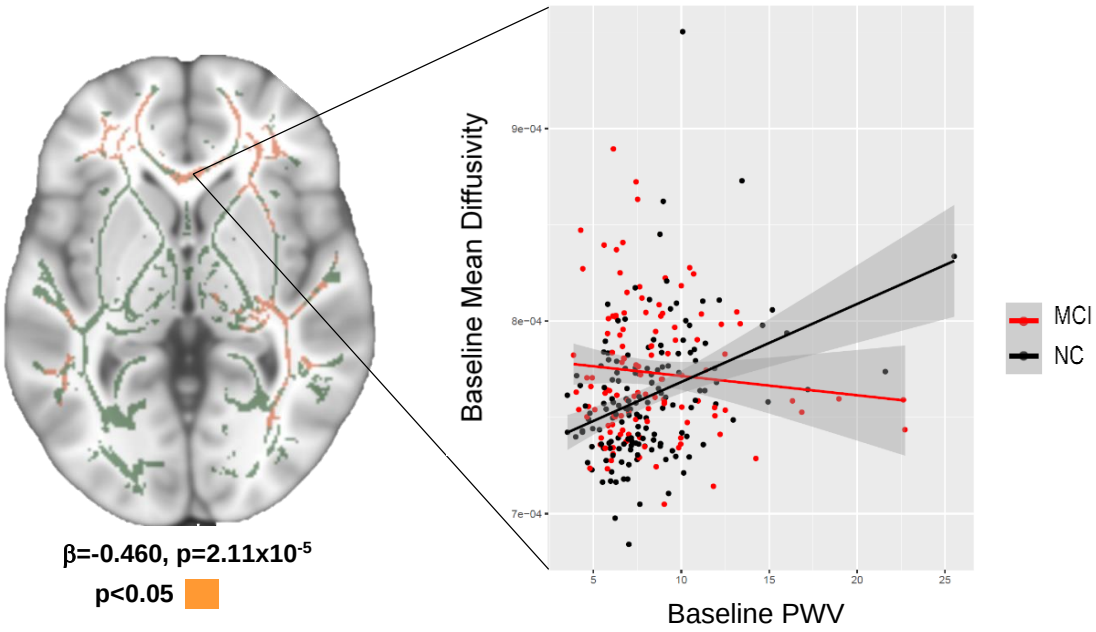

Figure 2.2. Cross-Sectional PWV x Diagnosis Interactions on Mean Diffusivity. Mean skeleton shows regions where PWV interacts with diagnosis on mean diffusivity. Scatterplot shows least squares regression relating PWV values for every participant to mean diffusivity values in one specific cluster. Parametric p-value and β listed only represent the cluster displayed here. Image taken at z=73; PWV=pulse wave velocity.

Table 2.2. Longitudinal Region Specific PWV Associations with DTI Metrics

	Anatomical Region	Hemisphere	Volume (mm^3)	Cluster Statistics		Corrected p-value†	MNI Coordinate‡		
				β	p-value*				
Fractional Anisotropy	Posterior Thalamic Radiation	Right	139	-8.05×10^{-4}	**8.13×10^{-8}**	0.00043	30	-66	1
	Posterior Corona Radiata	Right	128	-6.62×10^{-4}	**1.92×10^{-6}**	0.00092	27	-45	24
	Middle Occipital Gyrus	Right	83	-6.01×10^{-4}	**5.27×10^{-6}**	0.027	29	-67	25
	Cuneus	Left	78	-6.17×10^{-4}	**6.90×10^{-5}**	0.04	-25	-59	14
Mean Diffusivity	Superior Temporal Gyrus	Right	740	2.60×10^{-6}	**1.49×10^{-9}**	<0.001	49	-6	-12
	Middle Temporal Gyrus	Right	452	2.00×10^{-6}	8.63×10^{-8}	1.44×10^{-15}	49	-54	15
	Middle Temporal Gyrus	Right	433	1.52×10^{-6}	**3.55×10^{-7}**	4.66×10^{-15}	54	-14	-20
	Posterior Thalamic Radiation	Right	268	1.74×10^{-6}	**1.15×10^{-8}**	2.45×10^{-10}	36	-55	12
	Middle Occipital Gyrus	Right	245	9.69×10^{-7}	**2.67×10^{-8}**	1.31×10^{-9}	36	-69	20
	Middle Temporal Gyrus	Left	220	1.77×10^{-6}	1.09×10^{-6}	8.57×10^{-9}	-58	-25	-13
	Superior Occipital Gyrus	Left	81	1.43×10^{-6}	**1.28×10^{-4}**	0.0019	-14	-79	19
	Striatum	Left	78	9.67×10^{-7}	**3.25×10^{-6}**	0.0026	-34	-21	-6
	Superior Temporal Gyrus	Left	74	2.38×10^{-6}	**3.77×10^{-5}**	0.004	-45	3	-20
	Cuneus	Left	69	9.44×10^{-7}	**4.17×10^{-5}**	0.007	-26	-60	14
	Superior Corona Radiata	Left	68	8.67×10^{-7}	**8.88×10^{-6}**	0.0078	-17	-12	36
	External Capsule	Right	61	9.32×10^{-7}	**1.90×10^{-5}**	0.017	30	-4	18
	Middle Occipital Gyrus	Right	61	1.62×10^{-6}	1.86×10^{-3}	0.017	22	-84	7
	Inferior Temporal Gyrus	Right	57	1.18×10^{-6}	3.16×10^{-6}	0.028	53	-37	-16

	Superior Temporal Gyrus	Left	53	$8.38x10^{-7}$	**$1.98x10^{-6}$**	0.045	-48	-28	3
Radial Diffusivity	Insular Gyrus	Right	811	$2.35x10^{-6}$	**$5.39x10^{-9}$**	<0.001	49	-6	12
	Middle Temporal Gyrus	Right	432	$1.26x10^{-6}$	**$1.69x10^{-8}$**	$3.97x10^{-14}$	36	-54	12
	Middle Temporal Gyrus	Right	371	$1.55x10^{-6}$	**$3.16x10^{-7}$**	$1.49x20^{-12}$	54	-14	-20
	Middle Temporal Gurus	Right	327	$2.08x10^{-6}$	$1.84x10^{-7}$	$2.30x10^{-11}$	45	-50	12
	Posterior Thalamic Radiation	Right	198	$1.51x10^{-6}$	**$1.22x10^{-7}$**	$1.62x10^{-7}$	31	-48	17
	Middle Temporal Gyrus	Left	152	$1.80x10^{-6}$	$1.09x10^{-6}$	$5.94x10^{-6}$	-58	-25	-13
	Posterior Thalamic Radiation	Right	113	$1.51x10^{-6}$	**$7.49x10^{-5}$**	0.00017	26	-78	4
	Cuneus	Left	110	$9.57x10^{-7}$	**$2.17x10^{-5}$**	0.00022	-25	-59	14
	Striatum	Left	91	$9.18x10^{-7}$	**$5.84x10^{-7}$**	0.0013	-37	-18	-8
	Angular Gyrus	Right	72	$1.06x10^{-6}$	$8.38x10^{-7}$	0.0091	44	-41	24
	Angular Gyrus	Right	68	$1.33x10^{-6}$	**$3.63x10^{-8}$**	0.014	46	-55	26
	Posterior Thalamic Radiation	Right	63	$1.02x10^{-6}$	$8.15x10^{-6}$	0.024	35	-63	-2
	Superior Temporal Gyrus	Left	62	$8.20x10^{-7}$	**$1.37x10^{-6}$**	0.026	-49	-30	5
	Middle Occipital Gyrus	Left	61	$1.16x10^{-6}$	**$3.37x10^{-6}$**	0.03	-24	-83	1
	Cuneus	Left	60	$1.27x10^{-6}$	$2.37x10^{-4}$	0.033	-16	-76	16
	Middle Temporal Gyrus	Left	59	$2.11x10^{-6}$	**$3.19x10^{-4}$**	0.037	-42	1	-25
Axial Diffusivity	Superior Temporal Gyrus	Right	449	$3.92x10^{-6}$	$8.99x10^{-11}$	$1.44x10^{-15}$	49	-6	-12
	Middle Temporal Gyrus	Right	253	$1.88x10^{-6}$	**$1.93x10^{-9}$**	$6.35x10^{-10}$	60	-30	-7
	Middle Temporal Gyrus	Right	219	$2.99x10^{-6}$	$3.33x10^{-9}$	$8.21x10^{-9}$	53	-53	11
	Middle Temporal Gyrus	Left	156	$2.29x10^{-6}$	**$9.86x10^{-9}$**	$1.38x10^{-6}$	-58	-25	-13

	Body of the Corpus Callosum	Left	73	$1.57x10^{-6}$	**$2.96x10^{-6}$**	0.0042	-15	-9	33
	Superior Temporal Gyrus	Left	62	$3.66x10^{-6}$	**$1.59x10^{-5}$**	0.015	-45	3	-20
	Cuneus	Left	62	$1.90x10^{-6}$	**$2.57x10^{-5}$**	0.015	-12	-76	18
	External Capsule	Left	54	$1.51x10^{-6}$	**$1.54x10^{-8}$**	0.038	-33	-14	6

Note. Bold values indicate p-values that remain significant after excluding outliers. *parametric p-values were calculated using linear mixed effects models to relate baseline PWV and raw DTI values extracted from each participant skeleton; †p-value has been corrected for multiple comparisons; ‡coordinates and region represent the location of the minimum p-value for each cluster; DTI=diffusion tensor imaging; MNI=Montreal Neurological Institute; PWV=pulse wave velocity.

Table 2.3. Cross-Sectional Region Specific PWV x Diagnosis Interactions on DTI Metrics

	Anatomical Region	**Hemisphere**	**Volume (mm^3)**	**Cluster Statistics**		**Corrected p-value†**	**MNI Coordinate‡**		
				β	**p-value***				
Fractional Anisotropy	--	--	--	--	--	--	--	--	--
Mean Diffusivity	Inferior Frontal Gyrus	Left	32501	-0.460	**$2.11x10^{-5}$**	0.019	-34	37	-3
Radial Diffusivity	--	--	--	--	--	--	--	--	--
Axial Diffusivity	Splenium of the Corpus Callosum	Right	22686	-0.750	**$3.80x10^{-12}$**	0.001	21	-46	26
	Superior Frontal Gyrus	Left	152	-0.514	**$2.27x10^{-5}$**	0.046	-18	52	4
	Medial Orbital Gyrus	Left	114	-0.509	**$1.54x10^{-5}$**	0.048	-13	46	-14
	Superior Frontal Gyrus	Left	12	-0.390	**$1.38x10^{-3}$**	0.05	-14	46	26
	Superior Frontal Gyrus	Left	1	-0.403	**$8.34x10^{-4}$**	0.05	-17	40	26
	Superior Frontal Gyrus	Left	1	-0.340	$4.78x10^{-3}$	0.05	-12	49	29

Note. Bold values indicate p-values that remain significant after excluding outliers. Empty rows indicate no significant clusters for that metric. *parametric p-values were calculated using least squares regression to relate raw DTI values extracted from each participant skeleton and PWV; †p-value has been corrected for

multiple comparisons; ‡coordinates and region represent the voxel with the minimum p-value in each cluster; DTI=diffusion tensor imaging; MNI=Montreal Neurological Institute; NC=normal cognition; PWV=pulse wave velocity.

Table 2.4. Longitudinal Region Specific PWV x Diagnosis Interactions on DTI Metrics

	Anatomical Region	Hemisphere	Volume (mm^3)	Cluster Statistics		Corrected p-value†	MNI Coordinate‡		
				β	p-value*				
Fractional Anisotropy	--	--	--	--	--	--	--	--	--
Mean Diffusivity	Superior Temporal Gyrus	Right	503	$5.32x10^{-6}$	$4.77x10^{-7}$	$1.11x10^{-16}$	51	-4	-8
	Inferior Temporal Gyrus	Right	493	$3.06x10^{-6}$	$1.14x10^{-7}$	$1.11x10^{-16}$	50	-29	-15
	Angular Gyrus	Right	293	$4.23x10^{-6}$	$5.82x10^{-8}$	$4.57x10^{-11}$	43	-56	30
	Superior Longitudinal Fasciculus	Right	269	$3.91x10^{-6}$	$2.66x10^{-7}$	$2.48x10^{-10}$	41	-49	11
	Middle Occipital Gyrus	Right	141	$2.17x10^{-6}$	$8.76x10^{-7}$	$5.97x10^{-6}$	37	-69	22
	Superior Temporal Gyrus	Right	100	$2.31x10^{-6}$	$7.78x10^{-6}$	0.00028	41	-15	-11
	Superior Temporal Gyrus	Right	91	$2.71x10^{-6}$	$1.99x10^{-4}$	0.00069	41	-31	-5
	Precentral Gyrus	Right	85	$1.33x10^{-6}$	**$1.99x10^{-6}$**	0.0013	46	0	23
	Middle Temporal Gyrus	Right	74	$2.44x10^{-6}$	$1.03x10^{-5}$	0.0042	56	-18	-15
	Anterior Corona Radiata	Right	74	$1.09x10^{-6}$	$5.37x10^{-3}$	0.0042	18	42	-6
	Anterior Corona Radiata	Left	57	$1.39x10^{-6}$	**$8.66x20^{-6}$**	0.029	-20	38	11
	Middle Temporal Gyrus	Left	117	$-4.01x10^{-6}$	$4.33x10^{-6}$	$5.35x10^{-5}$	-57	-17	-16
	Middle Temporal Gyrus	Left	105	$-3.19x10^{-6}$	**$1.25x10^{-7}$**	0.00017	-57	-27	-12
	Cuneus	Left	101	$-3.68x10^{-6}$	**$1.06x10^{-5}$**	0.00025	-14	-75	16

	Middle Occipital Gyrus	Left	95	-3.21×10^{-6}	$\mathbf{5.60 \times 10^{-8}}$	0.00046	-20	-87	4
	Middle Temporal Gyrus	Left	69	-5.14×10^{-6}	6.22×10^{-4}	0.0072	-43	4	-24
	Fusiform Gyrus	Left	60	-4.01×10^{-6}	1.96×10^{-4}	0.02	-38	-27	-20
	Middle Occipital Gyrus	Right	60	-4.37×10^{-6}	1.57×10^{-4}	0.02	23	-87	2
Radial Diffusivity	Superior Temporal Gyrus	Right	504	5.16×10^{-6}	4.79×10^{-7}	8.88×10^{-16}	51	-4	-8
	Middle Temporal Gyrus	Right	362	3.04×10^{-6}	2.04×10^{-7}	3.31×10^{-12}	59	-36	-6
	Middle Temporal Gyrus	Right	358	4.42×10^{-6}	3.42×10^{-7}	4.23×10^{-12}	46	-52	15
	Angular Gyrus	Right	93	3.30×10^{-6}	1.04×10^{-9}	0.0012	46	-56	26
	Striatum	Right	77	2.40×10^{-6}	8.26×10^{-5}	0.0059	41	-31	-5
	Middle Temporal Gyrus	Right	76	2.20×10^{-6}	4.68×10^{-6}	0.0065	42	-18	-12
	Middle Temporal Gyrus	Left	217	-3.48×10^{-6}	1.33×10^{-6}	4.73×10^{-8}	-57	-27	-12
	Cuneus	Left	102	-3.52×10^{-6}	$\mathbf{1.12 \times 10^{-5}}$	0.00052	-14	-75	16
	Middle Occipital Gyrus	Left	95	-2.90×10^{-6}	$\mathbf{2.31 \times 10^{-8}}$	0.001	-20	-87	4
	Fusiform Gyrus	Left	72	-3.74×10^{-6}	2.16×10^{-4}	0.0099	-39	-29	-19
Axial Diffusivity	Middle Temporal Gyrus	Right	364	4.18×10^{-6}	$\mathbf{2.29 \times 10^{-9}}$	3.59×10^{-13}	55	-37	-7
	Middle Temporal Gyrus	Right	244	3.77×10^{-6}	$\mathbf{9.08 \times 10^{-10}}$	1.42×10^{-9}	41	-49	11
	Superior Temporal Gyrus	Right	228	8.28×10^{-6}	4.85×10^{-7}	4.69×10^{-9}	51	-5	-9
	Angular Gyrus	Right	157	5.54×10^{-6}	1.96×10^{-8}	1.41×10^{-6}	44	-53	23
	Superior Temporal Gyrus	Right	115	3.65×10^{-6}	1.80×10^{-7}	6.19×10^{-5}	59	-23	6
	Posterior Thalamic Radiation	Right	106	4.02×10^{-6}	5.29×10^{-7}	0.00015	33	-59	15
	Splenium of the Corpus Callosum	Right	83	3.27×10^{-6}	$\mathbf{2.47 \times 10^{-5}}$	0.0015	15	-41	13

	Precentral Gyrus	Right	69	$2.24x10^{-6}$	**$2.24x10^{-6}$**	0.007	39	3	23
	Superior Temporal Gyrus	Right	68	$4.12x10^{-6}$	$2.98x10^{-4}$	0.0079	41	-31	-5
	Precentral Gyrus	Right	58	$2.76x10^{-6}$	**$4.73x10^{-8}$**	0.025	40	-4	40
	Middle Temporal Gyrus	Right	53	$3.24x10^{-6}$	$3.56x10^{-8}$	0.045	53	-16	-18
	Superior Temporal Gyrus	Right	53	$3.64x10^{-6}$	**$9.91x10^{-6}$**	0.045	41	-15	-11
	Middle Occipital Gyrus	Left	111	$-4.13x10^{-6}$	**$1.84x10^{-7}$**	$9.08x10^{-5}$	-24	-82	1
	Middle Temporal Gyrus	Left	97	$-4.62x10^{-6}$	$7.74x10^{-7}$	0.00036	-55	-18	-17
	Cuneus	Left	96	$-4.26x10^{-6}$	**$2.26x10^{-5}$**	0.0004	-14	-71	14
	Posterior Thalamic Radiation	Right	77	$-5.18x10^{-6}$	$3.47x10^{-4}$	0.0029	25	-80	3
	Superior Temporal Gyrus	Left	60	$-7.15x10^{-6}$	$1.28x10^{-3}$	0.02	-42	8	-25

Note. Empty rows indicate no significant clusters. Bold values indicate p-values that remain significant after excluding outliers. Mean, radial, and axial diffusivity clusters with a negative β indicate clusters driven by participants with MCI. *parametric p-values were calculated using linear mixed effects models to relate baseline *PWV x diagnosis* and raw DTI values extracted from each participant skeleton; †p-value has been corrected for multiple comparisons; ‡coordinates and region represent the location of the minimum p-value for each cluster; DTI=diffusion tensor imaging; MCI=mild cognitive impairment; MNI=Montreal Neurological Institute; PWV=pulse wave velocity.

Table 2.5. Longitudinal Region Specific PWV x *APOE*-ε4 Status Interactions on DTI Metrics

	Anatomical Region	Hemisphere	Volume (mm^3)	Cluster Statistics		Corrected p-value†	MNI Coordinate‡		
				β	p-value*				
Fractional Anisotropy	Caudate Nucleus	Left	113	$1.63x10^{-3}$	$5.72x10^{-11}$	0.0026	-13	21	7
	Body of the Corpus Callosum	Left	120	$-1.53x10^{-3}$	**$1.39x10^{-6}$**	0.0016	-7	25	14

	Genu of the Corpus Callosum	Right	110	$-1.53x10^{-3}$	$1.53x10^{-4}$	0.0033	4	-33	22
	Posterior Limb of the Internal Capsule	Left	102	$-1.42x10^{-3}$	$7.33x10^{-6}$	0.0060	-23	-12	10
	Precentral Gyrus	Right	79	$-1.23x10^{-3}$	**$8.48x10^{-6}$**	0.036	20	-21	47
Mean Diffusivity	Middle Occipital Gyrus	Left	868	$5.34x10^{-6}$	$2.32x10^{-14}$	<0.001	-19	-90	1
	Fusiform Gyrus	Left	359	$7.02x10^{-6}$	$9.88x10^{-13}$	$4.90x10^{-13}$	-32	-46	-14
	Middle Temporal Gyrus	Right	317	$1.21x20^{-5}$	**$3.20x10^{-13}$**	$7.99x10^{-12}$	40	8	-27
	Middle Temporal Gyrus	Left	243	$1.10x10^{-5}$	$1.38x10^{-11}$	$1.51x10^{-9}$	-43	5	-24
	Middle Occipital Gyrus	Right	233	$6.47x10^{-6}$	**$6.63x10^{-15}$**	$3.18x10^{-9}$	22	-85	4
	Fusiform Gyrus	Left	134	$1.02x10^{-5}$	$1.40x10^{-9}$	$1.05x10^{-5}$	-30	-32	-14
	Cuneus	Left	128	$6.36x10^{-6}$	$1.92x10^{-12}$	$1.82x10^{-5}$	-13	-75	17
	Body of the Corpus Callosum	Left	104	$2.56x10^{-6}$	**$1.12x10^{-5}$**	0.00018	-15	19	25
	Hippocampus	Right	92	$8.21x10^{-6}$	**$1.94x10^{-12}$**	0.00059	34	-29	-16
	Genu of the Corpus Callosum	Left	92	$2.57x10^{-6}$	$3.30x10^{-7}$	0.00059	-16	27	19
	Pulvinar	Left	92	$8.51x10^{-6}$	**$1.63x10^{-4}$**	0.00059	-13	-30	6
	Superior Corona Radiata	Right	74	$1.48x10^{-6}$	**$4.60x10^{-5}$**	0.0040	26	-20	33
	Lingual Gyrus	Left	68	$3.80x10^{-6}$	$3.67x10^{-7}$	0.0078	-13	-83	-6
	Fusiform Gyrus	Right	59	$8.46x10^{-6}$	**$3.30x10^{-12}$**	0.0022	39	-29	-18
	Superior Occipital Gyrus	Left	58	$2.27x10^{-6}$	**$2.31x10^{-8}$**	0.025	-26	-82	12
	Middle Temporal Gyrus	Left	86	$-3.11x10^{-6}$	**$1.14x10^{-11}$**	0.0011	-48	-35	-8
	Middle Temporal Gyrus	Right	53	$-3.13x10^{-6}$	**$9.75x10^{-5}$**	0.045	57	-33	-9
Radial Diffusivity	Posterior Thalamic Radiation	Left	654	$5.11x10^{-6}$	$5.40x10^{-14}$	<0.001	-30	-67	0

	Middle Temporal Gyrus	Right	379	$9.75x10^{-6}$	**$7.47x10^{-14}$**	$8.99x10^{-13}$	40	9	-27
	Fusiform Gyrus	Left	366	$6.51x10^{-6}$	$1.74x10^{-12}$	$1.98x10^{-12}$	-32	-46	-14
	Middle Temporal Gyrus	Left	247	$9.40x10^{-6}$	$1.23x10^{-11}$	$4.61x10^{-9}$	-43	5	-24
	Anterior Corona Radiata	Left	189	$2.31x10^{-6}$	$2.64x10^{-6}$	$3.16x10^{-7}$	-16	27	19
	Posterior Thalamic Radiation	Right	165	$7.07x10^{-6}$	$9.89x10^{-14}$	$2.05x10^{-6}$	23	-86	2
	Cuneus	Left	128	$6.17x10^{-6}$	$1.27x10^{-12}$	$4.46x10^{-5}$	-13	-75	17
	Fusiform Gyrus	Left	115	$9.89x10^{-6}$	$8.55x10^{-9}$	0.00014	-30	-32	-14
	Posterior Limb of the Internal Capsule	Left	106	$1.60x10^{-6}$	$4.41x10^{-5}$	0.00032	-23	-17	11
	Pulvinar	Left	88	$7.71x10^{-6}$	**$1.49x10^{-4}$**	0.00062	-13	-30	6
	Hippocampus	Right	88	$7.35x10^{-6}$	**$2.00x10^{-11}$**	0.0018	34	-29	-16
	Splenium of the Corpus Callosum	Right	81	$2.23x10^{-6}$	**$6.26x10^{-4}$**	0.0036	3	-39	17
	Body of the Corpus Callosum	Left	77	$2.23x10^{-6}$	**$4.37x10^{-5}$**	0.0054	-15	19	25
	Middle Occipital Gyrus	Left	74	$3.21x10^{-6}$	**$1.29x10^{-9}$**	0.0073	-22	-87	14
	Body of the Corpus Callosum	Right	72	$2.85x10^{-6}$	**$6.84x10^{-6}$**	0.0090	6	24	14
	Fusiform Gyrus	Right	69	$1.05x10^{-5}$	**$9.70x10^{-5}$**	0.012	39	-29	-18
	Pulvinar	Right	58	$7.54x10^{-6}$	**$1.92x10^{-12}$**	0.041	18	-29	9
	Middle Temporal Gyrus	Left	71	$-2.83x10^{-6}$	$9.42x10^{-9}$	0.010	-49	-33	-11
Axial Diffusivity	Middle Occipital Gyrus	Left	795	$7.05x10^{-6}$	**$1.30x10^{-14}$**	<0.001	-24	-86	-3
	Striatum	Left	321	$8.60x10^{-6}$	$4.22x10^{-13}$	$5.04x10^{-12}$	-33	-47	-13
	Superior Temporal Gyrus	Right	311	$1.51x10^{-5}$	$4.39x10^{-12}$	$9.99x10^{-12}$	48	5	-18
	Middle Temporal Gyrus	Left	231	$1.48x10^{-5}$	**$1.80x10^{-11}$**	$3.18x10^{-9}$	-43	5	-24

Middle Occipital Gyrus	Right	186	$8.78x10^{-6}$	**$1.64x10^{-14}$**	$1.09x10^{-7}$	21	-86	4
Cuneus	Left	111	$7.26x10^{-6}$	$2.22x10^{-11}$	$8.22x10^{-5}$	-14	-70	15
Hippocampus	Right	89	$1.09x10^{-5}$	**$1.09x10^{-13}$**	0.00075	33	-29	-16
Superior Corona Radiata	Left	78	$3.77x10^{-6}$	**$2.64x10^{-5}$**	0.0024	-19	18	27
Fusiform Gyrus	Left	77	$1.29x10^{-5}$	$6.91x10^{-8}$	0.0027	-30	-32	-14
Middle Frontal Gyrus	Left	62	$2.88x10^{-6}$	**$2.79x10^{-6}$**	0.015	-24	19	29
Lingual Gyrus	Left	61	$4.43x10^{-6}$	$9.41x10^{-7}$	0.016	-13	-83	-6
Superior Temporal Gyrus	Right	58	$5.17x10^{-6}$	**$6.83x10^{-12}$**	0.023	28	-6	-16
Fusiform Gyrus	Right	54	$9.77x10^{-6}$	$3.21x10^{-10}$	0.038	39	-29	-18
Superior Corona Radiata	Right	54	$2.26x10^{-6}$	**$2.72x10^{-5}$**	0.038	26	-14	31
Middle Temporal Gyrus	Left	98	$-4.20x10^{-6}$	**$1.79x10^{-11}$**	0.00030	-47	-32	-10

Note. Bold values indicate p-values that remain significant after excluding outliers. FA clusters with a negative β and mean, radial, and axial diffusivity clusters with a positive β indicate clusters driven by *APOE*-ε4 positive participants. *parametric p-values were calculated using linear mixed effects models to relate baseline *PWV x APOE-ε4 status* and raw DTI values extracted from each participant skeleton; †p-value has been corrected for multiple comparisons; ‡coordinates and region represent the location of the minimum p-value for each cluster; APOE=apolipoprotein E; DTI=diffusion tensor imaging; FA=fractional anisotropy; MNI=Montreal Neurological Institute; PWV=pulse wave velocity.

BBB Integrity Analyses

Participant Characteristics

The sample included 152 adults age 60-90 years (72±6 years, 67% males, 93% non-Hispanic White). CSF MMP-2 concentrations ranged 37485 to 117861 pg/mL, MMP-3 concentrations ranged 84 to 884 pg/mL, and MMP-9 concentrations ranged 6 to 507 pg/mL. The CSF/plasma albumin ratio ranged 1.3 to 16.8. See **Table 2.6** for participant characteristics for the total sample and stratified by diagnosis.

Table 2.6. Participant Characteristics for CSF Sample

	Total n=152	**NC n=80**	**Early MCI n=15**	**MCI n=57**	**p-value**
Demographic & Health Characteristics					
Age, years	72±6	72±7	73±6	73±6	0.77
Sex, % male	67	70	80	60	0.24
Race, % Non-Hispanic White	93	94	93	91	0.85
Education, years	16±3	17±2	16±3	15±3	**0.001**†
APOE-ε4, % positive	33	29	13	44	**0.04***
FSRP, total score§	12±4	11±4	13±3	12±4	0.12
Systolic blood pressure, mmHg	142±16	139±15	148±15	145±15	0.06
Antihypertensive medication usage, %	46	46	40	47	0.88
Diabetes, %	17	12	27	21	0.25
Current smoking, %	1	0	7	2	0.11
Atrial fibrillation, %	4	6	0	2	0.29
Prevalent CVD, %	3	5	0	2	0.43
Left ventricular hypertrophy, %	3	1	7	5	0.11
Pulse wave velocity, m/sec	8±3	8±3	9±3	8±3	0.62
Follow-up time, years	3.9±1.7	4.4±1.5	3.7±1.8	3.4±1.9	**0.007**‡
CSF Fluid Biomarkers, pg/mL					
Aβ42	720±244	773±223	817±282	621±232	**<0.001**†‡
Amyloid positive (≤530), %	28	18	20	46	**0.001**†

Aβ40	6165±1637	6296±1745	6494±1868	5894±1390	0.57
Aβ42/Aβ40 ratio	0.09±0.03	0.10±0.03	0.10±0.03	0.08±0.03	**<0.001‡**
P-tau	61±26	56±22	63±17	68±31	0.06
P-tau positive (≥80), %	22	18	13	30	0.16
T-tau	428±228	375±177	429±125	502±288	**0.02‡**
T-tau positive ((≥400), %	43	31	60	56	**0.006‡**
NFL	1069±583	933±454	1088±465	1250±712	0.28
MMP-2	66991±16611	68115±17533	70744±15310	77135±15057	0.65
MMP-3	314±166	295±160	422±230	311±144	0.12
MMP-9	122±87	119±83	121±66	125±99	0.81
CSF/plasma albumin ratio	5.72±2.39	5.46±2.35	5.69±2.05	6.08±2.51	0.26

Note. Values denoted as mean±standard deviation or frequency. Participant characteristics were compared across cognitive diagnosis using Kruskal-Wallis test for continuous variables and chi-square test for categorical variables. *Early MCI different than MCI, †Early MCI different than NC, ‡NC different from MCI. §a modified FSRP score was included in statistical models excluding points assigned to age (Total=7±3, NC=6±3, Early MCI=8±2, MCI=7±3); APOE=apolipoprotein E; CVD=cardiovascular disease; FSRP=Framingham Stroke Risk Profile; MCI=mild cognitive impairment; NC=normal cognition; CSF=cerebrospinal fluid; Aβ=amyloid-β; p-tau=phosphorylated tau; MMP=matrix metalloproteinase; NFL=neurofilament light; T-tau=total tau

MMP-2 Analyses

MMP-2 & DTI Metrics

In the whole sample, CSF MMP-2 was cross-sectionally associated with compromised white matter microstructure (corrected p-values<0.05, **Table 2.7, Figure 2.3**). Specifically, higher CSF MMP-2 was associated with higher FA primarily in the inferior frontal gyrus and lateral occipital gyrus, lower mean diffusivity in the splenium of the corpus callosum, lower radial diffusivity in the body of the corpus callosum, and lower axial diffusivity primarily in the splenium of the corpus callosum. Clusters remained significant when removing outliers (**Table 2.7**).

Baseline CSF MMP-2 was also associated with DTI metric trajectory in small clusters (corrected p-values<0.02, **Table 2.8, Figure 2.4**). Specifically, higher baseline

CSF MMP-2 was associated with a faster increase in mean diffusivity, radial diffusivity, and axial diffusivity in one small cluster in the external capsule. Associations remained significant when removing outliers (**Table 2.8**).

MMP-2 x Diagnosis Interactions & DTI Metrics

In cross-sectional analyses, CSF MMP-2 interacted with diagnosis on DTI metrics (corrected p-values<0.05, **Table 2.9, Figure 2.3**). Specifically, CSF MMP-2 interacted with diagnosis on fractional anisotropy in the cingulum bundle, mean diffusivity primarily in the inferior frontal gyrus, radial diffusivity primarily in the inferior frontal gyrus, and axial diffusivity primarily in the superior corona radiata. Stratification revealed that in all clusters, higher CSF MMP-2 was associated with compromised white matter microstructure among NC participants, but associations were reversed among participants with MCI. These associations persisted when removing outliers (**Table 2.9**).

In longitudinal analyses, baseline CSF MMP-2 interacted with diagnosis on DTI metric trajectory in small clusters (**Table 2.10, Figure 2.4**). Specifically, baseline CSF MMP-2 interacted with diagnosis on trajectory of mean and radial diffusivity primarily in the cuneus. Stratification revealed that in all clusters, higher baseline CSF MMP-2 was associated with a faster increase in mean and radial diffusivity among NC participants, but associations were reversed among participants with MCI. When removing outliers, associations remained significant (**Table 2.10**).

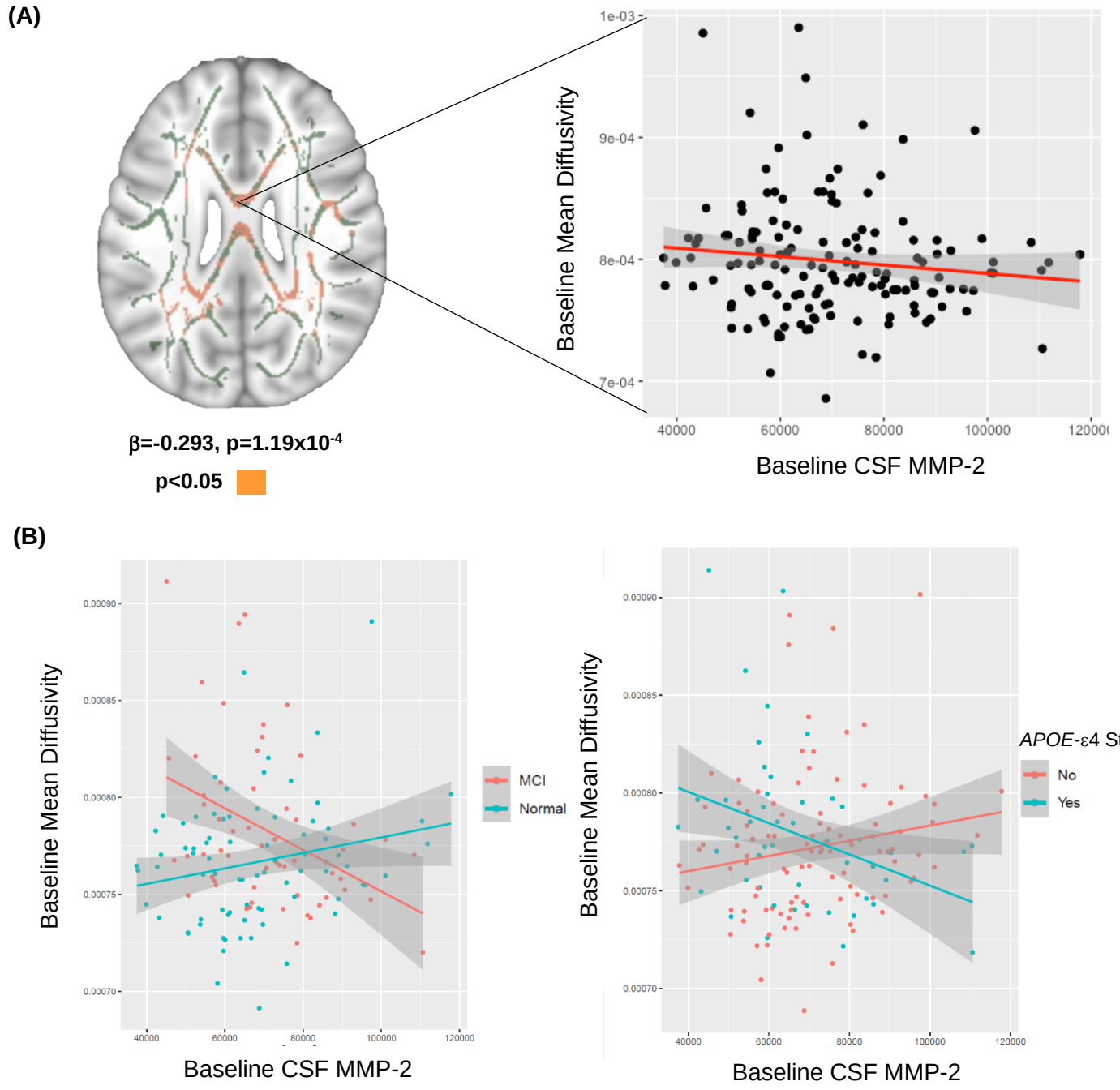

Figure 2.3. Cross-sectional CSF MMP-2 and DTI Metric Associations. **(A)** Mean skeleton shows regions where baseline CSF MMP-2 is associated with mean diffusivity over time. Scatterplot shows a linear regression model relating baseline CSF MMP-2 values for every participant to mean diffusivity values in one specific cluster. Parametric p-value and β listed only represent the cluster displayed here. Image taken at z=98. **(B)** *CSF MMP-2 x diagnosis* interaction on mean diffusivity (β=1.398, p=1.04x10^{-4}) and *CSF MMP-2 x APOE-ε4 status* interaction on mean diffusivity (β=-1.154, p=3.57x10^{-4}). Scatterplots show interactions at one specific cluster. Parametric p-value and β listed only represent the cluster displayed here. APOE=apolipoprotein E; CSF=cerebrospinal fluid; DTI=diffusion tensor imaging; MCI=mild cognitive impairment; MMP=matrix metalloprotein.

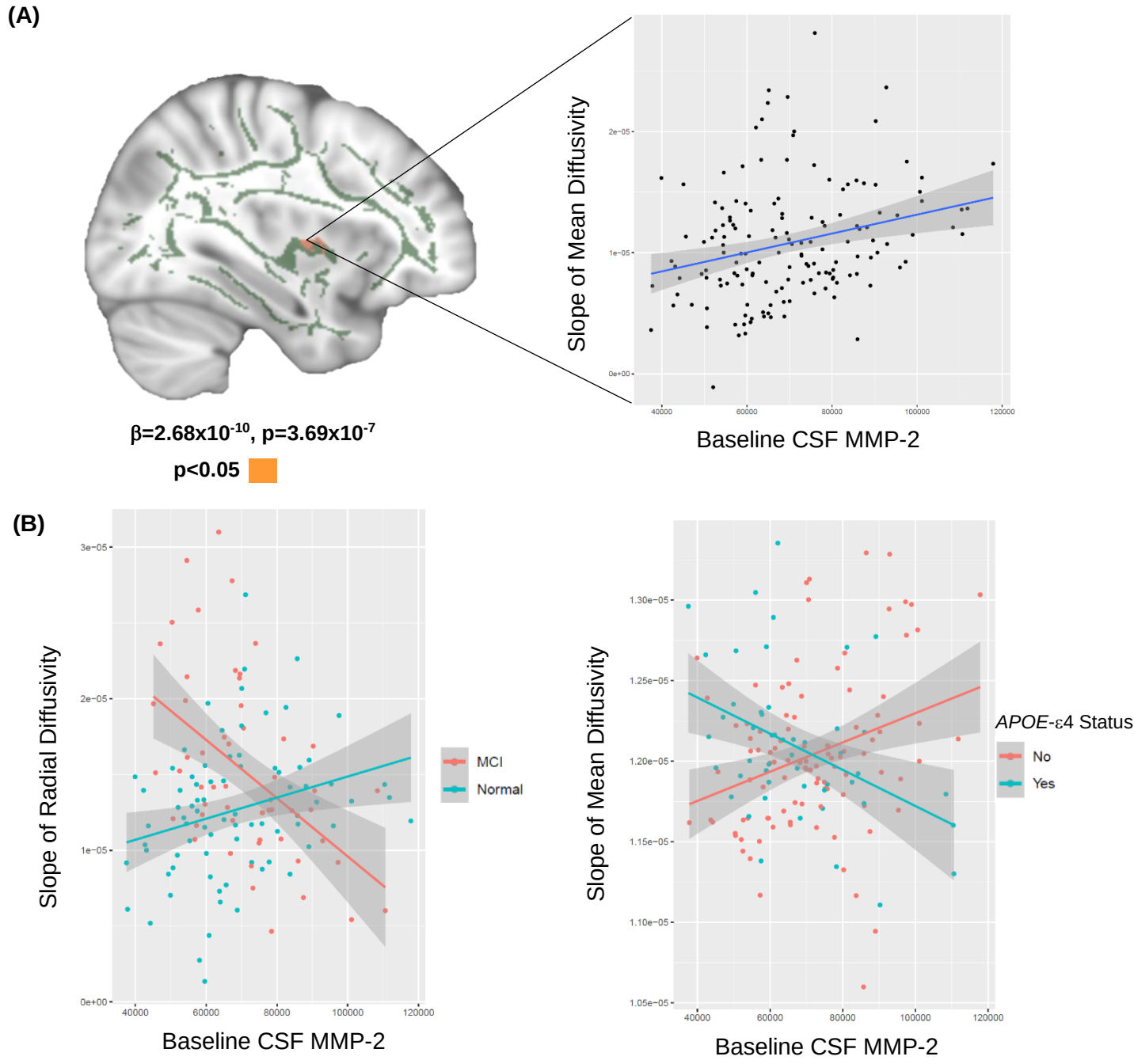

Figure 2.4. Baseline CSF MMP-2 and Longitudinal DTI Trajectory Associations. **(A)** Mean skeleton shows regions where baseline CSF MMP-2 is associated with a faster increase in mean diffusivity over time. Scatterplot shows a linear mixed effects model relating baseline CSF MMP-2 values for every participant to the slope of mean diffusivity values in one specific cluster. Parametric p-value and β listed only represent the cluster displayed here. Image taken at z=73. **(B)** *CSF MMP-2 x diagnosis* interaction on radial diffusivity trajectory ($\beta=6.28x10^{-10}$, $p=2.59x10^{-8}$) and *CSF MMP-2 x APOE-ε4 status* interaction on mean diffusivity trajectory ($\beta=-3.45x10^{-10}$, $p=3.13x10^{-4}$). Scatterplots show interactions at one specific cluster. Parametric p-value and β listed only represent the cluster displayed here. APOE=apolipoprotein E; CSF=cerebrospinal fluid; DTI=diffusion tensor imaging; MCI=mild cognitive impairment; MMP=matrix metalloprotein.

MMP-2 x APOE-ε4 Interactions & DTI Metrics

In cross-sectional analyses, CSF MMP-2 interacted with *APOE*-ε4 status on DTI metrics (corrected p-values<0.05, **Table 2.11, Figure 2.3**). Specifically, CSF MMP-2 interacted with *APOE*-ε4 status on mean diffusivity in the superior longitudinal fasciculus, radial diffusivity primarily in the splenium of the corpus callosum, and axial diffusivity primarily in the middle frontal gyrus. Stratification revealed that in all clusters, higher CSF MMP-2 was associated with compromised white matter microstructure among *APOE*-ε4 negative participants, but associations were reversed among *APOE*-ε4 positive participants. These associations persisted when removing outliers (**Table 2.11**).

In longitudinal analyses, baseline CSF MMP-2 interacted with *APOE*-ε4 status on DTI metric trajectory in small clusters (**Table 2.12, Figure 2.4**). Specifically, baseline CSF MMP-2 interacted with *APOE*-ε4 status on trajectory of mean and axial diffusivity primarily in the internal capsule. Stratification revealed that in all clusters, higher baseline CSF MMP-2 was associated with a faster increase in mean and axial diffusivity among *APOE*-ε4 negative participants, but associations were reversed among *APOE*-ε4 positive participants. When removing outliers, associations remained significant (**Table 2.12**).

Table 2.7. Cross-Sectional Region Specific MMP-2 Associations with DTI Metrics

	Anatomical Region	Hemisphere	Volume (mm^3)	Cluster Statistics		Corrected p-value†	MNI Coordinate‡		
				β	p-value*				
Fractional Anisotropy	Inferior Frontal Gyrus	Left	8432	0.343	**$1.18x10^{-5}$**	0.007	-26	35	4
	Lateral Occipital Gyrus	Left	573	0.311	**$8.95x10^{-5}$**	0.043	-27	-51	26
	Inferior Frontal Gyrus	Left	211	0.353	**$1.46x10^{-5}$**	0.049	-49	5	8
	Inferior Frontal Gyrus	Left	149	0.351	**$1.56x10^{-5}$**	0.049	-43	12	12
	Postcentral Gyrus	Right	18	0.244	**$4.81x10^{-3}$**	0.05	15	-35	57
	Lateral Occipital Gyrus	Left	4	0.308	**$3.21x10^{-4}$**	0.05	-34	-61	31
	Postcentral Gyrus	Right	1	0.245	**$5.41x10^{-3}$**	0.05	8	-39	61
Mean Diffusivity	Splenium of the Corpus Callosum	Right	11576	-0.293	**$1.19x10^{-4}$**	0.026	24	-47	23
Radial Diffusivity	Body of the Corpus Callosum	Right	15371	-0.293	**$1.86x10^{-4}$**	0.023	3	20	16
	Precentral Gyrus	Right	384	-0.319	**$7.97x10^{-5}$**	0.048	44	-6	26
Axial Diffusivity	Splenium of the Corpus Callosum	Right	5192	-0.386	**$2.48x10^{-7}$**	0.004	19	-47	21
	Splenium of the Corpus Callosum	Left	1981	-0.349	**$5.39x10^{-6}$**	0.027	-15	-45	21
	Anterior Limb of the Internal Capsule	Left	48	-0.332	**$4.74x10^{-5}$**	0.046	-17	1	11
	Posterior Limb of the Internal Capsule	Left	33	-0.304	**$5.86x10^{-4}$**	0.049	-14	-5	2
	Posterior Limb of the Internal Capsule	Left	27	-0.285	**$8.79x10^{-4}$**	0.049	-19	-9	5
	Anterior Limb of the Internal Capsule	Left	6	-0.259	**$1.91x10^{-3}$**	0.05	-14	4	8

Note. Bold values indicate p-values that remain significant after excluding outliers. *parametric p-values were calculated using linear regression models to relate MMP-2 and raw DTI values extracted from each participant skeleton; †p-value has been corrected for multiple comparisons; ‡coordinates and region represent the location of the minimum p-value for each cluster; DTI=diffusion tensor imaging; MMP=matrix metalloproteinase; MNI=Montreal Neurological Institute.

Table 2.8. Longitudinal Region Specific MMP-2 Associations with DTI Metrics

	Anatomical Region	Hemisphere	Volume (mm^3)	Cluster Statistics		Corrected p-value†	MNI Coordinate‡		
				β	p-value*				
Fractional Anisotropy	--	--	--	--	--	--	--	--	--
Mean Diffusivity	External Capsule	Right	97	$2.68x10^{-10}$	**$3.69x10^{-7}$**	$2.87x10^{-5}$	33	-6	7
Radial Diffusivity	External Capsule	Right	82	$2.64x10^{-10}$	**$6.02 x10^{-7}$**	$3.42x10^{-4}$	33	-5	7
Axial Diffusivity	External Capsule	Right	47	$3.34x10^{-10}$	**$2.75x10^{-6}$**	0.017	33	-6	7

Note. Bold values indicate p-values that remain significant after excluding outliers. Empty rows indicate no significant clusters for that metric. *parametric p-values were calculated using linear mixed effects models to relate baseline MMP-2 and raw DTI values extracted from each participant skeleton; †p-value has been corrected for multiple comparisons; ‡coordinates and region represent the location of the minimum p-value for each cluster; DTI=diffusion tensor imaging; MMP=matrix metalloproteinase; MNI=Montreal Neurological Institute.

Table 2.9. Cross-Sectional Region Specific MMP-2 x Diagnosis Interactions on DTI Metrics

	Anatomical Region	Hemisphere	Volume (mm^3)	Cluster Statistics		Corrected p-value†	MNI Coordinate‡		
				β	p-value*				
Fractional Anisotropy	Cingulum Bundle	Right	1777	-1.817	**$1.75x10^{-6}$**	0.04	16	-37	37
Mean Diffusivity	Inferior Frontal Gyrus	Right	40241	1.398	**$1.04x10^{-4}$**	0.015	40	34	4
	Fornix	Left	14	1.370	**$5.98x10^{-4}$**	0.05	-17	-19	-10
Radial Diffusivity	Inferior Frontal Gyrus	Right	34487	1.365	**$1.41x10^{-4}$**	0.014	38	34	7
	Inferior Temporal Gyrus	Right	1595	1.355	**$1.15x10^{-4}$**	0.043	52	-35	-17
Axial Diffusivity	Superior Corona Radiata	Left	1828	1.682	**$1.89x10^{-6}$**	0.031	-29	6	27
	Inferior Frontal Gyrus	Left	145	1.694	**$2.09x10^{-5}$**	0.048	-34	37	1

	Inferior Frontal Gyrus	Left	26	1.722	**1.25x10^{-5}**	0.049	-37	20	17

Note. Bold values indicate p-values that remain significant after excluding outliers. *parametric p-values were calculated using linear regression models to relate *MMP-2 x diagnosis* and raw DTI values extracted from each participant skeleton; †p-value has been corrected for multiple comparisons; ‡coordinates and region represent the voxel with the minimum p-value in each cluster; DTI=diffusion tensor imaging; MCI=mild cognitive impairment; MMP=matrix metalloproteinase; MNI=Montreal Neurological Institute.

Table 2.10. Longitudinal Region Specific MMP-2 x Diagnosis Interactions on DTI Metrics

	Anatomical Region	Hemisphere	Volume (mm^3)	Cluster Statistics		Corrected p-value†	MNI Coordinate‡		
				β	p-value*				
Fractional Anisotropy	Cuneus	Left	212	-3.90x10-7	**2.18x10-8**	1.75x10^{-7}	-27	-68	14
Mean Diffusivity	--	--	--	--	--	--	--	--	--
Radial Diffusivity	Cuneus	Left	185	6.28x10^{-10}	**2.59x10^{-8}**	1.38x10^{-8}	-29	-65	14
	External Capsule	Right	44	6.53x10^{-10}	**8.03x10^{-7}**	0.05	22	20	4
Axial Diffusivity	--	--	--	--	--	--	--	--	--

Note. Bold values indicate p-values that remain significant after excluding outliers. Empty rows indicate no significant clusters for that metric. *parametric p-values were calculated using linear mixed effects models to relate baseline *MMP-2 x diagnosis* and raw DTI values extracted from each participant skeleton; †p-value has been corrected for multiple comparisons; ‡coordinates and region represent the location of the minimum p-value for each cluster; DTI=diffusion tensor imaging; MMP=matrix metalloproteinase; MNI=Montreal Neurological Institute.

Table 2.11. Cross-Sectional Region Specific MMP-2 x *APOE*-ε4 Status Interactions on DTI Metrics

	Anatomical Region	Hemisphere	Volume (mm^3)	Cluster Statistics		Corrected p-value†	MNI Coordinate‡		
				β	p-value*				

Fractional Anisotropy	--	--	--	--	--	--	--	--	--
Mean Diffusivity	Superior Longitudinal Fasciculus	Left	29541	-1.154	**$3.57x10^{-4}$**	0.019	-29	-30	35
Radial Diffusivity	Splenium of the Corpus Callosum	Left	398	-1.211	**$3.14x10^{-4}$**	0.047	-20	-39	27
	Supramarginal Gyrus	Left	50	-1.377	**$7.57x10^{-5}$**	0.049	-31	-31	40
Axial Diffusivity	Middle Frontal Gyrus	Right	6509	-1.629	**$4.77x10^{-7}$**	0.018	21	36	22
	Postcentral Gyrus	Left	1987	-1.457	**$1.12x10^{-5}$**	0.032	-35	-15	25
	Genu of the Corpus Callosum	Right	738	-1.326	**$1.04x10^{-4}$**	0.038	1	27	0
	Insular Gyrus	Right	297	-1.079	**$1.66x10^{-3}$**	0.048	32	-15	9
	Retrolenticular Part of the Internal Capsule	Right	89	-1.242	**$4.19x10^{-4}$**	0.048	27	-22	12
	Inferior Frontal Gyrus	Left	60	-1.243	**$1.79x10^{-4}$**	0.049	-28	15	23
	Putamen	Right	46	-0.988	**$5.75x10^{-3}$**	0.049	35	-14	-7
	Inferior Frontal Gyrus	Left	39	-1.160	**$1.03x10^{-3}$**	0.049	-36	27	15
	Posterior Limb of the Internal Capsule	Left	21	-1.139	**$5.56x10^{-4}$**	0.049	-25	-14	16
	Superior Corona Radiata	Left	11	-0.962	**$3.20x10^{-3}$**	0.05	-26	10	23

Note. Bold values indicate p-values that remain significant after excluding outliers. Empty rows indicate no significant clusters for that metric. *parametric p-values were calculated using linear regression models to relate *MMP-2 x APOE-ε4 status* and raw DTI values extracted from each participant skeleton; †p-value has been corrected for multiple comparisons; ‡coordinates and region represent the voxel with the minimum p-value in each cluster; APOE=apolipoprotein E; DTI=diffusion tensor imaging; MMP=matrix metalloproteinase; MNI=Montreal Neurological Institute.

Table 2.12. Longitudinal Region Specific MMP-2 x *APOE*-ε4 Status Interactions on DTI Metrics

	Anatomical Region	**Hemisphere**	**Volume (mm^3)**	**Cluster Statistics**		**Corrected p-value†**	**MNI Coordinate‡**		
				β	**p-value***				

Fractional Anisotropy	--	--	--	--	--	--	--	--	--
Mean Diffusivity	Posterior Limb of the Internal Capsule	Right	50	-3.45×10^{-10}	**3.13×10^{-4}**	0.012	22	-10	7
	Fornix	Right	46	-7.35×10^{-10}	**7.12×10^{-5}**	0.021	27	-27	0
Radial Diffusivity	--	--	--	--	--	--	--	--	--
Axial Diffusivity	Posterior Limb of the Internal Capsule	Right	48	-5.53×10^{-10}	**1.90×10^{-5}**	0.015	21	-5	12

Note. Bold values indicate p-values that remain significant after excluding outliers. Empty rows indicate no significant clusters for that metric. *parametric p-values were calculated using linear mixed effects models to relate baseline *MMP-2 x APOE-ε4 status* and raw DTI values extracted from each participant skeleton; †p-value has been corrected for multiple comparisons; ‡coordinates and region represent the location of the minimum p-value for each cluster; APOE=apolipoprotein E; DTI=diffusion tensor imaging; MMP=matrix metalloproteinase; MNI=Montreal Neurological Institute.

MMP-3 Analyses

MMP-3 & DTI Metrics

In the whole sample, CSF MMP-3 was cross-sectionally associated with compromised white matter microstructure (corrected p-values<0.05, **Table 2.13, Figure 2.5**). Specifically, higher CSF MMP-3 was associated with lower FA in the posterior corona radiata and higher radial diffusivity in the superior corona radiata. Clusters remained significant when removing outliers (**Table 2.13**).

Baseline CSF MMP-3 was also associated with DTI metric trajectory (corrected p-values<0.05, **Table 2.14, Figure 2.6**). Specifically, higher baseline CSF MMP-3 was associated with a faster increase in mean diffusivity primarily in the postcentral gyrus, radial diffusivity primarily in the superior parietal lobule, and axial diffusivity primarily in the precentral gyrus. Associations remained significant when removing outliers (**Table 2.14**).

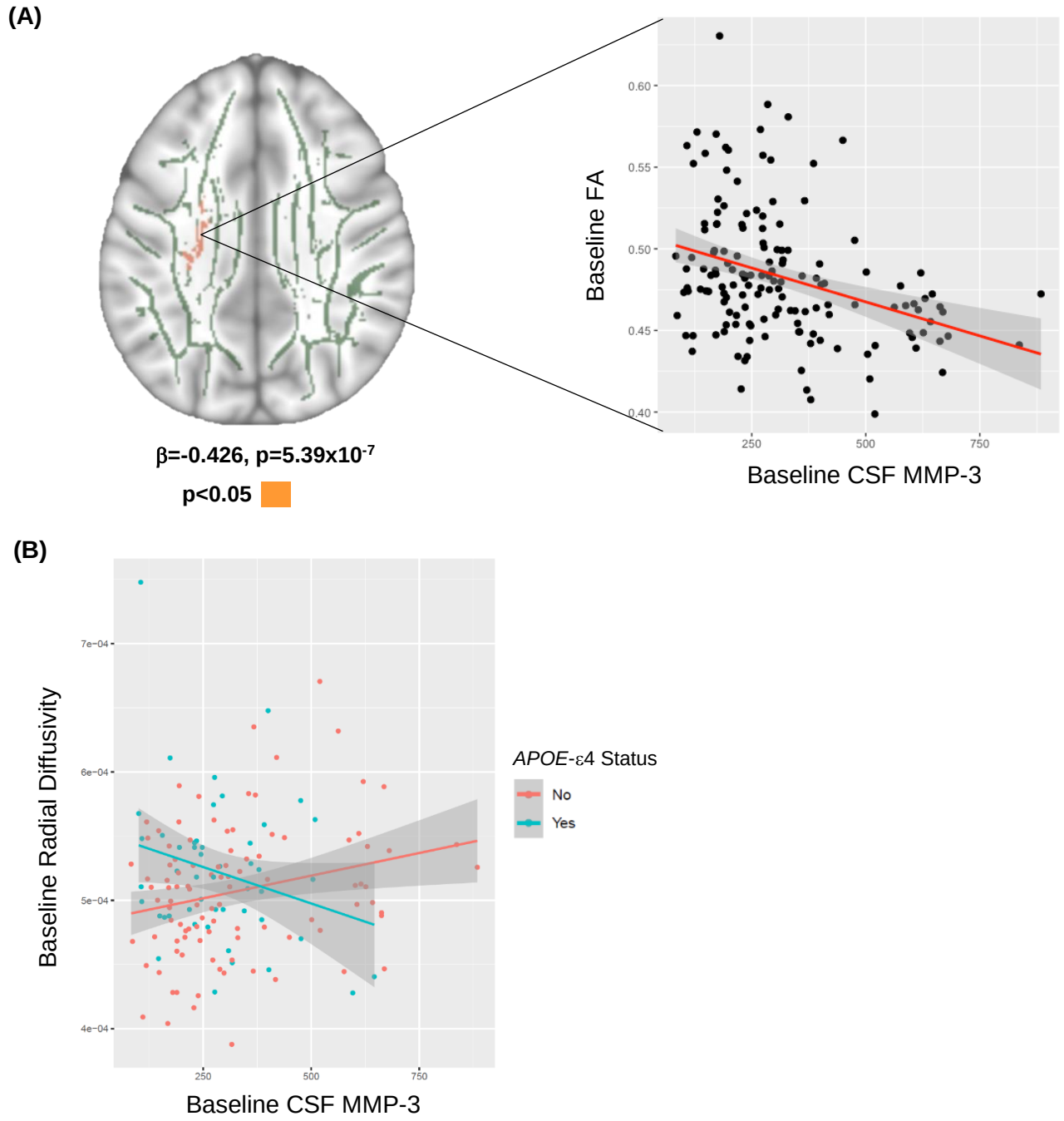

Figure 2.5. Cross-sectional CSF MMP-3 and DTI Metric Associations. **(A)** Mean skeleton shows regions where baseline CSF MMP-3 is associated with FA over time. Scatterplot shows a linear regression model relating baseline CSF MMP-3 values for every participant to FA values in one specific cluster. Parametric p-value and β listed only represent the cluster displayed here. Image taken at z=108. **(B)** *CSF MMP-3 x APOE-ε4 status* interaction on radial diffusivity (β=-0.681, p=1.79x10^{-4}). Scatterplots show interactions at one specific cluster. Parametric p-value and β listed only represent the cluster displayed here. APOE=apolipoprotein E; CSF=cerebrospinal fluid; DTI=diffusion tensor imaging; FA=fractional anisotropy; MMP=matrix metalloprotein.

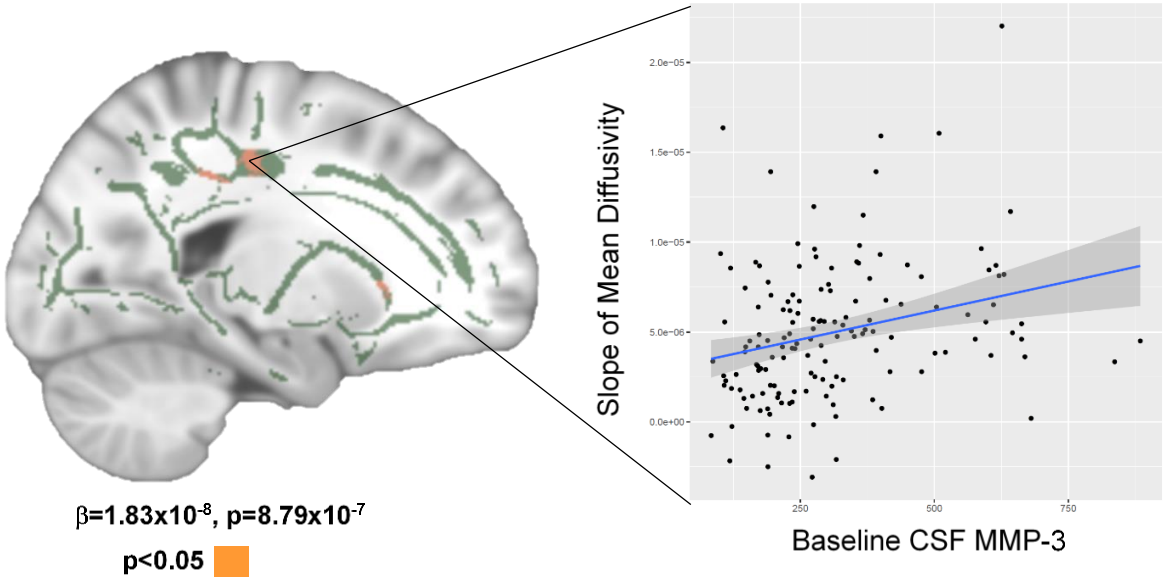

Figure 2.6. Baseline CSF MMP-3 and Longitudinal DTI Trajectory Associations. Mean skeleton shows regions where baseline CSF MMP-3 is associated with a faster increase in mean diffusivity over time. Scatterplot shows a linear mixed effects model relating baseline CSF MMP-3 values for every participant to the slope of mean diffusivity values in one specific cluster. Parametric p-value and β listed only represent the cluster displayed here. Image taken at z=76. CSF=cerebrospinal fluid; DTI=diffusion tensor imaging; MMP=matrix metalloprotein.

MMP-3 x Diagnosis Interactions & DTI Metrics

In cross-sectional analyses, CSF MMP-3 did not interact with diagnosis on DTI metrics (corrected p-values>0.14). However, in longitudinal analyses, baseline CSF MMP-3 interacted with diagnosis on radial diffusivity in one small cluster in the postcentral gyrus (**Table 2.15**). Stratification revealed that the association between higher baseline CSF MMP-3 and a faster increase in radial diffusivity was stronger among participants with MCI, though still present in participants with NC. However, the association was attenuated when removing outliers (**Table 2.15**).

Table 2.13. Cross-Sectional Region Specific MMP-3 Associations with DTI Metrics

	Anatomical Region	Hemisphere	Volume (mm^3)	Cluster Statistics		Corrected p-value†	MNI Coordinate‡		
				β	p-value*				
Fractional Anisotropy	Posterior Corona Radiata	Left	764	-0.426	**$5.39x10^{-7}$**	0.025	-25	-23	28
Mean Diffusivity	--	--	--	--	--	--	--	--	--
Radial Diffusivity	Superior Corona Radiata	Left	12	0.400	**$1.35x10^{-6}$**	0.05	-2	-11	36
	Superior Corona Radiata	Left	8	0.369	**$1.35x10^{-5}$**	0.05	-24	-9	31
Axial Diffusivity	--	--	--	--	--	--	--	--	--

Note. Bold values indicate p-values that remain significant after excluding outliers. Empty rows indicate no significant clusters for that metric. *parametric p-values were calculated using linear regression models to relate MMP-3 and raw DTI values extracted from each participant skeleton; †p-value has been corrected for multiple comparisons; ‡coordinates and region represent the location of the minimum p-value for each cluster; DTI=diffusion tensor imaging; MMP=matrix metalloproteinase; MNI=Montreal Neurological Institute.

Table 2.14. Longitudinal Region Specific MMP-3 Associations with DTI Metrics

	Anatomical Region	Hemisphere	Volume (mm^3)	Cluster Statistics		Corrected p-value†	MNI Coordinate‡		
				β	p-value*				
Fractional Anisotropy	--	--	--	--	--	--	--	--	--
Mean Diffusivity	Postcentral Gyrus	Right	111	$1.83x10^{-8}$	**$8.79x10^{-7}$**	$5.87x10^{-6}$	26	-29	42
	Superior Parietal Lobule	Right	88	$1.71x10^{8}$	**$1.34x10^{-6}$**	$8.36x10^{-5}$	17	-42	41
	Superior Parietal Lobule	Left	87	$1.58x10^{-8}$	**$7.41x10^{-7}$**	$9.43x10^{-5}$	-20	-37	39
	Precentral Gyrus	Left	78	$1.91x10^{-8}$	**$1.68x10^{-8}$**	$2.85x10^{-4}$	-29	-17	51

	Precentral Gyrus	Right	78	$1.98x10^{-8}$	**$3.43x10^{-7}$**	$2.85x10^{-4}$	27	-12	44
	Precentral Gyrus	Left	62	$1.38x10^{-8}$	**$2.14x10^{-6}$**	0.002	-20	-24	44
	Anterior Corona Radiata	Left	61	$2.01x10^{-8}$	**$1.39x10^{-6}$**	0.003	-22	22	5
	Superior Parietal Lobule	Left	49	$2.38x10^{-8}$	**$2.86x10^{-8}$**	0.014	-27	-42	41
	Middle Frontal Gyrus	Left	42	$1.67x10^{-8}$	**$9.25x10^{-7}$**	0.039	-32	28	25
Radial Diffusivity	Superior Parietal Lobule	Left	105	$1.73x10^{-8}$	**$8.79x10^{-7}$**	$2.61x10^{-5}$	-20	-37	39
	Postcentral Gyrus	Right	92	$1.70x10^{-8}$	**$5.09x10^{-6}$**	$1.10x10^{-4}$	26	-29	42
	Postcentral Gyrus	Left	85	$1.57x10^{-8}$	**$4.10x10^{-6}$**	$2.43x10^{-4}$	-20	-23	43
	Postcentral Gyrus	Left	79	$1.60x10^{-8}$	**$2.87x10^{-7}$**	$4.92x10^{-4}$	-32	-29	45
	Precentral Gyrus	Left	74	$1.92x10^{-8}$	**$4.09x10^{-7}$**	$8.96x10^{-4}$	-28	-14	49
	Superior Frontal Gyrus	Left	68	$1.64x10^{-8}$	**$8.98x10^{-7}$**	0.002	-15	19	46
	Superior Corona Radiata	Right	66	$1.74x10^{-8}$	**$3.34x10^{-5}$**	0.002	26	-21	37
	Cingulum Bundle	Right	51	$1.85x10^{-8}$	**$4.82x10^{-6}$**	0.017	14	-36	36
	Precentral Gyrus	Right	51	$1.84x10^{-8}$	**$7.76x10^{-6}$**	0.017	31	-15	50
	External Capsule	Right	49	$2.58x10^{-8}$	**$1.72x10^{-6}$**	0.022	21	20	2
Axial Diffusivity	Precentral Gyrus	Right	50	$3.12x10^{-8}$	**$1.89x10^{-7}$**	0.011	27	-15	50
	Cingulum Bundle	Right	45	$2.67x10^{-8}$	**$2.97x10^{-8}$**	0.023	12	-38	40
	Postcentral Gyrus	Right	40	$2.62x10^{-8}$	**$1.20x10^{-6}$**	0.049	26	-29	42

Note. Bold values indicate p-values that remain significant after excluding outliers. Empty rows indicate no significant clusters for that metric. *parametric p-values were calculated using linear mixed effects models to relate MMP-3 and raw DTI values extracted from each participant skeleton; †p-value has been corrected for multiple comparisons; ‡coordinates and region represent the location of the minimum p-value for each cluster; DTI=diffusion tensor imaging; MNI=Montreal Neurological Institute; MMP=matrix metalloproteinase.

Table 2.15. Longitudinal Region Specific MMP-3 x Diagnosis Interactions on DTI Metrics

	Anatomical Region	Hemisphere	Volume (mm^3)	Cluster Statistics		Corrected p-value†	MNI Coordinate‡		
				β	p-value*				
Fractional Anisotropy	--	--	--	--	--	--	--	--	--
Mean Diffusivity	--	--	--	--	--	--	--	--	--
Radial Diffusivity	Postcentral Gyrus	Right	48	-3.53×10^{-8}	1.65×10^{-4}	0.028	26	-28	42
Axial Diffusivity	--	--	--	--	--	--	--	--	--

Note. Bold values indicate p-values that remain significant after excluding outliers. Empty rows indicate no significant clusters for that metric. *parametric p-values were calculated using linear mixed effects models to relate baseline *MMP-3 x diagnosis* and raw DTI values extracted from each participant skeleton; †p-value has been corrected for multiple comparisons; ‡coordinates and region represent the location of the minimum p-value for each cluster; DTI=diffusion tensor imaging; MMP=matrix metalloproteinase; MNI=Montreal Neurological Institute.

Table 2.16. Cross-Sectional Region Specific MMP-3 x *APOE*-ε4 Status Interactions on DTI Metrics

	Anatomical Region	Hemisphere	Volume (mm^3)	Cluster Statistics		Corrected p-value†	MNI Coordinate‡		
				β	p-value*				
Fractional Anisotropy	Body of the Corpus Callosum	Left	1260	0.791	**2.22×10^{-5}**	0.027	-14	-15	31
	Body of the Corpus Callosum	Right	276	0.716	**2.65×10^{-4}**	0.047	14	18	24
	Genu of the Corpus Callosum	Right	20	0.552	**4.35×10^{-3}**	0.05	14	20	15
Mean Diffusivity	--	--	--	--	--	--	--	--	--
Radial Diffusivity	Superior Corona Radiata	Left	3494	-0.681	**1.79×10^{-4}**	0.036	-16	-13	34
	Body of the Corpus Callosum	Right	1596	-0.624	**4.23×10^{-4}**	0.043	15	17	26
	Posterior Limb of the Internal Capsule	Left	242	-0.641	**4.48×10^{-4}**	0.048	-21	-6	12

	Cerebral Peduncle	Left	229	-0.790	**6.03×10^{-5}**	0.047	-14	-11	-9
	Cingulum	Right	193	-0.683	**3.11×10^{-4}**	0.048	17	-38	33
	Posterior Thalamic Radiation	Right	103	-0.546	**2.94×10^{-3}**	0.049	28	-57	15
	Posterior Corona Radiata	Right	97	-0.605	**2.16×10^{-3}**	0.049	27	-29	36
	Splenium of the Corpus Callosum	Right	78	-0.523	**5.89×10^{-3}**	0.05	17	-42	26
	Insular Gyrus	Left	55	-0.717	**2.04×10^{-4}**	0.059	-33	-15	0
	Splenium of the Corpus Callosum	Right	13	-0.526	**6.16×10^{-3}**	0.05	22	-52	23
	Splenium of the Corpus Callosum	Right	3	-0.600	**2.83×10^{-3}**	0.05	23	-48	22
	Cingulum	Right	3	-0.483	**1.36×10^{-2}**	0.05	16	-40	37
Axial Diffusivity	Superior Longitudinal Fasciculus	Left	15	-0.831	**2.19×10^{-5}**	0.049	-29	-24	37

Note. Bold values indicate p-values that remain significant after excluding outliers. Empty rows indicate no significant clusters for that metric. *parametric p-values were calculated using linear regression models to relate *MMP-3 x APOE-ε4 status* and raw DTI values extracted from each participant skeleton; †p-value has been corrected for multiple comparisons; ‡coordinates and region represent the voxel with the minimum p-value in each cluster; APOE=apolipoprotein E; DTI=diffusion tensor imaging; MMP=matrix metalloproteinase; MNI=Montreal Neurological Institute.

MMP-3 x APOE-ε4 Interactions & DTI Metrics

In cross-sectional analyses, CSF MMP-3 interacted with *APOE*-ε4 status on DTI metrics (corrected p-values<0.05, **Table 2.16, Figure 2.5**). Specifically, CSF MMP-3 interacted with *APOE*-ε4 status on FA in the body of the corpus callosum, radial diffusivity primarily in the superior corona radiata, and axial diffusivity in the superior longitudinal fasciculus. Stratification revealed that in all clusters, higher CSF MMP-3 was associated with compromised white matter microstructure among *APOE*-ε4 negative participants, but associations were reversed among *APOE*-ε4 positive

participants. These associations persisted when removing outliers (**Table 2.16**). In longitudinal analyses, baseline CSF MMP-3 did not interact with *APOE*-ε4 status (corrected p-values>0.09).

MMP-9 Analyses

MMP-9 & DTI Metrics

In the whole sample, CSF MMP-9 was not cross-sectionally associated with DTI metrics (corrected p-values>0.16). In longitudinal analyses, CSF MMP-9 was not associated with DTI metric trajectory (corrected p-values>0.21).

MMP-9 x Diagnosis Interactions & DTI Metrics

In cross-sectional analyses, CSF MMP-9 did not interact with diagnosis on DTI metrics (corrected p-values<0.14). In longitudinal analyses, baseline CSF MMP-9 interacted with diagnosis on axial diffusivity in one small cluster in the lateral occipital gyrus (**Table 2.17**). Stratification revealed that the association between higher baseline CSF MMP-9 and a faster increase in axial diffusivity was present among participants with NC, but the association was reversed among participants with MCI. The association remained significant when removing outliers (**Table 2.17**).

MMP-9 x APOE-ε4 Interactions & DTI Metrics

In cross-sectional analyses, CSF MMP-9 did not interact with *APOE*-ε4 status on DTI metrics (corrected p-values>0.15). In longitudinal analyses, baseline CSF MMP-9 did not interact with *APOE*-ε4 status on DTI metric trajectory (corrected p-values>0.50).

Table 2.17. Longitudinal Region Specific MMP-9 x Diagnosis Interactions on DTI Metrics

	Anatomical Region	Hemisphere	Volume (mm^3)	Cluster Statistics		Corrected p-value†	MNI Coordinate‡		
				β	p-value*				
Fractional Anisotropy	--	--	--	--	--	--	--	--	--
Mean Diffusivity	--	--	--	--	--	--	--	--	--
Radial Diffusivity	--	--	--	--	--	--	--	--	--
Axial Diffusivity	Lateral Occipital Gyrus	Left	41	$1.97x10^{-7}$	**$4.69x10^{-5}$**	0.044	-32	-82	-5

Note. Bold values indicate p-values that remain significant after excluding outliers. Empty rows indicate no significant clusters for that metric. *parametric p-values were calculated using linear mixed effects models to relate baseline *MMP-9 x diagnosis* and raw DTI values extracted from each participant skeleton; †p-value has been corrected for multiple comparisons; ‡coordinates and region represent the location of the minimum p-value for each cluster; DTI=diffusion tensor imaging; MMP=matrix metalloproteinase; MNI=Montreal Neurological Institute.

CSF/Plasma Albumin Ratio Analyses

CSF/Plasma Albumin Ratio & DTI Metrics

In the whole sample, the CSF/plasma albumin ratio was not cross-sectionally associated with DTI metrics (corrected p-values>0.42). However, baseline CSF/plasma albumin ratio was associated with faster decline in white matter integrity over time (corrected p-values<0.04, **Table 2.18, Figure 2.7**). Specifically, a higher baseline ratio was associated with a faster increase in mean diffusivity primarily in the superior frontal gyrus, radial diffusivity primarily in the superior longitudinal fasciculus, and axial diffusivity primarily in the splenium of the corpus callosum. When removing outliers, clusters remained significant (**Table 2.18**).

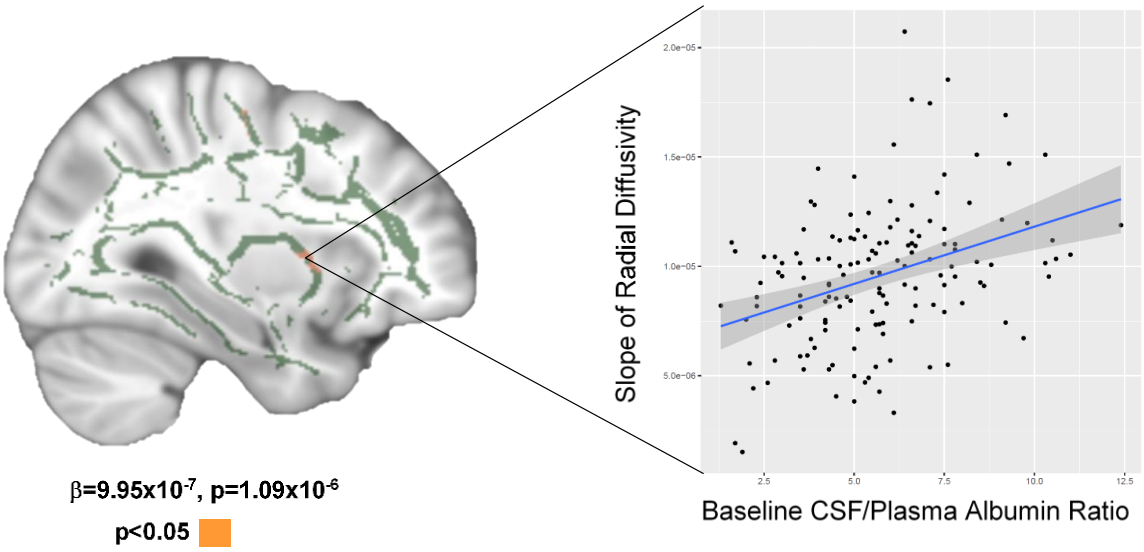

Figure 2.7. Baseline CSF/Plasma Albumin Ratio and Longitudinal DTI Trajectory Associations**.** Mean skeleton shows regions where the baseline CSF/plasma albumin ratio is associated with a faster increase in radial diffusivity over time. Scatterplot shows a linear mixed effects model relating baseline CSF/plasma albumin ratio for every participant to the slope of radial diffusivity values in one specific cluster. Parametric p-value and β listed only represent the cluster displayed here. Image taken at z=122. CSF=cerebrospinal fluid; DTI=diffusion tensor imaging.

CSF/Plasma Albumin Ratio x Diagnosis Interactions & DTI Metrics

In cross-sectional analyses, the CSF/plasma albumin ratio did not interact with diagnosis on DTI metrics (corrected p-values>0.08). However, in longitudinal analyses, the baseline CSF/plasma albumin ratio interacted with diagnosis on DTI metric trajectory in small clusters (**Table 2.19**). Specifically, the baseline ratio interacted with diagnosis on trajectory of mean and radial diffusivity in the anterior corona radiata. Stratification revealed that in all clusters, a higher baseline ratio was associated with a faster increase in mean and radial diffusivity among NC participants, but associations were reversed among participants with MCI. When removing outliers, associations with mean diffusivity remained significant (**Table 2.19**).

CSF/Plasma Albumin Ratio x APOE-ε4 Interactions & DTI Metrics

In cross-sectional analyses, the CSF/plasma albumin ratio interacted with *APOE*-ε4 status on DTI metrics (corrected p-values<0.05, **Table 2.20, Figure 2.8**). Specifically, the ratio interacted with *APOE*-ε4 status on FA in the posterior corona radiata, on mean diffusivity in the inferior temporal gyrus, on radial diffusivity in the anterior corona radiata, and axial diffusivity in the superior corona radiata. Stratification revealed that in all clusters, a higher ratio was associated with compromised white matter microstructure among *APOE*-ε4 negative participants, but associations were reversed among *APOE*-ε4 positive participants. These associations persisted when removing outliers (**Table 2.20**).

In longitudinal analyses, the baseline CSF/plasma albumin ratio interacted with *APOE*-ε4 status on DTI metric trajectory in small clusters (**Table 2.21**). Specifically, the baseline ratio interacted with *APOE*-ε4 status on trajectory of mean and radial diffusivity in the superior longitudinal fasciculus. Stratification revealed that in all clusters, a higher baseline ratio was associated with a faster increase in mean and radial diffusivity among *APOE*-ε4 negative participants, but associations were reversed among *APOE*-ε4 positive participants. When removing outliers, associations remained significant (**Table 2.21**).

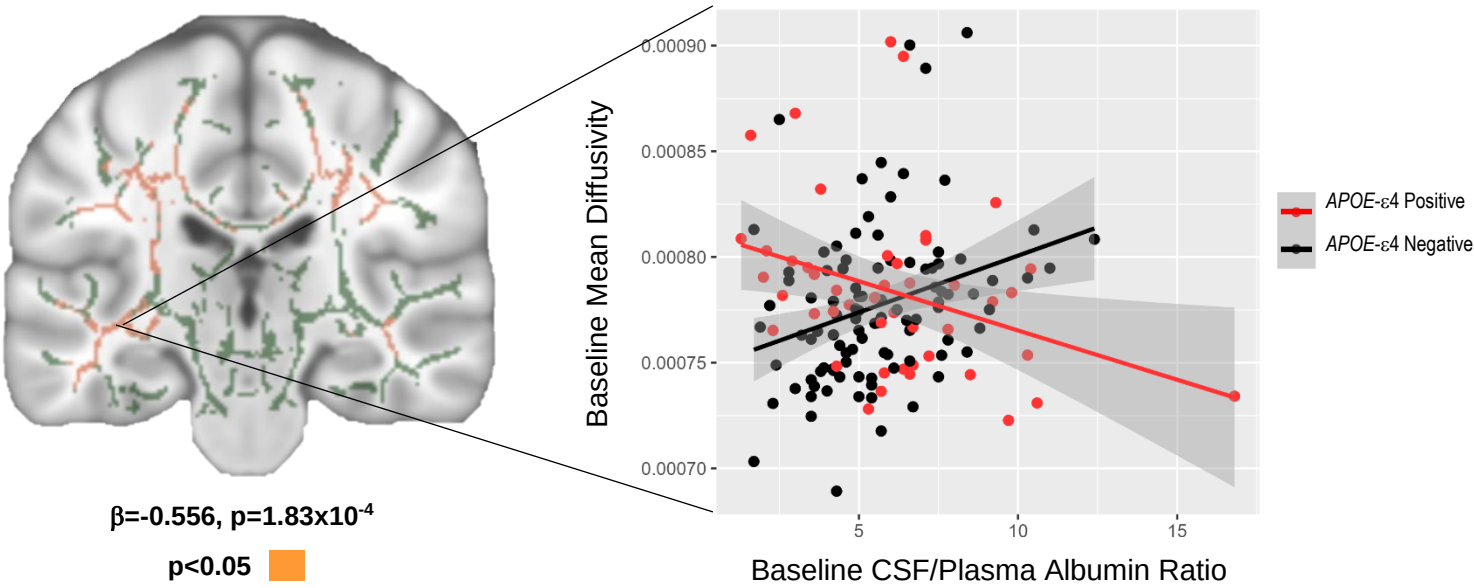

Figure 2.8. Cross-Sectional CSF/Plasma Albumin x *APOE*-ε4 Status Interaction on Mean Diffusivity. Mean skeleton shows regions where the CSF/plasma albumin ratio interacts with *APOE*-ε4 Status on mean diffusivity. Scatterplot shows least squares regression relating the CSF/plasma albumin ratio for every participant to mean diffusivity values in one specific cluster. Parametric p-value and β listed only represent the cluster displayed here. Image taken at z=68; APOE=apolipoprotein E; CSF=cerebrospinal fluid.

Table 2.18. Longitudinal Region Specific CSF/Plasma Albumin Ratio Associations with DTI Metrics

	Anatomical Region	Hemisphere	Volume (mm^3)	Cluster Statistics		Corrected p-value†	MNI Coordinate‡		
				β	p-value*				
Fractional Anisotropy	--	--	--	--	--	--	--	--	--
Mean Diffusivity	Superior Frontal Gyrus	Right	65	$9.82x10^{-7}$	**$2.82x10^{-8}$**	0.002	16	-3	52
	Body of the Corpus Callosum	Left	57	$1.41x10^{-6}$	**$2.74x10^{-7}$**	0.005	-13	-1	30
	Precentral Gyrus	Right	54	$1.18x10^{-6}$	**$9.14x10^{-6}$**	0.007	29	-13	46
	Superior Longitudinal Fasciculus	Right	46	$1.11x10^{-6}$	**$1.90x10^{-5}$**	0.023	42	-11	28
	Superior Corona Radiata	Left	46	$8.17x10^{-7}$	**$6.16x10^{-5}$**	0.023	-26	-26	33
	External Capsule	Right	43	$1.63x10^{-6}$	**$4.68x10^{-6}$**	0.035	33	8	1
	Superior Longitudinal Fasciculus	Left	42	$1.08x10^{-6}$	**$9.27x10^{-7}$**	0.041	-34	-18	35
Radial Diffusivity	Superior Longitudinal Fasciculus	Left	110	$9.95x10^{-7}$	**$1.09\ x10^{-6}$**	$1.73x10^{-5}$	-33	-17	37
	Precentral Gyrus	Right	64	$1.24x10^{-6}$	**$1.42x10^{-10}$**	0.003	36	-7	39
	Precentral Gyrus	Right	59	$1.26x10^{-6}$	**$2.17x10^{-6}$**	0.006	29	-13	46
	External Capsule	Right	53	$1.64x10^{-6}$	**$4.61x10^{-6}$**	0.014	32	7	6
Axial Diffusivity	Splenium of the Corpus Callosum	Left	55	$3.53x10^{-6}$	**$8.90x10^{-6}$**	0.006	-18	-48	15
	Superior Longitudinal Fasciculus	Right	44	$2.20x10^{-6}$	**$8.46x10^{-6}$**	0.028	41	-11	29
	Middle Temporal Gyrus	Left	51	$-4.00x10^{-6}$	**$3.30x10^{-5}$**	0.01	-43	-23	-11

Note. Bold values indicate p-values that remain significant after excluding outliers. Empty rows indicate no significant clusters for that metric. *parametric p-values were calculated using linear mixed effects models to relate baseline CSF/plasma albumin ratio and raw DTI values extracted from each participant skeleton; †p-value has been corrected for multiple comparisons; ‡coordinates and region represent the location of the minimum p-value for each cluster; CSF=cerebrospinal fluid; DTI=diffusion tensor imaging; MMP=matrix metalloproteinase; MNI=Montreal Neurological Institute.

Table 2.19. Longitudinal Region Specific CSF/Plasma Albumin Ratio x Diagnosis Interactions on DTI Metrics

	Anatomical Region	Hemisphere	Volume (mm^3)	Cluster Statistics		Corrected p-value†	MNI Coordinate‡		
				β	p-value*				
Fractional Anisotropy	--	--	--	--	--	--	--	--	--
Mean Diffusivity	Anterior Corona Radiata	Left	70	$4.03x10^{-6}$	**$5.69x10^{-6}$**	$8.98x10^{-4}$	-24	18	15
Radial Diffusivity	Anterior Corona Radiata	Left	49	$3.76x10^{-6}$	$8.51x10^{-5}$	0.026	-24	20	14
Axial Diffusivity	--	--	--	--	--	--	--	--	--

Note. Bold values indicate p-values that remain significant after excluding outliers. Empty rows indicate no significant clusters for that metric. *parametric p-values were calculated using linear mixed effects models to relate baseline *CSF/plasma albumin ratio x diagnosis* and raw DTI values extracted from each participant skeleton; †p-value has been corrected for multiple comparisons; ‡coordinates and region represent the location of the minimum p-value for each cluster; CSF=cerebrospinal fluid; DTI=diffusion tensor imaging; MMP=matrix metalloproteinase; MNI=Montreal Neurological Institute.

Table 2.20. Cross-Sectional Region Specific CSF/Plasma Albumin Ratio x *APOE*-ε4 Status Interactions on DTI Metrics

	Anatomical Region	Hemisphere	Volume (mm^3)	Cluster Statistics		Corrected p-value†	MNI Coordinate‡		
				β	p-value*				
Fractional Anisotropy	Posterior Corona Radiata	Left	1105	0.677	**$2.12x10^{-5}$**	0.036	-20	-30	37
	Posterior Corona Radiata	Right	341	0.610	**$2.37x10^{-4}$**	0.046	23	-36	28
Mean Diffusivity	Inferior Temporal Gyrus	Left	38395	-0.556	**$1.83x10^{-4}$**	0.005	-41	-10	-18
Radial Diffusivity	Anterior Corona Radiata	Right	33600	-0.548	**$2.07x10^{-4}$**	0.011	20	39	4
Axial Diffusivity	Superior Corona Radiata	Left	25318	-0.829	**$1.19x10^{-8}$**	0.005	-28	17	22

Note. Bold values indicate p-values that remain significant after excluding outliers. *parametric p-values were calculated using linear regression models to relate baseline *CSF/plasma albumin ratio x APOE-ε4 status* and raw DTI values extracted from each participant skeleton; †p-value has been corrected for multiple

comparisons; ‡coordinates and region represent the voxel with the minimum p-value in each cluster; APOE=apolipoprotein E; CSF=cerebrospinal fluid; DTI=diffusion tensor imaging; MNI=Montreal Neurological Institute.

Table 2.21. Longitudinal Region Specific CSF/Plasma Albumin Ratio x *APOE*-ε4 Status Interactions on DTI Metrics

	Anatomical Region	Hemisphere	Volume (mm^3)	Cluster Statistics		Corrected p-value†	MNI Coordinate‡		
				β	p-value*				
Fractional Anisotropy	--	--	--	--	--	--	--	--	--
Mean Diffusivity	Splenium of the Corpus Callosum	Left	55	-4.10×10^{-6}	**1.48×10^{-5}**	0.006	-10	-38	11
	Superior Longitudinal Fasciculus	Right	48	-1.70×10^{-6}	**9.45×10^{-5}**	0.017	28	-23	36
Radial Diffusivity	Superior Longitudinal Fasciculus	Right	70	-1.70×10^{-6}	**9.72×10^{-5}**	0.002	28	-25	40
Axial Diffusivity	--	--	--	--	--	--	--	--	--

Note. Bold values indicate p-values that remain significant after excluding outliers. *parametric p-values were calculated using linear mixed effects models to relate baseline *CSF/plasma albumin ratio x APOE-ε4 status* and raw DTI values extracted from each participant skeleton; †p-value has been corrected for multiple comparisons; ‡coordinates and region represent the location of the minimum p-value for each cluster; APOE=apolipoprotein E; CSF=cerebrospinal fluid; DTI=diffusion tensor imaging; MNI=Montreal Neurological Institute.

Discussion

Among community-dwelling older adults free of clinical stroke and dementia, higher baseline arterial stiffness was associated with faster decline of white matter integrity, specifically in the temporal and occipital lobes. Cross-sectional associations were driven by participants with NC, whereas longitudinal associations were driven by participants with MCI and *APOE*-ε4 positive participants. In the entire sample, measures of ECM remodeling, including lower levels of CSF MMP-2 and higher levels of MMP-3, were cross-sectionally associated with associated with compromised white matter microstructure primarily in the frontal lobe and deep white matter tracts. Cross-sectionally, increased CSF evidence of ECM remodeling and BBB permeability were associated with compromised white matter microstructure among participants with NC and *APOE*-ε4 negative participants. We observed the opposite effect among participant with MCI and *APOE*-ε4 positive participants, such that increased MMP levels and BBB integrity were associated with healthier white matter microstructure among these participants. In longitudinal models, baseline ECM remodeling and BBB permeability were associated with a faster decline in white matter integrity in small clusters, driven by NC and *APOE*-ε4 negative participants.

While vascular disease is thought to be the largest driver of white matter damage in aging, large vessel changes and small vessel changes likely influence brain health differently. It is necessary to better understand where large and small vessel dysfunction affect white matter integrity to better characterize competing etiologies of white matter damage in aging adults. Importantly, we discovered that white matter tracts in the temporal and occipital lobes are especially vulnerable to age-related changes in

large vessel health, namely arterial stiffening. As arterial stiffness increases with age, the aorta is less able to buffer pulsatile energy[51] and that energy is transmitted to the cerebral microcirculation.[60] This process leads to lower CBF, especially in the temporal and occipital lobes,[56] and subsequent oligemia. Oligodendrocytes, the primary component of white matter, are particularly susceptible to oligemia, as these cells are more vulnerable to hypoxia-induced oxidative stress.[146] Further, the temporal and occipital lobe white matter tracts are at border zones between cerebral arterial supplies[57] and both perfused by segments of the posterior cerebral artery (see **Figure 1.4** for an illustration). The posterior circulation may be less able to buffer pulsatile changes over time, leading to greater white matter damage in these regions. This hypothesis is supported by our prior work showing that associations between higher aortic stiffness and cerebral hemodynamic changes are most robust in temporal and occipital regions.[56] Additionally, the BBB is thought to initially breakdown in the temporal lobe during aging,[147] possibly making the surrounding tissue more vulnerable to pulsatile energy. Importantly, given that AD pathology first develops in the temporal lobe[3] and temporal lobe white matter damage is often associated with AD pathology,[99] our results suggest that arterial stiffness may be an additional pathway to white matter damage in this region.

We also found that diagnosis modifies associations between arterial stiffness and white matter integrity. In cross-sectional analyses, associations between higher arterial stiffness and compromised white matter microstructure were driven by NC participants.[148] This observation aligns with prior work showing cardiovascular hemodynamics may have the largest effect on brain health prior to the onset of

cognitive impairment.[149] It is possible that once cognitive impairment is present, multiple other neuropathologies[11] are already present that also compromise white matter, obscuring cross-sectional associations between arterial stiffness and white matter integrity in participants with MCI. However, participants with MCI may be more susceptible to the longitudinal effects of arterial stiffness on brain health. The longitudinal results presented here suggest that higher arterial stiffness accelerates white matter injury in the temporal and occipital lobes. MCI participants likely have greater levels of AD pathology accumulating in the temporal lobe[3] and leakier BBBs,[150] making the white matter more susceptible to subtle changes in CBF due to increased arterial stiffness.[56] Additionally, the posterior circulation, responsible for perfusing the temporal and occipital lobes, may be more vulnerable in MCI, as prior work has shown reduced posterior CBF[151] and greater posterior white matter damage in MCI compared to anterior regions.[152] Collectively, these findings suggest that arterial stiffness may not only be an early driver of white matter injury prior to cognitive symptom manifestation but also exacerbate white matter damage in key regions where AD pathology develops. Notably, results suggest that the frontal lobe may be particularly susceptible to arterial stiffening in individuals with NC, whereas temporal and occipital lobe white matter are more susceptible to arterial stiffness in MCI. This discrepancy highlights how the effect of large vessel health on white matter may change depending on underlying neurodegenerative changes, and the regional vulnerability of white matter tracts changes based on cognitive profile. Future work is needed to further understand how the effects of arterial stiffness on brain health vary by cognitive status and intersect with underlying pathologic burden.

Additionally, we found that associations between baseline arterial stiffness and faster decline in white matter microstructural integrity were primarily driven by *APOE*-ε4 carriers. This finding is consistent with prior work showing that the effects of arterial stiffness on other markers of brain health are exacerbated in *APOE*-ε4 carriers.[56,153] *APOE*-ε4 contributes to cerebrovascular injury[154] and BBB permeability,[155] possibly making the vasculature more vulnerable to the harmful effects of the increased pulsatile energy of blood. *APOE* also transports cholesterol,[156] a primary component of myelin.[157] *APOE*-ε4 is less efficient at transporting and recycling cholesterol than other *APOE* alleles, resulting in less remyelination in *APOE*-ε4 carriers when the white matter is injured.[158] Thus, *APOE*-ε4 carriers may be less able to respond to subtle oligodendrocyte damage due to increases in arterial stiffening. Future work is needed to delineate the molecular mechanism connecting arterial stiffness, *APOE*, and white matter damage, but the results presented here further suggest that *APOE*-ε4 is a modifier of vascular damage and increased susceptibility to white matter damage may be one way *APOE*-ε4 adversely affects brain health outcomes in aging adults.

While large vessel health seems to primarily affect temporal and occipital lobe white matter tracts and exacerbate white matter damage in individuals at risk for AD, a different pattern emerged for markers of small vessel health and BBB integrity. Specifically, we found that baseline markers of ECM remodeling or BBB permeability are not robust predictors of future white matter damage but may reflect active white matter damage cross-sectionally. We found that higher levels of CSF MMP-3 are associated with compromised white matter microstructure among the entire sample and *APOE*-ε4 negative participants. MMP-3 is a stromelysin that degrades collagen, laminin,

and elastin, among other substrates. In vascular cognitive impairment, MMP-3 localizes to macrophages and endothelium throughout the white matter[159] and disrupts the BBB.[160] MMP-3 induced BBB breakdown may lead to local hypoxia[161] or leakage of toxic proteins, such as fibrinogen[162] into the brain parenchyma, both etiologies of white matter damage.[64,163] Our results suggest that a similar process may be occurring in older adults in the absence of vascular disease. Subtle but chronic changes in cerebral blood flow that occur throughout aging[164] may upregulate MMP-3 expression,[165] leading to subsequent white matter damage through the pathways described above. This hypothesis is consistent with prior work showing that MMP-3 may mediate a chronic response to cerebral hypoxia and subsequent damage, rather than an acute response.[159,166] Further, MMP-3 is primarily associated with damage to deep white matter tracts, including the internal capsule, corona radiata, and corpus callosum. These structures are the last to receive blood during cerebral perfusion,[57] making them the most susceptible to subclinical changes in the cerebra blood flow.[164] It is also possible differences in the structure and orientation of deep white matter tracts may make them more susceptible to damage.[167]

Similarly, we found that higher levels of CSF MMP-2 and a higher CSF/plasma albumin ratio related to compromised white matter integrity among NC and *APOE*-ε4 negative participants. MMP-2 is a gelatinase that is upregulated after ischemia and is critical for neovascularization.[168] Chronic ischemia in animal models leads to the upregulation of MMP-2 in the white matter[169] and MMP-2 has previously been implicated in white matter damage after hypoperfusion.[75] The effect of CSF MMP-2 on white matter microstructure seemed to localize to the frontal lobe, possibly due to the

frontal watershed region[57] (see **Figure 1.4**). Subtle reductions in CBF in the frontal watershed region between the anterior and middle cerebral arteries could lead to MMP-2 upregulation and subsequent local white matter damage. However, previous neuropathological studies have not found an increase in MMP-2 expression in the frontal lobe,[128] suggesting that the effect on white matter health may be global. It should be noted that the clusters are large, and more studies are needed to better localize where MMP-2 is upregulated after oligemia or ischemia. A higher CSF/plasma albumin ratio was also associated with compromised white matter microstructure in the temporal lobe among *APOE*-ε4 negative participants. Albumin is a protein typically found in plasma that should not cross the BBB. Thus, a higher ratio is thought to reflect an increase in BBB permeability. The BBB is thought to first break down in the temporal lobe,[147] consistent with these findings. Collectively, these findings suggest that in normal aging, MMP-3 may affect deep white matter, MMP-2 may preferentially affect frontal lobe white matter, and increased BBB permeability may indicate temporal lobe white matter damage.

Unexpectedly, associations were opposite among individuals with MCI or *APOE*-ε4 positive participants, such that higher levels of CSF MMP-2, CSF MMP-3, and the CSF/plasma albumin ratio related to healthier white matter microstructure. These results suggest that ECM remodeling and BBB permeability, though detrimental in normal aging, may be protective from white matter injury in the context of cognitive impairment, or the *APOE*-ε4 allele, both associated with AD. MMP-2 and MMP-3 cleave Aβ[170] and tau,[171] limiting abnormal protein aggregation. In the presence of AD pathology, MMPs may primarily interact with Aβ and p-tau, rather than ECM proteins, thereby limiting

damaging effects of MMPs on the BBB and white matter. Additionally, Aβ[81] and p-tau[100] are themselves associated with white matter damage. The breakdown of these proteins by MMP-2 and MMP-3 may further protect white matter from damage primarily associated with AD pathology. Similar findings in MCI and *APOE*-ε4 positive participants could be driven by greater levels of AD pathology[172] in these groups, or there could be an additional variable contributing to the associations. For example, the chronic effect of *APOE*-ε4 on BBB permeability[155] could influence the function and effects of MMPs and BBB permeability on white matter integrity. Larger studies are needed to better understand if *APOE*-ε4 affects MMP function independent of AD pathology and the mechanisms underlying the associations reported here.

Additionally, while MMP-2 and MMP-3 were strongly associated with white matter damage, MMP-9 associations were primarily null or driven by statistical outliers. It is possible that MMP-9 modulates ECM remodeling in grey matter instead of white matter. This hypothesis is consistent with studies showing MMP-2 and MMP-3, but not MMP-9, are upregulated in white matter after vascular injury.[159,173] Additionally, it is possible that CSF MMP-9 may represent a different pathological process than MMP-2 or MMP-3, consistent with prior work showing that CSF MMP-9 levels do not correlate with CSF MMP-2 or MMP-3.[135] Finally, the null MMP-9 findings could also be due to limitations of the assay used to quantify MMP-9. Many of the MMP-9 values were low, possibly reducing variance in the measurement and diminishing associations.[135] More work is needed to determine the distinct tissue-specific roles of each MMP in normal aging and AD utilizing more sensitive assays.

Another important observation is the MMPs and CSF/plasma albumin ratio were not robust predictors for future decline in white matter integrity. A majority of the longitudinal effects were in small clusters, with the largest effects including higher baseline CSF MMP-3 predicting faster decline in parietal lobe white matter and a higher baseline CSF/plasma albumin ratio predicting faster decline in frontal lobe white matter. The absence of longitudinal effects could be due to the dynamic nature of MMPs. Many different pathologies can affect MMP expression (e.g. vascular disease,[128] AD pathology,[174] inflammation),[175] so it is likely that measurable CSF concentrations at one time point do not accurately predict future levels. The small longitudinal findings could also be due to the relatively small sample size for the CSF analyses. Future work is needed with larger sample sizes.

Our study has several strengths, including gold-standard methods for non-invasively assessing central arterial stiffening at the aorta, excellent methods for quantifying ECM remodeling, stringent quality control procedures, a longitudinal study design, and reliable methods for quantifying cerebral white matter microstructure. Additional strengths include comprehensive ascertainment of potential confounders and the application of cluster enhancement and cluster-wise inference to correct for multiple comparisons,[145] reducing the possibility of a false positive finding. The application of a longitudinal voxel-wise pipeline allows for the robust and comprehensive assessment of the trajectory of white matter damage throughout the entire brain. Finally, core laboratories using quality control procedures analyzed all CMR, MRI, and CSF measurements in batch, and technicians were blinded to clinical information. Despite these strengths, there are limitations. Limitations include the observational design and

the predominantly White, well-educated, and relatively healthy sample, limiting generalizability. Additionally, CSF methods for quantifying MMP levels cannot determine MMP enzyme activity or the precise epitopes detected. It is possible that the measures reflect enzyme fragments, rather than full proteins. Future work is needed to develop more sensitive assays for the biomarkers studied here and other ECM remodeling proteins, such as other MMPS or A Disintegrin and Metalloproteinase with Thrombospondin motifs (ADAMTS) proteins.[73]

In summary, we found novel associations between age-related arterial stiffening and greater white matter microstructural damage over time, specifically within the temporal and occipital lobes. Results suggest that the posterior circulation may be particularly vulnerable to age-related increases in arterial stiffening and may be an alternative pathway to temporal lobe white matter damage, especially in individuals at a higher risk for AD. We also found that MMP-3, MMP-2, or BBB permeability may be an etiology of white matter injury in normal aging, even in the absence of overt cerebrovascular disease. However, among older adults at genetic risk for AD or with cognitive impairment, higher levels of MMP-2, MMP-3, and BBB permeability relate to healthier white matter microstructure. AD pathology may affect MMP function, such that MMPs are protective against white matter damage in the presence of AD pathology. Taken together, our results suggest that systemic vascular health may have a larger effect on white matter integrity than cerebrovascular health. Arterial stiffness may be a more robust predictor of future white matter damage whereas ECM remodeling and BBB permeability have greater utility as current markers of white matter health, in conjunction with other biomarkers. Finally, we found that temporal and occipital lobe

white matter may be more susceptible to arterial stiffening, deep white matter tracts may be more susceptible to MMP-3, and frontal lobe white matter may be more susceptible to MMP-2. Future work is needed to understand the mechanisms behind the associations reported here.

CHAPTER 3

THE EFFECTS OF AMYLOIDOSIS ON WHITE MATTER INTEGRITY

Portions of this chapter are published under the title “Neurofilament Relates to White Matter Microstructure in Older Adults” in *Neurobiology of Aging*

Introduction

Amyloid-β (Aβ) 42 plaques are one of the primary pathologies that accumulates in Alzheimer’s disease (AD).[2] Extracellular plaques are formed as Aβ42 monomers, aggregate together, and accumulate initially in the frontal and parietal lobes.[3] Though typically not associated with neurodegeneration[176] in disease progression, recent evidence has implicated Aβ42 plaques as a potential etiology of white matter damage in AD. Cross-sectionally, cognitively normal individuals who are positive for Aβ42 have greater white matter damage in the frontal lobe,[177] and *in vivo* measures of Aβ42 are associated with white matter damage in similar regions.[178] Additionally, animal models of amyloidosis show white matter changes[85-87] and *in vitro* studies suggest Aβ42 disrupts myelin synthesis and leads to oligodendrocyte death.[88,89] However, it is unknown if cerebral Aβ42 predicts future damage in certain white matter tracts.

While the presence of Aβ42 is one of the pathological criteria for a diagnosis of AD,[179] up to 80% of individuals with a clinical diagnosis of AD also have concomitant cerebral amyloid angiopathy (CAA).[180] CAA is defined by the pathologic accumulation of Aβ40 in arterial walls,[94] leading to fractured blood vessels, microbleeds, and

downstream hypoxia.[94] While patients with CAA have white matter damage on magnetic resonance imaging (MRI),[181,182] it is unclear if this white matter damage is related to Aβ40 burden or other vascular changes. It is hypothesized that Aβ40 restricts blood vessels,[94] leading to downstream hypoxia and subsequent white matter damage, but it remains unknown if Aβ40 predicts future damage in white matter tracts. Given the co-occurrence of AD and CAA,[180] it is necessary to understand which tracts are vulnerable to Aβ42 or Aβ40 to better delineate which white matter changes are specific to primary AD pathology.

The aim of the present chapter was to examine how two common forms of amyloidosis in AD, including Aβ42 and Aβ40, relate to white matter integrity, assessed by diffusion tensor imaging (DTI), among older adults free of clinical stroke and dementia. We also examined the cerebrospinal fluid (CSF) Aβ42/Aβ40 ratio, as this ratio is thought to be a more precise measure of pathologic Aβ42 levels by normalizing values to background levels of amyloidosis.[183] We hypothesized that lower levels of CSF Aβ42, Aβ40, and the CSF Aβ42/Aβ40 ratio, indicating greater levels of cerebral amyloidosis, would relate to compromised white matter microstructure at baseline and a faster decline in white matter microstructural integrity over time. We hypothesized that CSF Aβ42 and the CSF Aβ42/Aβ40 ratio would have the largest effect in the frontal and parietal lobes, where Aβ42 first accumulates in AD, and CSF Aβ40 would have the largest effect in cortical regions, where Aβ40 accumulates in CAA..[3] Since amyloidosis is more prevalent in individuals with mild cognitive impairment (MCI) compared to individuals with normal cognition (NC)[184] and apolipoprotein E (APOE) ε4 is associated with increased amyloid burden,[185] we also investigated whether associations were

modified by cognitive diagnosis (NC versus MCI) or *APOE*-ε4 status. We hypothesized that associations will be stronger among participants with MCI and *APOE*-ε4 positive participants.

Methods

For details about study cohort, brain MRI acquisition and post-processing, and covariates, please refer to the Methods in Chapter 2 (pages 27-33).

Lumbar Puncture & Biochemical Analysis

For details about the lumbar puncture acquisition, please refer to the Methods in Chapter 2 (pages 29-30). Commercially available enzyme-linked immunosorbent assays (Fujirebio, Ghent, Belgium) were used to measure CSF concentrations of Aβ42 (INNOTEST® β-AMYLOID(1-42)) and Aβ40 (INNOTEST® β-AMYLOID(1-40)). A CSF Aβ42/Aβ40 ratio was calculated to better assess Aβ42 accumulation due to AD pathology and account for individual differences in amyloid production and clearance.[183] Board certified laboratory technicians processed data blinded to clinical information.[186] Intra-assay coefficients of variation were <10%.

Analytical Plan

For cross-sectional analyses, voxel-wise linear regressions were conducted using the FSL randomise[143] procedure with 5000 permutations. General linear models using permutation testing related CSF Aβ42, CSF Aβ40, and the CSF Aβ42/40 ratio to FA, mean diffusivity, radial diffusivity, and axial diffusivity, adjusting for baseline age,

sex, education, race/ethnicity, FSRP (excluding points assigned to age), cognitive diagnosis, *APOE-ε4* status (one predictor per model). Multiple comparison correction was performed using the established cluster enhancement permutation procedure in FSL.[144]

For longitudinal analyses, voxel-wise linear mixed effects models with random intercepts and slopes and a follow-up time interaction related baseline CSF Aβ42, CSF Aβ40, and the CSF Aβ42/40 ratio to DTI metric trajectory. Models adjusted for identical covariates as cross-sectional analyses, plus follow-up time. Cluster-wise inference[145] was used to identify clusters of results and spatially correct the output images. Clusters were further corrected for multiple comparisons using a family-wise error rate of α=0.05.

All cross-sectional and longitudinal models were repeated with *predictor x cognitive diagnosis* (excluding individuals with early MCI due to the small sample size) and *predictor x APOE-ε4 status* interactions. Models were subsequently stratified by cognitive diagnosis (NC, MCI) and *APOE-ε4* status (positive or negative). Parametric estimates of statistically significant associations were calculated in R version 3.6.0 (www.r-project.org) using least squares regression for illustration and interpretation purposes. Sensitivity analyses were also performed in R, excluding participants with predictor or outcome variables ±4 standard deviations from the group mean. Significance was set *a priori* at $p<0.05$.

Results

Participant Characteristics

For the 152 participants included in these analyses (72±6 years, 67% male, 93% non-Hispanic White), mean follow-up time was 3.9 years. CSF Aβ42 concentrations ranged 2283 to 10919 pg/mL, Aβ40 concentrations ranged 84 to 884 pg/mL, and the Aβ42/Aβ40 ratio ranged 0.03 to 0.15. See **Table 2.6** in Chapter 2 for participant characteristics for the entire sample and stratified by diagnosis.

Aβ42 Analyses

Aβ42 & DTI Metrics

In the whole sample, CSF Aβ42 was cross-sectionally associated with DTI metrics (corrected p-values<0.05, **Table 3.1, Figure 3.1**). Specifically, lower CSF levels of Aβ42 were associated with higher mean diffusivity in the genu of the corpus callosum, higher radial diffusivity primarily in the medial orbital gyrus, and higher axial

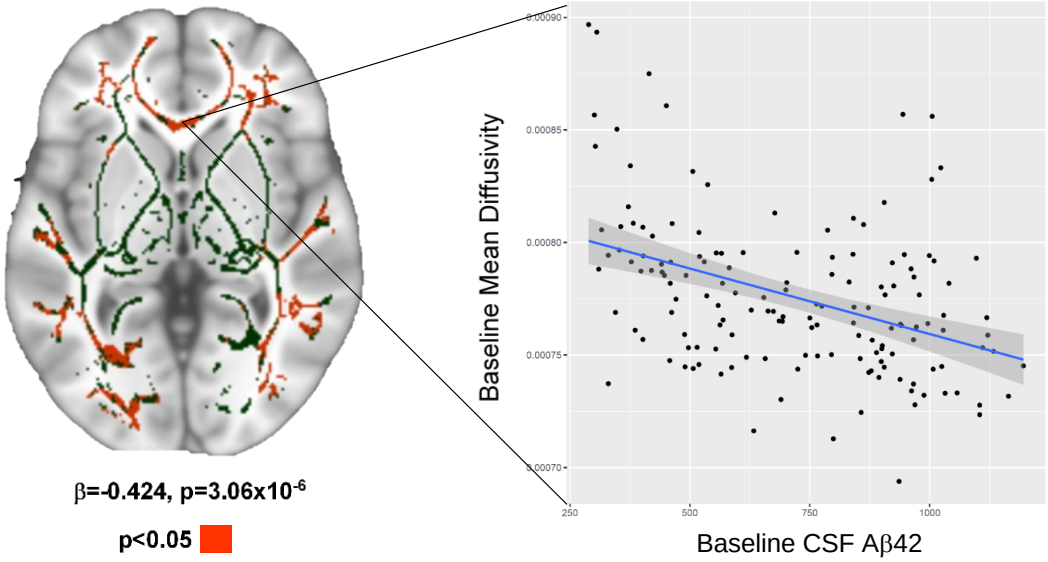

Figure 3.1. Cross-Sectional CSF Aβ42 Associations with Mean Diffusivity. Mean skeleton shows regions where CSF Aβ42 is associated with mean diffusivity. Scatterplot shows least squares regression relating CSF Aβ42 values for every participant to mean diffusivity values in one specific cluster. Parametric p-value and β listed only represent the cluster displayed here. Image taken at z=73. Aβ=amyloid-β; CSF=cerebrospinal fluid.

diffusivity in the posterior corona radiata. Associations persisted when removing outliers (**Table 3.1**).

In longitudinal analyses, lower baseline CSF Aβ42 was associated with a faster decline in white matter integrity over time. Specifically, lower baseline CSF Aβ42 was associated with a greater increase in mean (corrected p-values<0.03) and axial diffusivity (corrected p-value=0.008) in small clusters primarily in the superior longitudinal fasciculus and superior frontal gyrus (**Table 3.2, Figure 3.2**). Associations persisted when removing outliers (**Table 3.2**).

Aβ42 x Diagnosis Interactions & DTI Metrics

In cross-sectional analyses, CSF Aβ42 did not interact with diagnosis on DTI metrics (corrected p-values>0.14). However, in longitudinal analyses, baseline CSF Aβ42 did interact with diagnosis on DTI metrics (corrected p-values<0.03, **Table 3.3, Figure 3.2**). Specifically, baseline CSF Aβ42 interacted with diagnosis on mean diffusivity in the posterior limb of the internal capsule, radial diffusivity primarily in the superior temporal gyrus, and axial diffusivity in the posterior limb of the internal capsule. Stratification revealed that in all clusters, associations between lower baseline CSF Aβ42 and faster decline in white matter integrity were present in participants with NC, but associations were reversed in participants with MCI. Clusters remained significant when removing outliers (**Table 3.3**).

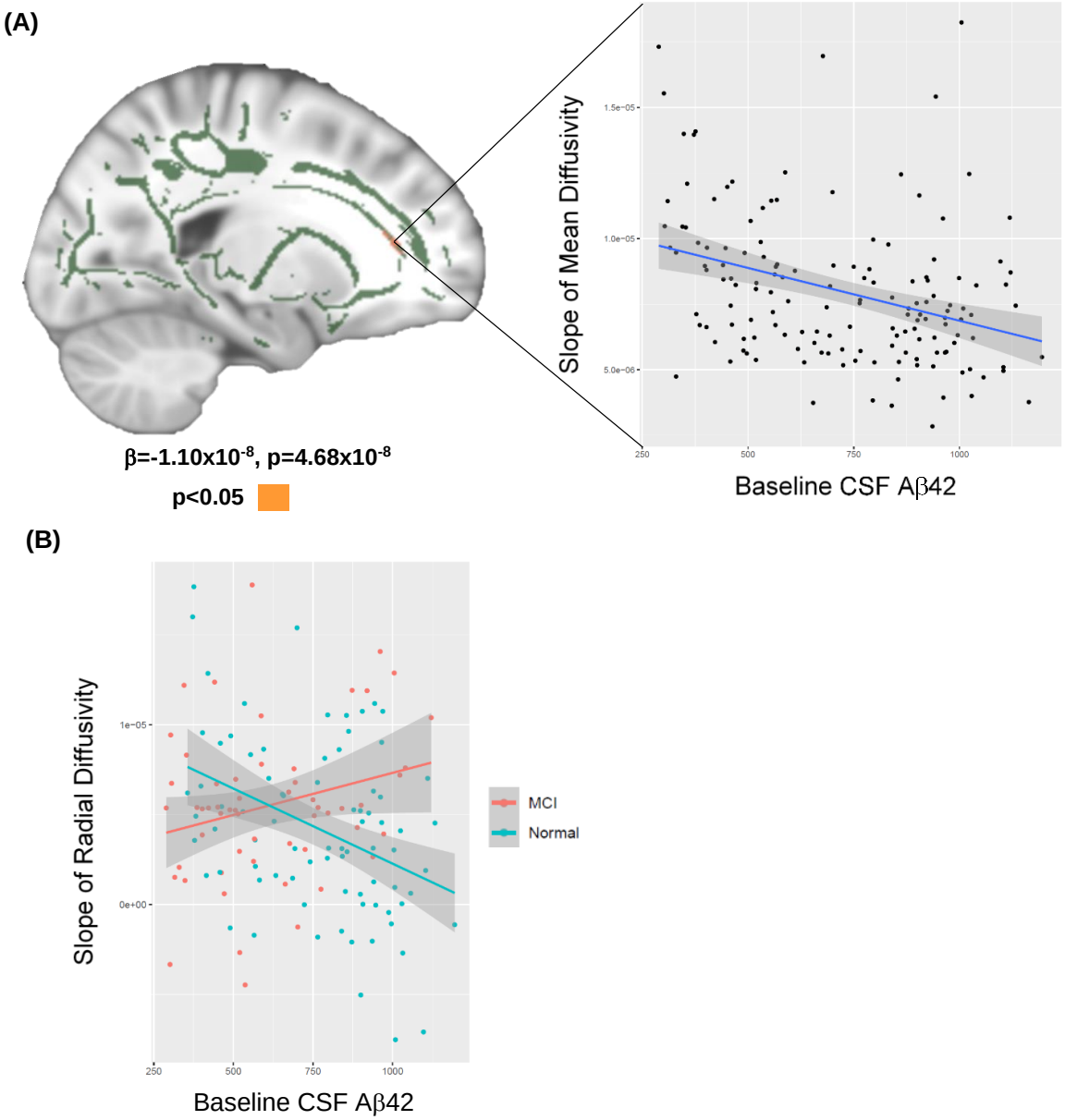

Figure 3.2. Baseline CSF Aβ42 and Longitudinal DTI Trajectory Associations. **(A)** Mean skeleton shows regions where baseline CSF Aβ42 is associated with a faster increase in mean diffusivity over time. Scatterplot shows a linear mixed effects model relating baseline CSF Aβ42 values for every participant to the slope of mean diffusivity values in one specific cluster. Parametric p-value and β listed only represent the cluster displayed here. Image taken at z=85. **(B)** *CSF Aβ42 x diagnosis* interaction on radial diffusivity trajectory. Scatterplots show interactions at one specific cluster ($\beta=-4.20\times10^{-8}$, $p=1.60\times10^{-5}$). Parametric p-value and β listed only represent the cluster displayed here. Aβ=amyloid-β; CSF=cerebrospinal fluid; DTI=diffusion tensor imaging; MCI=mild cognitive impairment.

Aβ42 x APOE-ε4 Interactions & DTI Metrics

In cross-sectional analyses, CSF Aβ42 did not interact with *APOE*-ε4 status on DTI metrics (corrected p-values>0.09). In longitudinal analyses, CSF Aβ42 did not interact with *APOE*-ε4 status on DTI metric trajectory (corrected p-values>0.81).

Table 3.1. Cross-Sectional Region Specific CSF Aβ42 Associations with DTI Metrics

	Anatomical Region	Hemisphere	Volume (mm^3)	Cluster Statistics		Corrected p-value†	MNI Coordinate‡		
				β	p-value*				
Fractional Anisotropy	--	--	--	--	--	--	--	--	--
Mean Diffusivity	Genu of the Corpus Callosum	Left	50788	-0.424	**$3.06x10^{-6}$**	0.005	-14	34	9
Radial Diffusivity	Medial Orbital Gyrus	Left	38839	-0.388	**$1.78x10^{-5}$**	0.021	-16	32	-17
	Middle Temporal Gyrus	Right	369	-0.400	**$1.44x10^{-5}$**	0.047	57	-27	-11
	Middle Temporal Gyrus	Right	146	-0.390	**$2.58x10^{-5}$**	0.049	58	-19	-15
	Middle Temporal Gyrus	Right	96	-0.398	**$1.10x10^{-5}$**	0.05	51	-2	-29
	Middle Temporal Gyrus	Right	80	-0.335	**$5.45x10^{-4}$**	0.05	47	-44	-2
Axial Diffusivity	Posterior Corona Radiata	Right	49276	-0.609	**$8.01x10^{-13}$**	0.001	27	-29	24

Note. Bold values indicate p-values that remain significant after excluding outliers. Empty rows indicate no significant clusters for that metric. *parametric p-values were calculated using linear regressions to relate baseline CSF Aβ42 and raw DTI values extracted from each participant skeleton; †p-value has been corrected for multiple comparisons; ‡coordinates and region represent the location of the minimum p-value for each cluster; Aβ=amyloid-β; CSF=cerebrospinal fluid; DTI=diffusion tensor imaging; MNI=Montreal Neurological Institute.

Table 3.2. Longitudinal Region Specific CSF Aβ42 Associations with DTI Metrics

	Anatomical Region	Hemisphere	Volume (mm^3)	Cluster Statistics		Corrected p-value†	MNI Coordinate‡		
				β	p-value*				
Fractional Anisotropy	--	--	--	--	--	--	--	--	--
Mean Diffusivity	Superior Longitudinal Fasciculus	Left	84	$-1.10x10^{-8}$	**$4.68x10^{-8}$**	0.001	-36	-45	26
	Anterior Corona Radiata	Left	57	$-1.40x10^{-8}$	**$7.50x10^{-7}$**	0.03	-20	35	13
Radial Diffusivity	--	--	--	--	--	--	--	--	--
Axial Diffusivity	Superior Frontal Gyrus	Left	67	$-1.90x10^{-8}$	**$2.74x10^{-5}$**	0.008	-19	7	40

Note. Bold values indicate p-values that remain significant after excluding outliers. Empty rows indicate no significant clusters for that metric. *parametric p-values were calculated using linear mixed effects models to relate baseline CSF Aβ42 and raw DTI values extracted from each participant skeleton; †p-value has been corrected for multiple comparisons; ‡coordinates and region represent the location of the minimum p-value for each cluster; Aβ=amyloid-β; CSF=cerebrospinal fluid; DTI=diffusion tensor imaging; MNI=Montreal Neurological Institute.

Table 3.3. Longitudinal Region Specific CSF Aβ42 x Diagnosis Interactions on DTI Metrics

	Anatomical Region	Hemisphere	Volume (mm^3)	Cluster Statistics		Corrected p-value†	MNI Coordinate‡		
				β	p-value*				
Fractional Anisotropy	--	--	--	--	--	--	--	--	--
Mean Diffusivity	Posterior Limb of the Internal Capsule	Right	184	$-2.90x10^{-8}$	**$2.53x10^{-6}$**	$1.58x10^{-7}$	24	-17	10
Radial Diffusivity	Superior Temporal Gyrus	Left	84	$-4.20x10^{-8}$	**$1.60x10^{-5}$**	0.003	-43	-21	-7
	Putamen	Right	61	$-3.10x10^{-8}$	**$3.34x10^{-7}$**	0.03	14	14	-7

Axial Diffusivity	Posterior Limb of the Internal Capsule	Right	64	-4.40x10^{-8}	**4.37x10^{-6}**	0.01	24	-17	9

Note. Bold values indicate p-values that remain significant after excluding outliers. Empty rows indicate no significant clusters for that metric. *parametric p-values were calculated using linear mixed effects models to relate baseline *CSF Aβ42 x diagnosis* interactions and raw DTI values extracted from each participant skeleton; †p-value has been corrected for multiple comparisons; ‡coordinates and region represent the location of the minimum p-value for each cluster; Aβ=amyloid-β; CSF=cerebrospinal fluid; DTI=diffusion tensor imaging; MNI=Montreal Neurological Institute.

Table 3.4. Cross-Sectional Region Specific CSF Aβ42/Aβ40 Associations with DTI Metrics

	Anatomical Region	Hemisphere	Volume (mm^3)	Cluster Statistics		Corrected p-value†	MNI Coordinate‡		
				β	p-value*				
Fractional Anisotropy	--	--	--	--	--	--	--	--	--
Mean Diffusivity	Middle Frontal Gyrus	Right	31624	-0.412	**9.67x10^{-6}**	0.018	26	26	25
Radial Diffusivity	--	--	--	--	--	--	--	--	--
Axial Diffusivity	Middle Temporal Gyrus	Left	32930	-0.588	**8.68x10^{-11}**	0.006	-42	-27	-15

Note. Bold values indicate p-values that remain significant after excluding outliers. Empty rows indicate no significant clusters for that metric. *parametric p-values were calculated using linear regressions to relate baseline CSF Aβ42/Aβ40 ratio and raw DTI values extracted from each participant skeleton; †p-value has been corrected for multiple comparisons; ‡coordinates and region represent the location of the minimum p-value for each cluster; Aβ=amyloid-β; CSF=cerebrospinal fluid; DTI=diffusion tensor imaging; MNI=Montreal Neurological Institute.

Table 3.5. Longitudinal Region Specific CSF Aβ42/Aβ40 Ratio Associations with DTI Metrics

	Anatomical Region	Hemisphere	Volume (mm^3)	Cluster Statistics		Corrected p-value†	MNI Coordinate‡		
				β	p-value*				
Fractional Anisotropy	--	--	--	--	--	--	--	--	--

Mean Diffusivity	Anterior Corona Radiata	Left	159	$-1.10x10^{-4}$	**$1.09x10^{-8}$**	$1.11x10^{-6}$	-19	28	21
	Anterior Corona Radiata	Left	113	$-1.00x10^{-4}$	**$1.81x10^{-7}$**	$7.23x10^{-5}$	-12	31	-13
	Superior Longitudinal Fasciculus	Left	73	$-8.90x10^{-5}$	**$5.85x10^{-8}$**	0.004	-36	-45	26
	Middle Frontal Gyrus	Right	57	$-8.10x10^{-5}$	**$5.54x10^{-6}$**	0.03	22	16	35
	Middle Frontal Gyrus	Right	56	$-1.10x10^{-4}$	**$3.17x10^{-5}$**	0.03	20	0	40
Radial Diffusivity	Anterior Corona Radiata	Left	151	$-9.70x10^{-5}$	**$3.57x10^{-7}$**	$5.72x10^{-6}$	-15	40	-11
	Anterior Corona Radiata	Left	134	$-1.10x10^{-4}$	**$6.57x10^{-9}$**	$2.42x10^{-5}$	-19	31	16
	Anterior Corona Radiata	Right	86	$-1.00x10^{-4}$	**$2.12x10^{-7}$**	0.002	17	33	-12
	Anterior Corona Radiata	Left	69	$-1.20x10^{-4}$	**$5.15x10^{-6}$**	0.01	-20	27	20
	Angular Gyrus	Right	62	$-1.00x10^{-4}$	**$1.23x10^{-6}$**	0.03	31	-59	33
	Angular Gyrus	Left	59	$-1.40x10^{-4}$	**$2.19x10^{-7}$**	0.04	-34	-55	26
Axial Diffusivity	Precentral Gyrus	Right	91	$-1.60x10^{-4}$	**$9.78x10^{-7}$**	0.001	24	-4	37

Note. Bold values indicate p-values that remain significant after excluding outliers. Empty rows indicate no significant clusters for that metric. *parametric p-values were calculated using linear mixed effects models to relate baseline CSF Aβ42/Aβ40 ratio and raw DTI values extracted from each participant skeleton; †p-value has been corrected for multiple comparisons; ‡coordinates and region represent the location of the minimum p-value for each cluster; Aβ=amyloid-β; CSF=cerebrospinal fluid; DTI=diffusion tensor imaging; MNI=Montreal Neurological Institute.

Table 3.6. Longitudinal Region Specific CSF Aβ42/Aβ40 Ratio x Diagnosis Interactions on DTI Metrics

	Anatomical Region	**Hemisphere**	**Volume (mm^3)**	**Cluster Statistics**		**Corrected p-value†**	**MNI Coordinate‡**		
				β	**p-value***				
Fractional Anisotropy	--	--	--	--	--	--	--	--	--

Mean Diffusivity	Posterior Limb of the Internal Capsule	Right	155	-2.10×10^{-4}	**2.73×10^{-5}**	1.75×10^{-6}	24	-16	9
Radial Diffusivity	--	--	--	--	--	--	--	--	--
Axial Diffusivity	Anterior Corona Radiata	Right	73	-3.10×10^{-4}	**4.98×10^{-6}**	0.004	20	27	23
	Retrolenticular Part of the Internal Capsule	Right	63	-3.20×10^{-4}	**1.46×10^{-5}**	0.01	24	-19	6

Note. Bold values indicate p-values that remain significant after excluding outliers. Empty rows indicate no significant clusters for that metric. *parametric p-values were calculated using linear mixed effects models to relate baseline *CSF Aβ42/Aβ40 ratio x diagnosis* interactions and raw DTI values extracted from each participant skeleton; †p-value has been corrected for multiple comparisons; ‡coordinates and region represent the location of the minimum p-value for each cluster; Aβ=amyloid-β; CSF=cerebrospinal fluid; DTI=diffusion tensor imaging; MNI=Montreal Neurological Institute.

Aβ42/Aβ40 Ratio Analyses

Aβ42/Aβ40 Ratio & DTI Metrics

In the whole sample, the CSF Aβ42/Aβ40 ratio was cross-sectionally associated with DTI metrics (corrected p-values<0.02, **Table 3.4**). Specifically, lower CSF levels of the Aβ42/Aβ40 ratio were associated with higher mean diffusivity in middle frontal gyrus and higher axial diffusivity in the middle temporal gyrus. Associations persisted when removing outliers (**Table 3.4**).

In longitudinal analyses, a lower baseline CSF Aβ42/Aβ40 ratio was associated with a faster decline in white matter integrity over time (**Table 3.5**). Specifically, a lower baseline CSF Aβ42/Aβ40 ratio was associated with a greater increase

in mean (corrected p-values<0.03), radial (corrected p-values<0.03), and axial diffusivity (corrected p-value=0.018) primarily in the anterior corona radiata and precentral gyrus. Associations persisted when removing outliers (**Table 3.5**).

Aβ42/Aβ40 Ratio x Diagnosis Interactions & DTI Metrics

In cross-sectional analyses, the CSF Aβ42/Aβ40 ratio did not interact with diagnosis on DTI metrics (corrected p-values>0.29). However, in longitudinal analyses, the baseline CSF Aβ42/Aβ40 ratio did interact with diagnosis on DTI metrics (corrected p-values<0.01, **Table 3.6**). Specifically, the baseline CSF Aβ42/Aβ40 ratio interacted with diagnosis on mean diffusivity in the posterior limb of the internal capsule and axial diffusivity primarily in the retrolenticular part of the internal capsule. Stratification revealed that in all clusters, associations between a lower baseline CSF Aβ42/Aβ40 ratio and faster decline in white matter integrity were present in participants with NC, but associations were reversed in participants with MCI. Clusters remained significant when removing outliers (**Table 3.6**).

Aβ42/Aβ40 Ratio x APOE-ε4 Interactions & DTI Metrics

In cross-sectional analyses, the CSF Aβ42/Aβ40 ratio did not interact with *APOE*-ε4 status on DTI metrics (corrected p-values>0.19). In longitudinal analyses, the CSF Aβ42/Aβ40 ratio did not interact with *APOE*-ε4 status on DTI metric trajectory (corrected p-values>0.28).

Aβ40 Analyses

Aβ40 *& DTI Metrics*

In the whole sample, lower CSF Aβ40 was cross-sectionally associated with higher axial diffusivity in the superior corona radiata (corrected p-value=0.03, **Table 3.7**). Associations remained significant when removing outliers (**Table 3.7**). In longitudinal models, baseline CSF Aβ40 was not associated with DTI metric trajectory (corrected p-values<0.28).

Aβ40 x Diagnosis Interactions & DTI Metrics

In cross-sectional analyses, CSF Aβ40 did not interact with diagnosis status on DTI metrics (corrected p-values>0.17). However, in longitudinal analyses, baseline CSF Aβ40 did interact with diagnosis status on DTI metric trajectory (corrected p-values<0.04, **Table 3.8, Figure 3.3**). Specifically, baseline CSF Aβ40 interacted with

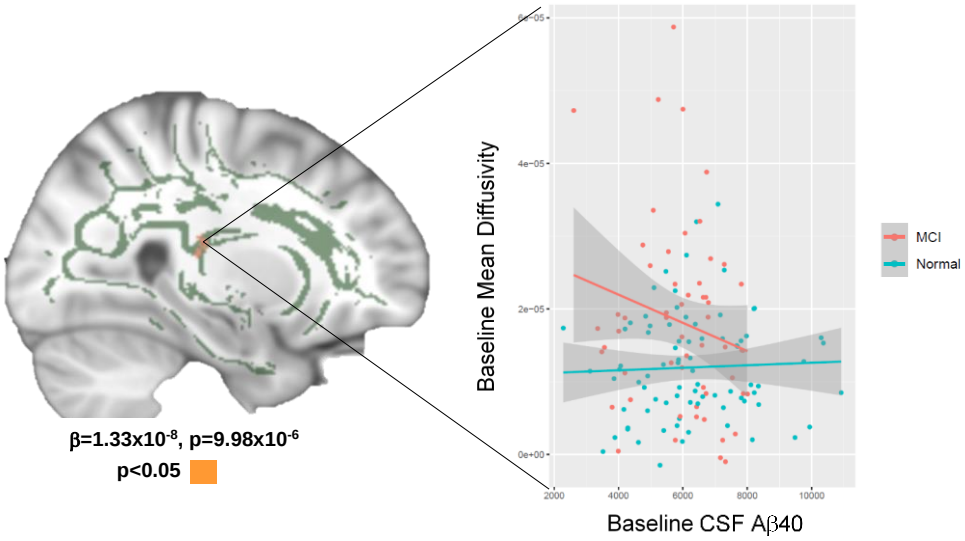

Figure 3.3. Longitudinal CSF Aβ40 x Diagnosis Interactions on Mean Diffusivity. Mean skeleton shows regions where CSF Aβ40 interacts with diagnosis on mean diffusivity trajectory. Scatterplot shows least squares regression relating CSF Aβ40 values for every participant to slope of mean diffusivity values in one specific cluster. Parametric p-value and β listed only represent the cluster displayed here. Image taken at z=73. Aβ=amyloid-β; CSF=cerebrospinal fluid; MCI=mild cognitive impairment.

diagnosis on mean, radial, and axial diffusivity primarily in the external capsule and thalamus. Stratification revealed that in all clusters, associations between lower baseline CSF Aβ40 and faster decline in white matter integrity were present in participants with MCI, but associations were null in participants with NC. A majority of clusters remained significant when removing outliers (**Table 3.8**).

Aβ40 x APOE-ε4 Interactions & DTI Metrics

In cross-sectional analyses, CSF Aβ40 interacted with *APOE*-ε4 status on DTI metrics (corrected p-values<0.03, **Table 3.9, Figure 3.4**). Specifically, CSF Aβ40 interacted with *APOE*-ε4 status on FA in the superior longitudinal fasciculus, mean diffusivity in the posterior corona radiata, and radial diffusivity in the angular gyrus.

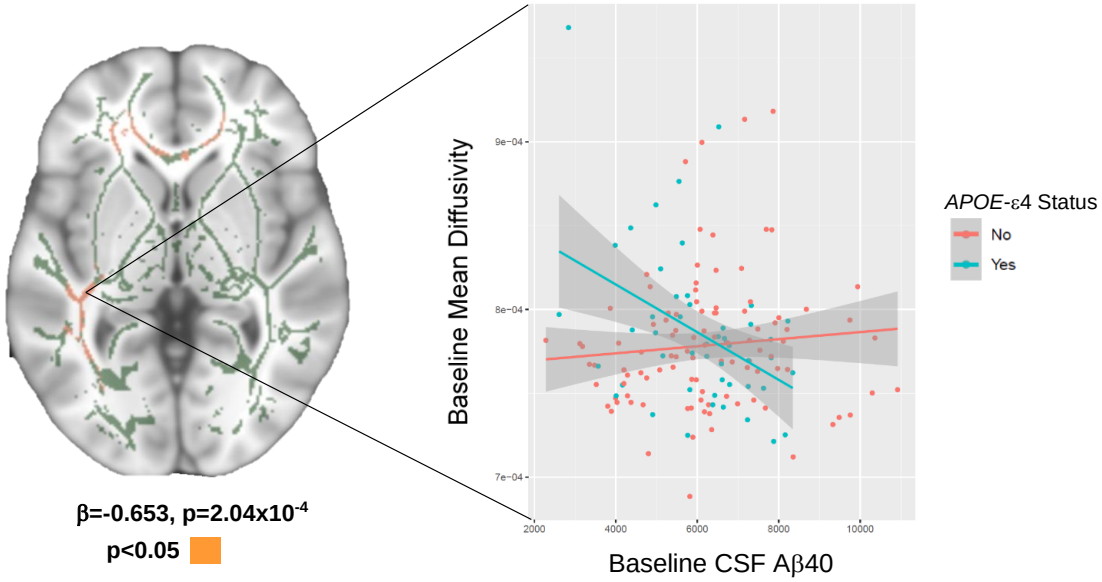

Figure 3.4. Cross-Sectional CSF Aβ40 x *APOE*-ε4 Status Interactions on FA. Mean skeleton shows regions where CSF Aβ40 interacts with *APOE*-ε4 status on mean diffusivity. Scatterplot shows least squares regression relating CSF Aβ40 values for every participant to mean diffusivity values in one specific cluster. Parametric p-value and β listed only represent the cluster displayed here. Image taken at z=73. Aβ=amyloid-β; APOE=apolipoprotein E; CSF=cerebrospinal fluid.

Stratification revealed that in all clusters, associations between lower baseline CSF Aβ40 and compromised white matter integrity were present in *APOE*-ε4 positive participants, but associations were null in *APOE*-ε4 negative participants. Associations persisted when removing outliers (**Table 3.9**).

In longitudinal analyses, baseline CSF Aβ40 interacted with *APOE*-ε4 status on DTI metric trajectory (corrected p-values<0.05, **Table 3.10, Figure 3.5**). Specifically, baseline CSF Aβ40 interacted with *APOE*-ε4 status on all 4 DTI metrics primarily in the external capsule and thalamus. Stratification revealed that in all clusters, associations between lower baseline CSF Aβ40 levels and faster decline in white matter integrity were present in *APOE*-ε4 positive participants, but associations were null in *APOE*-ε4 negative participants. A majority of clusters remained significant when removing outliers (**Table 3.10**).

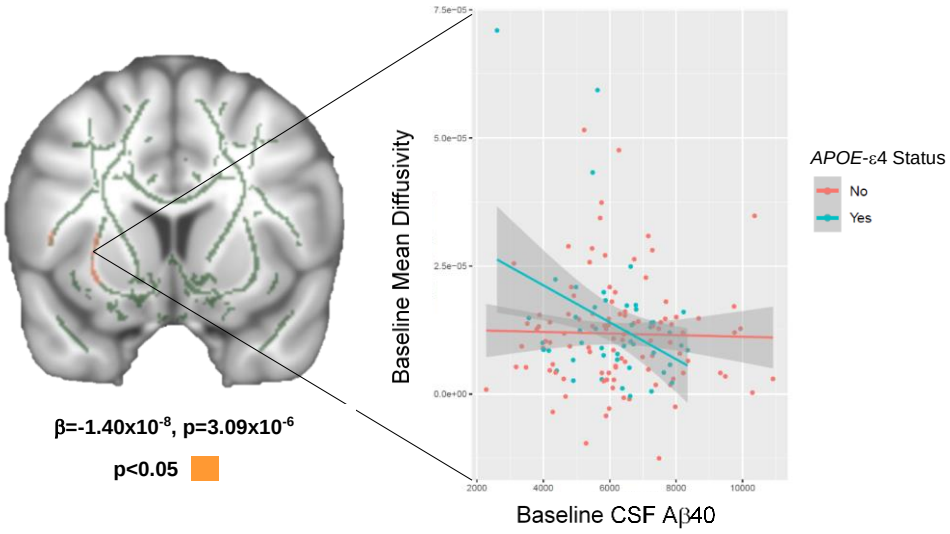

Figure 3.5. Longitudinal CSF Aβ40 x *APOE*-ε4 Status Interactions on Mean Diffusivity. Mean skeleton shows regions where CSF Aβ40 interacts with *APOE*-ε4 status on mean diffusivity trajectory. Scatterplot shows least squares regression relating CSF Aβ40 values for every participant to slope of mean diffusivity values in one specific cluster. Parametric p-value and β listed only represent the cluster displayed here. Image taken at z=70. Aβ=amyloid-β; APOE=apolipoprotein E; CSF=cerebrospinal fluid.

Table 3.7. Cross-Sectional Region Specific CSF Aβ40 Associations with DTI Metrics

	Anatomical Region	Hemisphere	Volume (mm^3)	Cluster Statistics		Corrected p-value†	MNI Coordinate‡		
				β	p-value*				
Fractional Anisotropy	--	--	--	--	--	--	--	--	--
Mean Diffusivity	--	--	--	--	--	--	--	--	--
Radial Diffusivity	--	--	--	--	--	--	--	--	--
Axial Diffusivity	Superior Corona Radiata	Left	705	-0.282	**$8.08x10^{-5}$**	0.03	-26	-1	30

Note. Bold values indicate p-values that remain significant after excluding outliers. Empty rows indicate no significant clusters for that metric. *parametric p-values were calculated using linear regressions to relate baseline CSF Aβ40 and raw DTI values extracted from each participant skeleton; †p-value has been corrected for multiple comparisons; ‡coordinates and region represent the location of the minimum p-value for each cluster; Aβ=amyloid-β; CSF=cerebrospinal fluid; DTI=diffusion tensor imaging; MNI=Montreal Neurological Institute.

Table 3.8. Longitudinal Region Specific CSF Aβ40 x Diagnosis Interactions on DTI Metrics

	Anatomical Region	Hemisphere	Volume (mm^3)	Cluster Statistics		Corrected p-value†	MNI Coordinate‡		
				β	p-value*				
Fractional Anisotropy	--	--	--	--	--	--	--	--	--
Mean Diffusivity	External Capsule	Left	137	$1.46x10^{-8}$	$1.09x10^{-3}$	$8.75x10^{-6}$	-28	16	-3
	Thalamus	Left	82	$1.33x10^{-8}$	**$9.98x10^{-6}$**	0.002	-11	-17	9
	Insular Gyrus	Left	57	$1.85x10^{-8}$	$1.71x10^{-3}$	0.03	-33	4	-2
Radial Diffusivity	External Capsule	Left	143	$1.34x10^{-8}$	$1.63x10^{-3}$	$1.33x10^{-5}$	-24	21	-3

	Thalamus	Left	60	$1.22x10^{-8}$	**$4.83x10^{-5}$**	0.04	-11	-17	9
Axial Diffusivity	External Capsule	Left	107	$1.90x10^{-8}$	**$5.07x10^{-4}$**	0.0001	-28	16	-3
	Thalamus	Left	81	$1.56x10^{-8}$	**$4.80x10^{-7}$**	0.002	-12	-17	8
	Body of the Corpus Callosum	Left	79	$8.69x10^{-9}$	**$3.09x10^{-6}$**	0.002	-19	23	24
	Thalamus	Right	60	$1.90x10^{-8}$	**$2.80x10^{-5}$**	0.02	7	-12	7
	External Capsule	Left	53	$2.17x10^{-8}$	$1.96x10^{-3}$	0.04	-31	4	7

Note. Bold values indicate p-values that remain significant after excluding outliers. Empty rows indicate no significant clusters for that metric. *parametric p-values were calculated using linear mixed effects models to relate baseline *CSF Aβ40 x diagnosis* interactions and raw DTI values extracted from each participant skeleton; †p-value has been corrected for multiple comparisons; ‡coordinates and region represent the location of the minimum p-value for each cluster; Aβ=amyloid-β; CSF=cerebrospinal fluid; DTI=diffusion tensor imaging; MNI=Montreal Neurological Institute.

Table 3.9. Cross-Sectional Region Specific CSF Aβ40 x *APOE*-ε4 Status Interactions on DTI Metrics

	Anatomical Region	**Hemisphere**	**Volume (mm^3)**	**Cluster Statistics**		**Corrected p-value†**	**MNI Coordinate‡**		
				β	**p-value***				
Fractional Anisotropy	Superior Longitudinal Fasciculus	Left	13905	0.802	**$6.71x10^{-6}$**	0.018	-36	-34	32
Mean Diffusivity	Posterior Corona Radiata	Left	17895	-0.653	**$2.04x10^{-4}$**	0.026	-29	-37	21
Radial Diffusivity	Angular Gyrus	Left	18290	-0.659	**$2.07x10^{-4}$**	0.017	-40	-44	19
Axial Diffusivity	--	--	--	--	--	--	--	--	--

Note. Bold values indicate p-values that remain significant after excluding outliers. Empty rows indicate no significant clusters for that metric. *parametric p-values were calculated using linear regression models to relate baseline *CSF Aβ40 x APOE-ε4* interactions and raw DTI values extracted from each participant skeleton; †p-value has been corrected for multiple comparisons; ‡coordinates and region represent the location of the minimum p-value for each cluster; Aβ=amyloid-β; APOE=apolipoprotein; CSF=cerebrospinal fluid; DTI=diffusion tensor imaging; MNI=Montreal Neurological Institute.

Table 3.10. Longitudinal Region Specific CSF Aβ40 x *APOE*-ε4 Status Interactions on DTI Metrics

	Anatomical Region	Hemisphere	Volume (mm^3)	Cluster Statistics		Corrected p-value†	MNI Coordinate‡		
				β	p-value*				
Fractional Anisotropy	External Capsule	Left	74	$3.77x10^{-6}$	**$9.41x10^{-5}$**	0.05	-27	12	8
Mean Diffusivity	External Capsule	Left	162	$-1.80x10^{-8}$	$5.52x10^{-5}$	$8.79x10^{-7}$	-29	12	6
	Thalamus	Right	112	$-1.40x10^{-8}$	**$3.09x10^{-6}$**	$8.11x10^{-5}$	8	-10	8
	External Capsule	Left	72	$-2.20x10^{-8}$	**$3.34x10^{-5}$**	0.005	-32	5	1
	Inferior Frontal Gyrus	Left	71	$-2.00x10^{-8}$	$1.43x10^{-4}$	0.006	-46	14	8
	Posterior Corona Radiata	Left	70	$-3.50x10^{-9}$	**$4.62x10^{-5}$**	0.006	-26	-23	34
Radial Diffusivity	External Capsule	Left	291	$-1.70x10^{-8}$	$3.87x10^{-5}$	$1.87x10^{-10}$	-29	12	6
	Thalamus	Right	80	$-1.30x10^{-8}$	**$2.92x10^{-6}$**	0.004	8	-10	8
	Superior Corona Radiata	Left	76	$-3.40x10^{-9}$	**$2.76x10^{-5}$**	0.006	-27	-24	35
	Inferior Frontal Gyrus	Left	69	$-1.80x10^{-8}$	$2.13x10^{-4}$	0.01	-46	14	8
Axial Diffusivity	External Capsule	Left	109	$-2.20x10^{-8}$	$6.74x10^{-5}$	$9.09x10^{-5}$	-29	12	6
	Thalamus	Right	96	$-1.70x10^{-8}$	**$1.32x10^{-6}$**	0.0003	8	-10	8
	Inferior Frontal Gyrus	Left	64	$-2.60x10^{-8}$	$6.70x10^{-5}$	0.01	-44	14	6
	External Capsule	Left	61	$-2.70x10^{-8}$	**$3.98x10^{-5}$**	0.02	-32	5	1
	Posterior Corona Radiata	Left	56	$-5.70x10^{-9}$	**$4.05x10^{-5}$**	0.03	-26	-24	34

Note. Bold values indicate p-values that remain significant after excluding outliers. Empty rows indicate no significant clusters for that metric. *parametric p-values were calculated using linear mixed effects models to relate baseline *CSF Aβ40 x APOE-ε4* interactions and raw DTI values extracted from each participant skeleton; †p-value has been corrected for multiple comparisons; ‡coordinates and region represent the location of the minimum p-value for each cluster; Aβ=amyloid-β; APOE=apolipoprotein; CSF=cerebrospinal fluid; DTI=diffusion tensor imaging; MNI=Montreal Neurological Institute.

Discussion

Among community-dwelling older adults free of clinical stroke and dementia, lower baseline CSF Aβ42 and the CSF Aβ42/Aβ40 ratio were cross-sectionally associated with compromised white matter microstructure, primarily in the frontal and temporal lobes. In longitudinal models, baseline CSF Aβ42 and the CSF Aβ42/Aβ40 ratio were associated with faster decline of white matter integrity, specifically in small clusters in the frontal lobe. Findings were primarily driven by participants with NC. Lower baseline CSF Aβ40 cross-sectionally related to compromised white matter microstructure primarily in the parietal lobe and longitudinally related to faster decline in white matter integrity in deep white matter tracts. Both cross-sectional and longitudinal associations were driven by *APOE*-ε4 carriers.

These results add to a growing body of evidence showing cross-sectional associations between Aβ42 and white matter damage. PET and CSF measures of Aβ42 have been associated with regional white matter damage in sporadic[81] and familial AD,[25] and Aβ42 has been associated with axonopathy and DTI changes in animal models.[187] We found that CSF measures of Aβ42 and the CSF Aβ42/Aβ40 ratio were robustly associated with white matter microstructure cross-sectionally. Notably, associations were strongest in the frontal and temporal lobes, where Aβ42 is known to deposit.[3] This regional specificity suggests that Aβ42 may be directly damaging oligodendrocytes or interfering with myelination processes. Aβ42 is thought to regulate sphingomyelinase,[88,89] a critical enzyme in oligodendrocytes,[89] and increased expression is hypothesized to lead to apoptosis within oligodendrocytes.[90] Aβ42 also inhibits neuronal cholesterol transport,[91,92] hindering the remyelination process. Finally,

Aβ42 induces an inflammatory response[188] and the process of Aβ42 aggregation produces reactive oxygen species.[189] Given the relative vulnerability of oligodendrocytes to oxidative stress,[66] some white matter damage may be a consequence of Aβ42 aggregation and subsequent inflammatory activation. Future work is needed to determine the role of inflammation in white matter damage in normal aging and in AD.

In contrast to the robust cross-sectional findings, the association between baseline CSF Aβ42 or the CSF Aβ42/Aβ40 ratio and change in white matter integrity was relatively small. Lower levels of CSF Aβ42 or the CSF Aβ42/Aβ40 ratio at baseline were associated with a faster decline in white matter integrity in a small region in the frontal lobe. Taken together, the cross-sectional and longitudinal findings suggest that Aβ42 is not a robust driver of future white matter damage but may reflect active white matter damage. It is also possible that individuals with higher levels of cerebral Aβ42 develop additional pathologies over time[190] more likely to damage white matter, obscuring any direct associations between baseline CSF Aβ42 and change in white matter microstructure. Future work in larger samples is needed to determine how Aβ42 predicts future white matter damage in the presence of multiple pathologies, including phosphorylated tau[190] or TAR DNA binding protein 43.[191] Additionally, while the longitudinal findings are small, associations were driven by participants with NC, rather than MCI. Since Aβ42 is known to accumulate years before symptom onset,[84] these results suggest that the effect of Aβ42 on white matter may be most robust early in the disease process, prior to other pathologies or symptom onset. Of note, the CSF Aβ42 results and CSF Aβ42/Aβ40 ratio results both cross-sectionally and longitudinally

presented here are highly consistent with one another, further suggesting that both are sensitive measures of cerebral Aβ42 burden.

Lower baseline CSF Aβ40 was also cross-sectionally associated with compromised white matter microstructure, with associations most prominent in the superior longitudinal fasciculus. The superior longitudinal fasciculus is a large association tract important for information processing[192] and executive function[193] that primarily connects the parietal and frontal lobes. In CAA, Aβ40 is thought to deposit in cortical blood vessels, leading to vessel wall thickening, luminal narrowing, microaneurysms, and microhemorrhages.[94] It is likely that this vessel damage leads to relative ischemia in the underlying white matter, accounting for the associations between CSF Aβ40 and DTI changes reported here. Thus, white matter tracts with large cortical projections, including the superior longitudinal fasciculus, would be most vulnerable to damage due to vascular Aβ40 deposition. Interestingly, CSF Aβ40 cross-sectionally interacted with *APOE*-ε4 status on DTI metrics, such that the main results were driven by *APOE*-ε4 carriers. This result contrasts with the cross-sectional CSF Aβ42 findings, which were not moderated by *APOE*-ε4 status. While *APOE*-ε4 is traditionally thought to increase Aβ deposition,[185] it is also a known modifier of cerebrovascular health.[194] *APOE*-ε4 carriers have increased blood-brain barrier permeability compared to non-carriers[155] and are more susceptible to poor brain health outcomes associated with systemic vascular changes.[56,153] Thus, the cortical blood vessels of *APOE*-ε4 carriers may be more vulnerable to the effects of Aβ40 depositing in the vessel wall, leading to more severe downstream ischemia and white matter damage.

In the entire sample, baseline CSF Aβ40 was not associated with faster decline in white matter integrity. However, interaction and stratified analyses revealed that baseline CSF Aβ40 was associated with a faster decline in white matter integrity among participants with MCI and *APOE*-ε4 carriers only. Overall, the longitudinal associations were small, suggesting Aβ40 is not a robust driver of white matter damage even in these populations, similar to the Aβ42 results. Notably, longitudinal associations were most robust in the deep white matter tracts, which are thought to be most vulnerable to cerebrovascular disease.[195] Over time, it is likely that the vascular damage caused by Aβ40 deposition in the vessel wall would lead to ischemia in these areas, though it is somewhat surprising that results also do not localize in the white matter tracts directly underlying cortical regions.[182] However, given the relatively small size of the clusters, regional conclusions must be interpreted cautiously.

Our study has several strengths, including excellent methods for quantifying CSF Aβ42 and Aβ40, stringent quality control procedures, a longitudinal study design, and reliable methods for quantifying cerebral white matter microstructure. Additional strengths include comprehensive ascertainment of potential confounders and the application of cluster enhancement and cluster-wise inference to correct for multiple comparisons, reducing the possibility of a false positive finding. The application of a longitudinal voxel-wise pipeline allows for the robust and comprehensive assessment of the trajectory of white matter damage throughout the entire brain. Finally, core laboratories using quality control procedures analyzed all MRI and CSF measurements in batch, and technicians were blinded to clinical information. Despite these strengths, there are limitations, inclduing the observational design and the predominantly White,

well-educated, and relatively healthy sample, limiting generalizability. Additionally, CSF measures of Aβ42 and Aβ40 cannot provide information about the anatomic location of Aβ accumulation. Studies using brain positron emission tomography are needed to determine if Aβ accumulation and associated white matter damage are in the same location. Additionally, many of the longitudinal effects reported here are small, possible due to the small sample size. Larger studies are needed to further characterize longitudinal associations.

In summary, we found robust cross-sectional associations between CSF measures of Aβ42 and Aβ40 and compromised white matter microstructure. A lower level of CSF Aβ42 was associated with compromised white matter microstructure primarily in the frontal and temporal lobes, whereas a lower level of CSF Aβ40 was associated with compromised white matter microstructure primarily in the frontal and parietal lobes. Results suggest that Aβ42 may directly damage oligodendrocytes in regions that correspond to amyloid plaque burden, and Aβ40 may lead to white matter damage perfused by the vessels it deposits in. Neither Aβ42 nor Aβ40 were robust drivers of white matter damage over time. Taken together, our results suggest that CSF markers of amyloidosis may reflect active white matter damage in regions where amyloid accumulates but are not good predictors of future white matter damage.

CHAPTER 4

THE EFFECTS OF PHOSPHORYLATED TAU AND NEURODEGENERATION ON WHITE MATTER INTEGRITY

Portions of this chapter are published under the title “Neurofilament Relates to White Matter Microstructure in Older Adults” in *Neurobiology of Aging*

Introduction

Tau tangles are the second primary neuropathology that accumulates in Alzheimer’s disease (AD), composed of hyperphosphorylated tau. Tau is an axonal protein that normally undergoes phosphorylation and dephosphorylation to stabilize microtubules, facilitating efficient transport across the axon.[6] However, in AD, tau becomes hyperphosphorylated, aggregates, and forms intracellular tau tangles that disrupt the axon and eventually cause neuronal dysfunction and death. Tau hyperphosphorylation in AD, which can be measured *in vivo* by an increase in cerebrospinal fluid (CSF) phosphorylated tau (p-tau), typically begins in the medial temporal lobe[3] and spreads through the axons of connecting neurons.[7] Since tau is an axonal protein and tangles propagate through adjacent white matter tracts, p-tau has emerged as one potential etiology of white matter damage in AD.

Basic science evidence suggests that hyperphosphorylated tau is mis-localized within the cell, leading to disruption in transport and axonal growth.[105] This process leads to axonal injury and hinders the transport of key nutrients to surrounding

oligodendrocytes,[108] further damaging the white matter. Additionally, human data suggest that tau deposition is cross-sectionally associated with white matter damage in the temporal lobe,[97] and individuals with a high tau burden have white matter changes in the hippocampus and entorhinal cortex.[99] Finally, the integrity of temporal lobe white matter tracts predicts future tau propagation,[196] further suggesting that white matter health and tau phosphorylation are linked. However, it is unknown if p-tau predicts future white matter damage, particularly throughout the medial temporal lobe where p-tau is known to first evolve in AD.[3]

An alternative etiology of white matter damage in AD is Wallerian degeneration due to concurrent neurodegeneration. Wallerian degeneration is the process by which damage to cell bodies in the grey matter leads to progressive damage of associated axons.[109] Traditionally, white matter injury in AD was thought to only be due to neurodegeneration, and *in vivo* molecular biomarkers of neurodegeneration (CSF total tau (t-tau))[197] and neuroaxonal injury[81] (CSF neurofilament light (NFL)) have been cross-sectionally associated with white matter damage. While some data suggest that p-tau affects white matter early in the disease process,[25] prior to neurodegeneration, it is possible that associations between p-tau and white matter damage are partially due to the simultaneous effects of p-tau on grey matter. To better understand these competing etiologies of white matter damage in AD and what white matter damage may be specific to AD pathology, it is necessary to determine where general markers of neurodegeneration predict future white matter damage and if the contributions of p-tau, t-tau, and NFL to white matter damage are independent.

The aim of the present chapter was to examine if CSF markers of p-tau, neurodegeneration (t-tau), and neuroaxonal injury (NFL) relate to white matter integrity, assessed by diffusion tensor imaging (DTI), among older adults free of clinical stroke and dementia, and determine if associations between p-tau and white matter integrity are independent of general neurodegeneration. We hypothesized that higher levels of CSF p-tau, t-tau, and NFL would relate to compromised white matter microstructure at baseline and a faster decline in white matter microstructural integrity over time. We hypothesized that p-tau would have the largest, independent effect in the medial temporal lobe, where tau tangles first develop,[3] but t-tau and NFL would not be regionally specific. Since p-tau and neurodegeneration are more prevalent in individuals with mild cognitive impairment (MCI)[198] and apolipoprotein E (APOE) ε4 carriers[199] compared to individuals with normal cognition (NC) and *APOE*-ε4 non-carriers, we also investigated whether associations were modified by cognitive diagnosis (NC versus MCI) or *APOE*-ε4 status. We hypothesized that associations would be stronger among participants with MCI and *APOE*-ε4 positive participants.

Methods

For details about study cohort, brain magnetic resonance imaging (MRI) acquisition and post-processing, and covariates, please refer to the Methods in Chapter 2 (pages 27-33).

Lumbar Puncture & Biochemical Analysis

For details about the lumbar puncture acquisition, please refer to the Methods in Chapter 2 (pages 29-30). Commercially available enzyme-linked immunosorbent assays (Fujirebio, Ghent, Belgium) were used to measure CSF concentrations of p-tau (INNOTEST® PHOSPHO-TAU$_{(181P)}$), and t-tau (INNOTEST® hTAU). An additional commercially available enzyme-linked immunosorbent assay was used to measure CSF NFL concentrations (UmanDiagnostics, Umeå, Sweden). Board certified laboratory technicians processed data blinded to clinical information.[186] Intra-assay coefficients of variation were <10%.

Analytical Plan

For cross-sectional analyses, voxel-wise linear regressions were conducted using the FSL randomise[143] procedure with 5000 permutations. General linear models using permutation testing related CSF p-tau, CSF t-tau and CSF NFL to fractional anisotropy (FA), mean diffusivity, radial diffusivity, and axial diffusivity, adjusting for baseline age, sex, education, race/ethnicity, FSRP (excluding points assigned to age), cognitive diagnosis, *APOE-ε4* status (one predictor per model). Multiple comparison correction was performed using the established cluster enhancement permutation procedure in FSL.[144]

For longitudinal analyses, voxel-wise linear mixed effects models with random intercepts and slopes and a follow-up time interaction related baseline CSF p-tau, CSF t-tau and CSF NFL to DTI metric trajectory. Models adjusted for identical covariates as cross-sectional analyses, plus follow-up time. Cluster-wise inference[145] was used to identify clusters of results and spatially correct the output images. Clusters were further

corrected for multiple comparisons using a family-wise error rate of α=0.05. For each DTI metric that related to CSF p-tau and >1 additional CSF biomarker, a combined linear mixed effects model was performed including all statistically significant CSF biomarkers for the DTI metric (with identical covariates) to determine whether p-tau represented a common or unique pathologic pathway to white matter damage.

All cross-sectional and longitudinal models were repeated with *predictor x cognitive diagnosis* (excluding individuals with early MCI due to the small sample size) and *predictor x APOE-ε4 status* interactions. Models were subsequently stratified by cognitive diagnosis (NC, MCI) and *APOE-ε4* status (positive or negative). Parametric estimates of statistically significant associations were calculated in R version 3.6.0 (www.r-project.org) using least squares regression for illustration and interpretation purposes. Sensitivity analyses were also performed in R, excluding participants with predictor or outcome variables ±4 standard deviations from the group mean. Significance was set *a priori* at p<0.05.

Results

Participant Characteristics

For the 152 participants included in these analyses (72±6 years, 67% male, 93% non-Hispanic White), mean follow-up time was 3.9 years. CSF p-tau concentrations ranged 13 to 157 pg/mL, t-tau concentrations ranged 77 to 1542 pg/mL, and NFL concentrations ranged 268 to 4025 pg/mL. See **Table 2.6** in Chapter 2 for participant characteristics for the entire sample and stratified by diagnosis.

P-tau Analyses

P-tau & DTI Metrics

In the whole sample, CSF p-tau was not cross-sectionally associated with DTI metrics (corrected p-values>0.06). However, higher levels of baseline CSF p-tau were associated with faster decline in white matter integrity over time (**Table 4.1, Figure 4.1**). Specifically, higher baseline CSF p-tau was associated with a greater decline in FA over time primarily in the anterior corona radiata (corrected p-values<0.005). Higher baseline CSF p-tau was associated with a greater increase in mean, radial, and axial diffusivity over time, particularly in the straight gyrus, genu of the corpus callosum, and external capsule (corrected p-values<0.02). These associations persisted when removing outliers (**Table 4.1**).

P-tau x Diagnosis Interactions & DTI Metrics

In cross-sectional analyses, CSF p-tau did not interact with diagnosis on DTI metrics (corrected p-values>0.16). However, in longitudinal analyses, baseline CSF p-tau did interact with diagnosis in two small clusters on the trajectory of axial diffusivity (**Table 4.2, Figure 4.1**) primarily in the superior parietal lobule (corrected p-value=0.021) and anterior corona radiata (corrected p-value=0.027). Stratification revealed that in all clusters, associations between higher baseline CSF p-tau and faster decline in white matter integrity were present by participants with NC, but associations were reversed in participants with MCI. Clusters remained significant when removing outliers (**Table 4.2**).

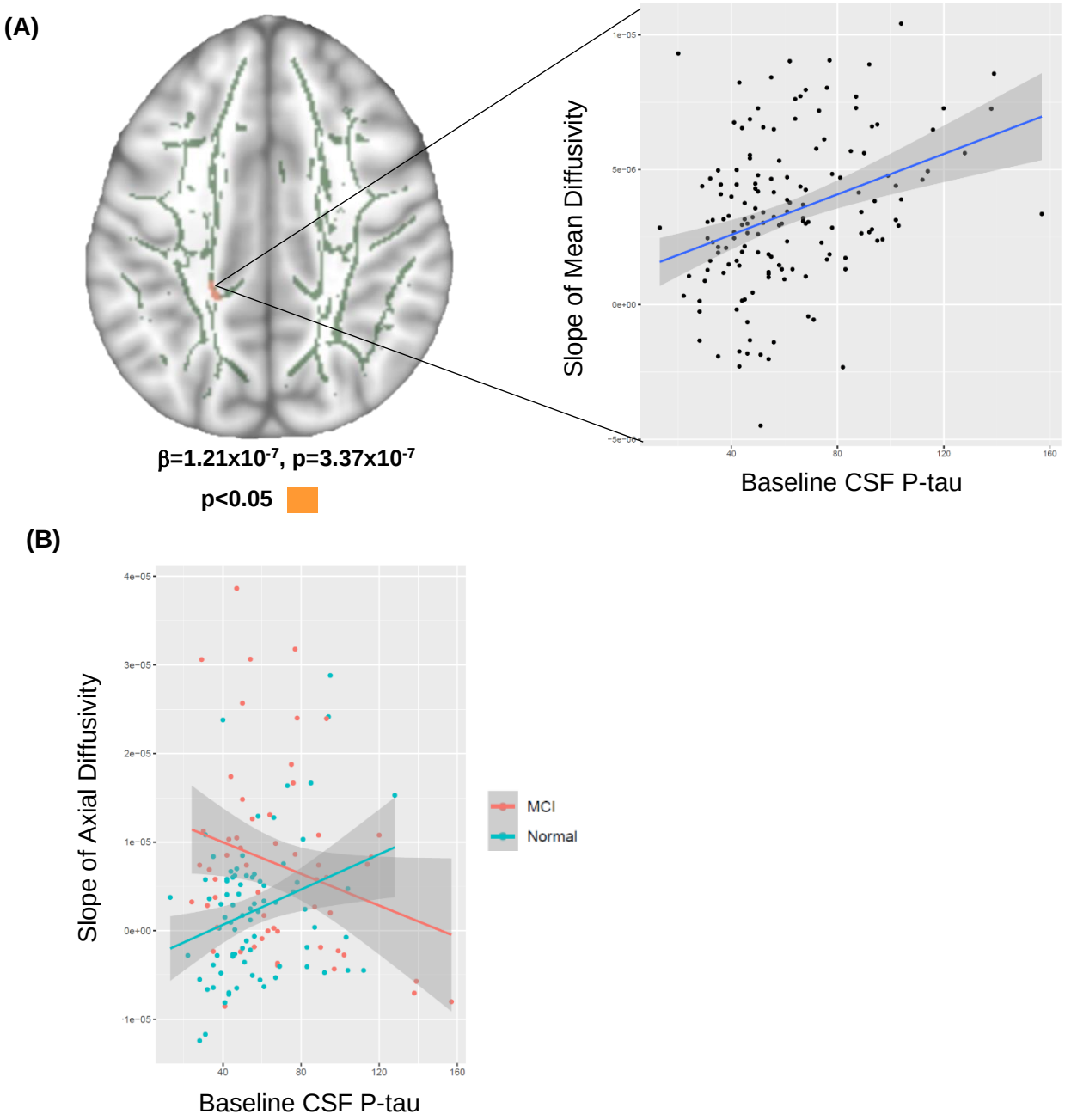

Figure 4.1. Baseline CSF P-tau and Longitudinal DTI Trajectory Associations. **(A)** Mean skeleton shows regions where baseline CSF p-tau is associated with a faster increase in mean diffusivity over time. Scatterplot shows a linear mixed effects model relating baseline CSF p-tau values for every participant to the slope of mean diffusivity values in one specific cluster. Parametric p-value and β listed only represent the cluster displayed here. Image taken at z=118. **(B)** *CSF p-tau x diagnosis* interaction on axial diffusivity trajectory. Scatterplots show interactions at one specific cluster. Parametric p-value and β listed only represent the cluster displayed here ($\beta=4.32x10^{-7}$, $p=4.00x10^{-5}$). CSF=cerebrospinal fluid; DTI=diffusion tensor imaging; MCI=mild cognitive impairment; P-tau=phosphorylated tau.

P-tau x APOE-ε4 Interactions & DTI Metrics

In cross-sectional analyses, CSF p-tau interacted with *APOE*-ε4 status on FA (corrected p-values <0.05, **Table 4.3, Figure 4.2**) primarily in the corpus callosum, posterior corona radiata, and superior parietal lobule. Stratification revealed that in all clusters, associations between lower CSF p-tau levels and compromised white matter integrity were present in *APOE*-ε4 positive participants, but associations were reversed in *APOE*-ε4 negative participants. Associations persisted when removing outliers (**Table 4.3**). In longitudinal analyses, CSF p-tau did not interact with *APOE*-ε4 status on DTI metric trajectory (corrected p-values>0.14).

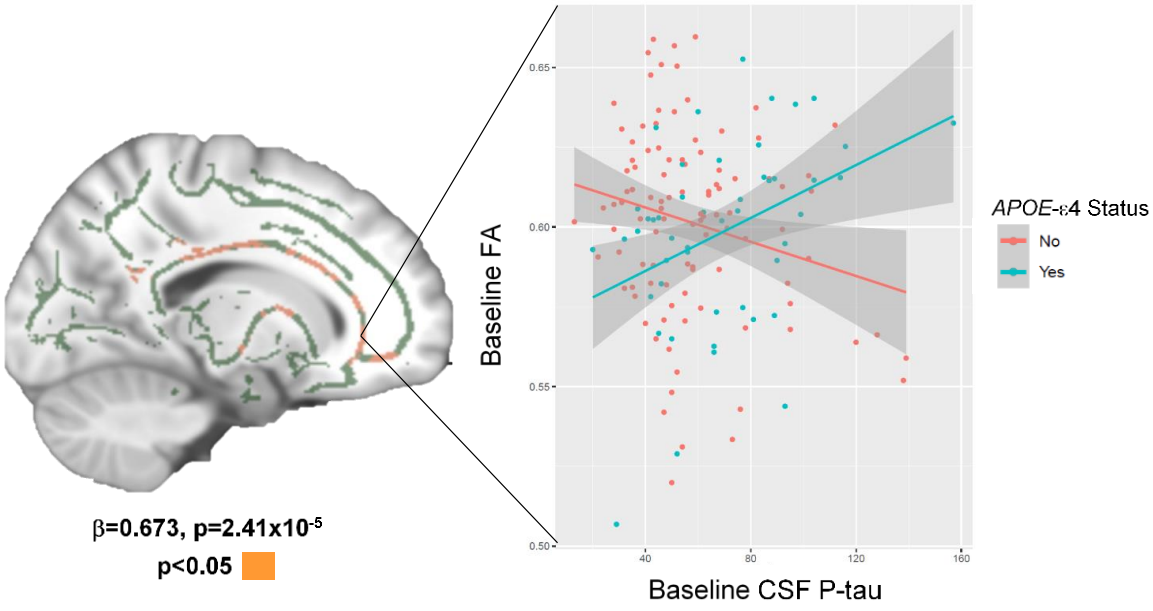

Figure 4.2. Cross-Sectional CSF P-tau x *APOE*-ε4 Status Interactions on FA. Mean skeleton shows regions where CSF p-tau interacts with *APOE*-ε4 status on FA. Scatterplot shows least squares regression relating CSF p-tau values for every participant to mean diffusivity values in one specific cluster. Parametric p-value and β listed only represent the cluster displayed here. Image taken at z=112. APOE=apolipoprotein E; CSF=cerebrospinal fluid; FA=fractional anisotropy; P-tau=phosphorylated tau.

Table 4.1. Longitudinal Region Specific CSF P-tau Associations with DTI Metrics

	Anatomical Region	Hemisphere	Volume (mm^3)	Cluster Statistics		Corrected p-value†	MNI Coordinate‡		
				β	p-value*				
Fractional Anisotropy	Anterior Corona Radiata	Right	132	-9.40×10^{-5}	**1.12×10^{-7}**	0.0005	20	27	23
	Superior Corona Radiata	Left	102	-9.90×10^{-5}	**4.13×10^{-6}**	0.0047	-19	-5	34
Mean Diffusivity	Straight Gyrus	Left	72	1.21×10^{-7}	**3.37×10^{-7}**	0.005	-10	29	-16
	Superior Parietal Lobule	Left	63	1.02×10^{-7}	**9.01×10^{-6}**	0.014	-20	-38	39
Radial Diffusivity	Genu of the Corpus Callosum	Left	73	1.13×10^{-7}	**2.00×10^{-6}**	0.0078	-16	31	23
	Straight Gyrus	Left	57	1.17×10^{-7}	**2.35×10^{-6}**	0.045	-10	29	-16
Axial Diffusivity	External Capsule	Left	65	2.06×10^{-7}	**9.49×10^{-10}**	0.01	-24	18	11
	Inferior Fronto-occipital Fasciculus	Right	59	1.86×10^{-7}	**2.39×10^{-9}**	0.02	25	19	-9

Note. Bold values indicate p-values that remain significant after excluding outliers. *parametric p-values were calculated using linear mixed effects models to relate baseline CSF p-tau and raw DTI values extracted from each participant skeleton; †p-value has been corrected for multiple comparisons; ‡coordinates and region represent the location of the minimum p-value for each cluster; CSF=cerebrospinal fluid; DTI=diffusion tensor imaging; MNI=Montreal Neurological Institute; P-tau=phosphorylated tau.

Table 4.2. Longitudinal Region Specific CSF P-tau x Diagnosis Interactions on DTI Metrics

	Anatomical Region	Hemisphere	Volume (mm^3)	Cluster Statistics		Corrected p-value†	MNI Coordinate‡		
				β	p-value*				
Fractional Anisotropy	--	--	--	--	--	--	--	--	--
Mean Diffusivity	--	--	--	--	--	--	--	--	--
Radial Diffusivity	--	--	--	--	--	--	--	--	--

Axial Diffusivity	Superior Parietal Lobule	Right	59	$3.86x10^{-7}$	**$1.40x10^{-6}$**	0.021	19	-46	40
	Anterior Corona Radiata	Left	57	$4.32x10^{-7}$	**$4.00x10^{-5}$**	0.027	-20	31	18

Note. Bold values indicate p-values that remain significant after excluding outliers. Empty rows indicate no significant clusters for that metric. *parametric p-values were calculated using linear mixed effects models to relate baseline CSF p-tau and raw DTI values extracted from each participant skeleton; †p-value has been corrected for multiple comparisons; ‡coordinates and region represent the location of the minimum p-value for each cluster; CSF=cerebrospinal fluid; DTI=diffusion tensor imaging; MNI=Montreal Neurological Institute; P-tau=phosphorylated tau.

Table 4.3. Cross-Sectional Region Specific CSF P-tau x *APOE*-ε4 Status Interactions on DTI Metrics

	Anatomical Region	**Hemisphere**	**Volume (mm^3)**	**Cluster Statistics**		**Corrected p-value†**	**MNI Coordinate‡**		
				β	**p-value***				
Fractional Anisotropy	Genu of the Corpus Callosum	Left	4355	0.673	**$2.41x10^{-5}$**	0.02	-4	26	10
	Posterior Corona Radiata	Left	1944	0.706	**$2.62x10^{-5}$**	0.038	-26	-42	23
	Superior Parietal Lobule	Right	1051	0.683	**$3.92x10^{-5}$**	0.032	31	-33	39
	Posterior Corona Radiata	Right	907	0.589	**$6.98x10^{-4}$**	0.046	30	-41	19
	Cingulum Gyrus	Right	471	0.683	**5.59x10-5**	0.045	20	-47	15
	Splenium of the Corpus Callosum	Left	112	0.585	**$7.12x10^{-4}$**	0.046	-2	-37	10
	Superior Temporal Gyrus	Left	45	0.554	**$9.04x10^{-4}$**	0.049	-47	-45	22
	Anterior Corona Radiata	Right	17	0.445	**$9.24x10^{-3}$**	0.049	14	42	-15
	Superior Longitudinal Fasciculus	Left	13	0.671	**$1.11x10^{-4}$**	0.049	-35	-27	35
	Splenium of the Corpus Callosum	Left	4	0.413	**0.02**	0.05	-17	-45	10
	Splenium of the Corpus Callosum	Right	2	0.380	**0.03**	0.05	12	-29	26
	Cingulum Gyrus	Right	2	0.293	0.11	0.05	36	-39	30

	Splenium of the Corpus Callosum	Right	1	0.445	**0.01**	0.05	8	-39	14
	Superior Longitudinal Fasciculus	Right	1	0.276	0.13	0.05	35	-39	32
Mean Diffusivity	--	--	--	--	--	--	--	--	--
Radial Diffusivity	--	--	--	--	--	--	--	--	--
Axial Diffusivity	--	--	--	--	--	--	--	--	--

Note. Bold values indicate p-values that remain significant after excluding outliers. Empty rows indicate no significant clusters for that metric. *parametric p-values were calculated using linear regression models to relate baseline *CSF p-tau x APOE-ε4 status* and raw DTI values extracted from each participant skeleton; †p-value has been corrected for multiple comparisons; ‡coordinates and region represent the location of the minimum p-value for each cluster; APOE=apolipoprotein; CSF=cerebrospinal fluid; DTI=diffusion tensor imaging; MNI=Montreal Neurological Institute; P-tau=phosphorylated tau.

T-tau Analyses

T-tau & DTI Metrics

In the whole sample, CSF t-tau was not cross-sectionally associated with DTI metrics (corrected p-values>0.15). However, higher levels of baseline CSF t-tau were associated with faster decline in white matter integrity over time (**Table 4.4, Figure 4.3**). Specifically, higher baseline CSF t-tau was associated with a greater decline in FA over time primarily in the corona radiata (corrected p-values<0.009). Higher baseline CSF t-tau was associated with a greater increase in mean, radial, and axial diffusivity over time, particularly in superior parietal lobule, anterior corona radiata, and medial orbital gyrus (corrected p-values<0.02). These associations persisted when removing outliers (**Table 4.4**).

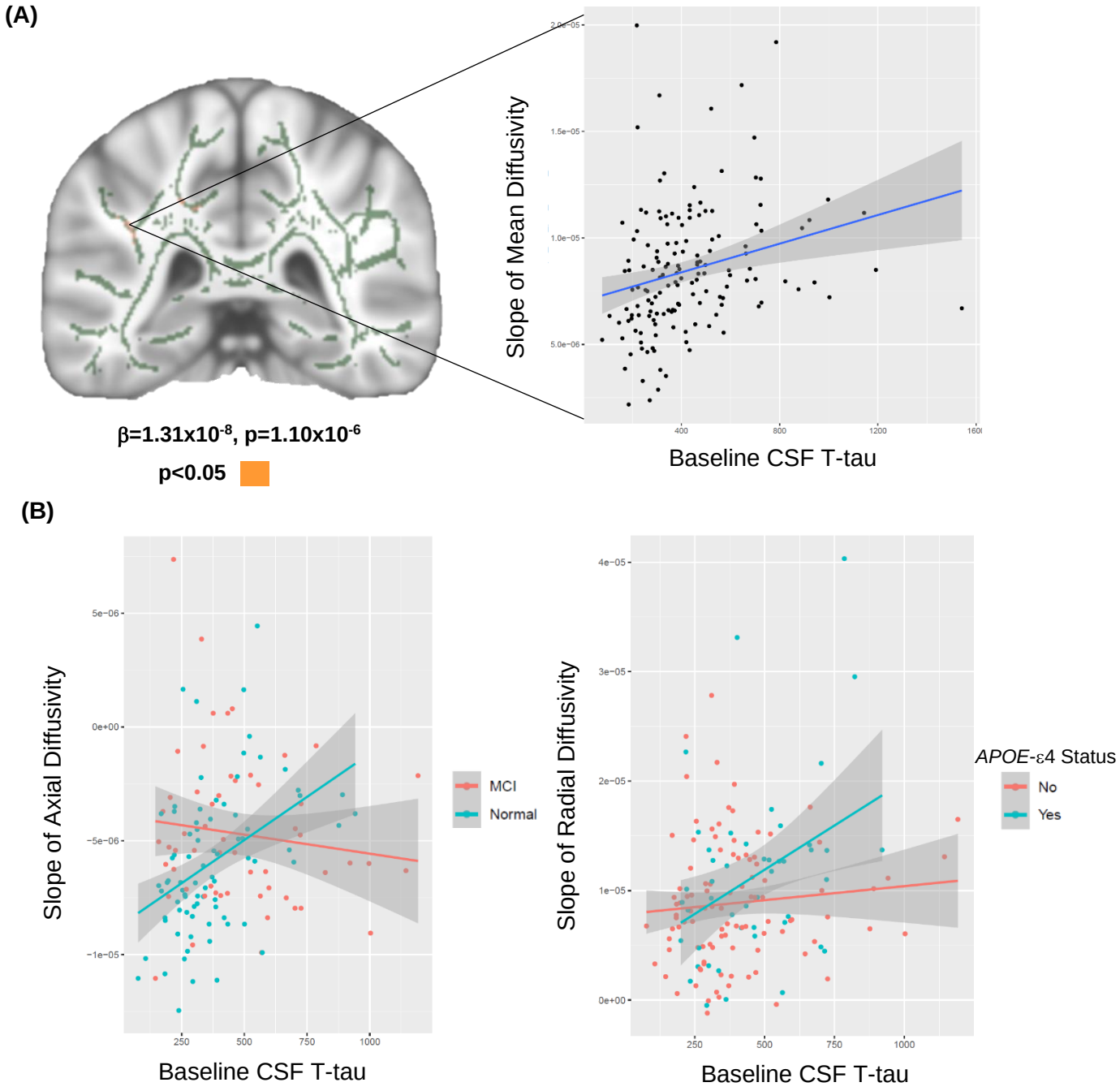

Figure 4.3. Baseline CSF T-tau and Longitudinal DTI Trajectory Associations. **(A)** Mean skeleton shows regions where baseline CSF t-tau is associated with a faster increase in mean diffusivity over time. Scatterplot shows a linear mixed effects model relating baseline CSF t-tau values for every participant to the slope of mean diffusivity values in one specific cluster. Parametric p-value and β listed only represent the cluster displayed here. Image taken at z=112. **(B)** *CSF t-tau x diagnosis* interaction on axial diffusivity trajectory ($\beta=4.68x10^{-8}$, $p=3.21x10^{-6}$) and *CSF t-tau x APOE-ε4 status* interaction on radial diffusivity trajectory ($\beta=5.80x10^{-8}$, $p=7.33x10^{-6}$). Scatterplots show interactions at one specific cluster. Parametric p-value and β listed only represent the cluster displayed here. APOE=apolipoprotein E; CSF=cerebrospinal fluid; DTI=diffusion tensor imaging; MCI=mild cognitive impairment; T-tau=total tau.

T-tau x Diagnosis Interactions & DTI Metrics

In cross-sectional analyses, CSF t-tau did not interact with diagnosis on DTI metrics (corrected p-values>0.06). However, in longitudinal analyses, baseline CSF t-tau did interact with diagnosis in one small cluster on the trajectory of axial diffusivity (**Table 4.5, Figure 4.3**) in the superior parietal lobule (corrected p-value=0.03). Stratification revealed that in this cluster, the association between higher baseline CSF t-tau and faster decline in white matter integrity was present in participants with NC, but the association was null in participants with MCI. Clusters remained significant when removing outliers (**Table 4.5**).

T-tau x APOE-ε4 Interactions & DTI Metrics

In cross-sectional analyses, CSF t-tau interacted with *APOE*-ε4 status on FA (corrected p-values<0.05, **Table 4.6, Figure 4.4**) primarily in the genu of the corpus callosum. Stratification revealed that in all clusters, associations between lower CSF t-tau levels and compromised white matter integrity were present in *APOE*-ε4 positive participants, but associations were reversed in *APOE*-ε4 negative participants. Associations persisted when removing outliers (**Table 4.6**).

In longitudinal analyses, CSF t-tau interacted with *APOE*-ε4 status in a small cluster on mean diffusivity (corrected p-value=0.036) and in a small cluster on radial diffusivity (corrected p-value=0.015, **Table 4.7, Figure 4.3**) in the precuneus. Stratification revealed that in both clusters, associations between higher baseline CSF t-tau levels and faster decline in white matter integrity were present by *APOE*-ε4 positive

participants, but associations were null in *APOE*-ε4 negative participants. One cluster remained significant when removing outliers (**Table 4.7**).

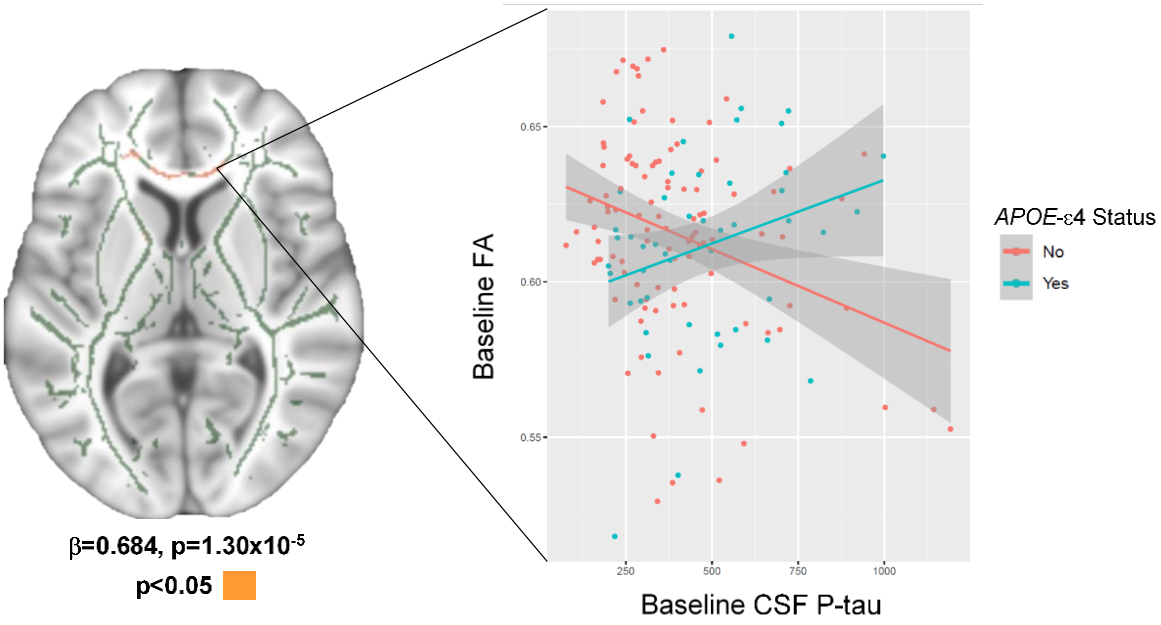

Figure 4.4. Cross-Sectional CSF T-tau x *APOE*-ε4 Status Interactions on FA. Mean skeleton shows regions where CSF t-tau interacts with *APOE*-ε4 status on FA. Scatterplot shows least squares regression relating CSF t-tau values for every participant to mean diffusivity values in one specific cluster. Parametric p-value and β listed only represent the cluster displayed here. Image taken at z=79. APOE=apolipoprotein E; CSF=cerebrospinal fluid; FA=fractional anisotropy; T-tau=total tau.

Table 4.4. Longitudinal Region Specific CSF T-tau Associations with DTI Metrics

	Anatomical Region	Hemisphere	Volume (mm^3)	Cluster Statistics		Corrected p-value†	MNI Coordinate‡		
				β	p-value*				
Fractional Anisotropy	Anterior Corona Radiata	Right	121	$-1.2x10^{-5}$	**$8.55x10^{-8}$**	0.0011	20	27	23
	Superior Corona Radiata	Left	111	$-1.2x10^{-5}$	**$1.34x10^{-6}$**	0.0024	-21	-12	38
	Anterior Corona Radiata	Left	94	$-1.1\ x10^{-5}$	**$9.13\ x10^{-7}$**	0.0089	-22	35	10
Mean Diffusivity	Superior Parietal Lobule	Left	77	$1.31x10^{-8}$	**$1.10x10^{-6}$**	0.0029	-20	-47	48
	Medial Orbital Gyrus	Left	77	$1.51x10^{-8}$	**$2.47x10^{-7}$**	0.0029	-10	29	-16
	Superior Longitudinal Fasciculus	Left	68	$1.22x10^{-8}$	**$2.93x10^{-8}$**	0.0078	-37	-40	26
	External Capsule	Right	59	$1.84x10^{-8}$	**$2.61x10^{-5}$**	0.022	31	3	12
Radial Diffusivity	Anterior Corona Radiata	Left	98	$1.41x10^{-8}$	**$3.62x10^{-7}$**	0.00064	-16	31	23
	Medial Orbital Gyrus	Left	78	$1.46x10^{-8}$	**$7.54x10^{-7}$**	0.0047	-10	29	-16
	Angular Gyrus	Left	74	$1.89x10^{-8}$	**$1.18x10^{-7}$**	0.0071	-33	-54	29
Axial Diffusivity	External Capsule	Left	71	$2.62x10^{-8}$	**$4.01x10^{-11}$**	0.005	-24	18	11
	Insular Gyrus	Right	61	$2.59x10^{-8}$	**$2.89x10^{-6}$**	0.016	32	-1	11

Note. Bold values indicate p-values that remain significant after excluding outliers. *parametric p-values were calculated using linear mixed effects models to relate baseline CSF t-tau and raw DTI values extracted from each participant skeleton; †p-value has been corrected for multiple comparisons; ‡coordinates and region represent the location of the minimum p-value for each cluster; CSF=cerebrospinal fluid; DTI=diffusion tensor imaging; MNI=Montreal Neurological Institute; T-tau=total tau.

Table 4.5. Longitudinal Region Specific CSF T-tau x Diagnosis Interactions on DTI Metrics

	Anatomical Region	Hemisphere	Volume (mm^3)	Cluster Statistics		Corrected p-value†	MNI Coordinate‡		
				β	p-value*				
Fractional Anisotropy	--	--	--	--	--	--	--	--	--
Mean Diffusivity	--	--	--	--	--	--	--	--	--
Radial Diffusivity	--	--	--	--	--	--	--	--	--
Axial Diffusivity	Superior Parietal Lobule	Right	56	$4.68x10^{-8}$	**$3.21x10^{-6}$**	0.03	16	-40	39

Note. Bold values indicate p-values that remain significant after excluding outliers. Empty rows indicate no significant clusters for that metric. *parametric p-values were calculated using linear mixed effects models to relate baseline CSF t-tau and raw DTI values extracted from each participant skeleton; †p-value has been corrected for multiple comparisons; ‡coordinates and region represent the location of the minimum p-value for each cluster; CSF=cerebrospinal fluid; DTI=diffusion tensor imaging; MNI=Montreal Neurological Institute; T-tau=total tau.

Table 4.6. Cross-Sectional Region Specific CSF T-tau x *APOE*-ε4 Status Interactions on DTI Metrics

	Anatomical Region	Hemisphere	Volume (mm^3)	Cluster Statistics		Corrected p-value†	MNI Coordinate‡		
				β	p-value*				
Fractional Anisotropy	Genu of the Corpus Callosum	Left	1686	0.684	**$1.30x10^{-5}$**	0.033	-4	26	11
	Anterior Limb of the Internal Capsule	Left	64	0.754	**$1.24x10^{-5}$**	0.046	-15	6	7
Mean Diffusivity	--	--	--	--	--	--	--	--	--
Radial Diffusivity	--	--	--	--	--	--	--	--	--
Axial Diffusivity	--	--	--	--	--	--	--	--	--

Note. Bold values indicate p-values that remain significant after excluding outliers. Empty rows indicate no significant clusters for that metric. *parametric p-values were calculated using linear regression models to relate baseline *CSF t-tau x APOE-ε4 status* and raw DTI values extracted from each participant skeleton; †p-

value has been corrected for multiple comparisons; ‡coordinates and region represent the location of the minimum p-value for each cluster; APOE=apolipoprotein; CSF=cerebrospinal fluid; DTI=diffusion tensor imaging; MNI=Montreal Neurological Institute; T-tau=total tau.

Table 4.7. Longitudinal Region Specific CSF T-tau x *APOE*-ε4 Status Interactions on DTI Metrics

	Anatomical Region	Hemisphere	Volume (mm^3)	Cluster Statistics		Corrected p-value†	MNI Coordinate‡		
				β	p-value*				
Fractional Anisotropy	--	--	--	--	--	--	--	--	--
Mean Diffusivity	Precuneus	Right	55	$5.25x10^{-8}$	0.00024	0.036	11	-48	45
Radial Diffusivity	Precuneus	Right	67	$5.80x10^{-8}$	**$7.33x10^{-6}$**	0.015	11	-48	45
Axial Diffusivity	--	--	--	--	--	--	--	--	--

Note. Bold values indicate p-values that remain significant after excluding outliers. Empty rows indicate no significant clusters for that metric. *parametric p-values were calculated using linear mixed effects models to relate baseline *CSF t-tau x APOE-ε4 status* and raw DTI values extracted from each participant skeleton; †p-value has been corrected for multiple comparisons; ‡coordinates and region represent the location of the minimum p-value for each cluster; APOE=apolipoprotein; CSF=cerebrospinal fluid; DTI=diffusion tensor imaging; MNI=Montreal Neurological Institute; T-tau=total tau.

NFL Analyses

NFL & DTI Metrics

In the whole sample, CSF NFL was cross-sectionally associated with DTI metrics (corrected p-values<0.05, **Table 4.8, Figure 4.5**). Specifically, higher CSF NFL was associated with lower FA in internal capsule and middle frontal gyrus,

and higher mean, radial, and axial diffusivity in the posterior thalamic radiation, superior frontal gyrus, and superior temporal gyrus. Significance persisted when removing outliers (**Table 4.8**).

In longitudinal models, higher levels of baseline CSF NFL were associated with faster decline in white matter integrity over time (**Table 4.9, Figure 4.6**). Specifically, higher baseline CSF NFL was associated with a greater decline in FA over time primarily in the precentral gyrus and inferior frontal gyrus (corrected p-values<0.05). Higher baseline CSF NFL was associated with a greater increase in mean, radial, and axial diffusivity over time, particularly in the postcentral gyrus, lateral occipital gyrus, superior parietal lobule, and insular gyrus (corrected p-values<0.04). These associations persisted when removing outliers (**Table 4.9**).

Table 4.8. Cross-Sectional Region Specific CSF NFL Associations with DTI Metrics

	Anatomical Region	Hemisphere	Volume (mm^3)	Cluster Statistics		Corrected p-value†	MNI Coordinate‡		
				β	p-value*				
Fractional Anisotropy	Retrolenticular Part of the Internal Capsule	Left	4912	-0.431	**$3.13x10^{-7}$**	0.025	-30	-30	7
	Striatum	Right	3875	-0.465	**$5.50x10^{-9}$**	0.01	41	-35	-12
	Middle Frontal Gyrus	Right	409	-0.381	**$1.58x10^{-5}$**	0.038	26	28	24
	Superior Frontal Gyrus	Left	343	-0.455	**$8.78x10^{-9}$**	0.046	-14	39	32
Mean Diffusivity	Posterior Thalamic Radiation	Right	23032	0.401	**$5.86x10^{-7}$**	0.008	38	-34	0
	Superior Frontal Gyrus	Left	17683	0.415	**$3.28x10^{-7}$**	0.02	-15	41	30
Radial Diffusivity	Superior Temporal Gyrus	Right	21444	0.391	**$7.67x10^{-7}$**	0.008	38	-33	-1

	Middle Temporal Gyrus	Left	17727	0.407	**3.95×10^{-7}**	0.02	-39	-45	-3
Axial Diffusivity	Anterior Corona Radiata	Right	33039	0.550	**1.94×10^{-11}**	0.003	13	40	-16
	Inferior Frontal Gyrus	Right	158	0.485	**3.30×10^{-8}**	0.047	33	25	-12

Note. Bold values indicate p-values that remain significant after excluding outliers. *parametric p-values were calculated using linear regressions to relate baseline CSF NFL and raw DTI values extracted from each participant skeleton; †p-value has been corrected for multiple comparisons; ‡coordinates and region represent the location of the minimum p-value for each cluster; CSF=cerebrospinal fluid; DTI=diffusion tensor imaging; MNI=Montreal Neurological Institute; NFL=neurofilament light.

Table 4.9. Longitudinal Region Specific CSF NFL Associations with DTI Metrics

	Anatomical Region	Hemisphere	Volume (mm^3)	Cluster Statistics		Corrected p-value†	MNI Coordinate‡		
				β	p-value*				
Fractional Anisotropy	Precentral Gyrus	Left	273	-3.90×10^{-6}	**2.91×10^{-8}**	7.21×10^{-8}	-16	-15	53
	Inferior Frontal Gyrus	Right	223	-4.80×10^{-6}	**4.16×10^{-7}**	1.32×10^{-6}	27	31	0
	Postcentral Gyrus	Right	194	-3.60×10^{-6}	**1.64×10^{-8}**	7.87×10^{-6}	19	-30	52
	Superior Frontal Gyrus	Right	182	-4.20×10^{-6}	**4.82×10^{-8}**	1.69×10^{-5}	20	-9	45
	Superior Parietal Lobule	Right	178	-4.20×10^{-6}	**8.51×10^{-8}**	2.19×10^{-5}	20	-47	46
	Body of the Corpus Callosum	Right	178	-4.20×10^{-6}	**4.72×10^{-10}**	2.19×10^{-5}	16	6	32
	Inferior Frontal Gyrus	Left	128	-4.10×10^{-6}	**9.91×10^{-9}**	0.00067	-26	35	1
	Anterior Corona Radiata	Right	109	-4.40×10^{-6}	**7.35×10^{-6}**	0.0027	18	41	-7
	Middle Frontal Gyrus	Right	102	-3.80×10^{-6}	**1.05×10^{-9}**	0.0047	26	15	30
	Superior Parietal Lobule	Left	86	-4.40×10^{-6}	**7.57×10^{-6}**	0.017	-20	-53	38
	Post limb of intern capsule	Left	74	-4.60×10^{-6}	**1.25×10^{-5}**	0.046	-21	-17	0

Mean Diffusivity	Postcentral Gyrus	Left	1406	$5.31x10^{-9}$	**$1.04x10^{-11}$**	$8.42 x10^{-39}$	-25	-33	42
	Superior Parietal Lobule	Right	849	$5.87x10^{-9}$	**$1.09x10^{-12}$**	$6.30x10^{-28}$	28	-33	42
	Insular Gyrus	Right	707	$7.38x10^{-9}$	**$2.59x10^{-12}$**	$8.39x10^{-25}$	31	-13	13
	Middle Frontal Gyrus	Left	551	$5.58x10^{-9}$	**$2.35x10^{-15}$**	$4.08x10^{-21}$	-31	4	34
	Insular Gyrus	Left	404	$9.00x10^{-9}$	**$2.28x10^{-13}$**	$2.38x10^{-14}$	-31	-7	11
	Angular Gyrus	Left	290	$5.35x10^{-9}$	**$2.31x10^{-13}$**	$4.62x10^{-11}$	-43	-44	31
	Middle Frontal Gyrus	Left	276	$7.31x10^{-9}$	**$1.20x10^{-15}$**	$1.25x10^{-10}$	-41	26	29
	Superior Parietal Lobule	Left	229	$6.54x10^{-9}$	**$1.02x10^{-11}$**	$3.99x10^{-9}$	-18	-60	43
	Inferior Frontal Gyrus	Left	199	$5.95x10^{-9}$	**$5.23x10^{-15}$**	$4.12x10^{-8}$	-32	39	5
	Precentral Gyrus	Right	182	$5.70x10^{-9}$	**$5.51x10^{-9}$**	$1.63x10^{-7}$	28	-20	51
	Insular gyrus	Left	175	$7.27x10^{-9}$	**$1.20x10^{-10}$**	$2.91x10^{-7}$	-31	7	-9
	Body of the Corpus Callosum	Right	161	$6.88x10^{-9}$	**$1.21x10^{-7}$**	$9.50x10^{-7}$	15	-14	32
	Inferior Temporal Gyrus	Left	159	$1.83x10^{-8}$	**$1.80x10^{-8}$**	$1.13x10^{-6}$	-33	-3	-30
	Cingulum Bundle	Left	152	$6.11x10^{-9}$	**$7.44x10^{-10}$**	$2.07x10^{-6}$	-9	-24	33
	Middle Frontal Gyrus	Right	117	$5.60x10^{-9}$	**$6.43x10^{-11}$**	$5.00x10^{-5}$	32	35	21
	Superior Corona Radiata	Right	111	$4.92x10^{-9}$	**$3.60x10^{-6}$**	$8.89x10^{-5}$	24	-13	35
	External Capsule	Left	104	$7.45x10^{-9}$	**$7.35x10^{-9}$**	0.00018	-27	12	8
	Lateral Occipital Gyrus	Left	102	$9.37x10^{-9}$	**$3.16x10^{-13}$**	0.00022	-33	-58	28
	Superior Frontal Gyrus	Left	102	$4.95x10^{-9}$	**$4.98x10^{-7}$**	0.00022	-18	16	40
	Middle Frontal Gyrus	Left	100	$5.50x10^{-9}$	**$2.25x10^{-6}$**	0.00026	-23	23	28
	External Capsule	Right	100	$5.71x10^{-9}$	**$1.67x10^{-5}$**	0.00026	22	-10	9

Inferior Frontal Gyrus	Right	99	5.41×10^{-9}	**1.18×10^{-8}**	0.00029	33	6	30
Cerebral Peduncle	Left	91	1.13×10^{-8}	**5.85×10^{-7}**	0.00066	-14	-22	-14
Cerebral Peduncle	Left	87	9.83×10^{-9}	**4.40×10^{-9}**	0.001	-9	-22	-16
Midbrain	Right	84	2.05×10^{-8}	**5.41×10^{-7}**	0.0014	5	-19	-9
Superior Frontal Gyrus	Right	82	6.31×10^{-9}	**1.03×10^{-11}**	0.0017	17	24	42
Body of the Corpus Callosum	Left	81	9.61×10^{-9}	**2.28×10^{-9}**	0.0019	-1	11	21
Thalamus	Left	81	8.43×10^{-9}	**3.15×10^{-11}**	0.0019	-8	-18	6
Superior Parietal Lobule	Left	77	5.38×10^{-9}	**7.34×10^{-7}**	0.0029	-20	-46	47
Splenium of the Corpus Callosum	Left	76	9.55×10^{-9}	**1.28×10^{-5}**	0.0033	-23	-52	17
Posterior Limb of the Internal Capsule	Left	72	7.59×10^{-9}	**2.51×10^{-8}**	0.0051	-11	-6	5
Retrolenticular Part of the Internal Capsule	Left	70	7.67×10^{-9}	**1.91×10^{-8}**	0.0063	-27	-22	15
Cingulum Bundle	Left	69	6.78×10^{-9}	**3.90×10^{-8}**	0.0071	-18	-41	30
Middle Temporal Gyrus	Right	68	7.42×10^{-9}	**3.16×10^{-10}**	0.0079	50	-55	16
Body of the Corpus Callosum	Right	66	7.91×10^{-9}	**3.94×10^{-7}**	0.01	4	-1	26
Posterior Limb of the Internal Capsule	Right	65	1.09×10^{-8}	**1.96×10^{-6}**	0.011	10	-7	5
Inferior Frontal Gyrus	Left	60	7.84×10^{-9}	**1.08×10^{-11}**	0.02	-35	39	16
Fornix	Left	59	2.85×10^{-8}	**1.76×10^{-6}**	0.023	-21	-33	5
Postcentral Gyrus	Left	58	6.66×10^{-9}	**3.27×10^{-10}**	0.025	-44	-18	32
Superior Frontal Gyrus	Left	57	5.45×10^{-9}	**1.48×10^{-10}**	0.029	-16	-15	53
Superior Parietal Lobule	Left	56	6.30×10^{-9}	**5.57×10^{-7}**	0.032	-19	-52	35

	Angular Gyrus	Left	55	$5.99x10^{-9}$	**$1.15x10^{-9}$**	0.036	-30	-54	34
	Inferior Frontal Gyrus	Right	55	$4.78x10^{-9}$	**$1.92x10^{-8}$**	0.036	38	32	12
	Poster Limb of the Internal Capsule	Left	54	$4.89x10^{-9}$	**$6.14x10^{-6}$**	0.041	-23	-9	14
	Inferior Frontal Gyrus	Right	54	$5.80x10^{-9}$	**$6.71x10^{-7}$**	0.041	29	28	-10
Radial Diffusivity	Lateral Occipital Gyrus	Left	2082	$5.77x10^{-9}$	**$2.79x10^{-15}$**	$9.01x10^{-48}$	-33	-58	28
	Superior Parietal Lobule	Right	1714	$5.90x10^{-9}$	**$2.46x10^{-13}$**	$4.74x10^{-42}$	20	-47	46
	Insular Gyrus	Right	1107	$7.46x10^{-9}$	**$3.09x10^{-12}$**	$1.33x10^{-31}$	31	-13	13
	Precuneus	Left	451	$6.74x10^{-9}$	**$3.47x10^{-10}$**	$9.33x10^{-15}$	-18	-52	28
	Precentral Gyrus	Left	440	$5.83x10^{-9}$	**$2.00x10^{-14}$**	$1.75x10^{-14}$	-35	1	30
	Insular Gyrus	Left	414	$9.01x10^{-9}$	**$7.53x10^{-12}$**	$8.13x10^{-14}$	-32	-7	8
	Inferior Fronto-Occipital Fasciculus	Left	321	$6.08x10^{-9}$	**$1.16x10^{-14}$**	$2.57x10^{-11}$	-18	21	-7
	Middle Frontal Gyrus	Left	291	$7.30x10^{-9}$	**$1.31x10^{-13}$**	$1.85x10^{-10}$	-41	26	29
	Middle Temporal Gyrus	Left	278	$1.39\ x10^{-8}$	**$1.40x10^{-9}$**	$4.43x10^{-10}$	-40	1	-26
	Superior Frontal Gyrus	Left	229	$5.39x10^{-9}$	**$8.13x10^{-8}$**	$1.37x10^{-8}$	-17	10	47
	Retrolenticular Part of the Internal Capsule	Left	207	$6.26x10^{-9}$	**$3.11x10^{-8}$**	$6.92x10^{-8}$	-27	-27	10
	Inferior Fronto-Occipital Fasciculus	Left	200	$7.55x10^{-9}$	**$3.94x10^{-8}$**	$1.17x10^{-7}$	-30	6	-9
	Superior Parietal Lobule	Left	163	$6.33x10^{-9}$	**$1.19x10^{-8}$**	$2.12x10^{-6}$	-20	-45	46
	External Capsule	Left	141	$7.49x10^{-9}$	**$2.45x10^{-8}$**	$1.32x10^{-5}$	-27	17	2
	Cerebral Peduncle	Left	139	$9.77x10^{-9}$	**$8.33x10^{-8}$**	$1.57x10^{-5}$	-13	-25	-15
	Middle Frontal Gyrus	Left	138	$5.62x10^{-9}$	**$1.11x10^{-6}$**	$1.71x10^{-5}$	-23	23	28
	Body of the Corpus Callosum	Left	133	$9.21x10^{-9}$	**$2.76x10^{-9}$**	$2.62x10^{-5}$	-3	14	20

Cingulum Bundle	Left	126	$6.28x10^{-9}$	**$9.49x10^{-10}$**	$4.84x10^{-5}$	-8	-16	34
Posterior Limb of the Internal Capsule	Right	117	$1.39x10^{-8}$	**$3.54x10^{-10}$**	0.00011	11	-6	6
Middle Frontal Gyrus	Right	114	$4.74x10^{-9}$	**$1.36x10^{-6}$**	0.00014	19	-3	47
Precentral Gyrus	Left	112	$5.73x10^{-9}$	**$7.51x10^{-10}$**	0.00017	-39	2	22
Body of the Corpus Callosum	Left	103	$8.96x10^{-9}$	**$1.81x10^{-9}$**	0.00040	-4	-14	26
Middle Frontal Gyrus	Left	102	$6.38x10^{-9}$	**$1.18x10^{-11}$**	0.00043	-31	4	34
Middle Frontal Gyrus	Right	97	$6.13x10^{-9}$	**$3.90x10^{-10}$**	0.00070	30	33	22
Middle Temporal Gyrus	Left	90	$9.19x10^{-9}$	**$2.34x10^{-10}$**	0.0014	-51	-11	-22
Inferior Frontal Gyrus	Right	89	$5.54x10^{-9}$	**$1.16x10^{-8}$**	0.0015	33	5	28
Middle Frontal Gyrus	Left	87	$5.23x10^{-9}$	**$9.02x10^{-7}$**	0.0019	-22	43	14
Superior Frontal Gyrus	Right	85	$5.85x10^{-9}$	**$6.98x10^{-10}$**	0.0023	16	22	46
Body of the Corpus Callosum	Right	82	$6.08x10^{-9}$	**$1.87x10^{-7}$**	0.0031	16	23	26
Midbrain	Right	74	$2.12x10^{-8}$	**$2.34x10^{-6}$**	0.0071	5	-19	-9
Midbrain	Left	66	$7.54x10^{-9}$	**$1.02x10^{-6}$**	0.017	-3	-23	-12
Superior Occipital Gyrus	Right	65	$6.19x10^{-9}$	**$3.91x10^{-6}$**	0.019	23	-52	24
Splenium of the Corpus Callosum	Left	64	$6.87x10^{-9}$	**$3.67x10^{-8}$**	0.021	-20	-38	30
Posterior Corona Radiata	Left	64	$6.31x10^{-9}$	**$9.83x10^{-6}$**	0.021	-24	-39	35
Precuneus	Right	64	$6.99x10^{-9}$	**$2.85x10^{-5}$**	0.021	28	-55	20
Angular Gyrus	Right	61	$8.63x10^{-9}$	**$2.84x10^{-16}$**	0.029	38	-60	40
Superior Parietal Lobule	Left	61	$6.42x10^{-9}$	**$5.10x10^{-8}$**	0.029	-24	-47	39

	Posterior Limb of the Internal Capsule	Left	59	$6.99x10^{-9}$	**$1.32x10^{-6}$**	0.036	-11	-6	5
	Posterior Limb of the Internal Capsule	Right	58	$5.69x10^{-9}$	**$2.25x10^{-4}$**	0.040	24	-14	10
Axial Diffusivity	External Capsule	Left	187	$1.24x10^{-8}$	**$1.16x10^{-15}$**	$9.01x10^{-8}$	-33	-4	3
	Inferior Frontal Gyrus	Left	153	$8.48x10^{-9}$	**$5.23x10^{-12}$**	$1.61x10^{-6}$	-33	3	31
	Superior Corona Radiata	Right	70	$1.27x10^{-8}$	**$2.61x10^{-9}$**	0.0058	17	-6	37
	Cerebral Peduncle	Left	69	$1.46x10^{-8}$	**$4.08x10^{-10}$**	0.0065	-7	-21	-16
	Superior Corona Radiata	Left	69	$9.16x10^{-9}$	**$7.27x10^{-6}$**	0.0065	-24	-9	31
	Superior Longitudinal Fasciculus	Right	65	$8.14x10^{-6}$	**$3.36x10^{-7}$**	0.010	29	-27	40
	Inferior Temporal Gyrus	Left	63	$2.53x10^{-8}$	**$5.42x10^{-8}$**	0.013	-33	-4	-30
	Thalamus	Left	61	$3.10x10^{-8}$	**$1.04x10^{-6}$**	0.016	-21	-33	5

Note. Bold values indicate p-values that remain significant after excluding outliers. *parametric p-values were calculated using linear mixed effects models to relate baseline CSF NFL and raw DTI values extracted from each participant skeleton; †p-value has been corrected for multiple comparisons; ‡coordinates and region represent the location of the minimum p-value for each cluster; CSF=cerebrospinal fluid; DTI=diffusion tensor imaging; MNI=Montreal Neurological Institute; NFL=neurofilament light.

Table 4.10. Cross-Sectional Region Specific CSF NFL x Diagnosis Interactions on DTI Metrics

	Anatomical Region	Hemisphere	Volume (mm^3)	Cluster Statistics		Corrected p-value†	MNI Coordinate‡		
				β	p-value*				
Fractional Anisotropy	--	--	--	--	--	--	--	--	--
Mean Diffusivity	--	--	--	--	--	--	--	--	--
Radial Diffusivity	--	--	--	--	--	--	--	--	--

Axial Diffusivity	Posterior Limb of the Internal Capsule	Left	874	1.106	**1.28×10^{-10}**	0.038	-27	-21	16
	Inferior Temporal Gyrus	Left	36	0.867	**1.01×10^{-6}**	0.045	-49	-25	-20

Note. Bold values indicate p-values that remain significant after excluding outliers. Empty rows indicate no significant clusters for that metric. *parametric p-values were calculated using linear regression models to relate baseline *CSF p-tau x diagnosis* and raw DTI values extracted from each participant skeleton; †p-value has been corrected for multiple comparisons; ‡coordinates and region represent the location of the minimum p-value for each cluster; CSF=cerebrospinal fluid; DTI=diffusion tensor imaging; MNI=Montreal Neurological Institute; NFL=neurofilament light.

NFL x Diagnosis Interactions & DTI Metrics

In cross-sectional analyses, CSF NFL interacted with diagnosis on axial diffusivity in two small clusters in internal capsule and inferior temporal gyrus (corrected p-values<0.05, **Table 4.10, Figure 4.5**). Stratification revealed that in all clusters, associations between higher levels of CSF NFL and compromised white matter integrity were present in participants with MCI, but associations were null in participants with NC. Associations remained significant when removing outliers (**Table 4.10**).

In longitudinal analyses, baseline CSF NFL interacted with diagnosis on all 4 DTI metrics (corrected p-values<0.05, **Table 4.11, Figure 4.6**). Specifically, CSF NFL interacted with diagnosis on FA primarily in the superior corona radiata, on mean diffusivity primarily in the postcentral gyrus, on radial diffusivity primarily in the postcentral gyrus, and axial diffusivity in the inferior temporal gyrus. Stratification revealed that in all clusters, associations between higher baseline CSF NFL and faster decline in white matter integrity were present in participants with MCI, but associations were null in participants with NC. Clusters remained significant when removing outliers (**Table 4.11**).

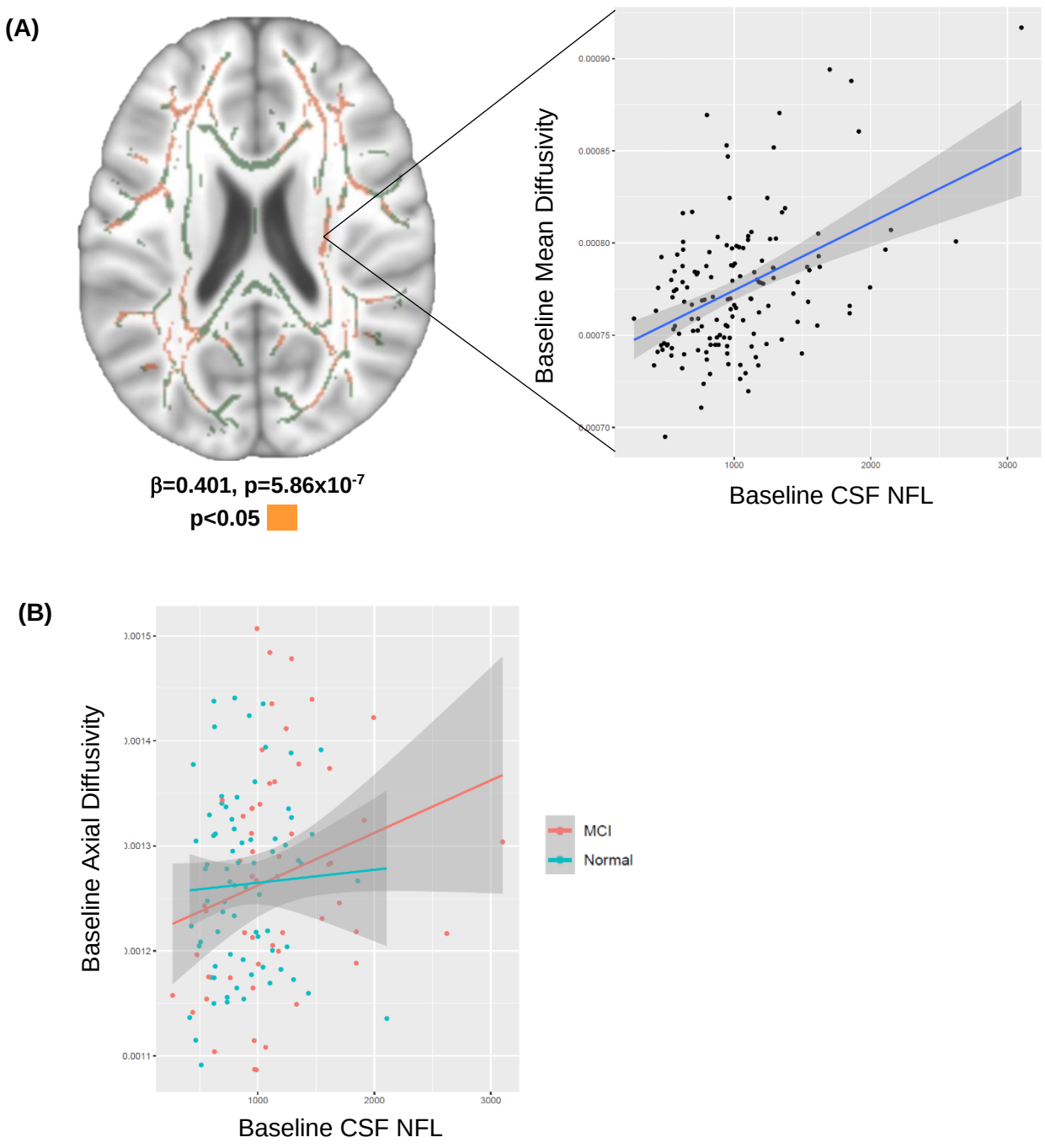

Figure 4.5. Cross-sectional CSF NFL and DTI Metric Associations. **(A)** Mean skeleton shows regions where baseline CSF NFL is associated with mean diffusivity over time. Scatterplot shows a linear regression model relating baseline CSF NFL values for every participant to mean diffusivity values in one specific cluster. Parametric p-value and β listed only represent the cluster displayed here. Image taken at z=94. **(B)** *CSF NFL x diagnosis* interaction on axial diffusivity (β=1.106, p=1.28x10^{-10}). Scatterplots show interactions at one specific cluster. Parametric p-value and β listed only represent the cluster displayed here. CSF=cerebrospinal fluid; DTI=diffusion tensor imaging; MCI=mild cognitive impairment; NFL=neurofilament light.

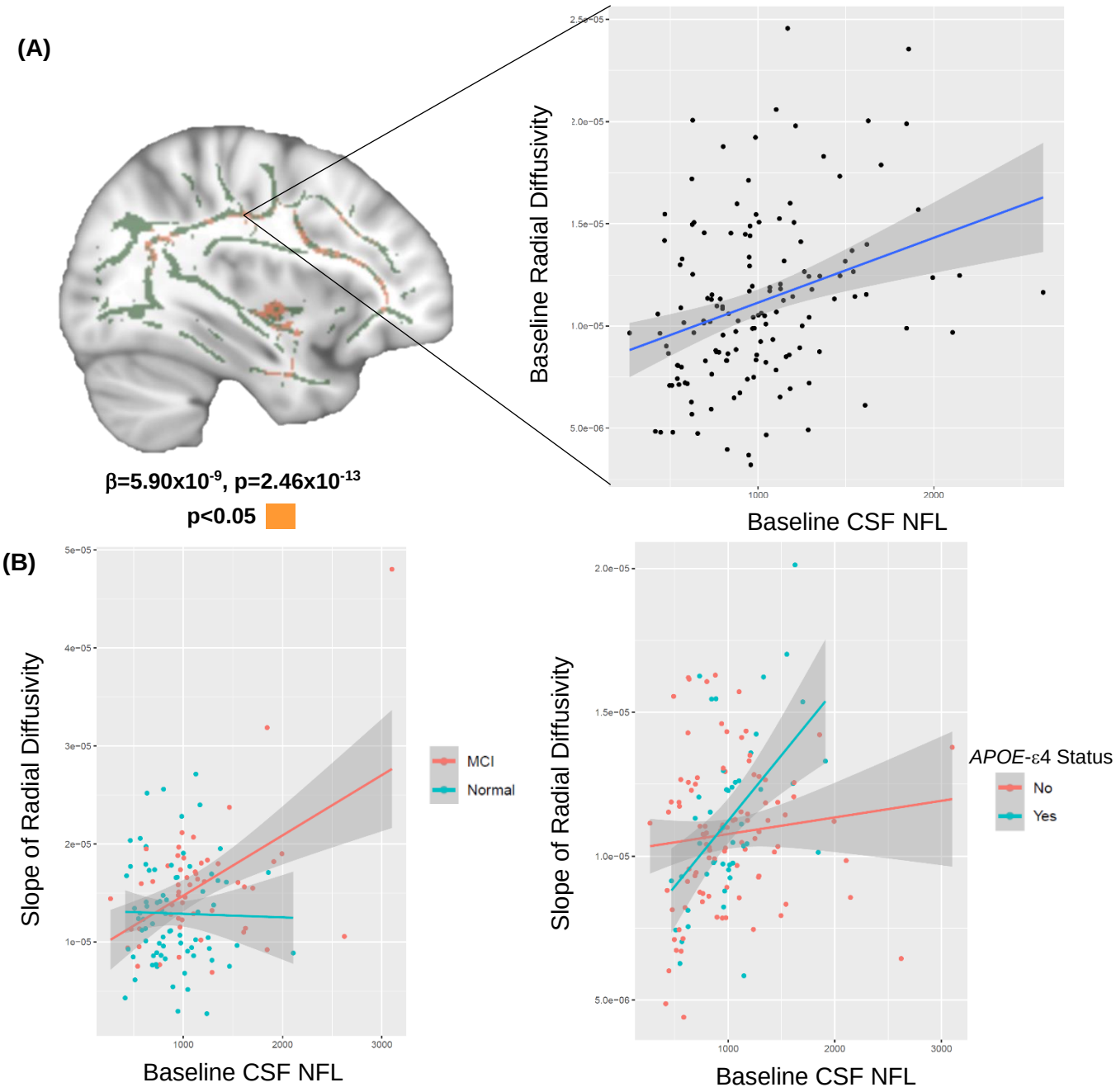

Figure 4.6. Baseline CSF NFL and Longitudinal DTI Trajectory Associations. **(A)** Mean skeleton shows regions where baseline CSF NFL is associated with a faster increase in radial diffusivity over time. Scatterplot shows a linear mixed effects model relating baseline CSF NFL values for every participant to the slope of radial diffusivity values in one specific cluster. Parametric p-value and β listed only represent the cluster displayed here. Image taken at z=73. **(B)** *CSF NFL x diagnosis* interaction on radial diffusivity trajectory (β=-2.40x10^{-8}, p=4.33x10^{-8}) and *CSF t-tau x APOE-ε4 status* interaction on radial diffusivity trajectory (β=2.14x10^{-8}, p=1.02x10^{-21}). Scatterplots show interactions at one specific cluster. Parametric p-value and β listed only represent the cluster displayed here. APOE=apolipoprotein E; CSF=cerebrospinal fluid; DTI=diffusion tensor imaging; MCI=mild cognitive impairment; NFL=neurofilament light.

NFL x APOE-ε4 Interactions & DTI Metrics

In cross-sectional analyses, CSF NFL did not interact with *APOE*-ε4 status on DTI metrics (corrected p-values>0.23). In longitudinal analyses, CSF NFL interacted with *APOE*-ε4 status on mean diffusivity primarily in the precentral gyrus (corrected p-values<0.02) on radial diffusivity primarily in the supramarginal gyrus (corrected p-values<0.05), and on axial diffusivity primarily in the thalamus (corrected p-values<0.003, **Table 4.12, Figure 4.6**). Stratification revealed that in all clusters, associations between higher baseline CSF NFL levels and faster decline in white matter integrity were stronger in *APOE*-ε4 positive participants, though associations were also present in *APOE*-ε4 negative participants. A majority of clusters remained significant when removing outliers (**Table 4.12**).

Table 4.11. Longitudinal Region Specific CSF NFL x Diagnosis Interactions on DTI Metrics

	Anatomical Region	Hemisphere	Volume (mm^3)	Cluster Statistics		Corrected p-value†	MNI Coordinate‡		
				β	p-value*				
Fractional Anisotropy	Superior Corona Radiata	Right	148	$1.10x10^{-5}$	**$2.22x10^{-10}$**	0.00021	17	-16	34
	Thalamus	Right	141	$1.23x10^{-5}$	**$3.05x10^{-7}$**	0.00034	10	-7	7
	Thalamus	Right	133	$1.05x10^{-5}$	$4.80x10^{-6}$	0.00059	22	-10	10
	Postcentral Gyrus	Right	116	$8.35x10^{-6}$	$8.08x10^{-8}$	0.002	22	-33	46
	Insular Gyrus	Right	77	$9.00x10^{-6}$	**$2.65x10^{-7}$**	0.042	30	10	7
Mean Diffusivity	Postcentral Gyrus	Right	313	$-1.10x10^{-8}$	$4.00x10^{-8}$	$1.04x10^{-11}$	28	-28	45

	Posterior Limb of the Internal Capsule	Right	202	-1.20×10^{-8}	**2.02×10^{-5}**	3.51×10^{-8}	22	-11	10
	External Capsule	Right	157	-1.10×10^{-8}	**2.69×10^{-7}**	1.43×10^{-6}	25	23	3
	Inferior Temporal Gyrus	Left	96	-2.80×10^{-8}	**2.18×10^{-6}**	0.00041	-35	-3	-29
	Insular Gyrus	Right	84	-1.20×10^{-8}	**1.02×10^{-8}**	0.0014	24	26	-11
	Inferior Fronto-occipital Fasciculus	Right	78	-1.40×10^{-9}	3.40×10^{-10}	0.0027	20	21	-11
	Posterior Limb of the Internal Capsule	Right	69	-1.90×10^{-8}	3.68×10^{-6}	0.0074	14	-5	-3
	Midbrain	Right	66	-2.10×10^{-8}	**2.18×10^{-7}**	0.01	5	-20	-9
	Superior Frontal Gyrus	Right	63	-1.40×10^{-8}	**6.97×10^{-11}**	0.015	19	36	30
	Superior Longitudinal Fasciculus	Right	63	-8.20×10^{-9}	0.00011	0.015	36	-14	34
	Thalamus	Right	61	-2.90×10^{-8}	**1.52×10^{-10}**	0.018	13	-21	7
	Thalamus	Right	59	-2.10×10^{-8}	**2.97×10^{-7}**	0.023	9	-6	11
	Middle Frontal Gyrus	Right	59	-1.40×10^{-8}	**2.25×10^{-11}**	0.023	33	43	16
	Supramarginal Gyrus	Right	57	-1.20×10^{-8}	**9.02×10^{-8}**	0.03	43	-39	29
Radial Diffusivity	Postcentral Gyrus	Right	396	-1.20×10^{-8}	3.89×10^{-9}	2.82×10^{-13}	28	-28	45
	Inferior Frontal Gyrus	Right	216	-1.20×10^{-8}	1.40×10^{-6}	3.97×10^{-8}	27	32	2
	Posterior Limb of the Internal Capsule	Right	203	-1.20×10^{-8}	**4.50×10^{-6}**	1.04×10^{-7}	22	-10	10
	Inferior Temporal Gyrus	Left	122	-2.50×10^{-8}	**1.72×10^{-6}**	7.47×10^{-5}	-35	-4	-30
	Inferior Fronto-occipital Fasciculus	Right	101	-2.00×10^{-8}	**2.84×10^{-13}**	0.00051	18	21	-11
	Thalamus	Right	99	-2.40×10^{-8}	**4.33×10^{-8}**	0.00062	6	-3	8
	Thalamus	Right	87	-2.60×10^{-8}	**2.07×10^{-10}**	0.002	13	-21	7

	Inferior Frontal Gyrus	Right	85	$-1.20x10^{-8}$	**$1.96x10^{-8}$**	0.0024	35	32	-4
	External Capsule	Right	81	$-1.40x10^{-8}$	$1.48x10^{-6}$	0.0036	28	16	5
	Supramarginal Gyrus	Right	76	$-1.20x10^{-8}$	**$7.80x10^{-8}$**	0.0061	43	-38	28
	Insular Gyrus	Right	64	$-1.40x10^{-8}$	$1.14x10^{-6}$	0.022	34	7	-1
	Superior Frontal Gyrus	Right	61	$-1.30x10^{-8}$	$3.86x10^{-9}$	0.03	19	43	24
	Posterior Thalamic Radiation	Right	58	$-1.80x10^{-8}$	$2.36x10^{-8}$	0.042	37	-53	-1
	Midbrain	Right	58	$-2.00x10^{-8}$	$3.63x10^{-7}$	0.042	5	-25	-10
	Angular Gyrus	Right	57	$-1.20x10^{-8}$	$9.80x10^{-9}$	0.047	33	-58	37
Axial Diffusivity	Inferior Temporal Gyrus	Left	66	$-3.70x10^{-8}$	**$2.16x10^{-7}$**	$9.01x10^{-8}$	-32	-4	-30
	Postcentral Gyrus	Right	53	$-1.30x10^{-8}$	$6.97x10^{-6}$	$1.61x10^{-6}$	28	-28	45

Note. Bold values indicate p-values that remain significant after excluding outliers. Empty rows indicate no significant clusters for that metric. *parametric p-values were calculated using linear mixed effects models to relate baseline *CSF NFL x diagnosis* and raw DTI values extracted from each participant skeleton; †p-value has been corrected for multiple comparisons; ‡coordinates and region represent the location of the minimum p-value for each cluster; CSF=cerebrospinal fluid; DTI=diffusion tensor imaging; MNI=Montreal Neurological Institute; NFL=neurofilament light.

Table 4.12. Longitudinal Region Specific CSF NFL x *APOE*-ε4 Status Interactions on DTI Metrics

	Anatomical Region	**Hemisphere**	**Volume (mm^3)**	**Cluster Statistics**		**Corrected p-value†**	**MNI Coordinate‡**		
				β	**p-value***				
Fractional Anisotropy	--	--	--	--	--	--	--	--	--
Mean Diffusivity	Precentral Gyrus	Right	125	$1.53x10^{-8}$	**$3.57x10^{-8}$**	$2.26x10^{-5}$	30	-9	43
	Supramarginal Gyrus	Right	118	$1.75x10^{-8}$	**$1.98x10^{-12}$**	$4.38x10^{-5}$	45	-40	23
	Thalamus	Left	93	$6.66x10^{-8}$	**$3.14x10^{-8}$**	0.00052	-16	-30	5

	Superior Longitudinal Fasciculus	Right	68	$1.33x10^{-8}$	**$2.59x10^{-7}$**	0.0077	39	-20	31
	Thalamus	Right	62	$9.37x10^{-8}$	**$2.78x10^{-7}$**	0.015	18	-30	7
Radial Diffusivity	Supramarginal Gyrus	Right	280	$2.14x10^{-8}$	**$1.02x10^{-21}$**	$3.62x10^{-10}$	53	-24	26
	Precentral Gyrus	Right	144	$1.50x10^{-8}$	**$3.38x10^{-9}$**	$9.82x10^{-6}$	30	-15	49
	Thalamus	Left	97	$5.83x10^{-8}$	**$7.11x10^{-8}$**	0.00068	-16	-30	5
	Thalamus	Right	64	$8.47x10^{-8}$	**$2.93x10^{-7}$**	0.02	18	-29	6
	Red Nucleus	Right	59	$8.16x10^{-8}$	$5.92x10^{-9}$	0.035	5	-21	-8
	Posterior Thalamic Radiation	Right	59	$2.47x10^{-8}$	$3.05x10^{-9}$	0.035	35	-59	14
	External Capsule	Right	58	$2.04x10^{-8}$	**$5.43x10^{-9}$**	0.039	32	-3	12
	Superior Frontal Gyrus	Right	56	$1.29x10^{-8}$	**$6.21x10^{-7}$**	0.049	18	-8	50
Axial Diffusivity	Thalamus	Left	85	$9.36x10^{-8}$	**$1.32x10^{-9}$**	0.0011	-19	-31	6
	Superior Corona Radiata	Left	75	$-2.30x10^{-8}$	$9.76x10^{-7}$	0.0033	-22	2	19

Note. Bold values indicate p-values that remain significant after excluding outliers. Empty rows indicate no significant clusters for that metric. *parametric p-values were calculated using linear mixed effects models to relate baseline *CSF NFL x APOE-ε4* and raw DTI values extracted from each participant skeleton; †p-value has been corrected for multiple comparisons; ‡coordinates and region represent the location of the minimum p-value for each cluster; APOE=apolipoprotein; CSF=cerebrospinal fluid; DTI=diffusion tensor imaging; MNI=Montreal Neurological Institute; NFL=neurofilament light.

Competitive Models

For the FA cluster in the anterior corona radiata, baseline CSF p-tau was still associated with faster decline in white matter integrity ($p<0.001$) when adjusting for CSF NFL. The addition of CSF p-tau to the model contributed 2.4% of variance beyond covariates and the addition of NFL contributed 0.44%. Together, p-tau and NFL contributed 3.4% of variance beyond covariates. See **Table 4.13**.

For the FA cluster in the superior corona radiata, baseline CSF p-tau was still associated with faster decline in white matter integrity ($p<0.001$) when adjusting for CSF NFL. The addition of CSF p-tau to the model contributed 3.3% of variance beyond covariates and the addition of NFL contributed 3.4%. Together, p-tau and NFL contributed 5.2% of variance beyond covariates. See **Table 4.13**.

For the mean diffusivity cluster in the straight gyrus, baseline CSF p-tau was still associated with faster decline in white matter integrity ($p<0.001$) when adjusting for CSF NFL. The addition of CSF p-tau to the model contributed 4.2% of variance beyond covariates and the addition of NFL contributed 4.2%. Together, p-tau and NFL contributed 6.6% of variance beyond covariates. See **Table 4.13**.

For the mean diffusivity cluster in the superior parietal lobule, baseline CSF p-tau was still associated with faster decline in white matter integrity ($p<0.001$) when adjusting for CSF NFL. The addition of CSF p-tau to the model contributed 1.7% of variance beyond covariates and the addition of NFL contributed 4.6%. Together, p-tau and NFL contributed 6.4% of variance beyond covariates. See **Table 4.13**.

For the radial diffusivity cluster in the genu of the corpus callosum, baseline CSF p-tau was still associated with faster decline in white matter integrity ($p<0.001$) when

adjusting for CSF NFL. The addition of CSF p-tau to the model contributed 1.4% of variance beyond covariates and the addition of NFL contributed 1.1%. Together, p-tau and NFL contributed 2.4% of variance beyond covariates. See **Table 4.13**.

For the radial diffusivity cluster in the straight gyrus, baseline CSF p-tau was still associated with faster decline in white matter integrity ($p<0.001$) when adjusting for CSF NFL. The addition of CSF p-tau to the model contributed 2.5% of variance beyond covariates and the addition of NFL contributed 5.5%. Together, p-tau and NFL contributed 6.5% of variance beyond covariates. See **Table 4.13**.

For the axial diffusivity cluster in the external capsule, baseline CSF p-tau was still associated with faster decline in white matter integrity ($p<0.001$) when adjusting for CSF NFL. The addition of CSF p-tau to the model contributed 2.0% of variance beyond covariates and the addition of NFL contributed 1.3%. Together, p-tau and NFL contributed 3.1% of variance beyond covariates. See **Table 4.13**.

For the axial diffusivity cluster in the inferior fronto-occipital fasciculus, baseline CSF p-tau was still associated with faster decline in white matter integrity ($p<0.001$) when adjusting for CSF NFL. The addition of CSF p-tau to the model contributed 1.6% of variance beyond covariates and the addition of NFL contributed 5.4%. Together, p-tau and NFL contributed 6.3% of variance beyond covariates. See **Table 4.13**.

Table 4.13. Combined Models of CSF Biomarkers in Relation to Longitudinal DTI

	β	**p-value**	**R^2**
FA Cluster 1			
CSF p-tau	-8.70×10^{-5}	**<0.001**	2.4%
CSF NFL	-1.80×10^{-6}	**0.03**	0.4%
FA Cluster 2			

CSF p-tau	$-9.81x10^{-5}$	**<0.001**	3.3%
CSF NFL	$-7.00x10^{-7}$	0.48	3.4%
MD Cluster 1			
CSF p-tau	$1.22x10^{-7}$	**<0.001**	4.2%
CSF NFL	$1.00x10^{-10}$	0.96	4.2%
MD Cluster 2			
CSF p-tau	$8.11x10^{-8}$	**<0.001**	1.7%
CSF NFL	$2.20x10^{-9}$	0.34	4.6%
RD Cluster 1			
CSF p-tau	$1.08x10^{-7}$	**<0.001**	1.4%
CSF NFL	$1.70x10^{-9}$	0.11	1.1%
RD Cluster 2			
CSF p-tau	$1.15x10^{-7}$	**<0.001**	2.5%
CSF NFL	$3.00x10^{-11}$	0.79	5.5%
AD Cluster 1			
CSF p-tau	$2.03x10^{-7}$	**<0.001**	2.0%
CSF NFL	$1.10x10^{-9}$	0.46	1.3%
AD Cluster 2			
CSF p-tau	$1.78x10^{-7}$	**<0.001**	1.6%
CSF NFL	$9.00x10^{-10}$	0.56	5.4%

Note. Models were adjusted for baseline age, sex race/ethnicity, education, diagnosis, FSRP (minus age points), *APOE*-ε4 status, and follow-up time. Bolded values represent significant findings. APOE=apolipoprotein E; CSF =cerebrospinal fluid; DTI=diffusion tensor imaging; FSRP=Framingham Stroke Risk Profile; NFL=neurofilament light; P-tau=phosphorylated tau.

Discussion

Among community-dwelling older adults free of clinical stroke and dementia, higher baseline levels of CSF p-tau, t-tau, and NFL related to faster decline in white matter integrity. The effects of CSF p-tau and CSF t-tau were greatest in the inferior frontal and parietal lobes, whereas the effects of CSF NFL were more widespread throughout the brain. All associations were more prominent in *APOE*-ε4 carriers compared to non-carriers, and associations between baseline NFL and faster decline in white matter integrity were also driven by participants with MCI. Notably, associations

between baseline CSF NFL and faster decline in white matter integrity were much more robust than the other CSF biomarkers, though the competitive models did show that CSF p-tau contributed unique variance to decline in white matter integrity beyond CSF NFL.

We found robust cross-sectional and longitudinal associations between higher levels of baseline CSF NFL and compromised white matter integrity across the entire brain. NFL is a protein that contributes to the structure of neurofilaments, which are responsible for supporting axonal integrity and neuronal transport.[200] Elevated CSF NFL concentrations may reflect structural or metabolic changes in axons due to a variety of causes, such as cerebral inflammation,[201] subclinical neural trauma,[202] and neurodegenerative disease.[203] As mechanical damage disrupts the integrity of the axonal membrane, neurofilaments enter the CSF, resulting in increased CSF NFL levels.[204] In addition, chemical changes, such as calcium dysregulation or increased intra-axonal calcium concentration, may lead to neurofilament disruption and compaction. These chemical changes may promote the movement of neurofilaments into the CSF when mechanical damage is present.[205] Thus, CSF NFL concentrations cross-sectionally indicate global neuroaxonal damage that is also reflected in imaging measures sensitive to white matter microstructure.

Further, the longitudinal results suggest that neuroaxonal injury is an important driver of white matter damage in normal aging and individuals at risk for AD. In longitudinal models, baseline CSF NFL interacted with diagnosis and *APOE*-ε4 status, such that associations with faster decline in white matter integrity were driven by participants with MCI and *APOE*-ε4 carriers. CSF NFL concentrations are higher in

individuals with MCI,[206] likely due to the multiple neuropathologies present in these individuals affecting neuroaxonal health. Further, these neuropathologies, such as Aβ[89] or vascular disease,[207] may contribute to oligodendrocyte damage, possibly rendering the axon more susceptible. While *APOE*-ε4 carriers have not been reported to have higher levels of CSF NFL,[208] *APOE*-ε4 is less efficient at transporting and recycling cholesterol than other *APOE* alleles, resulting in less remyelination in *APOE*-ε4 carriers when the white matter is injured.[158] Therefore, *APOE*-ε4 carriers are likely more susceptible to the effects of neuroaxonal injury. Overall, results suggest that CSF NFL may be a useful marker of active and future white matter damage, especially those at risk for AD. Future studies should examine how plasma measures of NFL may be used as a prognostic marker of white matter injury.

Notably, associations between NFL and white matter integrity were global, across the entire brain (**Figure 4.5** and **Figure 4.6**). The lack of regional specificity is possibly due to the range of underlying pathologies leading to neuroaxonal injury. For example, NFL is elevated in multiple neurodegenerative conditions, including AD,[206] frontotemporal dementia,[209] multiple sclerosis,[210] traumatic brain injury,[211] and stroke.[212] Thus, it is possible that vascular disease is driving increased NFL in watershed regions,[57] whereas AD pathology is driving increased NFL in frontal and temporal lobes.[3] Additional analyses in other populations are needed to determine if different etiologies of neuroaxonal injury lead to white matter damage in specific regions.

We also found associations between higher levels of baseline CSF p-tau and faster decline in white matter integrity, though associations were in fewer clusters compared to baseline NFL. P-tau likely leads to white matter damage through axonal

injury. Tau is a normal axonal protein that functions to stabilize microtubules and support transport through the axon.[6] However, hyperphosphorylation destabilizes tau, leading to tau accumulation in dendrites and axon destabilization,[105] which can be detected as changes on DTI. Interestingly, associations did not localize to the medial temporal lobe, as we hypothesized, where p-tau first accumulates in AD.[3] As seen in **Table 4.1**, higher baseline CSF p-tau was associated with faster decline in white matter integrity primarily in frontal and parietal lobe regions, including the superior and anterior corona radiata, the straight gyrus, the genu of the corpus callosum, and the superior parietal lobule. The lack of localization to the medial temporal lobe suggests that associations may not be due to p-tau directly but could be due to neurodegenerative processes that are caused by p-tau accumulation. This hypothesis is supported by the associations reported here between baseline CSF t-tau and faster decline in white matter microstructure. The locations of these associations were consistent with the longitudinal p-tau associations (**Table 4.4**), including the anterior corona radiata, superior corona radial, superior parietal lobule, and other frontal lobe regions (medial orbital gyrus). It is possible that that the frontal lobe findings are due to age-related vulnerability of frontal lobe white matter. Demyelination in aging normally begins in the frontal lobe,[213] possibly increasing the susceptibility of these axons to neurodegeneration and lowering the threshold of damage needed to detect DTI changes. Additionally, the effects in the parietal lobe overlap with regions contributing to the default mode network. The default mode network is a large-scale network that is active while the brain is “at rest”. Default mode network disruption has previously been implicated in AD,[214] as the network is thought to experience hypometabolism,[215] is a site

of amyloid accumulation,[216] and most recently has been identified as a site of tau accumulation.[217] Tau accumulation in these regions may contribute to the association with white matter damage reported here. Future studies using brain positron emission tomography are needed to determine if tau accumulation co-localizes with regions of white matter damage. Regardless of underlying mechanism, competitive models including both baseline p-tau and NFL revealed that p-tau and NFL contributed to unique variance in the decline of white matter integrity in specific clusters. Thus, while p-tau may not be a robust driver of white matter damage, our results suggest that small areas of white matter damage may be specific to AD pathology.

Additionally, we observed small diagnostic interactions between baseline CSF p-tau and t-tau markers and longitudinal DTI metrics. Stratification revealed that associations between higher baseline CSF values and faster decline in white matter integrity in those small clusters were driven by participants with NC (**Figure 4.1** and **Figure 4.3**). This finding is surprising, as we expected associations to be exacerbated in individuals with MCI, as they generally have a greater pathology burden. It is noteworthy that these small interactions only implicated axial diffusivity, not the remaining DTI metrics. Axial diffusivity is hypothesized to reflect axonal injury,[119] and prior studies have suggested that it decreases in early stages of axonal damage, followed by an increase.[218,219] This fluctuation, taken with the size of the clusters, makes the diagnostic interaction difficult to interpret with confidence. Replication is needed to better understand these findings.

Finally, we observed modest cross-sectional interactions with *APOE*-ε4 status, such that associations between higher baseline CSF p-tau or t-tau and compromised

white matter integrity were present in *APOE*-ε4 non-carriers only. It is possible that in a cross-sectional context, the independent effects that the *APOE*-ε4 allele has on white matter integrity[220] and myelination[158] skew any associations between tau and DTI metrics in *APOE*-ε4 carriers. Thus, the association is only observed in *APOE*-ε4 non-carriers and not the entire sample. There was one small cluster in the precuneus where baseline CSF t-tau interacted with *APOE*-ε4 status, such that associations were present in that cluster in *APOE*-ε4 carriers only. As discussed previously, it may be that while the *APOE*-ε4 allele obscures cross-sectional associations, it possibly renders white matter less able to remyelinate after injury,[158] leading to DTI changes in response to increased tau. However, this cluster was small, so replication is needed to clarify whether *APOE*-ε4 modifies associations between tau and white matter injury.

Our study has several strengths, including stringent quality control procedures, a longitudinal study design, and reliable methods for quantifying cerebral white matter microstructure. Additional strengths include comprehensive ascertainment of potential confounders and the application of cluster enhancement and cluster-wise inference to correct for multiple comparisons, reducing the possibility of a false positive finding. The application of a longitudinal voxel-wise pipeline allows for the robust and comprehensive assessment of the trajectory of white matter damage throughout the entire brain. Finally, core laboratories using quality control procedures analyzed all MRI and CSF measurements in batch, and technicians were blinded to clinical information. Despite these strengths, there are limitations. Limitations include the observational design and the predominantly White, well-educated, and relatively healthy sample, limiting generalizability. Additionally, CSF markers of p-tau, neurodegeneration, and

neuroaxonal injury cannot provide anatomic information about where those processes are occurring. Future studies using tau positron emission tomography are needed to determine if neurodegeneration is occurring in the same region as white matter damage. Finally, many of the longitudinal effects reported here are small. Larger studies are needed to further characterize longitudinal associations.

In summary, we found robust and novel cross-sectional and longitudinal associations between an *in vivo* biomarker of neuroaxonal injury and global compromised white matter integrity. Results suggest that neuroaxonal injury is a robust etiology of white matter injury, especially in individuals at risk for AD. These results add to a growing body of literature suggesting that NFL is a sensitive and potential prognostic marker, but not specific to one underlying pathology. More work is needed to understand if different etiologies of neuroaxonal injury lead to white matter damage in specific regions. We also found that p-tau and t-tau are weakly but independently associated with a faster decline in white matter damage, specifically in the frontal and parietal lobes. Notably, neither p-tau not t-tau were cross-sectionally associated with white matter integrity, suggesting that p-tau and general neurodegeneration may be drivers of white matter injury, but they do not reflect active white matter damage.

CHAPTER 5

THE EFFECTS OF TRACT-SPECIFIC WHITE MATTER INTEGRITY ON COGNITIVE DECLINE

Introduction

Cerebral white matter allows for efficient signal propagation between neurons, so damage to white matter tracts is a major cause of diminished signal propagation and cognitive decline. However, different white matter tracts support different cognitive functions based on their location and the structures they connect, so damage to specific tracts results in deficits in specific cognitive domains. For example, deep white matter tracts commonly susceptible to vascular disease,[24,57] including the internal capsule, external capsule, and subcortical projections to the cortex (corticostriatal tracts), have been cross-sectionally associated with information processing speed,[47] executive functioning,[47] and memory retrieval.[47] Alternatively, white matter tracts thought to be susceptible in Alzheimer's disease (AD), including tracts projecting to the medial temporal lobe,[25,82] are critically important for learning and episodic memory.[221] However, most prior research examining cognitive correlates of white matter injury rely on cross-sectional or lesion-based studies. It is still unknown if the integrity of certain white matter tracts may be used as a prognostic tool to predict future domain-specific cognitive decline.

It is possible that certain white matter tracts may be more potent predictors of cognitive decline than others. Tracts with greater anatomical connections, such as corticostriatal tracts, or tracts that are susceptible to multiple types of damage, such as

temporal lobe tracts susceptible to both vascular damage and AD pathology, may have a greater impact on cognitive decline than others. However, no studies to date have compared tract-specific contributions to cognitive decline. To optimize the prognostic value of white matter integrity and enhance understanding of the neurobiology driving cognitive decline, there is a need to understand how damage to certain tracts independently or synergistically contributes to cognitive trajectory.

The aim of the present chapter was to examine how baseline white matter integrity in certain tracts, assessed by diffusion tensor imaging (DTI), relates to domain-specific cognitive trajectory over time and if specific tracts explain separate or overlapping variance in cognitive decline. Since vascular disease is the most common etiology of white matter damage in older adults[24] and is the most common pathology to co-exist with AD,[11] this study focused on tracts traditionally thought to be susceptible to vascular disease (corticostriatal tracts)[24,57] and AD pathology (tracts projecting to the medial temporal lobe, including the cingulum bundle, tapetum, fornix, uncinate fasciculus (UF), and inferior longitudinal fasciculus (ILF)).[25,82] We hypothesized that reduced baseline integrity in corticostriatal tracts would relate to faster decline in information processing speed and executive function,[44] and reduced baseline integrity in medial temporal lobe tracts would relate to faster decline in episodic memory.[46] We also investigated whether associations were modified by cognitive diagnosis (normal cognition (NC) versus mild cognitive impairment (MCI)) or apolipoprotein (APOE*)* ε4 status, hypothesizing that associations will be stronger among participants with MCI and *APOE*-ε4 positive participants.

Methods

For details about the study cohort and covariates, please refer to the Methods in Chapter 2 (pages 27-28 and page 33).

Brain MRI Acquisition & Post-Processing

For details about the brain MRI acquisition and pre-processing, please refer to the Methods in Chapter 2 (pages 30-32). White matter tract templates (including the cingulum bundle, corticostriatal tract, tapetum, fornix. UF, and ILF) were constructed from Human Connectome Project DTI data[222] (resolution: 1.25 mm isotropic, b-values: 0, 1000, 2000, 3000 s/mm2, 90 directions per shell) using an established approach.[223] Consistent with prior work,[223-225] probabilistic tractography using default settings (samples: 5000, curvature threshold: 0.2, FA threshold: 0.2) was performed on 100 individuals from the Human Connectome Project[222] to create each tract. Details on creating the cingulum bundle,[226] UF[226], ILF,[226] tapetum,[224] fornix,[227] and corticocortical tract[225] have been published elsewhere. The tracts were then transformed into MNI space, averaged into a mean tract template across all participants, and thresholded used a novel slice-level thresholding approach described elsewhere.[223] Briefly, slice level thresholding allows higher threshold levels compared conventional tract level thresholding methods, reducing the likelihood of false positives and increasing tract coverage. The average FA within each tract was then calculated for all Vanderbilt Memory and Aging Project participants.

Neuropsychological Assessment

All participants underwent a comprehensive neuropsychological assessment protocol at each time point assessing global cognition, language, information processing speed, executive function, visuospatial skills, and episodic memory. Tests included the Boston Naming Test,[228] Animal Naming,[229] WAIS-IV Coding,[230] Delis-Kaplan Executive Function System (D-KEFS) Number Sequencing,[231] D-KEFS Tower Test,[231] D-KEFS Color-Word Inhibition,[231] D-KEFS Number-Letter Switching,[231] Letter Fluency (FAS),[232] Hooper Visual Organization Test (HVOT),[233] Biber Figure Learning Test,[234] and California Verbal Learning Test-II.[235] Measures were carefully selected to preclude floor or ceiling effects and were not utilized for screening, diagnosis, or selection of participants for the study. To minimize multiple comparisons, composite z-scores were derived separately for episodic memory and executive function performances.[236]

Analytical Plan

Linear mixed effects models with random intercepts and slopes and a follow-up time interaction related baseline FA within each of the tracts (one tract per model) to neuropsychological trajectory. Models adjusted for baseline age, sex, race/ethnicity, education, FSRP (minus age points), diagnosis, *APOE*-ε4 status, and follow-up time. For each neuropsychological outcome that related to baseline FA in >1 tract, a combined linear mixed effects model was performed including all statistically significant tracts for the selected outcome (with identical covariates) to determine whether specific tracts represent a common or unique pathologic pathway to cognitive decline.

All models were repeated with *predictor x cognitive diagnosis* (excluding individuals with early MCI due to the small sample size) and *predictor x APOE-ε4 status*

interactions. Models were subsequently stratified by cognitive diagnosis (NC, MCI) and *APOE-ε4* status (positive or negative).

To determine if outliers were driving the results, additional models were calculated excluding predictor or outcome values >4 standard deviations from the group mean. Significance was set *a priori* at $p<0.05$ and analyses were conducted using R 3.6.2.

Results

Participant Characteristics

For the 323 participants included (73±7years, 59% male, 87% non-Hispanic White), the mean follow-up time was 4.5±1.2 years. See **Table 5.1** for participant characteristics stratified by diagnosis.

Table 5.1. Participant Characteristics for Cognition Sample

	Total n=323	NC n=168	eMCI n=27	MCI n=128	p-value
Demographic & Health Characteristics					
Age, years	73±7	72±7	73±6	73±8	0.71
Sex, % male	59	58	74	56	0.22
Race, % White non-Hispanic	87	87	85	87	0.97
Education, years	16±3	16±3	16±3	15±3	**<0.001**‡
APOE-ε4, % carrier	35	29	22	45	**0.008**‡
Framingham Stroke Risk Profile, total*	13±4	12±4	14±3	13±4	0.052
Systolic blood pressure, mmHg	143±18	140±17	150±18	145±19	**0.003**†‡
Anti-hypertensive medication usage, %	54	53	56	55	0.94
Diabetes, %	18	16	22	19	0.68
Current Cigarette Smoking, %	2	2	4	3	0.70
Prevalent CVD, %	5	6	4	3	0.50
Atrial fibrillation, %	7	6	11	7	0.61
Left ventricular hypertrophy, %	4	3	4	6	0.39
Mean follow-up time, years	4.5±1.2	4.8±0.9	4.2±1.2	4.2±1.4	**<0.001**†
Cognition					
Boston naming test	27±3	28±2	27±2	25±4	**<0.001**†‡
Animal naming	19±5	21±5	19±3	16±5	**<0.001**§‡
WAIS-IV coding	53±13	57±12	53±11	47±12	**<0.001**§‡
D-KEFS number sequencing test	43±21	36±13	42±13	52±26	**<0.001**†‡
Executive composite	0.01±0.89	0.44±0.62	0.17±0.42	-0.58±0.95	**<0.001**§†‡
Hooper visual organization test	24±3	25±3	25±2	23±4	**<0.001**‡
Memory composite	-0.01±0.96	0.57±0.72	-0.06±0.76	-0.74±0.75	**<0.001**§†‡

Note. Values presented as mean±standard deviation or frequency. *a modified score was included in models excluding points for age (6±3). †eMCI different than NC. ‡NC different from MCI. §eMCI different than MCI. APOE=apolipoprotein E; CVD=cardiovascular disease; D-KEFS=Delis-Kaplan Executive Function System; eMCI=early mild cognitive impairment; NC= normal cognition; MCI=mild cognitive impairment; WAIS=Wechsler Adult Intelligence Scale.

White Matter Microstructure & Longitudinal Cognition

In the entire sample, lower baseline FA in the cingulum bundle, tapetum, fornix, UF, and ILF was associated with faster decline in all cognitive domains (**Table 5.2**, **Figure 5.1**). Specifically, lower baseline FA in the cingulum bundle was associated with

faster decline in the Boston Naming Test (β=9.48, p<0.001), Animal Naming (β=10.17, p=0.002), Coding (β=20.02, p=0.002), D-KEFS Number Sequencing (β=-51.63, p=0.001), executive function composite (β=2.05, p<0.001), HVOT (β=6.73, p<0.003), and episodic memory composite (β=2.62, p<0.001). Lower baseline FA in the tapetum was associated with faster decline in the Boston Naming Test (β=5.99, p=0.004), Animal Naming (β=6.67, p=0.01), Coding (β=14.01, p=0.01), D-KEFS Number Sequencing (β=-40.51, p=0.001), executive function composite (β=1.31, p=0.001), HVOT (β=4.15, p=0.03), and episodic memory composite (β=1.44, p<0.001). Lower baseline FA in the fornix was associated with faster decline in the Boston Naming Test (β=3.60, p=0.02), Animal Naming (β=4.57, p=0.02), Coding (β=10.41, p=0.01), D-KEFS Number Sequencing (β=-40.86, p<0.001), executive function composite (β=0.99, p=0.001), HVOT (β=3.57, p=0.01), and episodic memory composite (β=1.19 p<0.001). Lower baseline FA in the UF was associated with faster decline in the Boston Naming Test (β=10.89, p<0.001), Animal Naming (β=10.81, p=0.003), Coding (β=28.96, p<0.001), D-KEFS Number Sequencing (β=-65.49, p<0.001), executive function composite (β=2.10, p<0.001), HVOT (β=7.86, p=0.003), and episodic memory composite (β=2.96 p<0.001). Finally, lower baseline FA in the ILF was associated with faster decline in the Boston Naming Test (β=7.09, p=0.001), Animal Naming (β=8.89, p=0.001), Coding (β=16.34, p=0.004), D-KEFS Number Sequencing (β=-44.01, p=0.001), executive function composite (β=1.67, p<0.001), HVOT (β=5.34, p=0.01), and episodic memory composite (β=1.79 p<0.001).

Lower baseline FA in the corticostriatal tract was only associated with faster

decline in the episodic memory composite (β=1.01, p=0.03). Baseline FA in this tract was unrelated to trajectory of all other cognitive domains (p-values>0.11). All associations except baseline FA in the ILF and tapetum and D-KEFS number sequencing trajectory remained significant after removing outliers (**Table 5.2**).

Table 5.2. FA Associations with Longitudinal Cognition

	Boston Naming Test		Animal Naming		WAIS-IV Coding		D-KEFS Number Sequencing Test		Executive Composite		Hooper Visual Organization Test		Memory Composite	
	β	**p-value**	**β**	**p-value**	**β**	**p-value**	**β**	**p-value**	**β**	**p-value**	**β**	**p-value**	**β**	**p-value**
Cingulum Bundle	9.48	**<0.001***	10.17	**0.002***	20.02	**0.002***	-51.63	**0.001***	2.05	**<0.001***	6.73	**0.003***	2.62	**<0.001***
Corticostriatal Tract	3.15	0.18	3.49	0.24	6.70	0.26	-20.41	0.13	0.74	0.11	2.90	0.17	1.01	**0.03***
Tapetum	5.99	**0.004***	6.67	**0.01***	14.01	**0.01***	-40.51	**0.001**	1.31	**0.001***	4.15	**0.03***	1.44	**<0.001***
Fornix	3.60	**0.02***	4.57	**0.02***	10.41	**0.01***	-40.86	**<0.001***	0.99	**0.001***	3.57	**0.01***	1.19	**<0.001***
UF	10.89	**<0.001***	10.81	**0.003***	28.96	**<0.001***	-65.49	**<0.001***	2.10	**<0.001***	7.86	**0.003***	2.96	**<0.001***
ILF	7.09	**0.001***	8.89	**0.001***	16.34	**0.004***	-44.01	**0.001**	1.67	**<0.001***	5.34	**0.01***	1.79	**<0.001***

Note. Analyses performed on n=323 participants. Models were adjusted for baseline age, sex race/ethnicity, education, diagnosis, FSRP (minus age points), *APOE*-ε4 status, and follow-up time. Bolded values represent significant findings. *p-value remains significant after outlier removal. APOE=apolipoprotein E; DKEFS=Delis-Kaplan Executive Function System; FSRP=Framingham Stroke Risk Profile; ILF=inferior longitudinal fasciculus; UF=uncinate fasciculus; WAIS=Wechsler Adult Intelligence Scale.

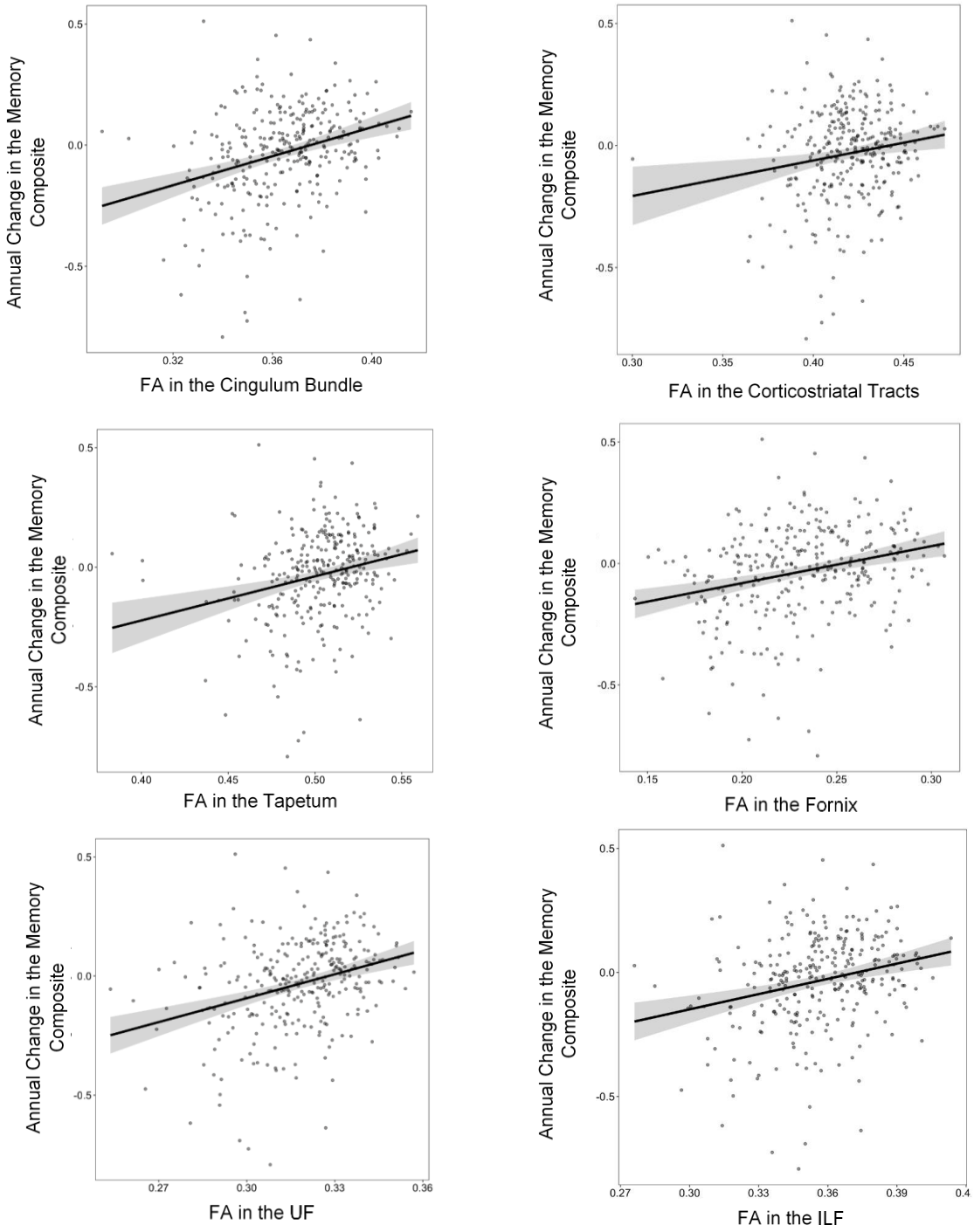

Figure 5.1. Baseline FA associations with longitudinal memory performance. Lower baseline FA in the cingulum bundle (β=2.62, p<0.001), corticostriatal tract (β=1.01, p=0.03), tapetum (β=1.44, p<0.001), fornix (β=1.19, p<0.001), UF (β=2.96, p<0.001), and ILF (β=1.79, p<0.001) is associated with faster decline in the memory composite. Models were adjusted for baseline age, sex, race/ethnicity, education, diagnosis, *APOE*-ε4 status, modified Framingham Stroke Risk Profile, and follow-up time. APOE=apolipoprotein; FA=fractional anisotropy; ILF=inferior longitudinal fasciculus; UF=uncinate fasciculus.

White Matter Tracts as Competing Predictors of Longitudinal Cognition

To determine whether decline in certain cognitive domains was driven by damage in certain tracts, combined models including all significant tract predictors for each cognitive domain were run (**Table 5.3**). For the Boston Naming Test, Animal Naming, executive function composite, and HVOT, no tract remained significant (p-values>0.13). For Coding, lower baseline FA in the UF remained significantly associated (β=38.84, p=0.01) when including the cingulum bundle, tapetum, fornix, and ILF in the model. For D-KEFS Number Sequencing, lower baseline FA in the fornix remained significantly associated (β=-34.57, p=0.004) when including the cingulum bundle, tapetum, UF, and ILF in the model. For the episodic memory composite, lower baseline FA in the cingulum bundle (β=2.59, p=0.01) and UF (β=3.23, p=0.008) remained significant when including the corticostriatal tract, tapetum, fornix, and ILF in the model.

Table 5.3. Combined Models of White Matter Tracts in Relation to Longitudinal Cognition

	β	p-value
Boston Naming Test		
Cingulum Bundle	8.25	0.13
Tapetum	-2.02	0.67
Fornix	0.27	0.89
UF	7.95	0.20
ILF	-2.38	0.62
Animal Naming		
Cingulum bundle	4.87	0.49
Tapetum	-4.93	0.43
Fornix	1.26	0.61
UF	3.20	0.69
ILF	6.66	0.29

WAIS-IV Coding		
Cingulum Bundle	4.47	0.75
Tapetum	-8.85	0.47
Fornix	4.28	0.38
UF	38.84	**0.01**
ILF	-7.58	0.54
D-KEFS Number Sequencing Test		
Cingulum Bundle	6.86	0.84
Tapetum	23.96	0.43
Fornix	-34.57	**0.004**
UF	-48.01	0.22
ILF	-9.64	0.75
Executive Composite		
Cingulum Bundle	1.43	0.18
Tapetum	-0.90	0.33
Fornix	0.42	0.26
UF	0.44	0.73
ILF	0.76	0.44
Hooper Visual Organization Test		
Cingulum Bundle	5.03	0.31
Tapetum	-2.77	0.52
Fornix	1.63	0.35
UF	5.42	0.34
ILF	-0.95	0.83
Memory Composite		
Cingulum Bundle	2.59	**0.01**
Corticostriatal	-0.75	0.30
Tapetum	-1.44	0.13
Fornix	0.28	0.49
UF	3.23	**0.008**
ILF	-0.63	0.50

Note. Analyses performed on n=296 participants. Models were adjusted for baseline age, sex race/ethnicity, education, diagnosis, FSRP (minus age points), *APOE*-ε4 status, and follow-up time. Bolded values represent significant findings. APOE=apolipoprotein E; DKEFS=Delis-Kaplan Executive Function System; FSRP=Framingham Stroke Risk Profile; ILF=inferior longitudinal fasciculus; UF=uncinate fasciculus; WAIS=Wechsler Adult Intelligence Scale.

White Matter Microstructure x Diagnosis Interactions & Longitudinal Cognition

The cingulum bundle (β=-104.28, p=0.001), tapetum (β=-69.72, p=0.003), fornix (β=-73.88, p<0.001), UF (β=-117.08 p=0.001), and ILF (β=-84.93, p=0.001) interacted with diagnosis on-D-KEFS Number Sequencing trajectory (**Table 5.4**). However, these findings were attenuated when excluding outliers (**Table 5.4**). In stratified models, lower baseline FA in the cingulum bundle (β=-102.86, p=0.008), tapetum (β=-65.16, p=0.02), fornix (β=-85.61, p<0.001), UF (β=130.45, p=0.003), and ILF (β=-86.27, p=0.01) were associated with faster decline in D-KEFS Number Sequencing in participants with MCI only.

The cingulum bundle (β=10.12, p=0.04), fornix (β=5.82, p=0.05), UF (β=11.68, p=0.04), and ILF (β=8.56, p=0.05) also interacted with diagnosis on HVOT trajectory (**Table 5.4**). However, these findings were attenuated when excluding outliers (**Table 5.4**). In stratified models, lower baseline FA in the cingulum bundle (β=11.49, p=0.05), fornix (β=6.78, p=0.04), UF (β=14.06, p=0.03), and ILF (β=9.93, p=0.06) were

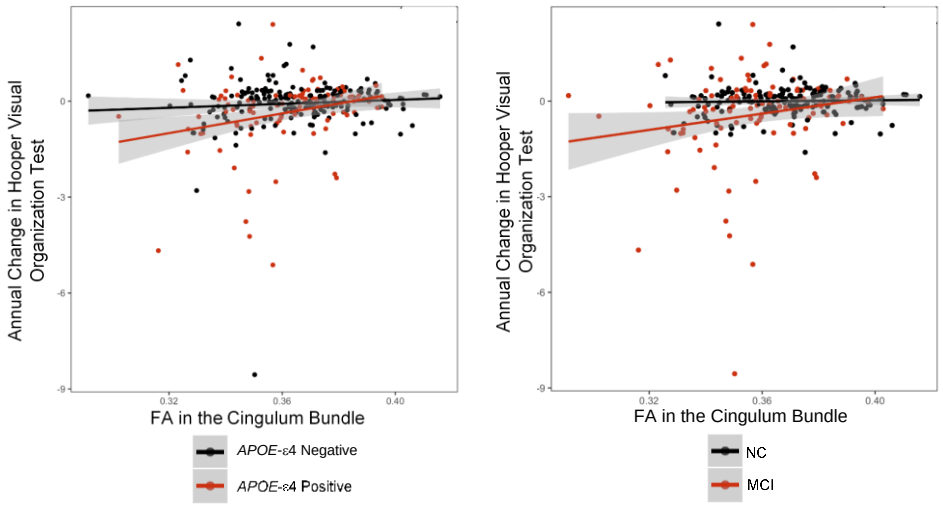

Figure 5.2. Baseline cingulum bundle FA interactions with diagnosis and *APOE*-ε4 status. Baseline cingulum bundle FA interacts with *APOE*-ε4 status (p=0.02) and diagnosis (p=0.04) on longitudinal Hooper Visual Organization Test. Associations between lower baseline FA and faster decline in visuospatial skills is driven by *APOE*-ε4 carriers and participants with MCI. APOE=apolipoprotein; FA=fractional anisotropy; MCI=mild cognitive impairment; NC=normal cognition.

associated with faster decline in HVOT in participants with MCI only (**Figure 5.2**).

Table 5.4. FA x Diagnosis Interactions on Longitudinal Cognition

	Boston Naming Test		Animal Naming		WAIS-IV Coding		D-KEFS Number Sequencing Test		Executive Composite		Hooper Visual Organization Test		Memory Composite	
	β	p-value	β	p-value	β	p-value	β	p-value	β	p-value	β	p-value	β	p-value
Cingulum Bundle	7.19	0.17	-2.79	0.67	10.46	0.43	-104.28	**0.001**	1.80	0.08	10.12	**0.04**	0.45	0.65
Corticostriatal Tract	1.68	0.74	-5.72	0.35	2.60	0.84	-36.02	0.20	0.55	0.59	5.51	0.24	0.76	0.43
Tapetum	2.23	0.60	-4.41	0.40	3.00	0.78	-69.72	**0.003**	0.84	0.33	4.29	0.28	-0.25	0.76
Fornix	3.58	0.25	-2.75	0.47	6.08	0.44	-73.88	**<0.001**	0.90	0.14	5.82	**0.05**	0.05	0.93
UF	9.28	0.12	-2.04	0.79	15.51	0.31	-117.08	**0.001**	1.44	0.24	11.68	**0.04**	0.29	0.80
ILF	5.28	0.25	-3.28	0.56	14.94	0.20	-84.93	**0.001**	1.18	0.19	8.56	**0.05**	0.63	0.46

Note. Analyses performed on n=296 participants. Models were adjusted for baseline age, sex race/ethnicity, education, diagnosis, FSRP (minus age points), *APOE*-ε4 status, and follow-up time. Bolded values represent significant findings. *p-value remains significant after outlier removal. APOE=apolipoprotein E; DKEFS=Delis-Kaplan Executive Function System; FSRP=Framingham Stroke Risk Profile; ILF=inferior longitudinal fasciculus; UF=uncinate fasciculus; WAIS=Wechsler Adult Intelligence Scale.

White Matter Microstructure x APOE-ε4 Interactions & Longitudinal Cognition

The tapetum (β=-11.52, p=0.03) and fornix (β=-10.17, p=0.01) interacted with *APOE*-ε4 status on Animal Naming trajectory (**Table 5.5**). Associations remained significant when excluding outliers (**Table 5.5**). In stratified models, lower baseline FA in the tapetum (β=-102.86, p=0.008) and fornix (β=-86.27, p=0.01) were associated with faster decline in Animal Naming in participants with *APOE*-ε4 negative participants only.

The UF (β=35.58, p=0.02) interacted with *APOE*-ε4 status on Coding trajectory (**Table 5.5**). This association

remained significant when excluding outliers (**Table 5.5**). In stratified models, lower baseline FA in the UF was associated with faster decline in HVOT in *APOE*-ε4 positive (β=56.29, p=0.002) and *APOE*-ε4 negative participants (β=16.27, p=0.01), but associations were stronger in *APOE*-ε4 positive participants.

The cingulum bundle (β=10.89, p=0.02) and ILF (β=10.02, p=0.01) interacted with *APOE*-ε4 status on HVOT trajectory (**Table 5.5**). The interaction with ILF remained significant when excluding outliers (**Table 5.5**). In stratified models, lower baseline FA in the cingulum bundle (β=13.82, p=0.02) and ILF (β=12.20, p=0.005) were associated with

Table 5.5. FA x *APOE*-ε4 Status Interactions with Longitudinal Cognition

	Boston Naming Test		Animal Naming		WAIS-IV Coding		D-KEFS Number Sequencing Test		Executive Composite		Hooper Visual Organization Test		Memory Composite	
	β	**p-value**	**β**	**p-value**	**β**	**p-value**	**β**	**p-value**	**β**	**p-value**	**β**	**p-value**	**β**	**p-value**
Cingulum Bundle	5.32	0.31	-4.78	0.47	23.89	0.08	-39.77	0.18	1.44	0.15	10.89	**0.02**	1.73	0.07
Corticostriatal Tract	-0.92	0.85	-8.19	0.19	6.48	0.61	-7.01	0.80	-0.02	0.98	7.80	0.08	1.06	0.25
Tapetum	-2.78	0.52	-11.52	**0.03***	13.35	0.23	-27.96	0.25	-0.54	0.51	6.41	0.11	-0.22	0.78
Fornix	-2.95	0.33	-10.17	**0.01***	0.93	0.90	-22.61	0.16	-0.04	0.94	1.71	0.53	-0.55	0.32
UF	2.19	0.72	-8.03	0.30	35.58	**0.02***	-62.77	0.07	1.00	0.39	10.63	0.06	1.92	0.08
ILF	1.12	0.80	-9.32	0.10	14.82	0.20	-44.32	0.08	0.58	0.50	10.02	**0.01***	0.62	0.46

Note. Analyses performed on n=323 participants. Models were adjusted for baseline age, sex race/ethnicity, education, diagnosis, FSRP (minus age points), *APOE*-ε4 status, and follow-up time. Bolded values represent significant findings. *p-value remains significant after outlier removal. APOE=apolipoprotein E; DKEFS=Delis-Kaplan Executive Function System; FSRP=Framingham Stroke Risk Profile; ILF=inferior longitudinal fasciculus; UF=uncinate fasciculus; WAIS=Wechsler Adult Intelligence Scale.

faster decline in HVOT in *APOE*-ε4 positive participants only (**Figure 5.2**).

Discussion

Among community-dwelling older adults free of clinical stroke and dementia, lower baseline FA in tracts traditionally susceptible in AD related to faster decline in language ability, information processing speed, executive function, episodic memory, and visuospatial skills. Baseline FA in the corticostriatal tracts, traditionally susceptible to vascular disease, was only associated with a faster decline in episodic memory. In combined models including multiple white matter tracts, baseline FA in both the cingulum bundle and UF independently contributed to faster decline in episodic memory beyond other white matter tracts. Results highlight the potential role of vascular damage to deep white matter tracts in memory decline and the importance of identifying etiologies of both cingulum bundle and UF damage to mitigate memory decline.

We found that all tracts with temporal lobe projections were associated with faster decline in all cognitive domains tested, including language, information processing speed, executive function, episodic memory, and visuospatial skills. These broad associations are not surprising based on previous data connecting white matter integrity to cognition.[237] Myelination of neurons allows for faster signal propagation through axons, so any damage to oligodendrocytes or axons slows communication between neurons, leading to cognitive decline. Interestingly, we found that reduced baseline FA in the corticostriatal tracts was only associated with a faster decline in episodic memory. These tracts connect subcortical regions, such as the basal ganglia and thalamus, to cortical regions, and are important for goal-oriented behavior and

decision making. Traditionally, these tracts have been implicated in executive functioning and information processing speed,[47] but we did not detect associations with decline in these domains. Corticostriatal tracts are known to have projections to the hippocampus,[238] so it is possible that damage in these projections could lead to faster decline in episodic memory. Additionally, corticostriatal tracts are thought to be particularly susceptible to cerebrovascular disease, as these deep white matter regions are perfused by penetrating arteries that are vulnerable to hypoperfusion.[57,58] Recent evidence suggests that individuals with subcortical ischemic vascular disease have memory deficits.[239] Taken together with the findings reported here, it is possible that cerebrovascular disease leads to decline in episodic memory through corticostriatal tract damage, though more work is needed to better understand how the corticostriatal tracts contribute to memory.

In the competitive models, lower baseline FA in the cingulum bundle and UF were independently associated with decline in episodic memory. Results suggest that these two tracts may be better but independent prognostic markers of memory decline compared to other tracts examined here. The cingulum bundle begins in the frontal lobe and wraps around the corpus callosum through the parietal lobe, connecting to the entorhinal cortex. Based on these medial temporal lobe projections, damage to the cingulum bundle has previously been associated with worse memory performance[240] and the cingulum bundle has been implicated in MCI[241] and AD,[242] consistent with the finding reported here. However, our results suggest that the cingulum bundle is not the only major white matter tract that contributes to memory decline in older adults. The UF runs from the prefrontal cortex to the deep temporal lobe structures, including the

parahippocampal gyrus and amygdala. It functions to guide decision making based on previous memories and emotions.[193] Thus, damage to the UF may impair the ability to use memories to inform current decision making. While the UF has been implicated in episodic memory in prior studies in both MCI[243] and temporal lobe epilepsy patients,[244,245] these studies examined the UF in isolation, without taking other white matter tracts into account.

Importantly, because the cingulum bundle and UF project to distinct anatomic regions, it is likely that different pathologies are responsible for the damage these tracts undergo throughout aging. The UF originates in the frontal lobe, so it is likely exposed to some age-related cerebrovascular remodeling that occurs in the frontal watershed region,[246] as well as possible amyloid-beta accumulation.[3] Normal demyelination that occurs with aging[213] also may contribute to lower FA in the UF. The UF is one of the last tracts to undergo myelination, often not fully myelinated until adulthood,[247] suggesting that it may be one of the first tracts to undergo age-related demyelination. Alternatively, the cingulum bundle has prominent projections to the hippocampus and entorhinal cortex, so phosphorylated tau that is known to accumulate in these regions[3] and spread through the cingulum bundle in AD[196] may be an important etiology of cingulum bundle damage. Both tracts terminate in the temporal lobe, suggesting that additional pathologies targeting this region, including blood-brain barrier breakdown or arterial stiffness, may contribute to damage in both. Taken together these results suggest that both the cingulum bundle and UF may be useful in predicting future memory decline, and identifying pathologies that contribute to damage in these tracts may be useful in mitigating memory decline.

Competitive models also revealed that the UF was the only tract associated with faster decline in Coding, reflective of processing speed, independent of other tracts. This result is consistent with one study showing that UF FA is weakly associated with processing speed when adjusting for a marker of global of white matter integrity.[248] Given the UF projections to the frontal lobe and its importance in decision making and higher order functions, it is possible that damage to UF fibers leads to difficulty making decisions and longer time is needed to make them. Additionally, we found that the fornix was the only tract associated with faster decline in D-KEFS Number Sequencing, independent of other tracts. This result is somewhat surprising, as the fornix is the major outflow tract from the hippocampus and is necessary for memory consolidation.[249] However, prior studies have found associations between fornix integrity and processing speed,[250,251] suggesting that damage to fornix projections to deep structures in the basal forebrain may be responsible for decline in processing speed. Finally, the competitive models showed that no tract was independently associated with executive function, visuospatial skills, or language. These findings may be because decline in these domains is driven by general white matter health and is not specific to damage in certain tracts. For example, visuospatial skills require connections between the visual cortex in the occipital lobe, motor cortex, and dorsolateral prefrontal cortex.[252] Similarly, while executive function is traditionally thought to localize to the frontal lobe, connections to the basal ganglia[253] and parietal lobe[254] are also necessary. Thus, results suggest that while any individual tract may robustly predict decline in these domains, each tract predicts overlapping variance in domain-specific decline.

We found that baseline FA in certain white matter tracts, including the cingulum bundle, fornix, UF, and ILF, interacted with diagnosis on decline on processing speed (D-KEFS Number Sequencing) and visuospatial skills (HVOT), such that associations between lower baseline FA and faster decline were present in participants with MCI only. The consistency of interactions for these two specific domains suggests that diagnosis is affecting the trajectory of those cognitive domains, rather than baseline integrity in specific tracts. It is possible that associations were present in participants with MCI for these domains because decline in processing speed and visuospatial skills[255] occurs later in the disease process. This hypothesis is consistent with prior work showing visual deficits are only evident later in the disease process[256,257] and cannot be detected in normal older adults,[258] likely because AD pathology initially spares the visual cortex.[3] Additionally, while processing speed declines with normal aging,[259] steeper declines may not occur until individuals with MCI[260] are progressing towards dementia. Future work should explore how integrity in certain tracts may predict future conversion from NC to MCI or from MCI to dementia. Alternatively, it is possible that the D-KEFS Number Sequencing test and the HVOT are not sensitive enough to detect subtle decline in participants with NC, so associations appear to be present in MCI only.

Finally, we found that baseline FA in certain tracts interacted with *APOE*-ε4 status on decline in processing speed, visuospatial skills, and coding. Specifically, baseline FA in the cingulum bundle and ILF interacted with *APOE*-ε4 status on HVOT, such that associations between lower baseline FA in these tracts and faster decline in visuospatial skills were driven by *APOE*-ε4 carriers. Previous work has shown that *APOE*-ε4 may preferentially affect posterior white matter,[261] possibly leading to damage

in tracts with occipital projections, such as the ILF, and faster decline in cognitive domains mediated by the occipital lobe, including visuospatial skills.[262] Baseline FA in the UF also interacted with *APOE*-ε4 status on Coding, such that associations between lower baseline FA in this tract and faster decline in processing speed was also driven by *APOE*-ε4 carriers. Some evidence suggests that *APOE*-ε4 carriers have shortened fiber bundle length in the UF compared to non-carriers,[263] possibly accounting for the faster decline in processing speed. Finally, baseline FA in the tapetum and fornix interacted with *APOE*-ε4 status on the Animal Naming Test, such that associations between lower baseline FA in these tracts and faster decline in language ability was present in *APOE*-ε4 non-carriers only. This finding was unexpected given the effect of *APOE*-ε4 on white matter health and cognitive decline, and future work is needed to better understand these associations. It should be noted that these interactions would not survive correction for multiple comparisons. Findings must be interpreted with caution and replication is needed.

Our study has several strengths, including a well-characterized cohort, stringent quality control procedures, a longitudinal study design, and reliable methods for quantifying cerebral white matter microstructure. An additional strength is the incorporation of novel medial temporal lobe white matter tract templates. The use of white matter tract templates increases consistency between studies as the identical voxels are being evaluated in the Montreal Neurological Institute space, and these tracts provide significantly more coverage of the brain compared to conventional tractography templates.[226] Future work should utilize additional tract templates to interrogate associations with tracts not included here. Despite these strengths, this

study used a cohort which is both highly educated and primarily non-Hispanic white individuals, thus limiting the generalizability to other cohorts. Additionally, partial volume effects within each tract may confound measures of white matter microstructure. Future studies should utilize free water analysis of DTI data, which allows for the separation of extracellular and intracellular components of the diffusion image.[264]

In summary, we found robust associations between lower baseline integrity in tracts traditionally susceptible in AD and cognitive decline in multiple domains. These results add to a growing body of evidence suggesting the importance of incorporating DTI measures as biomarkers of future cognitive decline. Importantly, we found that damage to deep white matter tracts traditionally susceptible to vascular disease related to faster decline in episodic memory, not executive function or processing speed, highlighting the potential role for vascular disease in memory deficits. Finally, we found that damage in both the cingulum bundle and UF independently predicted faster decline in episodic memory, above and beyond other tracts. Results suggest that pathologies leading to damage in either the cingulum bundle or UF may be important to mitigate to slow memory decline in aging and AD.

CHAPTER 6

SUMMARY AND FUTURE DIRECTIONS

Alzheimer's disease (AD) is a growing public health crisis and there are currently no disease modifying treatments,[265] highlighting the need to reconsider traditional models of AD pathogenesis. While AD is traditionally considered a disease of grey matter damage, recent studies suggest that white matter damage may have a greater role in disease pathogenesis than previously recognized. Some white matter changes precede neurodegeneration in sporadic[77] and familial AD,[25] and white matter damage has been cross-sectionally associated with AD pathology, including amyloid-β (Aβ)[81] and phosphorylated tau (p-tau).[25,99] However, AD pathology rarely exists in isolation. Up to 95% of brains with AD pathology at autopsy have additional pathologies present,[11] and up to 87% have concomitant vascular pathology.[11] Vascular disease is thought to be the most prominent etiology of white matter damage in older adults,[24] making it difficult to determine the independent or synergistic effects of vascular disease and AD pathology on white matter integrity.

We set out to determine if age-related changes in systemic and cerebrovascular health, AD pathology, and other concomitant pathologies (including Aβ40, total tau (t-tau), and neurofilament light (NFL)) related to decline in white matter integrity and which white matter tracts were most vulnerable to each pathology. Further, we tested whether certain tracts that may be susceptible to multiple pathologies were more robust predictors of cognitive decline compared to tracts only susceptible to one pathology. To

answer these questions, we leveraged data from the Vanderbilt Memory and Aging Project, a longitudinal cohort of older adults free of stroke and dementia.[130] We utilized sensitive cerebrospinal fluid (CSF) and cardiac magnetic resonance biomarkers of systemic vascular health, cerebrovascular heath, AD pathology, and neurodegeneration, in combination with longitudinal diffusion tensor imaging (DTI) data. We hypothesized that certain tracts may be susceptible to multiple pathologies, resulting in greater cognitive decline primarily in the domains that are supported by those tracts. For example, frontal lobe tracts may be susceptive to both Aβ and vascular disease, leading to faster decline in processing speed and executive function.[44] Similarly, temporal lobe white matter tracts may be susceptible to vascular disease, Aβ, and p-tau, leading to faster decline in memory.[46] A summary of our findings can be found in **Table 6.1**.

Temporal lobe white matter is traditionally considered to be most susceptible to AD pathology, as it corresponds to regions where AD pathology first develops and spreads.[3] However, we found that white matter in the temporal lobe is most susceptible to age-related arterial stiffening, increased blood-brain barrier (BBB) permeability, and neuroaxonal injury, and Aβ42 seems to be a small driver of temporal lobe white matter damage (**Table 6.1, Figure 6.1**). These findings are consistent with prior data showing that the temporal lobe is specifically vulnerable to increases in age-related arterial stiffness[56] and is a site of early BBB breakdown,[147] independent of concomitant AD pathology. Notably, p-tau was not associated with temporal lobe white matter damage, though we hypothesized it would be a robust predictor of white matter damage in that region. Taken together, our results highlight the potential role for vascular disease in AD

progression and that damage to temporal lobe white matter may be one key intersection point for vascular and AD pathology. Temporal lobe white matter integrity predicts future tau propagation,[196] suggesting that vascular disease may confer initial white matter damage and create a more vulnerable environment for tau spread. This hypothesis would provide a possible mechanism for the known associations between vascular disease and tau pathology.[266-268] Additionally, Aβ42 may confer some vulnerability to temporal lobe white matter, promoting tau spread and accounting for some associations between Aβ42 and tau progression.[269] Larger studies are needed to determine how vascular changes and AD pathology synergistically affect white matter health.

Table 6.1. Pathologies Affecting Regional White Matter Tracts

Frontal Lobe Tracts	Temporal Lobe Tracts	Parietal Lobe Tracts	Occipital Lobe Tracts	Deep White Matter Tracts
	Arterial Stiffness		Arterial Stiffness	
MMP-2				
				MMP-3
	BBB Permeability			
Aβ42	Aβ42			
Aβ40		Aβ40		
p-tau		p-tau		
t-tau		t-tau		
NFL	NFL	NFL	NFL	NFL

Note. Arterial stiffness and NFL were the most robust predictors of future white matter damage. Associations between arterial stiffness and white matter microstructure were most robust in MCI and *APOE*-ε4 positive participants. Associations between MMPs and white matter microstructure were most robust in NC and *APOE*-ε4 negative participants. Associations between BBB permeability and white matter microstructure were most robust in *APOE*-ε4 negative participants. Associations between NFL and white matter microstructure were most robust in MCI and *APOE*-ε4 positive participants. Aβ=amyloid-β; APOE=apolipoprotein E; BBB=blood-brain barrier; MCI=mild cognitive impairment; MMP=matrix metalloproteinase; NC=normal cognition; NFL=neurofilament light; p-tau=phosphorylated tau; t-tau=total tau.

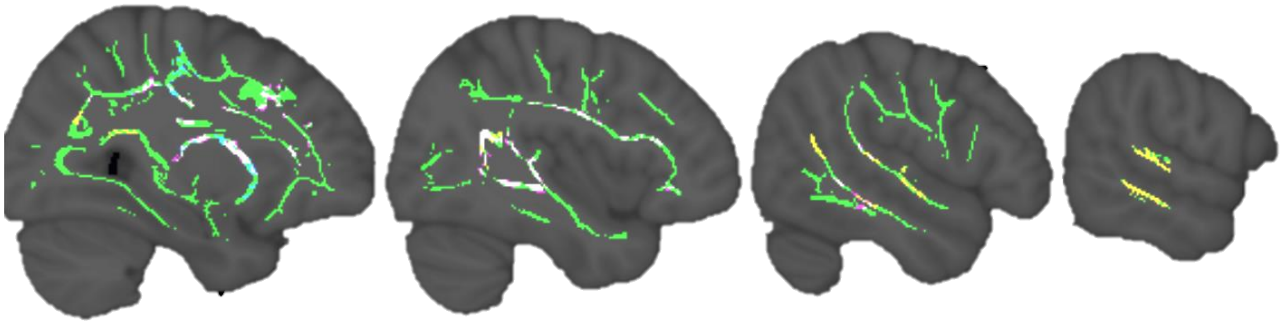

Figure 6.1. Arterial stiffness, NFL, and BBB permeability associations with temporal lobe white matter damage. Locations susceptible to arterial stiffness are in yellow, location susceptible to NFL are in blue, locations susceptible to BBB permeability are in violet, and locations susceptible to multiple pathologies are in white. Z=112,122,132,142 in MNI. BBB=blood-brain barrier; NFL=neurofilament light.

Importantly, we found that the cingulum bundle, which has large temporal lobe projections, independently predicts future memory decline above and beyond other white matter tracts. This finding is consistent with our results showing temporal lobe white matter is susceptible to multiple pathologies. It is possible that each pathology (arterial stiffness, BBB permeability, NFL, and Aβ42, **Figure 6.1**) damages oligodendrocytes or axons through different mechanisms, each individually leading to slower signal propagation and subsequent cognitive deficits. Each mechanism of damage may have an additive affect, leading to faster decline in memory. Future studies should examine if white matter damage mediates associations between various pathologies and cognitive decline. Identifying mechanisms of white matter damage from these pathologies in animal or cell models may provide new therapeutic targets that help mitigate critical white matter injury leading to memory deficits.

A second region that we found is susceptible to multiple etiologies of white matter damage is the frontal lobe. Aβ42, Aβ40, p-tau, t-tau, NFL, and matrix metalloproteinases (MMPs) were all associated with decline in frontal lobe white matter integrity (**Table 6.1, Figure 6.2**), though some associations were relatively small. We also found that the uncinate fasciculus, which projects from the temporal lobe to the prefrontal cortex, independently contributed to decline in episodic memory beyond the cingulum bundle and other white matter tracts. While we did not expect p-tau and t-tau to contribute to white matter damage in the frontal lobe, it is interesting that the two regions where multiple etiologies affect white matter health correspond to the tracts that are the most robust predictors of memory decline. This localization supports our hypothesis that tracts may be susceptible to multiple pathologies, resulting in greater cognitive decline primarily in the domains that are supported by those tracts. Additionally, the association between uncinate fasciculus integrity and memory decline suggests that targeting pathologies affecting the uncinate fasciculus may help mitigate

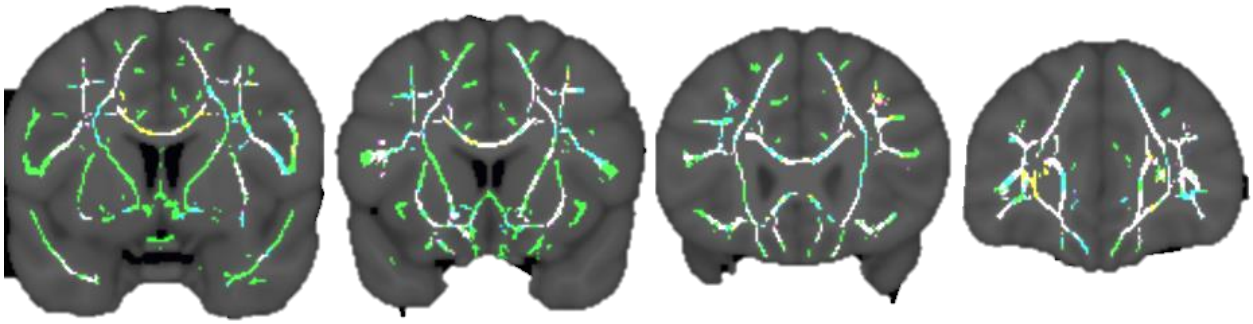

Figure 6.2. MMP-2, NFL, and Aβ42 associations with frontal lobe white matter damage. Locations susceptible to MMP-2 are in yellow, location susceptible to NFL are in violet, locations susceptible to Aβ42 permeability are in blue, and locations susceptible to multiple pathologies are in white. Z=112,122,132,142 in MNI. Aβ=amyloid β; MMP=matrix metalloproteinase; NFL=neurofilament light.

memory decline and frontal lobe white matter may be more important in memory consolidation than previously recognized.

There are some key considerations when interpreting this work. First, the CSF biomarkers examined here represent global pathology burden, so we cannot conclude that pathology accumulation is associated with white matter damage in the same region. We could use positron emission tomography (PET) data to examine this question. By co-registering Aβ or tau PET images with DTI images, we could determine if pathology burden in a specific region is associated with white matter damage in that region. These studies would help confirm that certain pathologies are directly contributing to white matter damage. Additionally, it is still unclear how some of the CSF biomarkers examined here relate to cerebral protein expression and function. For example, increased MMP biomarkers in the CSF may not truly reflect increased MMP expression, and function of the MMP proteins cannot be deduced from the CSF assays. In future experiments, post-mortem pathologic analysis could be used to determine location of MMP expression and if the protein was functional. If combined with post-mortem DTI imaging, we could determine if increased MMP function or lack of function account for white matter damage in certain regions.

Another consideration when interpreting these data is the limitations of DTI. While DTI is sensitive to white matter microstructure, each voxel contains an intracellular and extracellular component. Thus, it is difficult to determine if the DTI changes are due to intracellular or extracellular pathology.[270] Recently, new methods for post-processing DTI data have been established, including free water imaging[271] and neurite orientation and dispersion and density imaging,[272] that may differentiate

between different kinds of white matter damage. Further, while some evidence suggests that certain DTI metrics are specific to axonal injury[119] or demyelination,[119] more work is needed to clarify the biology underlying changes in individual DTI metrics. To study the underlying cellular changes, we could use post-mortem DTI in conjunction with pathologic grading of white matter injury. Comparing individual DTI metrics to white matter damage detected on histopathology (e.g., tissue rarefaction, axonal loss, hyalinization) in the same region could inform the biological interpretation of these metrics. We could also use cerebral organoid models to assess how different pathologies affect white matter. By reconstructing the neurovascular unit through co-culturing neurons, endothelial cells, microglia, astrocytes, and oligodendrocytes, we could examine how the structure or protein expression levels within the oligodendrocyte or axon change in response to different pathologies, such as Aβ or p-tau.

A final consideration is the longitudinal post-processing method implemented here. We adapted the well-established cross-sectional tract-based spatial statistics[141] processing pipeline to a longitudinal framework to perform longitudinal voxel-wise analyses. This approach allowed us to examine if a certain pathology affected white matter health across the entire brain, rather than focusing on a set of regions *a priori,* which is currently the most common approach in longitudinal DTI studies. Tract-based spatial statistics creates a white matter skeleton, only including voxels in the center of major white matter tracts. This approach reduces the number of comparisons made and increases confidence that we are truly detecting changes in white matter. However, we would expect that the first and most robust changes to white matter integrity occur on the periphery of smaller tracts, possibly leading to some false negatives in our findings.

Additionally, the cluster-wise inference used to correct the voxel-wise analyses was based on functional magnetic resonance imaging (MRI) data. The skeleton includes significantly less voxels than a typical functional MRI image, also possibly leading to false negative findings. Therefore, though some of the clusters were rather small, it is important to consider that the analytical methods used were quite robust, increasing confidence in these small findings.

Future work should also examine the pathologies mediating findings reported here. For example, studies should compare if reduced cerebral blood flow[56] or inflammation,[268] both related to increased arterial stiffness, are associated with white matter damage in the same regions as pulse wave velocity. Finally, examining which white matter tracts may be most susceptible to other aspects of vascular health, such as cardiac output, ejection fraction, or pericyte function, is necessary to further characterize different profiles of white matter damage in aging adults.

Collectively, this body of work has shown that white matter injury may be a critical point of intersection between AD and concomitant pathologies. While some white matter damage is due to AD pathology directly, other pathologies, including arterial stiffening and neuroaxonal injury, were more robust predictors of white matter damage. Given the rate at which these pathologies co-occur, these additional pathologies may provide an initial hit to white matter health in the temporal and frontal lobes, making some tracts more vulnerable to additional damage and worse cognitive outcomes. Future work should focus on integrating white matter damage into models of AD pathogenesis, investigating how tract-specific measures of white matter integrity may be used to assess risk of disease progression, and examining the cellular mechanisms

leading to white matter injury to develop new therapies aimed at attenuating white matter damage.

REFERENCES

1. 2021 Alzheimer's disease facts and figures. *Alzheimers Dement*. 2021;17:327-406.
2. Wilkins HM and Swerdlow RH. Amyloid precursor protein processing and bioenergetics. *Brain Res Bull*. 2017;133:71-79.
3. Braak H and Braak E. Neuropathological stageing of Alzheimer-related changes. *Acta Neuropathol*. 1991;82:239-259.
4. Olsson B, Lautner R, Andreasson U, Ohrfelt A, Portelius E, Bjerke M, . . . Zetterberg H. CSF and blood biomarkers for the diagnosis of Alzheimer's disease: a systematic review and meta-analysis. *The Lancet Neurology*. 2016;15:673-684.
5. Blennow K, Mattsson N, Schöll M, Hansson O and Zetterberg H. Amyloid biomarkers in Alzheimer's disease. *Trends in pharmacological sciences*. 2015;36:297-309.
6. Naseri NN, Wang H, Guo J, Sharma M and Luo W. The complexity of tau in Alzheimer's disease. *Neurosci Lett*. 2019;705:183-194.
7. Franzmeier N, Neitzel J, Rubinski A, Smith R, Strandberg O, Ossenkoppele R, . . . Alzheimer’s Disease Neuroimaging I. Functional brain architecture is associated with the rate of tau accumulation in Alzheimer’s disease. *Nat Commun*. 2020;11:347.
8. Hall B, Mak E, Cervenka S, Aigbirhio FI, Rowe JB and O'Brien JT. In vivo tau PET imaging in dementia: Pathophysiology, radiotracer quantification, and a systematic review of clinical findings. *Ageing research reviews*. 2017;36:50-63.
9. Jack CR, Jr., Knopman DS, Jagust WJ, Shaw LM, Aisen PS, Weiner MW, . . . Trojanowski JQ. Hypothetical model of dynamic biomarkers of the Alzheimer's pathological cascade. *Lancet Neurology*. 2010;9:119-28.
10. Storandt M, Balota DA, Aschenbrenner AJ and Morris JC. Clinical and psychological characteristics of the initial cohort of the Dominantly Inherited Alzheimer Network (DIAN). *Neuropsychology*. 2014;28:19-29.
11. Kapasi A, DeCarli C and Schneider JA. Impact of multiple pathologies on the threshold for clinically overt dementia. *Acta Neuropathol*. 2017;134:171-186.
12. Snowdon DA, Greiner LH, Mortimer JA, Riley KP, Greiner PA and Markesbery WR. Brain infarction and the clinical expression of Alzheimer disease. The Nun Study. *Journal of American Medical Association*. 1997;277:813-817.
13. Rossi R, Geroldi C, Bresciani L, Testa C, Binetti G, Zanetti O and Frisoni GB. Clinical and neuropsychological features associated with structural imaging patterns in patients with mild cognitive impairment. *Dementia & Geriatric Cognitive Disorders*. 2007;23:175-183.
14. Debette S, Bombois S, Bruandet A, Delbeuck X, Lepoittevin S, Delmaire C, . . . Pasquier F. Subcortical hyperintensities are associated with cognitive decline in patients with mild cognitive impairment. *Stroke*. 2007;38:2924-30.
15. Vemuri P, Lesnick TG, Przybelski SA, Knopman DS, Preboske GM, Kantarci K, . . . Jack CR, Jr. Vascular and amyloid pathologies are independent predictors of cognitive decline in normal elderly. *Brain*. 2015;138:761-71.
16. Rabin JS, Schultz AP, Hedden T and et al. Interactive associations of vascular risk and β-amyloid burden with cognitive decline in clinically normal elderly individuals: Findings from the harvard aging brain study. *JAMA Neurol*. 2018;75:1124-1131.

17. Kim HJ, Park S, Cho H, Jang YK, San Lee J, Jang H, . . . Seo SW. Assessment of Extent and Role of Tau in Subcortical Vascular Cognitive Impairment Using 18F-AV1451 Positron Emission Tomography Imaging. *JAMA Neurol*. 2018.
18. Bangen KJ, Clark AL, Edmonds EC, Evangelista ND, Werhane ML, Thomas KR, . . . Delano-Wood L. Cerebral blood flow and amyloid-beta interact to affect memory performance in cognitively normal older adults. *Front Aging Neurosci*. 2017;9:181.
19. Yew B and Nation DA. Cerebrovascular resistance: effects on cognitive decline, cortical atrophy, and progression to dementia. *Brain*. 2017;140:1987-2001.
20. Longstreth WT, Jr., Manolio TA, Arnold A, Burke GL, Bryan N, Jungreis CA, . . . Fried L. Clinical correlates of white matter findings on cranial magnetic resonance imaging of 3301 elderly people. The Cardiovascular Health Study. *Stroke*. 1996;27:1274-1282.
21. Liao D, Cooper L, Cai J, Toole J, Bryan N, Burke G, . . . Heiss G. The prevalence and severity of white matter lesions, their relationship with age, ethnicity, gender, and cardiovascular disease risk factors: the ARIC Study. *Neuroepidemiology*. 1997;16:149-62.
22. Carmichael O, Schwarz C, Drucker D, Fletcher E, Harvey D, Beckett L, . . . DeCarli C. Longitudinal changes in white matter disease and cognition in the first year of the Alzheimer disease neuroimaging initiative. *Arch Neurol*. 2010;67:1370-8.
23. Vernooij MW, Ikram MA, Vrooman HA, Wielopolski PA, Krestin GP, Hofman A, . . . Breteler MM. White matter microstructural integrity and cognitive function in a general elderly population. *Archives of general psychiatry*. 2009;66:545-53.
24. Black S, Gao F and Bilbao J. Understanding white matter disease: imaging-pathological correlations in vascular cognitive impairment. *Stroke*. 2009;40:S48-52.
25. Araque Caballero MA, Suarez-Calvet M, Duering M, Franzmeier N, Benzinger T, Fagan AM, . . . Ewers M. White matter diffusion alterations precede symptom onset in autosomal dominant Alzheimer's disease. *Brain*. 2018;141:3065-3080.
26. Einheber S, Zanazzi G, Ching W, Scherer S, Milner TA, Peles E and Salzer JL. The axonal membrane protein Caspr, a homologue of neurexin IV, is a component of the septate-like paranodal junctions that assemble during myelination. *The Journal of cell biology*. 1997;139:1495-506.
27. Rios JC, Rubin M, St Martin M, Downey RT, Einheber S, Rosenbluth J, . . . Salzer JL. Paranodal interactions regulate expression of sodium channel subtypes and provide a diffusion barrier for the node of Ranvier. *J Neurosci*. 2003;23:7001-11.
28. Eshed Y, Feinberg K, Poliak S, Sabanay H, Sarig-Nadir O, Spiegel I, . . . Peles E. Gliomedin mediates Schwann cell-axon interaction and the molecular assembly of the nodes of Ranvier. *Neuron*. 2005;47:215-29.
29. Zhou D, Lambert S, Malen PL, Carpenter S, Boland LM and Bennett V. AnkyrinG is required for clustering of voltage-gated Na channels at axon initial segments and for normal action potential firing. *The Journal of cell biology*. 1998;143:1295-304.
30. Charles P, Tait S, Faivre-Sarrailh C, Barbin G, Gunn-Moore F, Denisenko-Nehrbass N, . . . Lubetzki C. Neurofascin is a glial receptor for the paranodin/Caspr-contactin axonal complex at the axoglial junction. *Current biology : CB*. 2002;12:217-20.
31. Poliak S, Gollan L, Martinez R, Custer A, Einheber S, Salzer JL, . . . Peles E. Caspr2, a new member of the neurexin superfamily, is localized at the juxtaparanodes of myelinated axons and associates with K+ channels. *Neuron*. 1999;24:1037-47.

32. Stolinski C, Breathnach AS, Martin B, Thomas PK, King RH and Gabriel G. Associated particle aggregates in juxtaparanodal axolemma and adaxonal Schwann cell membrane of rat peripheral nerve. *Journal of neurocytology*. 1981;10:679-91.
33. Aggarwal S, Snaidero N, Pahler G, Frey S, Sanchez P, Zweckstetter M, . . . Simons M. Myelin membrane assembly is driven by a phase transition of myelin basic proteins into a cohesive protein meshwork. *PLoS biology*. 2013;11:e1001577.
34. Branson HM. Normal myelination: a practical pictorial review. *Neuroimaging clinics of North America*. 2013;23:183-95.
35. Bennett IJ, Madden DJ, Vaidya CJ, Howard DV and Howard JH, Jr. Age-related differences in multiple measures of white matter integrity: A diffusion tensor imaging study of healthy aging. *Hum Brain Mapp*. 2010;31:378-90.
36. Kusano K and LaVail MM. Impulse conduction in the shrimp medullated giant fiber with special reference to the structure of functionally excitable areas. *The Journal of comparative neurology*. 1971;142:481-94.
37. Waxman SG and Sims TJ. Specificity in central myelination: evidence for local regulation of myelin thickness. *Brain research*. 1984;292:179-85.
38. Moore JW, Joyner RW, Brill MH, Waxman SD and Najar-Joa M. Simulations of conduction in uniform myelinated fibers. Relative sensitivity to changes in nodal and internodal parameters. *Biophysical journal*. 1978;21:147-60.
39. Garcia ML, Lobsiger CS, Shah SB, Deerinck TJ, Crum J, Young D, . . . Cleveland DW. NF-M is an essential target for the myelin-directed "outside-in" signaling cascade that mediates radial axonal growth. *The Journal of cell biology*. 2003;163:1011-20.
40. Sakaguchi T, Okada M, Kitamura T and Kawasaki K. Reduced diameter and conduction velocity of myelinated fibers in the sciatic nerve of a neurofilament-deficient mutant quail. *Neurosci Lett*. 1993;153:65-8.
41. Misgeld T, Kerschensteiner M, Bareyre FM, Burgess RW and Lichtman JW. Imaging axonal transport of mitochondria in vivo. *Nature Methods*. 2007;4:559.
42. Lee Y, Morrison BM, Li Y, Lengacher S, Farah MH, Hoffman PN, . . . Rothstein JD. Oligodendroglia metabolically support axons and contribute to neurodegeneration. *Nature*. 2012;487:443-8.
43. Namboodiri AM, Peethambaran A, Mathew R, Sambhu PA, Hershfield J, Moffett JR and Madhavarao CN. Canavan disease and the role of N-acetylaspartate in myelin synthesis. *Molecular and cellular endocrinology*. 2006;252:216-23.
44. Biesbroek JM, Weaver NA, Hilal S, Kuijf HJ, Ikram MK, Xu X, . . . Chen CP. Impact of Strategically Located White Matter Hyperintensities on Cognition in Memory Clinic Patients with Small Vessel Disease. *PLoS One*. 2016;11:e0166261.
45. Squire LR. The legacy of patient H.M. for neuroscience. *Neuron*. 2009;61:6-9.
46. Burgess N, Maguire EA and O'Keefe J. The human hippocampus and spatial and episodic memory. *Neuron*. 2002;35:625-41.
47. O'Brien JT, Wiseman R, Burton EJ, Barber B, Wesnes K, Saxby B and Ford GA. Cognitive associations of subcortical white matter lesions in older people. *Annals of the New York Academy of Sciences*. 2002;977:436-44.
48. Maillard P, Carmichael OT, Reed B, Mungas D and DeCarli C. Cooccurrence of vascular risk factors and late-life white-matter integrity changes. *Neurobiol Aging*. 2015;36:1670-1677.

49. Wen W and Sachdev PS. Extent and distribution of white matter hyperintensities in stroke patients: the Sydney Stroke Study. *Stroke*. 2004;35:2813-9.
50. Ferris JK, Edwards JD, Ma JA and Boyd LA. Changes to white matter microstructure in transient ischemic attack: A longitudinal diffusion tensor imaging study. *Hum Brain Mapp*. 2017;38:5795-5803.
51. Avolio A. Arterial Stiffness. *Pulse (Basel, Switzerland)*. 2013;1:14-28.
52. Wang M, Takagi G, Asai K, Resuello RG, Natividad FF, Vatner DE, . . . Lakatta EG. Aging increases aortic MMP-2 activity and angiotensin II in nonhuman primates. *Hypertension*. 2003;41:1308-16.
53. Urry DW. Neutral sites for calcium ion binding to elastin and collagen: a charge neutralization theory for calcification and its relationship to atherosclerosis. *Proc Natl Acad Sci U S A*. 1971;68:810-4.
54. Sims TJ, Rasmussen LM, Oxlund H and Bailey AJ. The role of glycation cross-links in diabetic vascular stiffening. *Diabetologia*. 1996;39:946-51.
55. Saphirstein RJ, Gao YZ, Jensen MH, Gallant CM, Vetterkind S, Moore JR and Morgan KG. The focal adhesion: a regulated component of aortic stiffness. *PLoS One*. 2013;8:e62461.
56. Jefferson AL, Cambronero FE, Liu D, Moore EE, Neal JE, Terry JG, . . . Carr JJ. Higher aortic stiffness is related to lower cerebral blood flow and preserved cerebrovascular reactivity in older adults. *Circulation*. 2018;138:1951-1962.
57. Torvik A. The pathogenesis of watershed infarcts in the brain. *Stroke*. 1984;15:221-3.
58. Nishimura N, Schaffer CB, Friedman B, Lyden PD and Kleinfeld D. Penetrating arterioles are a bottleneck in the perfusion of neocortex. *Proc Natl Acad Sci U S A*. 2007;104:365-70.
59. Cipolla MJ, Li R and Vitullo L. Perivascular innervation of penetrating brain parenchymal arterioles. *Journal of cardiovascular pharmacology*. 2004;44:1-8.
60. Coutinho T, Turner ST and Kullo IJ. Aortic pulse wave velocity is associated with measures of subclinical target organ damage. *JACC Cardiovascular imaging*. 2011;4:754-61.
61. Kang CK, Park CA, Lee H, Kim SH, Park CW, Kim YB and Cho ZH. Hypertension correlates with lenticulostriate arteries visualized by 7T magnetic resonance angiography. *Hypertension*. 2009;54:1050-6.
62. Pantoni L, Garcia JH and Gutierrez JA. Cerebral white matter is highly vulnerable to ischemia. *Stroke*. 1996;27:1641-6; discussion 1647.
63. Shibata M, Hisahara S, Hara H, Yamawaki T, Fukuuchi Y, Yuan J, . . . Miura M. Caspases determine the vulnerability of oligodendrocytes in the ischemic brain. *J Clin Invest*. 2000;106:643-53.
64. Tekkok SB and Goldberg MP. Ampa/kainate receptor activation mediates hypoxic oligodendrocyte death and axonal injury in cerebral white matter. *J Neurosci*. 2001;21:4237-48.
65. Tekkok SB, Ye Z and Ransom BR. Excitotoxic mechanisms of ischemic injury in myelinated white matter. *J Cereb Blood Flow Metab*. 2007;27:1540-52.
66. Thorburne SK and Juurlink BH. Low glutathione and high iron govern the susceptibility of oligodendroglial precursors to oxidative stress. *Journal of neurochemistry*. 1996;67:1014-22.

67. Merrill JE, Ignarro LJ, Sherman MP, Melinek J and Lane TE. Microglial cell cytotoxicity of oligodendrocytes is mediated through nitric oxide. *Journal of immunology (Baltimore, Md : 1950)*. 1993;151:2132-41.
68. Freitas-Rodríguez S, Folgueras AR and López-Otín C. The role of matrix metalloproteinases in aging: Tissue remodeling and beyond. *Biochimica et biophysica acta Molecular cell research*. 2017;1864:2015-2025.
69. Zlokovic BV. The blood-brain barrier in health and chronic neurodegenerative disorders. *Neuron*. 2008;57:178-201.
70. Farrall AJ and Wardlaw JM. Blood-brain barrier: ageing and microvascular disease--systematic review and meta-analysis. *Neurobiol Aging*. 2009;30:337-52.
71. Rempe RG, Hartz AMS and Bauer B. Matrix metalloproteinases in the brain and blood-brain barrier: Versatile breakers and makers. *J Cereb Blood Flow Metab*. 2016;36:1481-507.
72. Duca L, Blaise S, Romier B, Laffargue M, Gayral S, El Btaouri H, . . . Maurice P. Matrix ageing and vascular impacts: focus on elastin fragmentation. *Cardiovascular research*. 2016;110:298-308.
73. Lu P, Takai K, Weaver VM and Werb Z. Extracellular matrix degradation and remodeling in development and disease. *Cold Spring Harbor perspectives in biology*. 2011;3.
74. Candelario-Jalil E, Thompson J, Taheri S, Grossetete M, Adair JC, Edmonds E, . . . Rosenberg GA. Matrix Metalloproteinases Are Associated With Increased Blood-Brain Barrier Opening in Vascular Cognitive Impairment. *Stroke*. 2011;42:1345-1350.
75. Corbin ZA, Rost NS, Lorenzano S, Kernan WN, Parides MK, Blumberg JB, . . . Furie KL. White matter hyperintensity volume correlates with matrix metalloproteinase-2 in acute ischemic stroke. *J Stroke Cerebrovasc Dis*. 2014;23:1300-6.
76. Li Y, Li M, Zhang X, Shi Q, Yang S, Fan H, . . . Hu W. Higher blood-brain barrier permeability is associated with higher white matter hyperintensities burden. *J Neurol*. 2017;264:1474-1481.
77. Agosta F, Pievani M, Sala S, Geroldi C, Galluzzi S, Frisoni GB and Filippi M. White matter damage in Alzheimer disease and its relationship to gray matter atrophy. *Radiology*. 2011;258:853-63.
78. Lee S, Viqar F, Zimmerman ME, Narkhede A, Tosto G, Benzinger TL, . . . Brickman AM. White matter hyperintensities are a core feature of Alzheimer's disease: Evidence from the dominantly inherited Alzheimer network. *Ann Neurol*. 2016;79:929-39.
79. Scott JA, Braskie MN, Tosun D, Thompson PM, Weiner M, DeCarli C and Carmichael OT. Cerebral Amyloid and Hypertension are Independently Associated with White Matter Lesions in Elderly. *Front Aging Neurosci*. 2015;7:221.
80. Hwang SJ, Adluru N, Kim WH, Johnson SC, Bendlin BB and Singh V. Associations Between Positron Emission Tomography Amyloid Pathology and Diffusion Tensor Imaging Brain Connectivity in Pre-Clinical Alzheimer's Disease. *Brain connectivity*. 2019;9:162-173.
81. Moore EE, Hohman TJ, Badami FS, Pechman KR, Osborn KE, Acosta LMY, . . . Jefferson AL. Neurofilament relates to white matter microstructure in older adults. *Neurobiol Aging*. 2018;70:233-241.

82. Kantarci K, Schwarz CG, Reid RI, Przybelski SA, Lesnick TG, Zuk SM, . . . Jack CR, Jr. White matter integrity determined with diffusion tensor imaging in older adults without dementia: influence of amyloid load and neurodegeneration. *JAMA Neurol*. 2014;71:1547-54.
83. Collins-Praino LE, Francis YI, Griffith EY, Wiegman AF, Urbach J, Lawton A, . . . Brickman AM. Soluble amyloid beta levels are elevated in the white matter of Alzheimer's patients, independent of cortical plaque severity. *Acta Neuropathol*. 2014;2:83.
84. Bateman RJ, Xiong C, Benzinger TLS, Fagan AM, Goate A, Fox NC, . . . Morris JC. Clinical and biomarker changes in dominantly inherited Alzheimer's disease. *N Engl J Med*. 2012;367:795-804.
85. Song SK, Kim JH, Lin SJ, Brendza RP and Holtzman DM. Diffusion tensor imaging detects age-dependent white matter changes in a transgenic mouse model with amyloid deposition. *Neurobiology of disease*. 2004;15:640-7.
86. Desai MK, Sudol KL, Janelsins MC, Mastrangelo MA, Frazer ME and Bowers WJ. Triple-transgenic Alzheimer's disease mice exhibit region-specific abnormalities in brain myelination patterns prior to appearance of amyloid and tau pathology. *Glia*. 2009;57:54-65.
87. Gu L, Wu D, Tang X, Qi X, Li X, Bai F, . . . Zhang Z. Myelin changes at the early stage of 5XFAD mice. *Brain Res Bull*. 2018;137:285-293.
88. Allaman I, Gavillet M, Belanger M, Laroche T, Viertl D, Lashuel HA and Magistretti PJ. Amyloid-beta aggregates cause alterations of astrocytic metabolic phenotype: impact on neuronal viability. *J Neurosci*. 2010;30:3326-38.
89. Lee JT, Xu J, Lee JM, Ku G, Han X, Yang DI, . . . Hsu CY. Amyloid-beta peptide induces oligodendrocyte death by activating the neutral sphingomyelinase-ceramide pathway. *The Journal of cell biology*. 2004;164:123-31.
90. Bose R, Verheij M, Haimovitz-Friedman A, Scotto K, Fuks Z and Kolesnick R. Ceramide synthase mediates daunorubicin-induced apoptosis: an alternative mechanism for generating death signals. *Cell*. 1995;82:405-14.
91. Liu Y, Peterson DA and Schubert D. Amyloid beta peptide alters intracellular vesicle trafficking and cholesterol homeostasis. *Proc Natl Acad Sci U S A*. 1998;95:13266-71.
92. Roher AE, Weiss N, Kokjohn TA, Kuo YM, Kalback W, Anthony J, . . . Beach T. Increased A beta peptides and reduced cholesterol and myelin proteins characterize white matter degeneration in Alzheimer's disease. *Biochemistry*. 2002;41:11080-90.
93. Horiuchi M, Maezawa I, Itoh A, Wakayama K, Jin LW, Itoh T and Decarli C. Amyloid beta1-42 oligomer inhibits myelin sheet formation in vitro. *Neurobiol Aging*. 2012;33:499-509.
94. Viswanathan A and Greenberg SM. Cerebral amyloid angiopathy in the elderly. *Ann Neurol*. 2011;70:871-80.
95. Greenberg SM, Bacskai BJ, Hernandez-Guillamon M, Pruzin J, Sperling R and van Veluw SJ. Cerebral amyloid angiopathy and Alzheimer disease — one peptide, two pathways. *Nature Reviews Neurology*. 2020;16:30-42.
96. Whitwell JL, Josephs KA, Murray ME, Kantarci K, Przybelski SA, Weigand SD, . . . Jack CR, Jr. MRI correlates of neurofibrillary tangle pathology at autopsy: a voxel-based morphometry study. *Neurology*. 2008;71:743-9.

97. Strain JF, Smith RX, Beaumont H, Roe CM, Gordon BA, Mishra S, . . . Ances BM. Loss of white matter integrity reflects tau accumulation in Alzheimer disease defined regions. *Neurology*. 2018;91:e313-e318.
98. Amlien IK, Fjell AM, Walhovd KB, Selnes P, Stenset V, Grambaite R, . . . Fladby T. Mild cognitive impairment: cerebrospinal fluid tau biomarker pathologic levels and longitudinal changes in white matter integrity. *Radiology*. 2013;266:295-303.
99. Kantarci K, Murray ME, Schwarz CG, Reid RI, Przybelski SA, Lesnick T, . . . Dickson DW. White-matter integrity on DTI and the pathologic staging of Alzheimer's disease. *Neurobiol Aging*. 2017;56:172-179.
100. McAleese KE, Firbank M, Dey M, Colloby SJ, Walker L, Johnson M, . . . Attems J. Cortical tau load is associated with white matter hyperintensities. *Acta Neuropathol Commun*. 2015;3:60.
101. McAleese KE, Walker L, Graham S, Moya ELJ, Johnson M, Erskine D, . . . Attems J. Parietal white matter lesions in Alzheimer's disease are associated with cortical neurodegenerative pathology, but not with small vessel disease. *Acta Neuropathol*. 2017;134:459-473.
102. Colgan N, Siow B, O'Callaghan JM, Harrison IF, Wells JA, Holmes HE, . . . Lythgoe MF. Application of neurite orientation dispersion and density imaging (NODDI) to a tau pathology model of Alzheimer's disease. *Neuroimage*. 2016;125:739-744.
103. Sahara N, Perez PD, Lin WL, Dickson DW, Ren Y, Zeng H, . . . Febo M. Age-related decline in white matter integrity in a mouse model of tauopathy: an in vivo diffusion tensor magnetic resonance imaging study. *Neurobiol Aging*. 2014;35:1364-74.
104. Wells JA, O'Callaghan JM, Holmes HE, Powell NM, Johnson RA, Siow B, . . . Lythgoe MF. In vivo imaging of tau pathology using multi-parametric quantitative MRI. *Neuroimage*. 2015;111:369-78.
105. Hoover BR, Reed MN, Su J, Penrod RD, Kotilinek LA, Grant MK, . . . Liao D. Tau mislocalization to dendritic spines mediates synaptic dysfunction independently of neurodegeneration. *Neuron*. 2010;68:1067-81.
106. Hinzman JM, Thomas TC, Burmeister JJ, Quintero JE, Huettl P, Pomerleau F, . . . Lifshitz J. Diffuse brain injury elevates tonic glutamate levels and potassium-evoked glutamate release in discrete brain regions at two days post-injury: an enzyme-based microelectrode array study. *Journal of neurotrauma*. 2010;27:889-99.
107. Werner P, Pitt D and Raine CS. Multiple sclerosis: altered glutamate homeostasis in lesions correlates with oligodendrocyte and axonal damage. *Ann Neurol*. 2001;50:169-80.
108. Chakraborty G, Mekala P, Yahya D, Wu G and Ledeen RW. Intraneuronal N-acetylaspartate supplies acetyl groups for myelin lipid synthesis: evidence for myelin-associated aspartoacylase. *Journal of neurochemistry*. 2001;78:736-45.
109. Conforti L, Gilley J and Coleman MP. Wallerian degeneration: an emerging axon death pathway linking injury and disease. *Nature Reviews Neuroscience*. 2014;15:394-409.
110. Tosto G, Zimmerman ME, Hamilton JL, Carmichael OT and Brickman AM. The effect of white matter hyperintensities on neurodegeneration in mild cognitive impairment. *Alzheimers Dement*. 2015;11:1510-9.

111. Osborn KE, Liu D, Samuels LR, Moore EE, Cambronero FE, Acosta LMY, . . . Jefferson AL. Cerebrospinal fluid β-amyloid42 and neurofilament light relate to white matter hyperintensities. *Neurobiol Aging*. 2018;68:18-25.
112. Wen W, Sachdev PS, Chen X and Anstey K. Gray matter reduction is correlated with white matter hyperintensity volume: a voxel-based morphometric study in a large epidemiological sample. *Neuroimage*. 2006;29:1031-9.
113. Simpson JE, Ince PG, Higham CE, Gelsthorpe CH, Fernando MS, Matthews F, . . . Wharton SB. Microglial activation in white matter lesions and nonlesional white matter of ageing brains. *Neuropathology and applied neurobiology*. 2007;33:670-83.
114. Walker KA, Power MC, Hoogeveen RC, Folsom AR, Ballantyne CM, Knopman DS, . . . Gottesman RF. Midlife Systemic Inflammation, Late-Life White Matter Integrity, and Cerebral Small Vessel Disease: The Atherosclerosis Risk in Communities Study. *Stroke*. 2017;48:3196-3202.
115. Stejskal EO and Tanner JE. Spin Diffusion Measurements: Spin Echoes in the Presence of a Time-Dependent Field Gradient. 1965;42:288-292.
116. Chung S, Lu Y and Henry RG. Comparison of bootstrap approaches for estimation of uncertainties of DTI parameters. *Neuroimage*. 2006;33:531-41.
117. Moulton E, Amor-Sahli M, Perlbarg V, Pires C, Crozier S, Galanaud D, . . . Rosso C. Axial Diffusivity of the Corona Radiata at 24 Hours Post-Stroke: A New Biomarker for Motor and Global Outcome. *PLoS One*. 2015;10:e0142910.
118. Sun J, Zhou H, Bai F, Ren Q and Zhang Z. Myelin injury induces axonal transport impairment but not AD-like pathology in the hippocampus of cuprizone-fed mice. *Oncotarget*. 2016;7:30003-17.
119. Song SK, Sun SW, Ramsbottom MJ, Chang C, Russell J and Cross AH. Dysmyelination revealed through MRI as increased radial (but unchanged axial) diffusion of water. *Neuroimage*. 2002;17:1429-36.
120. Attems J and Jellinger KA. The overlap between vascular disease and Alzheimer's disease--lessons from pathology. *BMC Med*. 2014;12:206.
121. Vermeer SE, Hollander M, van Dijk EJ, Hofman A, Koudstaal PJ and Breteler MM. Silent brain infarcts and white matter lesions increase stroke risk in the general population: the Rotterdam Scan Study. *Stroke*. 2003;34:1126-1129.
122. Mitchell GF, Parise H, Benjamin EJ, Larson MG, Keyes MJ, Vita JA, . . . Levy D. Changes in arterial stiffness and wave reflection with advancing age in healthy men and women: the Framingham Heart Study. *Hypertension*. 2004;43:1239-1245.
123. Wardlaw JM, Makin SJ, Valdés Hernández MC, Armitage PA, Heye AK, Chappell FM, . . . Thrippleton MJ. Blood-brain barrier failure as a core mechanism in cerebral small vessel disease and dementia: evidence from a cohort study. *Alzheimer's & dementia : the journal of the Alzheimer's Association*. 2017;13:634-643.
124. Tamaki K, Sadoshima S, Baumbach GL, Iadecola C, Reis DJ and Heistad DD. Evidence that disruption of the blood-brain barrier precedes reduction in cerebral blood flow in hypertensive encephalopathy. *Hypertension*. 1984;6:I75-81.
125. Yang Y, Estrada EY, Thompson JF, Liu W and Rosenberg GA. Matrix metalloproteinase-mediated disruption of tight junction proteins in cerebral vessels is reversed by synthetic matrix metalloproteinase inhibitor in focal ischemia in rat. *J Cereb Blood Flow Metab*. 2007;27:697-709.

126. Clark AW, Krekoski CA, Bou SS, Chapman KR and Edwards DR. Increased gelatinase A (MMP-2) and gelatinase B (MMP-9) activities in human brain after focal ischemia. *Neurosci Lett*. 1997;238:53-6.
127. Yang Y, Jalal FY, Thompson JF, Walker EJ, Candelario-Jalil E, Li L, . . . Rosenberg GA. Tissue inhibitor of metalloproteinases-3 mediates the death of immature oligodendrocytes via TNF-α/TACE in focal cerebral ischemia in mice. *J Neuroinflammation*. 2011;8:108.
128. Rosell A, Ortega-Aznar A, Alvarez-Sabín J, Fernández-Cadenas I, Ribó M, Molina CA, . . . Montaner J. Increased brain expression of matrix metalloproteinase-9 after ischemic and hemorrhagic human stroke. *Stroke*. 2006;37:1399-406.
129. Raber J, Huang Y and Ashford JW. ApoE genotype accounts for the vast majority of AD risk and AD pathology. *Neurobiol Aging*. 2004;25:641-50.
130. Jefferson AL, Gifford KA, Acosta LM, Bell SP, Donahue MJ, Taylor Davis L, . . . Liu D. The Vanderbilt Memory & Aging Project: Study design and baseline cohort overview. *J Alzheimers Dis*. 2016;52:539-559.
131. Aisen PS, Petersen RC, Donohue MC, Gamst A, Raman R, Thomas RG, . . . Alzheimer's Disease Neuroimaging I. Clinical Core of the Alzheimer's Disease Neuroimaging Initiative: progress and plans. *Alzheimers Dement*. 2010;6:239-246.
132. Albert MS, DeKosky ST, Dickson D, Dubois B, Feldman HH, Fox NC, . . . Phelps CH. The diagnosis of mild cognitive impairment due to Alzheimer's disease: recommendations from the National Institute on Aging-Alzheimer's Association workgroups on diagnostic guidelines for Alzheimer's disease. *Alzheimers Dement*. 2011;7:270-279.
133. Chaosuwannakit N, D'Agostino R, Jr., Hamilton CA, Lane KS, Ntim WO, Lawrence J, . . . Hundley WG. Aortic stiffness increases upon receipt of anthracycline chemotherapy. *Journal of clinical oncology : official journal of the American Society of Clinical Oncology*. 2010;28:166-72.
134. Bjerke M, Zetterberg H, Edman A, Blennow K, Wallin A and Andreasson U. Cerebrospinal fluid matrix metalloproteinases and tissue inhibitor of metalloproteinases in combination with subcortical and cortical biomarkers in vascular dementia and Alzheimer's disease. *J Alzheimers Dis*. 2011;27:665-676.
135. Minta K, Brinkmalm G, Al Nimer F, Thelin EP, Piehl F, Tullberg M, . . . Andreasson U. Dynamics of cerebrospinal fluid levels of matrix metalloproteinases in human traumatic brain injury. *Scientific reports*. 2020;10:18075.
136. Schilling KG, Blaber J, Huo Y, Newton A, Hansen C, Nath V, . . . Landman BA. Synthesized b0 for diffusion distortion correction (Synb0-DisCo). *Magnetic resonance imaging*. 2019;64:62-70.
137. Andersson JL, Skare S and Ashburner J. How to correct susceptibility distortions in spin-echo echo-planar images: application to diffusion tensor imaging. *Neuroimage*. 2003;20:870-88.
138. Smith SM, Jenkinson M, Woolrich MW, Beckmann CF, Behrens TE, Johansen-Berg H, . . . Matthews PM. Advances in functional and structural MR image analysis and implementation as FSL. *Neuroimage*. 2004;23 Suppl 1:S208-19.
139. Andersson JLR and Sotiropoulos SN. An integrated approach to correction for off-resonance effects and subject movement in diffusion MR imaging. *Neuroimage*. 2016;125:1063-1078.

140. Garyfallidis E, Brett M, Amirbekian B, Rokem A, van der Walt S, Descoteaux M and Nimmo-Smith I. Dipy, a library for the analysis of diffusion MRI data. *Frontiers in neuroinformatics*. 2014;8:8.
141. Smith SM, Jenkinson M, Johansen-Berg H, Rueckert D, Nichols TE, Mackay CE, . . . Behrens TE. Tract-based spatial statistics: voxelwise analysis of multi-subject diffusion data. *Neuroimage*. 2006;31:1487-505.
142. D'Agostino RB, Wolf PA, Belanger AJ and Kannel WB. Stroke risk profile: Adjustment for antihypertensive medication. The Framingham Study. *Stroke*. 1994;25:40-43.
143. Winkler AM, Ridgway GR, Webster MA, Smith SM and Nichols TE. Permutation inference for the general linear model. *Neuroimage*. 2014;92:381-97.
144. Smith SM and Nichols TE. Threshold-free cluster enhancement: Addressing problems of smoothing, threshold dependence and localisation in cluster inference. *Neuroimage*. 2009;44:83-98.
145. Worsley KJ, Marrett S, Neelin P, Vandal AC, Friston KJ and Evans AC. A unified statistical approach for determining significant signals in images of cerebral activation. *Hum Brain Mapp*. 1996;4:58-73.
146. Lyons SA and Kettenmann H. Oligodendrocytes and microglia are selectively vulnerable to combined hypoxia and hypoglycemia injury in vitro. *J Cereb Blood Flow Metab*. 1998;18:521-30.
147. Nation DA, Sweeney MD, Montagne A, Sagare AP, D'Orazio LM, Pachicano M, . . . Zlokovic BV. Blood-brain barrier breakdown is an early biomarker of human cognitive dysfunction. *Nature medicine*. 2019;25:270-276.
148. Badji A, Noriega de la Colina A, Karakuzu A, Duval T, Desjardins-Crepeau L, Joubert S, . . . Cohen-Adad J. Arterial stiffness and white matter integrity in the elderly: A diffusion tensor and magnetization transfer imaging study. *Neuroimage*. 2018.
149. Moore EE and Jefferson AL. Impact of Cardiovascular Hemodynamics on Cognitive Aging. *Arteriosclerosis, thrombosis, and vascular biology*. 2021:Atvbaha120311909.
150. Montagne A, Barnes SR, Sweeney MD, Halliday MR, Sagare AP, Zhao Z, . . . Zlokovic BV. Blood-brain barrier breakdown in the aging human hippocampus. *Neuron*. 2015;85:296-302.
151. Binnewijzend MA, Kuijer JP, Benedictus MR, van der Flier WM, Wink AM, Wattjes MP, . . . Barkhof F. Cerebral blood flow measured with 3D pseudocontinuous arterial spin-labeling MR imaging in Alzheimer disease and mild cognitive impairment: a marker for disease severity. *Radiology*. 2013;267:221-230.
152. Cooley SA, Cabeen RP, Laidlaw DH, Conturo TE, Lane EM, Heaps JM, . . . Paul RH. Posterior brain white matter abnormalities in older adults with probable mild cognitive impairment. *J Clin Exp Neuropsychol*. 2015;37:61-9.
153. Cambronero FE, Liu D, Neal JE, Moore EE, Gifford KA, Terry JG, . . . Jefferson AL. APOE genotype modifies the association between central arterial stiffening and cognition in older adults. *Neurobiol Aging*. 2018;67:120-127.
154. Bell RD, Winkler EA, Singh I, Sagare AP, Deane R, Wu Z, . . . Zlokovic BV. Apolipoprotein E controls cerebrovascular integrity via cyclophilin A. *Nature*. 2012;485:512-6.

155. Montagne A, Nation DA, Sagare AP and Barisano G. APOE4 leads to blood-brain barrier dysfunction predicting cognitive decline. 2020;581:71-76.
156. Poirier J. Apolipoprotein E, cholesterol transport and synthesis in sporadic Alzheimer's disease. *Neurobiol Aging*. 2005;26:355-61.
157. Saher G, Brugger B, Lappe-Siefke C, Mobius W, Tozawa R, Wehr MC, . . . Nave KA. High cholesterol level is essential for myelin membrane growth. *Nature neuroscience*. 2005;8:468-75.
158. Bartzokis G, Lu PH, Geschwind DH, Edwards N, Mintz J and Cummings JL. Apolipoprotein E genotype and age-related myelin breakdown in healthy individuals: implications for cognitive decline and dementia. *Archives of general psychiatry*. 2006;63:63-72.
159. Rosenberg GA, Sullivan N and Esiri MM. White matter damage is associated with matrix metalloproteinases in vascular dementia. *Stroke*. 2001;32:1162-8.
160. Gurney KJ, Estrada EY and Rosenberg GA. Blood-brain barrier disruption by stromelysin-1 facilitates neutrophil infiltration in neuroinflammation. *Neurobiology of disease*. 2006;23:87-96.
161. Page S, Munsell A and Al-Ahmad AJ. Cerebral hypoxia/ischemia selectively disrupts tight junctions complexes in stem cell-derived human brain microvascular endothelial cells. *Fluids Barriers CNS*. 2016;13:16.
162. Ryu JK and McLarnon JG. A leaky blood-brain barrier, fibrinogen infiltration and microglial reactivity in inflamed Alzheimer's disease brain. *Journal of cellular and molecular medicine*. 2009;13:2911-25.
163. Davalos D, Ryu JK, Merlini M, Baeten KM, Le Moan N, Petersen MA, . . . Akassoglou K. Fibrinogen-induced perivascular microglial clustering is required for the development of axonal damage in neuroinflammation. *Nat Commun*. 2012;3:1227.
164. Chen JJ, Rosas HD and Salat DH. Age-associated reductions in cerebral blood flow are independent from regional atrophy. *Neuroimage*. 2011;55:468-78.
165. Lin JL, Wang MJ, Lee D, Liang CC and Lin S. Hypoxia-inducible factor-1alpha regulates matrix metalloproteinase-1 activity in human bone marrow-derived mesenchymal stem cells. *FEBS letters*. 2008;582:2615-9.
166. Yang Y, Thompson JF, Taheri S, Salayandia VM, McAvoy TA, Hill JW, . . . Rosenberg GA. Early inhibition of MMP activity in ischemic rat brain promotes expression of tight junction proteins and angiogenesis during recovery. *J Cereb Blood Flow Metab*. 2013;33:1104-14.
167. Guevara M, Guevara P, Román C and Mangin JF. Superficial white matter: A review on the dMRI analysis methods and applications. *Neuroimage*. 2020;212:116673.
168. Samolov B, Steen B, Seregard S, van der Ploeg I, Montan P and Kvanta A. Delayed inflammation-associated corneal neovascularization in MMP-2-deficient mice. *Experimental eye research*. 2005;80:159-66.
169. Nakaji K, Ihara M, Takahashi C, Itohara S, Noda M, Takahashi R and Tomimoto H. Matrix metalloproteinase-2 plays a critical role in the pathogenesis of white matter lesions after chronic cerebral hypoperfusion in rodents. *Stroke*. 2006;37:2816-23.
170. Hernandez-Guillamon M, Mawhirt S, Blais S, Montaner J, Neubert TA, Rostagno A and Ghiso J. Sequential Amyloid-β Degradation by the Matrix Metalloproteases MMP-2 and MMP-9. *J Biol Chem*. 2015;290:15078-91.

171. Nübling G, Levin J, Bader B, Israel L, Bötzel K, Lorenzl S and Giese A. Limited cleavage of tau with matrix-metalloproteinase MMP-9, but not MMP-3, enhances tau oligomer formation. *Experimental neurology*. 2012;237:470-6.
172. Morris JC, Roe CM, Xiong C, Fagan AM, Goate AM, Holtzman DM and Mintun MA. APOE predicts amyloid-beta but not tau Alzheimer pathology in cognitively normal aging. *Ann Neurol*. 2010;67:122-31.
173. Ihara M, Tomimoto H, Kinoshita M, Oh J, Noda M, Wakita H, . . . Shibasaki H. Chronic cerebral hypoperfusion induces MMP-2 but not MMP-9 expression in the microglia and vascular endothelium of white matter. *J Cereb Blood Flow Metab*. 2001;21:828-34.
174. Duits FH, Hernandez-Guillamon M, Montaner J, Goos JD, Montañola A, Wattjes MP, . . . van der Flier WM. Matrix Metalloproteinases in Alzheimer's Disease and Concurrent Cerebral Microbleeds. *J Alzheimers Dis*. 2015;48:711-20.
175. McQuibban GA, Gong JH, Tam EM, McCulloch CA, Clark-Lewis I and Overall CM. Inflammation dampened by gelatinase A cleavage of monocyte chemoattractant protein-3. *Science (New York, NY)*. 2000;289:1202-6.
176. Villain N, Fouquet M, Baron JC, Mezenge F, Landeau B, de La Sayette V, . . . Chetelat G. Sequential relationships between grey matter and white matter atrophy and brain metabolic abnormalities in early Alzheimer's disease. *Brain*. 2010;133:3301-14.
177. Racine AM, Adluru N, Alexander AL, Christian BT, Okonkwo OC, Oh J, . . . Johnson SC. Associations between white matter microstructure and amyloid burden in preclinical Alzheimer's disease: A multimodal imaging investigation. *NeuroImage Clinical*. 2014;4:604-14.
178. Caballero MÁ A, Song Z, Rubinski A, Duering M, Dichgans M, Park DC and Ewers M. Age-dependent amyloid deposition is associated with white matter alterations in cognitively normal adults during the adult life span. *Alzheimers Dement*. 2020;16:651-661.
179. Jack CR, Jr., Bennett DA, Blennow K, Carrillo MC, Dunn B, Haeberlein SB, . . . Sperling R. NIA-AA Research Framework: Toward a biological definition of Alzheimer's disease. *Alzheimer's & Dementia: The Journal of the Alzheimer's Association*. 2018;14:535-562.
180. Smith EE. Cerebral amyloid angiopathy as a cause of neurodegeneration. *Journal of neurochemistry*. 2018;144:651-658.
181. Charidimou A, Boulouis G, Haley K, Auriel E, van Etten ES, Fotiadis P, . . . Gurol ME. White matter hyperintensity patterns in cerebral amyloid angiopathy and hypertensive arteriopathy. *Neurology*. 2016;86:505-11.
182. Salat DH, Smith EE, Tuch DS, Benner T, Pappu V, Schwab KM, . . . Greenberg SM. White matter alterations in cerebral amyloid angiopathy measured by diffusion tensor imaging. *Stroke*. 2006;37:1759-64.
183. Janelidze S, Zetterberg H, Mattsson N, Palmqvist S, Vanderstichele H, Lindberg O, . . . Hansson O. CSF Aβ42/Aβ40 and Aβ42/Aβ38 ratios: better diagnostic markers of Alzheimer disease. *Annals of clinical and translational neurology*. 2016;3:154-65.
184. Maruyama M, Arai H, Sugita M, Tanji H, Higuchi M, Okamura N, . . . Sasaki H. Cerebrospinal fluid amyloid beta(1-42) levels in the mild cognitive impairment stage of Alzheimer's disease. *Experimental neurology*. 2001;172:433-6.

185. Schmechel DE, Saunders AM, Strittmatter WJ, Crain BJ, Hulette CM, Joo SH, . . . Roses AD. Increased amyloid beta-peptide deposition in cerebral cortex as a consequence of apolipoprotein E genotype in late-onset Alzheimer disease. *Proc Natl Acad Sci U S A*. 1993;90:9649-9653.
186. Palmqvist S, Zetterberg H, Blennow K, Vestberg S, Andreasson U, Brooks DJ, . . . Hansson O. Accuracy of brain amyloid detection in clinical practice using cerebrospinal fluid beta-amyloid 42: A cross-validation study against amyloid positron emission tomography. *JAMA Neurol*. 2014;71:1282-1289.
187. Nishioka C, Liang HF, Barsamian B and Sun SW. Amyloid-beta induced retrograde axonal degeneration in a mouse tauopathy model. *Neuroimage*. 2019;189:180-191.
188. Vukic V, Callaghan D, Walker D, Lue LF, Liu QY, Couraud PO, . . . Zhang W. Expression of inflammatory genes induced by beta-amyloid peptides in human brain endothelial cells and in Alzheimer's brain is mediated by the JNK-AP1 signaling pathway. *Neurobiology of disease*. 2009;34:95-106.
189. Hensley K, Carney JM, Mattson MP, Aksenova M, Harris M, Wu JF, . . . Butterfield DA. A model for beta-amyloid aggregation and neurotoxicity based on free radical generation by the peptide: relevance to Alzheimer disease. *Proc Natl Acad Sci U S A*. 1994;91:3270-4.
190. Mattsson-Carlgren N, Andersson E, Janelidze S, Ossenkoppele R, Insel P, Strandberg O, . . . Hansson O. Aβ deposition is associated with increases in soluble and phosphorylated tau that precede a positive Tau PET in Alzheimer's disease. *Science advances*. 2020;6:eaaz2387.
191. Thomas DX, Bajaj S, McRae-McKee K, Hadjichrysanthou C, Anderson RM and Collinge J. Association of TDP-43 proteinopathy, cerebral amyloid angiopathy, and Lewy bodies with cognitive impairment in individuals with or without Alzheimer's disease neuropathology. *Scientific reports*. 2020;10:14579.
192. Turken A, Whitfield-Gabrieli S, Bammer R, Baldo JV, Dronkers NF and Gabrieli JD. Cognitive processing speed and the structure of white matter pathways: convergent evidence from normal variation and lesion studies. *Neuroimage*. 2008;42:1032-44.
193. Barbey AK, Colom R, Solomon J, Krueger F, Forbes C and Grafman J. An integrative architecture for general intelligence and executive function revealed by lesion mapping. *Brain*. 2012;135:1154-64.
194. Tai LM, Thomas R, Marottoli FM, Koster KP, Kanekiyo T, Morris AW and Bu G. The role of APOE in cerebrovascular dysfunction. *Acta Neuropathol*. 2016;131:709-23.
195. Momjian-Mayor I and Baron JC. The pathophysiology of watershed infarction in internal carotid artery disease: review of cerebral perfusion studies. *Stroke*. 2005;36:567-77.
196. Jacobs HIL, Hedden T, Schultz AP, Sepulcre J, Perea RD, Amariglio RE, . . . Johnson KA. Structural tract alterations predict downstream tau accumulation in amyloid-positive older individuals. *Nature neuroscience*. 2018;21:424-431.
197. Maruyama M, Matsui T, Tanji H, Nemoto M, Tomita N, Ootsuki M, . . . Sasaki H. Cerebrospinal fluid tau protein and periventricular white matter lesions in patients with mild cognitive impairment: implications for 2 major pathways. *Arch Neurol*. 2004;61:716-20.

198. Mitchell AJ. CSF phosphorylated tau in the diagnosis and prognosis of mild cognitive impairment and Alzheimer's disease: a meta-analysis of 51 studies. *J Neurol Neurosurg Psychiatry*. 2009;80:966-75.
199. Liraz O, Boehm-Cagan A and Michaelson DM. ApoE4 induces Aβ42, tau, and neuronal pathology in the hippocampus of young targeted replacement apoE4 mice. *Mol Neurodegener*. 2013;8:16.
200. Friede RL and Samorajski T. Axon caliber related to neurofilaments and microtubules in sciatic nerve fibers of rats and mice. *The Anatomical Record*. 1970;167:379-387.
201. Melah KE, Lu SY, Hoscheidt SM, Alexander AL, Adluru N, Destiche DJ, . . . Bendlin BB. Cerebrospinal Fluid Markers of Alzheimer's Disease Pathology and Microglial Activation are Associated with Altered White Matter Microstructure in Asymptomatic Adults at Risk for Alzheimer's Disease. *J Alzheimers Dis*. 2016;50:873-886.
202. Zetterberg H, Hietala MA, Jonsson M, Andreasen N, Styrud E, Karlsson I, . . . Wallin A. Neurochemical aftermath of amateur boxing. *Arch Neurol*. 2006;63:1277-80.
203. Skillback T, Farahmand B, Bartlett JW, Rosen C, Mattsson N, Nagga K, . . . Zetterberg H. CSF neurofilament light differs in neurodegenerative diseases and predicts severity and survival. *Neurology*. 2014;83:1945-1953.
204. Petzold A. Neurofilament phosphoforms: surrogate markers for axonal injury, degeneration and loss. *Journal of the neurological sciences*. 2005;233:183-98.
205. Marmarou CR and Povlishock JT. Administration of the immunophilin ligand FK506 differentially attenuates neurofilament compaction and impaired axonal transport in injured axons following diffuse traumatic brain injury. *Experimental neurology*. 2006;197:353-62.
206. Zetterberg H, Skillback T, Mattsson N, Trojanowski JQ, Portelius E, Shaw LM, . . . Blennow K. Association of cerebrospinal fluid neurofilament light concentration with Alzheimer disease progression. *JAMA Neurol*. 2016;73:60-67.
207. McIver SR, Muccigrosso M, Gonzales ER, Lee JM, Roberts MS, Sands MS and Goldberg MP. Oligodendrocyte degeneration and recovery after focal cerebral ischemia. *Neuroscience*. 2010;169:1364-75.
208. Bruno D, Pomara N, Nierenberg J, Ritchie JC, Lutz MW, Zetterberg H and Blennow K. Levels of cerebrospinal fluid neurofilament light protein in healthy elderly vary as a function of TOMM40 variants. *Experimental gerontology*. 2012;47:347-52.
209. Delaby C, Alcolea D, Carmona-Iragui M, Illán-Gala I, Morenas-Rodríguez E, Barroeta I, . . . Lleó A. Differential levels of Neurofilament Light protein in cerebrospinal fluid in patients with a wide range of neurodegenerative disorders. *Scientific reports*. 2020;10:9161.
210. Martin SJ, McGlasson S, Hunt D and Overell J. Cerebrospinal fluid neurofilament light chain in multiple sclerosis and its subtypes: a meta-analysis of case-control studies. *J Neurol Neurosurg Psychiatry*. 2019;90:1059-1067.
211. Shahim P, Politis A, van der Merwe A, Moore B, Chou YY, Pham DL, . . . Chan L. Neurofilament light as a biomarker in traumatic brain injury. *Neurology*. 2020;95:e610-e622.

212. Pujol-Calderón F, Portelius E, Zetterberg H, Blennow K, Rosengren LE and Höglund K. Neurofilament changes in serum and cerebrospinal fluid after acute ischemic stroke. *Neurosci Lett*. 2019;698:58-63.
213. Gunning-Dixon FM, Brickman AM, Cheng JC and Alexopoulos GS. Aging of cerebral white matter: a review of MRI findings. *International journal of geriatric psychiatry*. 2009;24:109-17.
214. Mevel K, Chételat G, Eustache F and Desgranges B. The default mode network in healthy aging and Alzheimer's disease. *International journal of Alzheimer's disease*. 2011;2011:535816.
215. Greicius MD, Srivastava G, Reiss AL and Menon V. Default-mode network activity distinguishes Alzheimer's disease from healthy aging: evidence from functional MRI. *Proc Natl Acad Sci U S A*. 2004;101:4637-42.
216. Pereira JB, Ossenkoppele R, Palmqvist S, Strandberg TO, Smith R, Westman E and Hansson O. Amyloid and tau accumulate across distinct spatial networks and are differentially associated with brain connectivity. *eLife*. 2019;8.
217. Hoenig MC, Bischof GN, Seemiller J, Hammes J, Kukolja J, Onur Ö A, . . . Drzezga A. Networks of tau distribution in Alzheimer's disease. *Brain*. 2018;141:568-581.
218. Acosta-Cabronero J, Williams GB, Pengas G and Nestor PJ. Absolute diffusivities define the landscape of white matter degeneration in Alzheimer's disease. *Brain*. 2010;133:529-39.
219. Huang J and Auchus AP. Diffusion tensor imaging of normal appearing white matter and its correlation with cognitive functioning in mild cognitive impairment and Alzheimer's disease. *Annals of the New York Academy of Sciences*. 2007;1097:259-64.
220. Honea RA, Vidoni E, Harsha A and Burns JM. Impact of APOE on the healthy aging brain: a voxel-based MRI and DTI study. *J Alzheimers Dis*. 2009;18:553-64.
221. Brickman AM, Zimmerman ME, Paul RH, Grieve SM, Tate DF, Cohen RA, . . . Gordon E. Regional white matter and neuropsychological functioning across the adult lifespan. *Biological psychiatry*. 2006;60:444-53.
222. Van Essen DC, Smith SM, Barch DM, Behrens TE, Yacoub E and Ugurbil K. The WU-Minn Human Connectome Project: an overview. *Neuroimage*. 2013;80:62-79.
223. Archer DB, Vaillancourt DE and Coombes SA. A Template and Probabilistic Atlas of the Human Sensorimotor Tracts using Diffusion MRI. *Cereb Cortex*. 2018;28:1685-1699.
224. Archer DB, Coombes SA, McFarland NR, DeKosky ST and Vaillancourt DE. Development of a transcallosal tractography template and its application to dementia. *Neuroimage*. 2019;200:302-312.
225. Archer DB, Bricker JT, Chu WT, Burciu RG, McCracken JL, Lai S, . . . Vaillancourt DE. Development and Validation of the Automated Imaging Differentiation in Parkinsonism (AID-P): A Multi-Site Machine Learning Study. *The Lancet Digital health*. 2019;1:e222-e231.
226. Archer DB, Moore EE, Shashikumar N, Dumitrescu L, Pechman KR, Landman BA, . . . Hohman TJ. Free-water metrics in medial temporal lobe white matter tract projections relate to longitudinal cognitive decline. *Neurobiol Aging*. 2020;94:15-23.
227. Brown CA, Johnson NF, Anderson-Mooney AJ, Jicha GA, Shaw LM, Trojanowski JQ, . . . Gold BT. Development, validation and application of a new fornix template for

studies of aging and preclinical Alzheimer's disease. *NeuroImage Clinical*. 2017;13:106-115.
228. Kaplan E, Goodglass H and Weintraub S. *The Boston Naming Test.* 3 ed. Philadelphia, PA: Lea & Febiger; 1983.
229. Goodglass H and Kaplan E. *The assessment of aphasia and related disorders.* 2 ed. Philadelphia, PA: Lea & Febiger; 1983.
230. Wechsler D. *Wechsler Adult Intelligence Scale- 4th Edition*. San Antonio, TX Pearson; 2008.
231. Delis DC, Kaplan E and Kramer JH. *Delis-Kaplan Executive Function System (D-KEFS): Examiner's Manual*. San Antonio, TX: The Psychological Corporation; 2001.
232. Benton AL, Hamsher K and Sivan AB. *Multilingual Aphasia Examination.* 3 ed. Iowa City, IA: AJA Associates; 1994.
233. Hooper H. *Hooper Visual Organization Test (HVOT)*. Los Angeles, CA: Western Psychological Services; 1983.
234. Glosser G, Cole L, Khatri U, DellaPietra L and Kaplan E. Assessing nonverbal memory with the Biber Figure Learning Test - extended in temporal lobe epilepsy patients. *Archives of clinical neuropsychology : the official journal of the National Academy of Neuropsychologists*. 2002;17:25-35.
235. Delis DC, Kramer J, Kaplan E and Ober B. *California Verbal Learning Test–II, Second Edition*. San Antonio, TX: The Psychological Corporation; 2000.
236. Kresge HA, Khan OA, Wagener MA, Liu D, Terry JG, Nair S, . . . Jefferson AL. Subclinical Compromise in Cardiac Strain Relates to Lower Cognitive Performances in Older Adults. *Scientific reports*. 2018;7.
237. Madden DJ, Bennett IJ, Burzynska A, Potter GG, Chen NK and Song AW. Diffusion tensor imaging of cerebral white matter integrity in cognitive aging. *Biochim Biophys Acta*. 2012;1822:386-400.
238. Russchen FT, Bakst I, Amaral DG and Price JL. The amygdalostriatal projections in the monkey. An anterograde tracing study. *Brain research*. 1985;329:241-57.
239. Scherr M, Krenn Y, Sorg C, Manoliu A, Trinka E, Förstl H, . . . McCoy M. Patterns of cognitive performance in Subcortical Ischemic Vascular Disease (SIVD). *The Journal of neuropsychiatry and clinical neurosciences*. 2014;26:150-4.
240. Wu TC, Wilde EA, Bigler ED, Yallampalli R, McCauley SR, Troyanskaya M, . . . Levin HS. Evaluating the relationship between memory functioning and cingulum bundles in acute mild traumatic brain injury using diffusion tensor imaging. *Journal of neurotrauma*. 2010;27:303-7.
241. Gozdas E, Fingerhut H, Chromik LC, O'Hara R, Reiss AL and Hosseini SMH. Focal white matter disruptions along the cingulum tract explain cognitive decline in amnestic mild cognitive impairment (aMCI). *Scientific reports*. 2020;10:10213.
242. Catheline G, Periot O, Amirault M, Braun M, Dartigues J-F, Auriacombe S and Allard M. Distinctive alterations of the cingulum bundle during aging and Alzheimer's disease. *Neurobiol Aging*. 2010;31:1582-1592.
243. Fujie S, Namiki C, Nishi H, Yamada M, Miyata J, Sakata D, . . . Murai T. The role of the uncinate fasciculus in memory and emotional recognition in amnestic mild cognitive impairment. *Dementia and geriatric cognitive disorders*. 2008;26:432-9.

244. Diehl B, Busch RM, Duncan JS, Piao Z, Tkach J and Lüders HO. Abnormalities in diffusion tensor imaging of the uncinate fasciculus relate to reduced memory in temporal lobe epilepsy. *Epilepsia*. 2008;49:1409-18.
245. Alexander RP, Concha L, Snyder TJ, Beaulieu C and Gross DW. Correlations between Limbic White Matter and Cognitive Function in Temporal-Lobe Epilepsy, Preliminary Findings. *Front Aging Neurosci*. 2014;6:142.
246. Kalaria RN. Cerebrovascular disease and mechanisms of cognitive impairment: evidence from clinicopathological studies in humans. *Stroke*. 2012;43:2526-34.
247. Lebel C, Walker L, Leemans A, Phillips L and Beaulieu C. Microstructural maturation of the human brain from childhood to adulthood. *Neuroimage*. 2008;40:1044-55.
248. Penke L, Muñoz Maniega S, Murray C, Gow AJ, Hernández MC, Clayden JD, . . . Deary IJ. A general factor of brain white matter integrity predicts information processing speed in healthy older people. *J Neurosci*. 2010;30:7569-74.
249. Sutherland RJ and Rodriguez AJ. The role of the fornix/fimbria and some related subcortical structures in place learning and memory. *Behavioural brain research*. 1989;32:265-77.
250. Burzynska AZ, Jiao Y, Knecht AM, Fanning J, Awick EA, Chen T, . . . Kramer AF. White Matter Integrity Declined Over 6-Months, but Dance Intervention Improved Integrity of the Fornix of Older Adults. *Front Aging Neurosci*. 2017;9:59.
251. Valdés Cabrera D, Stobbe R, Smyth P, Giuliani F, Emery D and Beaulieu C. Diffusion tensor imaging tractography reveals altered fornix in all diagnostic subtypes of multiple sclerosis. *Brain and behavior*. 2020;10:e01514.
252. Ng VW, Bullmore ET, de Zubicaray GI, Cooper A, Suckling J and Williams SC. Identifying rate-limiting nodes in large-scale cortical networks for visuospatial processing: an illustration using fMRI. *J Cogn Neurosci*. 2001;13:537-45.
253. Tekin S and Cummings JL. Frontal-subcortical neuronal circuits and clinical neuropsychiatry: an update. *J Psychosom Res*. 2002;53:647-54.
254. Reineberg AE, Andrews-Hanna JR, Depue BE, Friedman NP and Banich MT. Resting-state networks predict individual differences in common and specific aspects of executive function. *Neuroimage*. 2015;104:69-78.
255. Saunders NL and Summers MJ. Longitudinal deficits to attention, executive, and working memory in subtypes of mild cognitive impairment. *Neuropsychology*. 2011;25:237-48.
256. Binetti G, Cappa SF, Magni E, Padovani A, Bianchetti A and Trabucchi M. Visual and spatial perception in the early phase of Alzheimer's disease. *Neuropsychology*. 1998;12:29-33.
257. Backman L, Jones S, Berger AK, Laukka EJ and Small BJ. Cognitive impairment in preclinical Alzheimer's disease: a meta-analysis. *Neuropsychology*. 2005;19:520-31.
258. Iachini I, Iavarone A, Senese VP, Ruotolo F and Ruggiero G. Visuospatial memory in healthy elderly, AD and MCI: a review. *Current aging science*. 2009;2:43-59.
259. Eckert M, Keren N, Roberts D, Calhoun V and Harris K. Age-related changes in processing speed: Unique contributions of cerebellar and prefrontal cortex. *Frontiers in human neuroscience*. 2010;4:10.

260. Summers MJ and Saunders NL. Neuropsychological measures predict decline to Alzheimer's dementia from mild cognitive impairment. *Neuropsychology*. 2012;26:498-508.
261. Brickman AM, Schupf N, Manly JJ, Stern Y, Luchsinger JA, Provenzano FA, . . . Portet F. APOE epsilon4 and risk for Alzheimer's disease: do regionally distributed white matter hyperintensities play a role? *Alzheimers Dement*. 2014;10:619-29.
262. Santangelo G, Trojano L, Vitale C, Improta I, Alineri I, Meo R and Bilo L. Cognitive dysfunctions in occipital lobe epilepsy compared to temporal lobe epilepsy. *Journal of neuropsychology*. 2017;11:277-290.
263. Salminen LE, Schofield PR, Lane EM, Heaps JM, Pierce KD, Cabeen R, . . . Paul RH. Neuronal fiber bundle lengths in healthy adult carriers of the ApoE4 allele: a quantitative tractography DTI study. *Brain imaging and behavior*. 2013;7:274-81.
264. Bergamino M, Walsh RR and Stokes AM. Free-water diffusion tensor imaging improves the accuracy and sensitivity of white matter analysis in Alzheimer's disease. *Scientific reports*. 2021;11:6990.
265. Cummings J, Lee G, Ritter A, Sabbagh M and Zhong K. Alzheimer's disease drug development pipeline: 2020. *Alzheimer's & dementia (New York, N Y)*. 2020;6:e12050.
266. Laing KK, Simoes S, Baena-Caldas GP, Lao PJ, Kothiya M, Igwe KC, . . . Brickman AM. Cerebrovascular disease promotes tau pathology in Alzheimer's disease. *Brain communications*. 2020;2:fcaa132.
267. Albrecht D, Isenberg AL, Stradford J, Monreal T, Sagare A, Pachicano M, . . . Pa J. Associations between Vascular Function and Tau PET Are Associated with Global Cognition and Amyloid. *J Neurosci*. 2020;40:8573-8586.
268. Moore EE, Liu D, Li J, Schimmel SJ, Cambronero FE, Terry JG, . . . Jefferson AL. Association of aortic stiffness with biomarkers of neuroinflammation, synpatic dysfunction, and neurodegeneration. *Neurology*. In Press.
269. Pooler AM, Polydoro M, Maury EA, Nicholls SB, Reddy SM, Wegmann S, . . . Hyman BT. Amyloid accelerates tau propagation and toxicity in a model of early Alzheimer's disease. *Acta Neuropathol Commun*. 2015;3:14.
270. Alexander AL, Hasan KM, Lazar M, Tsuruda JS and Parker DL. Analysis of partial volume effects in diffusion-tensor MRI. *Magn Reson Med*. 2001;45:770-80.
271. Pasternak O, Sochen N, Gur Y, Intrator N and Assaf Y. Free water elimination and mapping from diffusion MRI. *Magn Reson Med*. 2009;62:717-30.
272. Zhang H, Schneider T, Wheeler-Kingshott CA and Alexander DC. NODDI: practical in vivo neurite orientation dispersion and density imaging of the human brain. *Neuroimage*. 2012;61:1000-16.